International Committee for Future Accelerators

Sponsored by the Particles and Fields Commission of IUPAP

Beam Dynamics
Newsletter

No. 62

Issue Editors:
M. E. Biagini, Y. Papaphilippou

Editor in Chief:
W. Chou

December 2013

Contents

1 Foreword

1.1 From the ICFA Chair

Nigel Lockyer, Fermilab
Mail to: lockyer@fnal.gov

This short forward is to thank Pier Oddone for his leadership of International Committee for Future Accelerators (ICFA) for the last three years and highlight his accomplishments as Chair. The most impressive accomplishment which has just been completed during Pier's tenure, is the report for the ILC Global Design Effort (GDE). The International Linear Collider Steering Committee (ILCSC), a subcommittee of ICFA performed research and development (R&D) efforts aimed at a 500-1000 GeV electron-positron linear collider. Major laboratories around the world have invested in linear collider accelerator technology for more than a decade. The GDE was the first time all three regions have worked together on a common goal with such a lofty ambition. Barry Barish, as GDE Director, with guidance from ICFA and ILCSC, was able to accomplish the goals as laid out eight years ago.

In order to provide an international framework for the ILC technical design, the ILCSC drafted a Memorandum of Understanding (MoU), which was signed in 2005 by ILCSC members representing their laboratories to jointly create the Global Design Effort (GDE).

Several phases followed and by the end of 2012 the GDE had successfully completed the Technical Design Report (TDR) and submitted it to the ILCSC. After technical and cost reviews, the final version of the TDR was completed in June 2013. The next phase, which aims at working towards the construction of the ILC, has been taken over by the Linear Collider Collaboration (LCC) that is led by the Directorate of the Central Team (the successor of the GDE) and overseen by the Linear Collider Board (the successor of the ILCSC) established again by ICFA.

The Technical Design Report completion was one milestone while the achievements in R&D were also very significant. In particular is the accomplishment associated with consistent high gradients of the superconducting cavities. The GDE delivered a cost that was reviewed and accepted by FALC, the Funding Agencies for Large Colliders. The outreach efforts were considerable, including a team of communicators, an annual "International Accelerator School for Linear Colliders," and a linear collider conference.

As major particle physics projects become more costly, and sharing of costs becomes essential, ICFA will have a more important role to play. I encourage my colleagues on ICFA to be proactive and work towards developing a plan for international collaboration.

1.2   From the Beam Dynamics Panel Chair

Weiren Chou, Fermilab
Mail to: chou@fnal.gov

Nigel Lockyer, Director of Fermilab and new ICFA Chair, wrote a forward in this issue of the Newsletter. He highlighted the progresses of the International Linear Collider (ILC) in the past years under the guidance of the ICFA and encouraged people to be proactive and work towards developing a plan for international collaboration.

Thanks to the extensive efforts of the HEP communities in the past months in all three regions – Asia, Europe and North America – the world HEP program in the next 10-20 years is taking shape. In Europe, the highest priority is the LHC, which will dominate the world HEP program in the foreseeable future. CERN has also launched a study on Future Circular Colliders (FCC). The goal is to build a new 80-100 km ring to accommodate a future 100 TeV proton-proton collider (VHE-LHC), with an intermediate phase to build an e^+e^- collider serving as a Higgs factory (TLEP). The P5, which will set priorities for the US HEP program, is making progress. The emphasis will be on the Long Baseline Neutrino Experiment (LBNE) with a large underground liquid argon detector. In the meantime, Project X will be replaced by PIP-II, a plan to increase the power on the neutrino target to above 1 MW by constructing a new 800 MeV SRF linac at Frmilab. Japan is focused on the ILC. The Japanese government has initiated an investigation for possible cost sharing among various countries with the goal of hosting the ILC construction in Japan. China has started a study on an energy-frontier circular collider termed CEPC-SppC, which would be a 50-70 km ring, first for an e^+e^- collider (a Higgs factory), then upgraded to a superconducting pp collider.

In addition to these exciting developments in the "traditional" particle accelerator field, significant progress is being made in the collaboration between accelerator and laser communities. For example, there is an active discussion on possible application of the fibre laser technology for a circular $\gamma\gamma$ collider, which could lead to a breakthrough to a new type of colliders.

The Eighth International Accelerator School for Linear Colliders (http://www.linearcollider.org/school/2013/), organized jointly by the Linear Collider Collaboration (LCC) and ICFA Beam Dynamics Panel and hosted by the Institute of Accelerator Technologies (IAT) of Ankara University, took place from December 4 to 15, 2013 at Hotel Rixos Downtown, Antalya, Turkey. A report can be found in Section 4.2.

The editors of this issue are Dr. Marica Biagini, a panel member from INFN-LNF, Italy, and Dr. Yannis Papaphilippou from CERN, Switzerland. The theme is "*The CLIC Challenge.*" They collected 17 well-written articles that give a comprehensive review of the CLIC technical challenges.

In this issue there are four activity reports (SPARC, Swiss Light Source, Australian Synchrotron Storage Ring and PETRA III), two articles in memoriam of Gus Voss (one by DESY, another by Herman Winick), a workshop report (FFAG'13), three workshops announcements (LOWeRING, EIC'14, ICFA mini-workshop on wakefields and impedance), and five doctoral thesis abstracts (Xiaohao Cui, IHEP, China; Matthias Scholz, Univ. of Hamburg, Germany; Grygorii Vashchenko, Univ. of Hamburg, Germany; Simone Maria Liuzzo, Univ. of Roma Tor Vergata, Italy; and Yi Wei Wang,

IHEP, China). I thank Marica and Yannis for editing and producing a newsletter of rich contents and high quality for our community.

1.3   From the Editors

M. E. Biagini, INFN-Laboratori Nazionali di Frascati
Mail to: marica.biagini@lnf.infn.it

Y. Papaphilippou, CERN
Mail to: ioannis.papaphilippou@cern.ch

The Theme articles in **Section 2** start with a review of the CLIC project status and perspectives by **E. Adli**. The CLIC complex is Multi-TeV e+/e-collider, to be built in stages, based on normal-conducting X-band technology and composed by many quite complicated pieces: Combiner Rings, Delay Loops, Damping Ring, Linac, Drive Beam generation section, Beam Delivery System. A Conceptual Design Report was completed in 2012. The CLIC study will continue, until 2018, with technical studies on power and cost optimization, system tests including full CLIC module tests with rf and beam, and experimental verifications of methods to preserve nm emittances. The R&D on CLIC drive beam sources is described by **S. Doebert**, including the optimization longitudinal beam dynamics of the injectors by **S. Sanaye Hajari**, the design of the wide band bunchers by **Hamed Shaker**, and the developments on the thermionic gun. The CLIC Beam Delivery System and QD0 quadrupole design were already presented in the Newsletter n.61 (August 2013), dedicated to the Final Focus systems of Linear Colliders, however they are repeated here for completeness in two separate and more detailed papers by **R. Tomas** and **M. Modena**. **A. Latina** presents the studies done for emittance preservation through the RTML (the "Ring to Main Linac" section that transports the beam from the damping ring extraction to the main Linac entrance) and the main Linac (about 50 km in total). The X-band RF design of the CLIC Main Linac accelerating Structure is the subject of the paper by **A. Grudiev**, with a description of the cavity design, wakefields estimation, wakefield monitor and fabrication tolerances. The design of the CLIC Power Extraction and Transfer Structure (PETS) is reported by **I. Syratchev**, a key component to generate the short (250 ns) high peak power (135 MW) RF pulses by decelerating a high current (100 A) bunched (12 GHz) drive beam. The feasibility such high RF power generation using the drive beam was successfully demonstrated in a dedicated testing program conducted at CERN in the years 2008-2012. The alignment of passive and active components along the CLIC accelerator shall reach unprecedented small values at micrometer level and with nanometer resolution: a study on Particle Accelerator Components Metrology and Alignment to the Nanometer scale (PACMAN), a EU funded "Initial Training Network" project, is reported by **H. Mainaud Durand** et al. Achieving high luminosity in CLIC will require colliding beams with nanometer spot size and short bunch length: this puts a high demand on the performances of most of the beam instrumentation systems. **T. Lefevre** presents a review of the status of some of the current developments. The CLIC high charge density beams will require non-invasive diagnostic systems. In alternative to the laser wire scanners, Diffraction Radiation (DR) monitors are being investigated. Experimental validation of this technique is in progress at CesrTA and is described by **L. Bobb**. A particularly challenging system of CLIC is certainly the Damping Ring (DR), which

requires ultra-low emittance and high intensity bunches with high stability. The status of the DR design is presented in an exhaustive paper by **Y. Papaphilippou**, which summarizes the parameters choice, optics design, wiggler specifications, study of collective effects and injection/extraction requirements. Related to the DR topics are the instability studies and impedance measurements presented by **E. Koukovini Platia**, the SC wiggler design and experimental plans by **A. Bernhard**, and the stripline kicker design for the beam extraction from DR reported by **C. Belver-Aguilar**. The CLIC Test Facility CTF3 was built at CERN to prove the main feasibility issues of the two-beam acceleration technology. CTF3 consists of a 150 MeV electron Linac followed by a 42 m long Delay Loop and a 84 m Combiner Ring, and was a big success, its progresses and plans are reviewed by **R. Corsini** et al. Results of the CTF3 two beams test stand, where individual components and complete modules can be tested, are described by **R. Ruber**. The two beams acceleration scheme asks for precise synchronization between the Main Beam and the RF power produced by the Drive Beam in order to keep the energy of the Main Beam constant. This synchronization must be implemented by means of a feed-forward system, where the two beams arrival time are compared and the proper correction is applied to the Drive Beam. The cavity monitor and stripline kicker design are presented by **F. Marcellini**.

Section 3 contains other interesting papers on different topics. C-band Linac technology is a hot topic and **D. Alesini** reports on the recent work performed at LNF for the SPARC facility upgrade in energy, under the TIARA EU FP7 program, where two accelerating sections in C-band were designed, constructed and tested. This work will allow to get the necessary know-how to build similar structures also for other future projects. The effort in reaching and measuring very low emittances in modern Synchrotron Light Sources is a key issue. Two articles by **A. Streun** et al (Swiss Light Source at PSI) and by **M. Borland** (Australian Light Source at Melbourne) describe how they got to achieve and measure their picometer vertical emittances with new instrumentation and methods. In the same field, **A. Kling and R. Wanzenberg** report on Beam Dynamics Activities at PETRA III, that since January 2013 is running with electrons. To contribute to the R&D for an "ultimate storage ring (USR)", diffraction limited next generation SR, the ring was operated at an energy of 3 GeV for the first time during a study period in July 2013. It was possible to achieve a horizontal emittance of 160 pm rad which seems to be a new world record with respect to smallest achieved beam emittance in storage rings.

As many of us know, Professor **Gustav-Adolf Voss**, former Director of the DESY Accelerator Division, passed away on October 5th in Hamburg. He dedicated his life to our field and will be remembered for his many contributions, the latest being the donation of the BESSY I ring to the Middle East community for the SESAME project in Jordan. He will be also rememebered for his defence of human rights. We host here the DESY mourning article and a beautiful personal contribution from his longlife friend Prof. **Herman Winick** of SSRL (SLAC), who has also been the principal motor of the SESAME enterprise.

For the **Section 4** on Workshop and Events report we have the report on 2013 Linear Collider School by our Chairman **W. Chou**, and the report on the FFAG Workshop by **S. Koscielniak**.

Five recent doctoral theses are reported in **Section 5**, on "Lattice Design and beam dynamics study of ERL-FEL test-facility at IHEP, Beijing" by X. Cui from IHEP, "Design of the Extraction Arc for the 2nd Beam Line of the Free–Electron Laser

FLASH" by M. Scholz, and "Transverse phase space studies with the new CDS booster cavity at PITZ", by G. Vashchenko both from DESY, "Optimization studies and measurements for ultra-low emittance lattices" by S.M. Liuzzo from Rome II University and ESRF, "Study on the Beam Dynamics of the CLIC Main Linac and the Beam Optics of the ILC/CEPC Final Focus System" by Y. Wang from IHEP.

In **Section 6** are announced two interesting beam dynamics events:

* EIC14, International Workshop on Accelerator Science and Technology for Electron-Ion Colliders, that will be held March 17-21, 2014 at Jefferson Lab, Virginia (US),
* Mini-Workshop on "Electromagnetic wake fields in particle accelerators" to be held in April 23-29, 2014 at Erice (Italy).

Finally, we wish to thank the CLIC scientists who took some of their time to review for us the most interesting topics and results of this challenging project, making this Issue a very dense one. In particular, one of the editors (MEB) wish to thank Y. Papaphilippou who did a great work to set up the table of contents and convinced CLIC colleagues to write for us.

The most grateful acknowledgments go of course to Manuela Giabbai (LNF), who assisted us in the editing, getting quite crazy in the effort of harmonize the format of the many, different papers and pictures.

We hope you will enjoy this Newsletter and you will find it useful for your personal knowledge and your activity in the Accelerator Physics and Technology fields.

2   Theme Section: The CLIC Challenge

2.1   The CLIC Project - Status and Prospects

Erik Adli, University of Oslo, Norway
On behalf of the CLIC/CTF3 collaboration
Mail to: Erik.Adli@fys.uio.no

2.1.1   **Introduction**

The high luminosity of a linear collider, at the lowest power, requires the generation of ultra-low emittance high-intensity bunches, with remarkable stability. Although conventional electron sources and positron production schemes provide beams with the intensity required, the emittances are several orders of magnitude larger than the ones needed. The natural synchrotron radiation damping of the beam when circulating in rings is the cooling mechanism used to reach these small emittances. The CLIC project is a study for a Multi-TeV e+/e-collider, to be built in stages, based on normal-conducting X band technology. A Two-Beam Acceleration scheme is used in order to provide compressed rf pulses for the main accelerating structures with high efficiency. The compressed rf pulses allow the main charge to be accelerated at a very high loaded gradient of 100 MV/m, in short beam pulses of 156 ns. Figure 1 shows the layout for a 3 TeV center of mass machine, illustrating the two-beam acceleration scheme. CLIC completed the CDR in 2012 [1]. The project is currently in a project preparation phase

where further optimization, system tests and detailed design of the machine is taking place, in a global collaboration of volunteer institutes. In addition, the CLIC project has started collaborations for the use of CLIC X band technology in compact free electron lasers and medical applications. The CLIC project is linked to the European Strategy Particle Physics priorities related to the Energy Frontier. The LHC may discover Beyond Standard Model physics when operation starts at full energy in 2015 and, depending on the findings, higher-energy hadrons as part of LHC energy upgrades or a high energy e+ e- collider might be the best option to access the new physics. The CLIC work in this period is also integrated in the Linear Collider collaboration, where the ILC technology provides an option for an early exploration of the Higgs sector in particular, while CLIC remains the only option for a Multi-TeV e+ e- collider. Wherever possible, shared activities for ILC and CLIC are being coordinated. This overview article reviews the main conclusions of the Conceptual Design Report and outlines key activities foreseen in the project period from 2012 to 2018, which we will refer to as the "next period"

2.1.2 Conceptual Design Report

The CLIC conceptual design report (CDR) was completed in 2012, and documents a proof of principle of all aspects related to the Two-Beam Acceleration scheme, both by comprehensive simulation studies of all parts of the machine and by a detailed experimental program in the CLIC Test Facility 3 at CERN [2]. Figure 2 shows a) the CLIC Test Facility Two-Beam Test Stand and b) data points for the achieved two-beam accelerating gradient as function of input power to the X band accelerating structure. Drive beam generation has been verified and the achieved gradient is up to and beyond the CLIC target of 100 MV/m. Furthermore, ongoing rf based tests of the main linac structure gradient are close to or on target for all parameters (gradient, pulse length and breakdown rate), and Figure 3 shows a summary of the latest results. Uncertainty from beam loading will be tested in the current next period. Studies of the deceleration versus power production show good consistency [3]. Concerning emittance generation, the CLIC damping ring has similar specification to an ambitious light source, and no showstoppers were identified for generation of the ultra low emittances. Concerning emittance preservation, the alignment system principle has been demonstrated, the stabilization system have been developed and benchmarked and integrated simulations of emittance preservation in the main linac meet or exceed the luminosity targets.
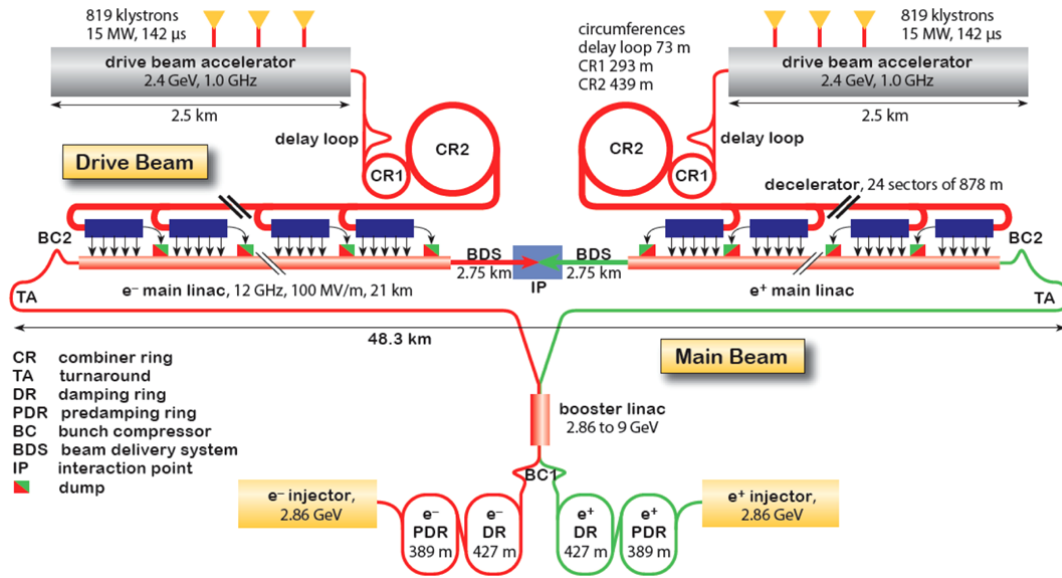
Figure 1: The layout of the 3 TeV CLIC accelerator complex. The main beams are generated and pre-accelerated in the injector linacs and then enter the damping rings for emittance reduction (lower part of the figure). The normalized beam emittances are 500 nm and 5 nm in the horizontal and vertical planes respectively at the exit of the injector complex. The small emittance beams are further accelerated in a common linac before being transported through the main tunnel to the turnarounds. After the turnarounds the beams are accelerated in the main linac with an accelerating gradient of 100 MV/m. The 12 GHz rf power for the accelerating structures are generated by extracting the energy of electron drive beams in decelerator, running in parallel with the main linac accelerators. The top part of the figure shows the Drive Beam generation and the successive time compression of the drive beam pulses in the delay loops and combiner rings (CR1 and CR2). The time-compressed drive beam reaches a current of 100 A at a beam energy of 2.4 GeV. The compressed drive beam is transported through the main linac tunnel. The beams collide after a long beam delivery section (BDS) in one interaction point (IP) in the centre of the complex, where two detectors share the beam-time in a push-pull detector configuration.
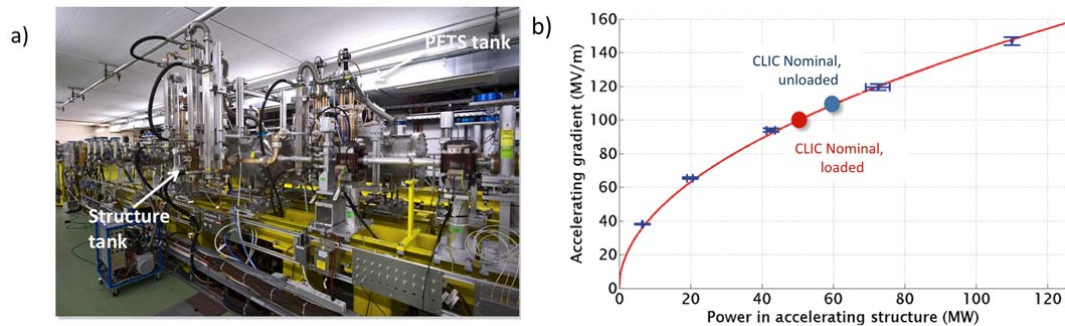
Figure 2: a) The Two-Beam Test Stand at the CLIC Test Facility where 12 GHz rf power is extracted from an up to 28 A drive beam and transferred to structure accelerating a 1 A probe beam. b) Experimental results of two-beam acceleration, up to and beyond the nominal CLIC gradient.

2.1.3   **Staging and Optimisation**

The Two-Beam Acceleration scheme is particularly suited for energy staging of the machine; once the drive beam complex is constructed, rf power for additional lengths of the main linac can be provided simply by increasing the drive beam length in the drive beam accelerator. No upgrades are needed for the drive beam complex, and once the drive beam complex has been constructed, the addition cost per GeV of center of mass energy is favourable to klystron-based alternatives. Furthermore, lower energy machines can run most of the time during the construction of the next stage. A consistent three-stage implementation scenario has been defined. Schedules, cost and power are being developed, although the energies of the individual stages will be determined by LHC physics results. The minimum center of mass energy being considered is about 375 GeV, which will allow precision studies of the Higgs and the Top quark. Figure 4 illustrates an example of the various stages of a CLIC machine.
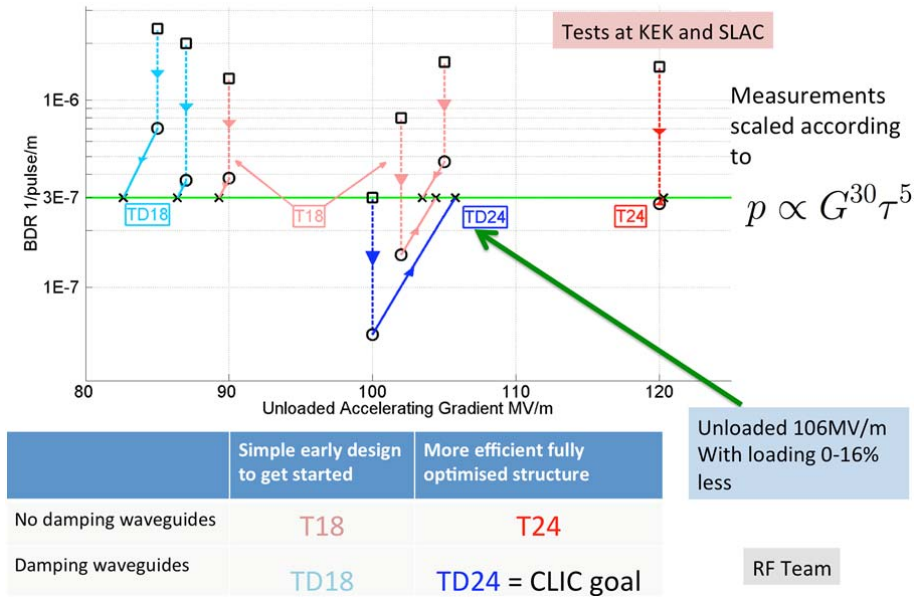
Figure 3: Structure test results, where gradients are scaled to the CLIC allowed breakdown rate of 3×10^{-7}. A fully optimized CLIC structure with damping waveguides has recently reached an unloaded gradient of 106 MV/m.

Figure 4: Example of CLIC energy stages. The center of mass energy can be increased without modifications to the drive beam accelerator complex. The actual energy of each stage will be guided by LHC physics results.

The CLIC machine is currently being re-optimized for the lowest energy stage (375 GeV). The optimization includes overall design and system optimization, technical parameters for all systems, cost, power/energy optimization, scheduling and site studies. Examples of areas, which can give increased machine power efficiency, are the use of permanent magnets for the drive beam, and studies of high-efficiency L-band multi-beam klystrons for the drive beam acceleration. The goal is to push the tube efficiency towards 80%, and increase the drive beam klystron power output. Estimates indicate that a reduction in the total machine power consumption of 20%, with respect to CDR figures, can be achieved. As part of the preparation for an optimal implementation strategy, a 500 GeV CLIC where the main linac are powered by klystrons (as opposed to a drive beam) has been studied in detail [4]. 4,400 klystrons would be required for a 500 GeV machine and a simple cost study indicated a cost comparable to a drive beam-based CLIC linac. The luminosity is comparable to that of the drive-beam based design. The pulse length is the same as for the drive-beam design. The drive beam design has the advantage of a comparably lower cost per additional GeV. Figure 5 shows one rf unit for a klystron-based CLIC, where a compressed rf pulse from two 60 MW klystrons powers 8 CLIC accelerating structures.
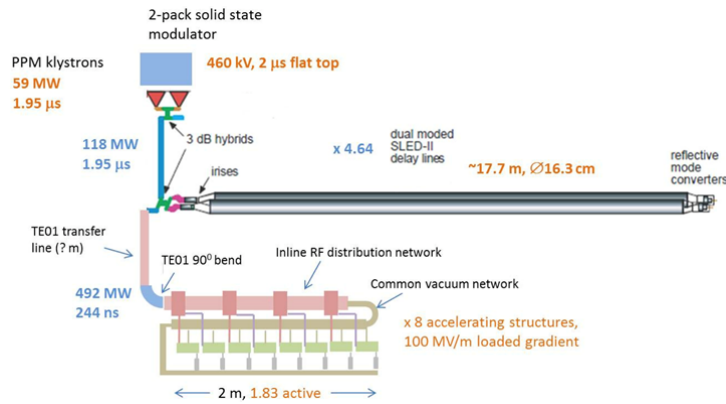
Figure 5: An rf unit for a klystron based CLIC. Two 60 MW klystrons can power 8 CLIC accelerating structures at a gradient of 100 MV/m.

2.1.4 Luminosity and Alignment

In order to reach the target luminosity of 10^{34}/cm^2/s CLIC requires a normalized vertical emittance of 20 nm at the interaction point, and a maximum emittance growth of 10 nm in the main linacs. Robust emittance preservation in the main linac will be achieved using beam-based alignment and by integrating wakefield monitors on the structures. In the next period, the two topics will be addressed experimentally. The 2 km FACET linac test facility at SLAC [5] now provides a unique opportunity to test beam-based alignment for linear colliders experimentally, and a proof of principle of the dispersion free correction algorithm as planned for CLIC has recently been demonstrated experimentally [6]. The experiments have shown that an automatic global correction scheme can successfully control the dispersion and reduce the emittance over 500 m of linac. Wakefield monitors are currently being developed, with the aim of providing the required resolution of 3.5 um with a robust and economical design. The monitors will be tested in CTF3 to ensure that the target precision can be reached [8]. Figure 6 illustrates the CLIC alignment techniques and some of the developments foreseen in the next period.
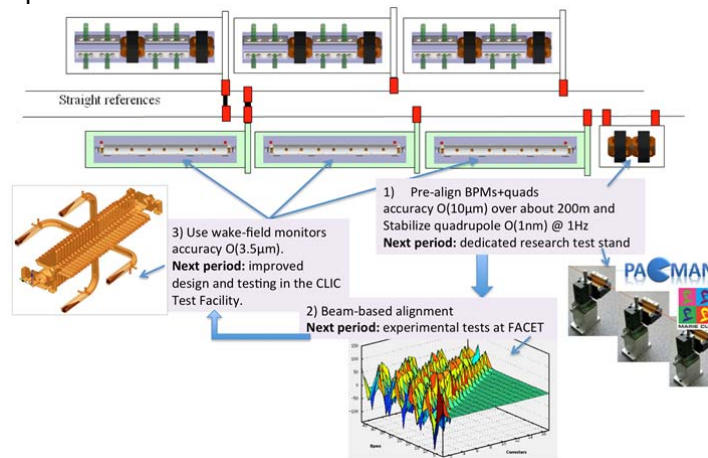
Figure 6: Three areas where alignment and stabilization will be further studied in the next period: 1) development of an automatic alignment and stabilization test stand, 2) experimental tests of beam-based alignment at FACET, 3) experimental tests of wakefield monitors.

Proof of principles of both pre-alignment and stabilization has been demonstrated with the CDR, and in the next period a sizable research project funding ten PhD student grants, "PACMAN", has been approved [7]. The technical goal of the program is to develop very high accuracy metrology and alignment tools and integrate them in a single automatic alignment test stand.

2.1.5 CLIC Test Facility

The CLIC Test Facility 3 (CTF3) at CERN is primarily a scaled version of the CLIC drive beam complex shown in Figure 1. CTF3 first accelerates a 4 A beam up to 120 MeV, in a fully loaded linac with more than 95% efficiency. A delay loop and one combiner ring subsequently compress the beam current up 28 A [2]. CTF3 has successfully demonstrated drive beam generation and two-beam acceleration in the CDR period, and will operate up to the end of 2016 to address further system tests and perform more detailed studies. The facility has recently demonstrated drive beam combination by a factor four with the nominal emittance of 150 um in both planes, and the current stability of the drive beam has earlier been demonstrated to better than the CLIC requirements of $\Delta I/I = 7.5 \times 10\text{-}4$ [9]. The final step of a full demonstration of the CTF3 drive beam generation is stable factor 8 combination. The progress has been impeded the last year by technical problems with the traveling wave tubes required for the sub-harmonic bunching, required for delay loop operation. A fast phase feed-forward system has been designed to correct the drive beam phase profile and jitter, with the aim of demonstrating the CLIC drive beam phase requirements [10]; the first kickers and amplifiers are to be installed in 2013.
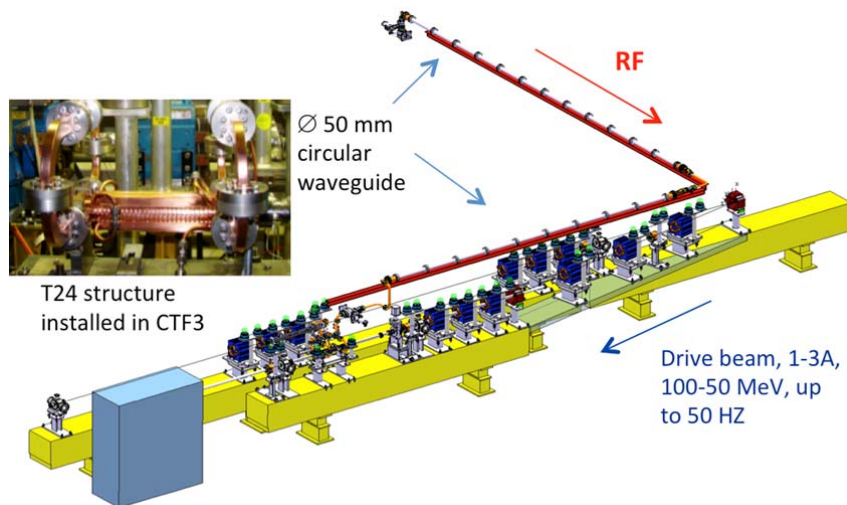
Figure 7: A new beam loading test facility: a 1 A CTF3 beam and X-band rf power will be simultaneously delivered to an accelerating structure.

In the two-beam test stand, new structures will be conditioned with drive beam rf and the breakdown rates measured. Kicks imparted to the beam during breakdown events will be measured and characterized, and the precision of the CLIC wakefield monitors will be measured. A dogleg halfway down the linac allows the drive beam to be directed to a test accelerating structure. Using this to deliver a 1 A beam from the linac, simultaneously as it is filled with the nominal X-band rf power [12], breakdown

rates in the accelerating structure can be tested with beam loading and compared to operation without beam loading. Figure 7 shows the sketch of the planned beam loading test facility.

As a prototype of a CLIC injector, a 1 GHz klystron test stand to test a drive beam accelerating structure at full power is planned, including a gun and a sub-harmonic buncher [11]. A 1 GHz multi-beam klystron with high efficiency (>70%) and a 1 GHz modulator is planned to be delivered to and tested at CERN in 2015-2016, and can potentially be the first stage of a larger test-facility followingCTF3. The 1 GHz injector will have the parameters of the full CLIC machine, and the hardware can be reused as the first part of CLIC.

Full prototypes of the CLIC two-beam modules are currently being constructed and tested [13]. Two modules will be build for system integration tests in the laboratory and key objectives are validation of different types of girders and movers, pre-alignment tests, magnet stabilization, identification of vibration sources, measurement of resonant frequencies and simulation of thermal cycles bench-marked with finite element modelling. Figure 8 shows a picture of a completed laboratory module, installed at CERN. The first tests results are promising and in line with simulations [14]. A similar two-beam module is currently under fabrication for installation in CTF3, fully equipped with X-band structures and components. The power extraction structures will provide the nominal power for the accelerating structures, thus giving a complete system test of a full CLIC main linac module with rf and beams.

2.1.6   **X-band Technology**

In the coming project period, the CLIC project will see a significant increase in X-band structure test capacity. One 12 GHz klystron based X-band test stand ("XBOX1") has been operating at CERN for a year [12], allowing 12 GHz structure to be tested at 50 Hz. This test stand uses a scaled version of the XL4 klystron tube developed for the NLC, provided by SLAC. With the use of a SLED1-type pulse compressor output power of up to 100 MW can be provided in pulses of 250 ns, sufficient to power two CLIC accelerating structures at nominal power and pulse length. Two new prototype accelerating structures with damping features are currently under test in XBOX1 and at NEXTEF at KEK. When these tests are completed the reproducibility of the CLIC structure performance will be better quantified.

A second test area ("XBOX2") is under construction and planned to be commissioned by the end of 2014. A SLAC XL5-type tube will be commercially procured from CPI, and will provide XBOX2 similar capabilities as XBOX1. A cluster of four 6 MW tubes from Toshiba ("XBOX3") is planned to be commissioned by the end of 2015 and will give additional test capabilities. In total, we estimate that more than 40 structures will be tested in these facilities by 2017, including structures with SiC damping material and X-band crab cavities. Figure 9 shows the XBOX test facilities.
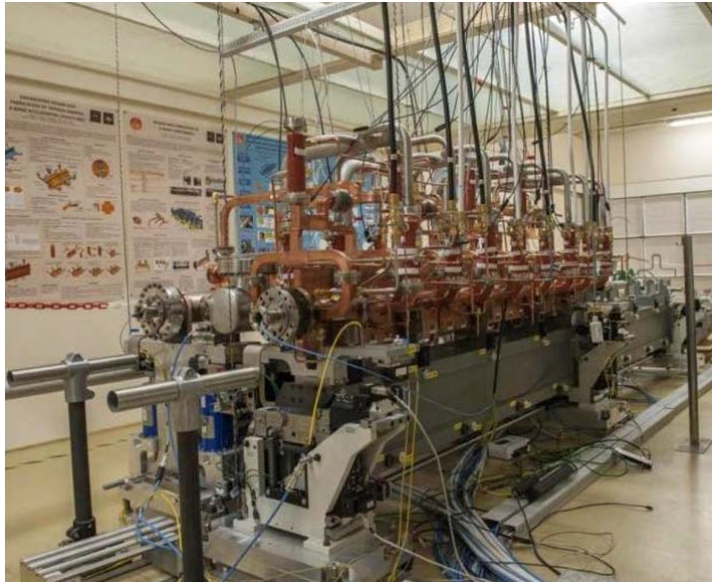
Figure 8: The first prototype of the CLIC two-beam module has been completed, and is undergoing thermo-mechanical validation.

The basic high gradient structure research will continue in the next period, including further development of the understanding of rf breakdown from first principles by theoretical studies, and multi-scale simulation studies. Modeling and simulations efforts for understanding the formation of vacuum arcs in breakdowns are being pursued [15], and the simulation results will be benchmarked against experiments at the DC spark test stand at CERN [16].

Two CLIC X-band technology application projects have recently been started. The first is use of CLIC X-band structures for compact FELs in the few GeV range. An early collaboration with Turkey has been followed by a recent initiative where countries or institutes can collaborate with CLIC on common CDR work for a FEL based on CLIC X-band technology [17]. Institutes from 5 different countries have already shown interest. Example parameters for an X-band FEL are an electron energy of 6 GeV and a charge of 250 pC as proposed in [18], however, collaborating institutes are free pick different parameters. Collaborators may profit from the planned X-band test facilities at CERN, thus reducing the risk of starting a new project. For CLIC, development and eventually operation of GeV level e-linacs with high gradient X-band structures will provide an increased technology maturity for the X-band technology. A second project studies the potential for technology transfer of CLIC high-gradient research to 3 GHz high gradient structures for proton therapy, where a main goal is to increase the effective gradient in proton therapy linac structures to about 50 MV/m (a factor of two with respect to the state of the art).
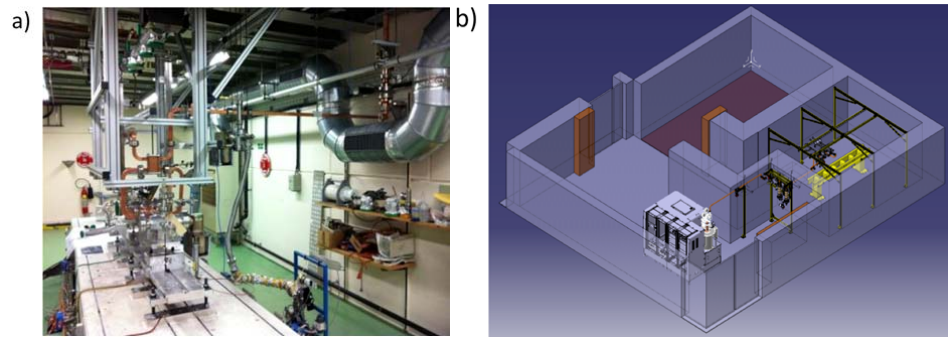
Figure 9: a) The new X-band test facility at CERN, with a SLAC-procured 12 GHz klystron. b) A planned X-band test facilities which will include commercially acquired tubes from CPI and Toshiba. In total these facilities will provide X-band power for testing up to 8 accelerating structures simultaneously.

2.1.7 Conclusions

The CLIC project has demonstrated the two-beam acceleration proof of principle, documented in the comprehensive Conceptual Design Report completed in 2012. In the next period up to 2018, the CLIC study will continue a number of technical studies on power and cost optimization, system tests including full CLIC module tests with rf and beam and experimental verifications of methods to preserve nm emittances. New X-band test facilities are being constructed at CERN and will greatly increase the capacity for 12 GHz rf testing. Systems testing can further profit from strengthening the exploitation of existing facilities worldwide (FACET, ATF2 and CesrTA). Finally, projects for the use of CLIC X-band technology in high-gradient FELs and for medical applications have been initiated with a potential outcome of increased technology maturity of linear collider X-band technology.

2.1.8 References

1. M. Aicheler et al., A Multi-TeV Linear Collider Based on CLIC Technology: CLIC Conceptual Design Report
2. G. Geschonke et al., CTF3 Design Report No. CERN-PS-2002-008 (RF), 2002
3. R. L. Lillestol et al., submitted to Phys. Rev. ST-AB
4. D. Schulte et al., in Proceedings of IPAC'13, TUPME049, 2013
5. http://facet.slac.stanford.edu
6. A. Latina et al., submitted to Phys. Rev. ST-AB
7. http://pacman.web.cern.ch/pacman/
8. F. Peauger et al., in Proceedings of LINAC'10, TUP098, 2010
9. A. Dubrovskiy et al., In Proceedings of LINAC'12, MOPB032, 2012
10. P.K. Skowronski et al., in Proceedings of IPAC'13, WEOBB203, 2013
11. H. Shaker et al., in Proceedings of IPAC'13, TUPME052, 2013
12. J. Kovermann et al., CERN-ATS-131
13. D. Gudkov et al., in Proceedings of IPAC'13, WEPFI055, 2013
14. F. Rossi et al., in Proceedings of IPAC'13, WEPFI056, 2013
15. H. Timko et al., Contrib. Plasma Phys. 51, 5–21, 2011
16. N. Shipman et al., in Proceedings of IPAC'12, THPPC027, 2012
17. http://indico.cern.ch/conferenceTimeTable.py?confId=270450
18. C. Adolphsen et al., in Proceedings of LINAC'10, TUP015, 2010

2.2   R&D on the Drive Beam Injector Frond End for CLIC

Steffen Doebert, CERN, CH 1211 Geneva 23, Switzerland
Mail to: steffen.doebert@cern.ch

2.2.1   Introduction

To build a high-energy accelerator as CLIC at a reasonable cost and size, a very high acceleration gradient (100 MV/m) is requested. In a classic approach, the RF power would be provided by klystrons. However, the klystrons with the required pulse length are not available on market. On the other hand, about 35000 high power klystrons are needed. This large number of klystrons is not feasible in terms of cost and maintenance [1]. In the novel acceleration scheme of CLIC, the RF power for the acceleration of the Main Beam is extracted from a high-current Drive Beam that runs parallel with the main linac. The Drive Beam loses its energy in 'decelerator' in special RF structures, which are called Power Extraction and Transfer Structures (PETS).

The drive beam accelerator (DBA) of CLIC accelerates a high current beam which stores the energy used for acceleration in the main beam. This high power source for CLIC has to be very efficient and stable. The DBA generates the 4.2 A, 142 μs long drive-beam pulses and accelerate them to a final energy of 2.4 GeV, using normal conducting fully-loaded accelerating structures with an RF frequency of 999.5 MHz. The long pulse gets transformed in 24 sub-pulses with a length of 240 ns a beam current of 101 A and a bunch repetition rate of 12 GHz using a series of delay loops and combiner rings. Key design goals of the DBA are to ensure the high-pulse current, short bunch length and stability of the beam current, energy and phase.

The DBA injector is supposed to produce electron beam pulses with a bunch charge of q_b = 8.4 nC, an r.m.s. bunch length of about 3 mm and an r.m.s. normalized emittance of 100 mm and bring them to a beam energy of 50MeV. The beam pulses are then accelerated to 300MeV in the first stage of the DBA linac (DBL1), individual bunches are compressed from 3mm to 1mm in a magnetic chicane, and then accelerated to their final energy of 2.4 GeV in the second stage of the DBA linac (DBL2). The schematic layout of one Drive-Beam accelerator is shown in Fig. 1.
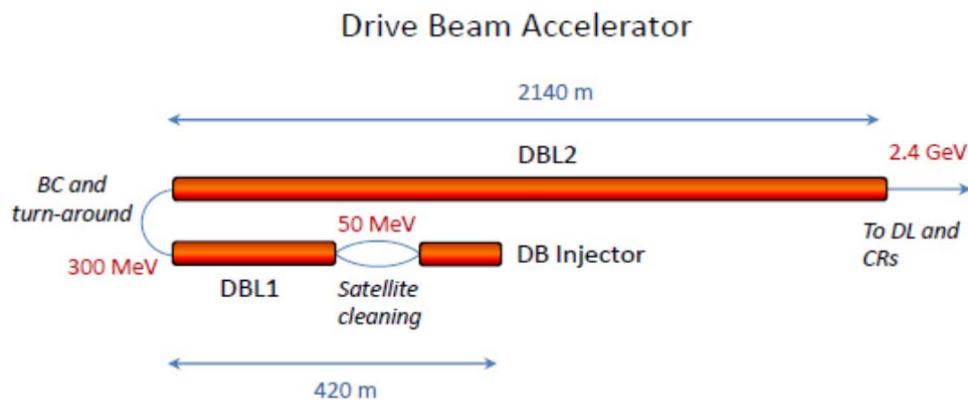
Figure 1: Schematic layout of a Drive-Beam accelerator.

The base-line design for the Drive Beam injector consists of a thermionic gun, followed by a sub-harmonic bunching system. A potential alternative scheme makes use of a photo-injector RF gun. We will discuss in the following only the thermionic gun approach.

The bunch charge of 8.4 nC and the initial beam current of 5A is well within the reach of standard cathodes. The phase-coding is done via a sub-harmonic bunching system operating at half the acceleration frequency at 499.75 MHz. This system must have a large enough bandwidth to allow fast switching of its phase by 180 deg every 240 ns to enable the CLIC bunch combination scheme. Due to the finite bandwidth a switching transient is present, during which the bunch phase and charge are ill defined. In order to limit the perturbation to the steady-state beam loading in the linac, it is required that the switching time should be lower than 10 ns.

The sub-harmonic bunching scheme will produce inevitable satellite bunches consisting of electron draped in the wrong rf bucket. One goal of the injector design is to minimize these satellites to avoid inefficiencies and machine activation (see next chapter).

The requirements on transverse emittance and bunch length can be met by using multiple sub-harmonic bunching cavities followed by a pre-buncher and a traveling wave buncher operating at the fundamental frequency, and by a careful design of the solenoidal field used to focus the beam and control space-charge induced emittance growth (see schematics in Figure 2).
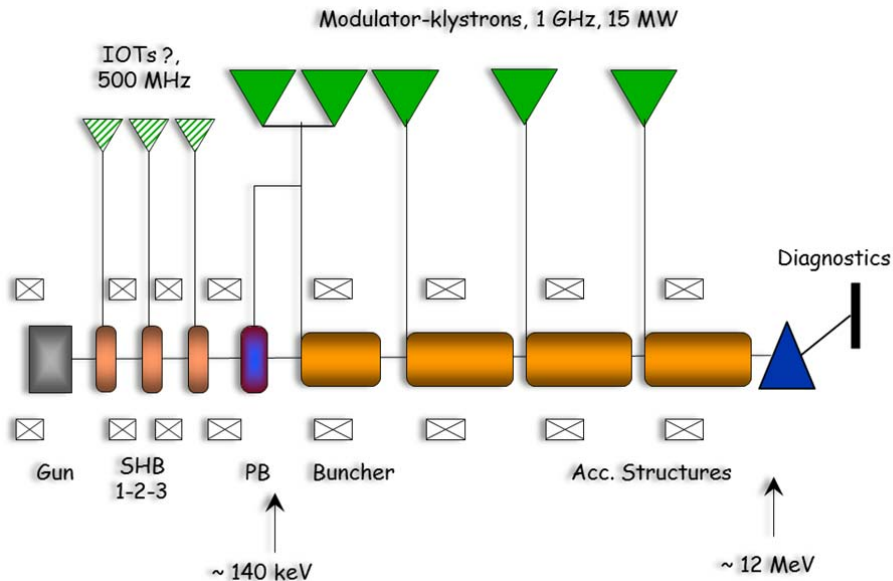
Figure 2: Schematics of the CLIC drive beam injector front end.

The Drive-Beam pulses are generated by a 140 keV thermionic gun. The gun is followed by a bunching system similar to the one used in CTF3 at CERN. It is composed of three sub-harmonic bunchers (SHB) which operate at a frequency of 499.75 MHz, followed by a pre-buncher (PB) and a travellingwave buncher, both operating at 999.5 MHz. Up to the pre-buncher the average beam momentum is 140 keV/c. After the buncher the beam momentum is increased with 12 units of travelling-

wave structures up to about 50MeV. A magntic schicane is used at an energy of 26 MeV for momentum collimation to clean up the longitudinal phase space (not shown in Figure 2). The key parameters of the drive beam injector are listed in table 1. More details about the CLIC drive beam and its injector can be found in the CLIC CDR [1].

Table 1: Key parameters of the CLIC drive beam injector at 50 MeV

Parameter	Nominal value	Unit
Beam Energy	50	MeV
Pulse Length	**140.3** / 243.7	μs / ns
Beam current	4.2	A
Bunch charge	**8.4**	nC
Number of bunches	70128	
Total charge per pulse	**590**	μC
Bunch spacing	**1.992**	ns
Emittance at 50 MeV	100	mm mrad
Repetition rate	100	Hz
Energy spread at 50 MeV	1	% FWHM
Bunch length at 50 MeV	3	mm rms
Charge variation shot to shot	**0.1**	%
Charge flatness on flat top	**0.1**	%
Allowed satellite charge	< 7	%
Allowed switching time	5	ns

The overall performance of the Drive Beam injector has been demonstrated fully in CTF3, with parameters very similar to the ones required in CLIC, including the feasibility of a fast (measured value equal to 6 ns) 180 deg phase switch in sub-harmonic bunching cavities. The measured performance of the CTF3 injector, in terms of emittance, bunch length and charge content of satellites, is in very good agreement with predictions from the PARMELA simulation code, which was as well used to design and optimize the CLIC injector.

The main remaining challenge is the operation at a pulse length of hundred times longer than CTF3, and the handling of the correspondingly high average beam power. The long pulse length is in particular challenging for the thermionic particle source using a gridded cathode.

The experimental verification of the injector front end comprising the gun, the buncher's and an rf-system including a nominal accelerating structure is planned in a small tests facility in the next few years.

In the following chapters the optimization of the sub-harmonic bunching system is described. In chapter 1.1.2 the longitudinal beam dynamics of the injectors is optimized while chapter 1.1.3 focuses on the design of the wide band bunchers themselves. Finally chapter 1.1.4. describes the developments on the thermionic gun.

2.2.2 Sub-Harmonic Bunching System of CLIC Drive Beam Injector

Shahin Sanaye Hajari
Mail to: Shahin.sanaye.hajari@cern.ch
CERN, CH 1211 Geneva 23, Switzerland

2.2.2.1 *Drive Beam Time Profile*

In the final time structure of the Drive Beam, as shown in Figure 1, the main pulse with the length of 140μs, consists of 24 bunch trains of 244ns length and each bunch trains contains 2922 bunches with a time separation correspond to 12 GHz.
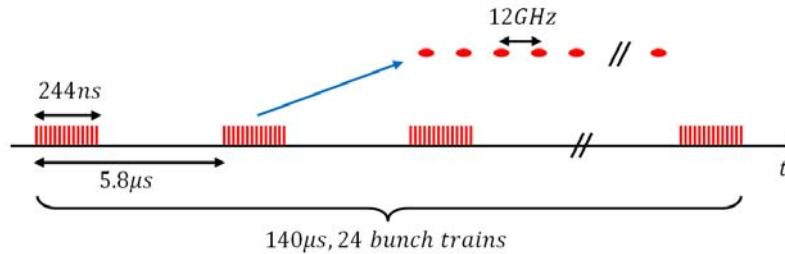
Figure 1: The final time structure of the Drive Beam.

To achieve such a time structure the continuous beam from the electron gun passes through the 0.5 GHz sub-harmonic bunching system. This system switches its phase by 180° every 244ns.
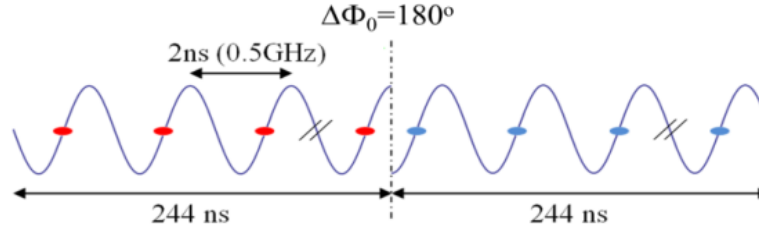
Figure 2: Phase switching

After the sub-harmonic bunching system a 1 GHz travelling wave buncher is used to reduce the bunch length more and then the beam is accelerated with 1 GHz frequency. Therefore, only every second of RF bucket of the accelerator is occupied. Thanks to the phase switching of the sub-harmonic bunching system the main pulse is made up of even and odd bunch trains (Figure 3). This procedure is called phase coding.
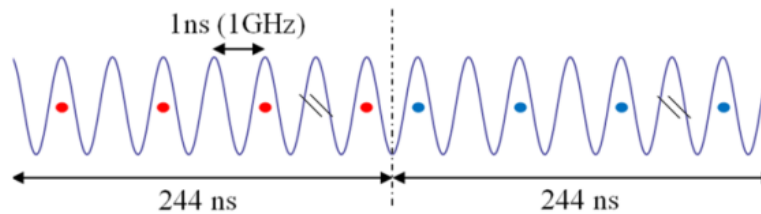
Figure 3: Phase coded Drive Beam

Although in real system about 5% of particles captured in wrong buckets, called satellite bunches. These bunches have to be eliminated for reasons of efficiency and

machine protection at the end of injector. Having even and odd bunch trains according to Figure 4 a delay loop is used to combine these trains to get twice bunch repetition frequency and twice peak current.
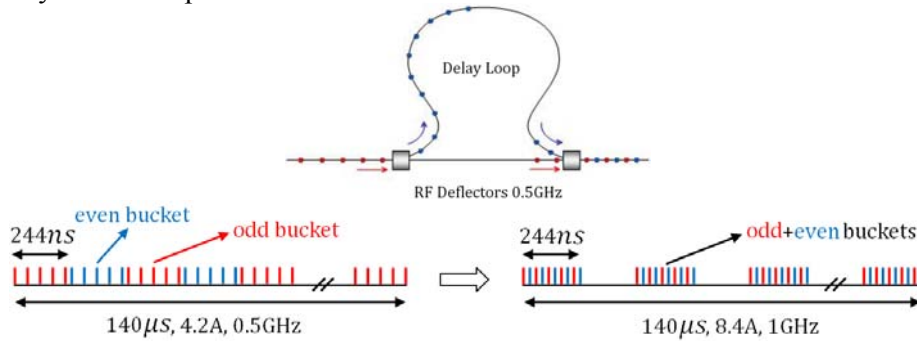
Figure 4: The principle of bunch combination in the delay loop [1].

In a roughly same procedure, the trains are recombined three and four times in the following two combiner rings. Therefore, the overall multiplication of the frequency and the peak current will be 24 and we will achieve the final time structure needed.

2.2.2.2 *Sub-harmonic bunching system*

The general layout of the CLIC Drive Beam bunching system is shown in Figure 5.
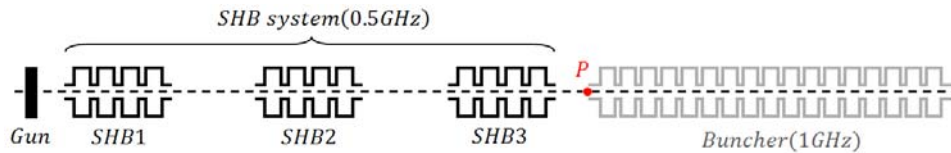
Figure 5: General layout of bunching system.

The sub-harmonic bunching system consists of three travelling wave sub-harmonic bunchers (SHB). This system has two functions. The first is to provide even and odd bunch trains and secondly to act as a prebuncher for the travelling wave buncher. This system should be optimized with the following optimization criteria.

- To maximize the population of the particles in the acceptance of the buncher.
- To minimize the population of satellite bunches.

The principle of bunching with sub-harmonic bunching system is based on velocity modulation bunching [2, 3]. The sub-harmonic bunching system is optimised in three stages. First, we ignore the effect of space charge and consider thin lens approximation for simplicity. Then the effect of space charge is considered and finally the realistic travelling wave structures are studied.

Thin lens approximation

In thin lens approximation the travelling wave structures is replaced with the simple thin lens cavities.
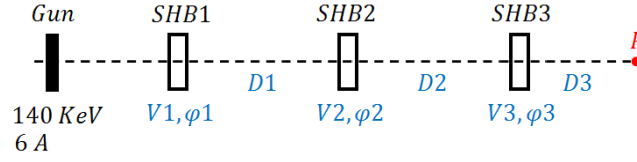
Figure 6: Thin lens approximation

In this approximation one can easily track particles in longitudinal phase space using the following relations.
In a drift space:

$$\Delta\varphi = 360\,fD\,/\,\beta c$$
$$\Delta w = 0 \tag{1}$$

In a SHB:

$$\Delta\varphi = 0$$
$$\Delta w = eV\sin[\Phi_0 + \varphi - \varphi_r] \tag{2}$$

Where φ and w are the phase and the kinetic energy of particles. φ_r is the phase of the reference particle and Φ_0 is the phase of the RF field seen by that particle. After tracking we can count the percentage of particle in the buncher acceptance and the satellite population according to relations (3) and (4) respectively.

$$-60 \le \varphi_P \le 60 \tag{3}$$
$$-180 \le \varphi_P \le -90 \vee 90 \le \varphi_P \le 180 \tag{4}$$

The buncher acceptance is found to be [-60, 60] after inserting and optimizing the buncher.

For the optimization of the thin lens system a simple computer code is written with *MATHEMATICA* software which changes the phases and voltages of the cavities and also the drift spaces between them to fine the optimum configuration. Figure 7 shows the final longitudinal phase space and the phase spectrum of the beam at the entrance of the buncher. In this configuration 92.3% of particles are in the acceptance of buncher and the satellite population is 5.0%.
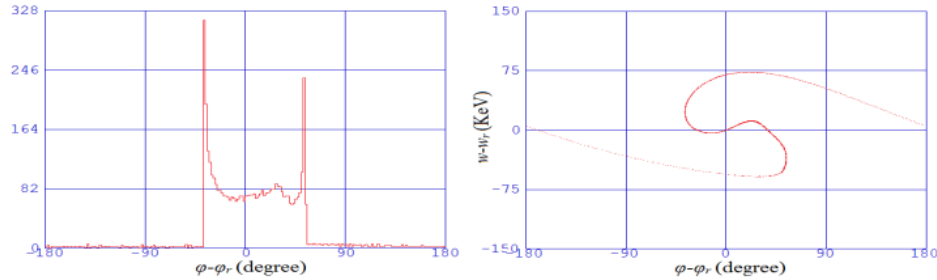
Figure 7: The final phase spectrum (left diagram) and longitudinal phase space (right diagram) of the beam at the entrance of the buncher (ignoring the space charge).

The space charge effect

The effect of the space charge forces is investigated in various configuration of the system. The destroying effects of the space charge on longitudinal beam profile start

when the phase spectrum becomes very narrow. In This situation particles are longitudinally close together. This mostly occurs in the first drift section.
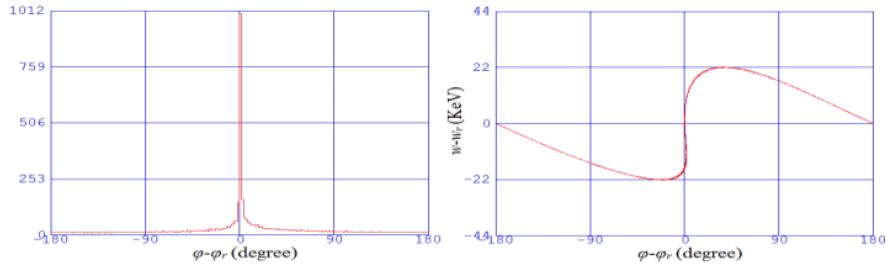
Figure 8: Phase spectrum (left) and phase space (right) of the beam at 110 cm away from a 22 KV SHB.

One can compare the phase space of the beam after passing through the first SHB ignoring the space charge effect and taking it into account in Figure 9.

a: At point A

b: At point B

c: At point C
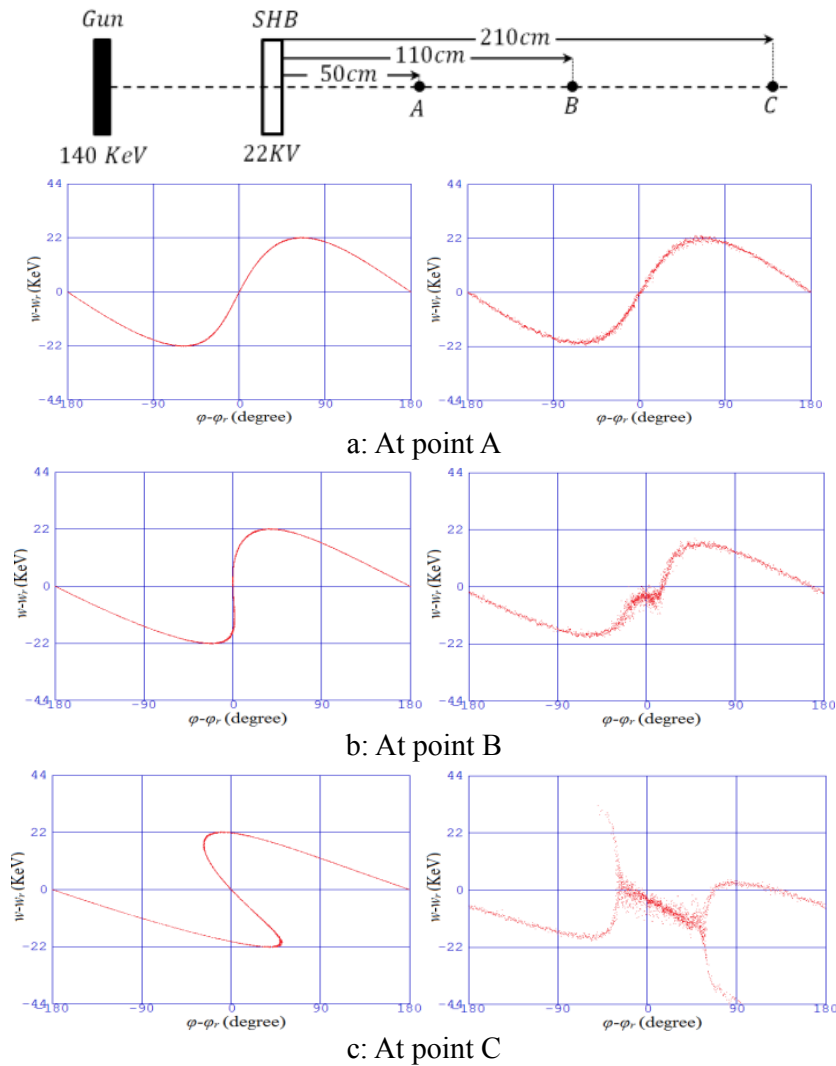
Figure 9: The phase space of the beam at several distances away from SHB ignoring the space charge (left diagram) and taking it into account (right diagram).

As shown in Figure 9 the effect of space charge can hardly be seen at distances less than 110 cm where the phase spectrum becomes narrow. After this point the debunching effect of space charge forces starts. And at point C the phase space is completely different from the case of ignoring the space charge forces and the bunch length is much bigger. To reduce the destroying effect of the space charge one should avoid long drift spaces, specially the first one. When the beam enters the second SHB the strong RF field of SHB reduces the effect of space charge forces. So in the optimization code we should restrict the maximum value of drift spaces. Following this procedure, Figure 10 shows the phase space of the optimum configuration of the Figure 7 with taking the space charge into acount. After turning on the space charge, 91.6 percent of particles lie in the buncher acceptance and the satellite population becomes 5.4%.
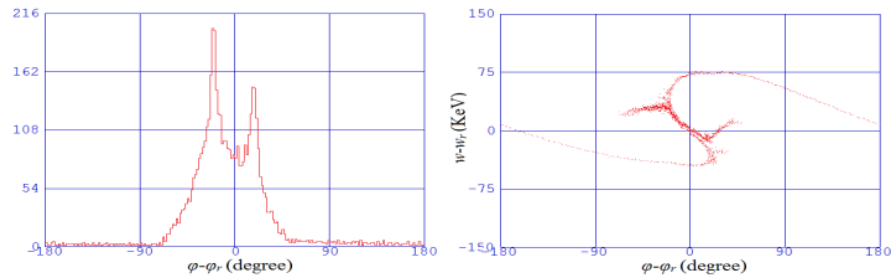
Figure 10: The phase spectrum (left diagram) and the phase space (right diagram) of the beam in thin lens model at the entrance of the buncher.

Travelling wave SHBs

If we look to the phase space of the beam after passing through a 50 cm travelling wave structure SHB we will interestingly find out that it is very similar to the case of simple thin lens cavity.
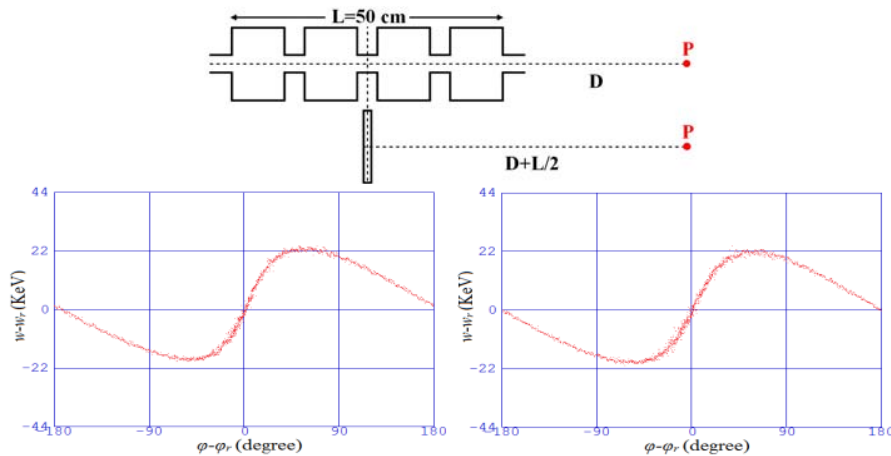
Figure 11: The phase space of the thin lens SHB (left diagram) and travelling wave SHB (right diagram).

This means that the thin lens approximation is a good approximation and the details of the electric field of the travelling wave structure is not important and the only important thing is the voltage of SHB. To be sure, Figure 12 provides more comparison been travelling wave structure and thin lens system.

a:

Replacing traveling wave structure instead of thin lens cavities.

b: At point P1

c: At point P2

d: At point P3
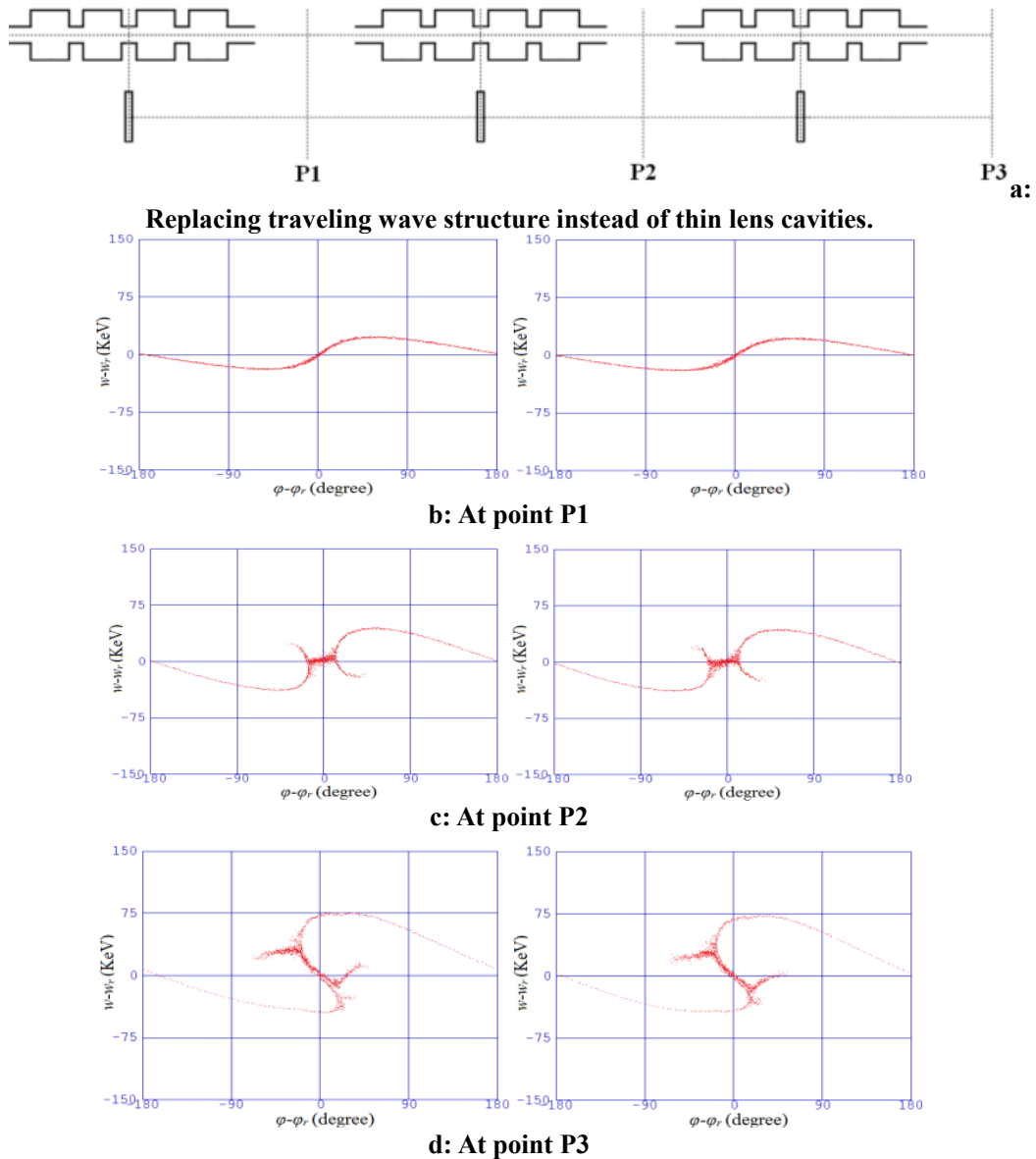
Figure 12: Comparison between thin lens system (left diagram) and travelling wave structure (right diagram).

For the travelling SHB system 92.0 percent of particles lie in the buncher acceptance and the satellite population is 5.0%.

2.2.2.3   *Conclusions*

The optimization process of the sub-harmonic bunching system can be summarized as follows:

- Optimization of the thin lens system with a code written in *MATHEMATICA*.
- Selection of an optimum configuration in which the effect of space charge is low, this occurs in configurations with the shorter drift spaces.

- Reconstruction of the SHB system with the travelling wave SHBs instead of thin lens cavities.

2.2.3 Sub-Harmonic Buncher Design for the CLIC Drive Beam Injector

Hamed Shaker, CERN, CH 1211 Geneva 23, Switzerland
Mail to: Hamed.Shaker@cern.ch

2.2.3.1 *Introduction*

Sub Harmonic Bunchers (SHBs) are the first RF components of the CLIC drive beam after the electron gun. The electron gun produces a continuous beam with about 140 µs pulse length, 50Hz repetition rate, 140 KeV energy and about 5A current. Inside SHBs the continuous beam is bunched and subdivided in 576(24x24) sub-trains with 243.7ns length. At the beginning of each sub-train, RF source phase is flipped by 180° as needed for further combination process in delay loop and combiner rings [1].
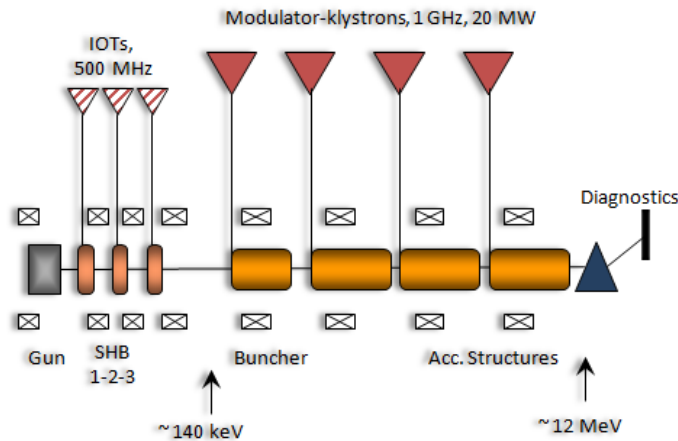
Figure 1: CLIC drive beam front-end layout.

Therefore, wide-band RF sources and SHBs is needed with fast 180° phase switching capability in 10 ns. For the combination process the SHBs resonant frequency (499.75 MHZ) should be half of the following RF accelerating structures resonant frequency (999.5 MHz). Figure 1 shows a layout of drive beam front-end as a first stage of the CLIC drive beam. At the moment, wide-band IOT seems to be the best option for SHBs RF sources.

2.2.3.2 *SHB Design*

Band-width requirement calculation

Equation 1 and Figure 2 show a simple model of smooth 180° phase switching in 10ns from section A to C. It shows two half amplitudes $\omega_0 \pm \Delta\omega = 499.75 \pm 50$ MHz RF wave is needed in transit section (B).

$$V = V_0 \begin{cases} \sin(\omega_0 t) : A \\ \frac{1}{2}\left[\cos(\omega_0 + \Delta\omega)t - \cos(\omega_0 - \Delta\omega)t\right] : B \\ -\sin(\omega_0 t) : C \end{cases}$$

(1)
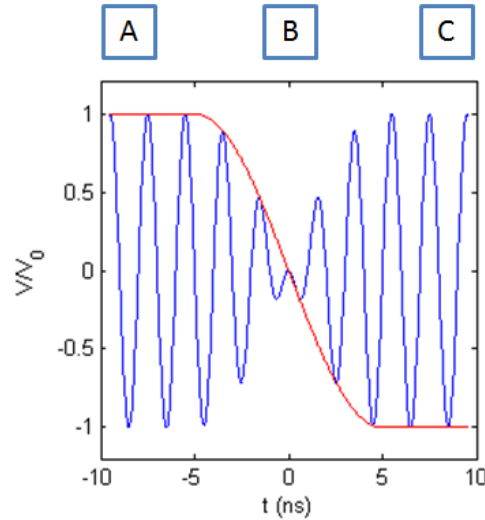
Figure 2: Smooth 180° phase switching model.

Equation (2) shows the relation between field amplitude (a), band-width (B_w) and difference between resonant and driving frequencies ($\Delta\omega$). This equation shows the required bandwidth for $\Delta\omega$=50 MHz as necessary for 10ns phase switching is about 58MHz. Direct measurement with an 800 MHz IOT approved this equation [4].

$$a \propto \frac{1}{1 + j\dfrac{2\Delta\omega}{B_w}} \overset{a=\frac{1}{2}}{\Rightarrow} B_w = \frac{2\Delta\omega}{\sqrt{3}}$$

(2)

2.2.3.3 *Cell-to-Cell Magnetic vs. Electrical Coupling*

The first design of CLIC type SHBs was done by L. Thorndahl for CTF3 (CLIC Test Facility 3) [5]. They are traveling wave structures with cell-to-cell electrical coupling via beam apertures. These structures have 1.5 GHz resonant frequency, 20 KV gap voltage and about 10ns filling time. Their RF sources are TWTs with 40KW output peak power, 1.5 µs pulse length and about 160 MHz bandwidth. The CLIC drive beam injector beam dynamic study [6] shows 22,28 and 34 KV gap voltage is needed respectively for three CLIC SHBs. CTF3 SHBs rescaling calculation for 0.5 GHz resonant frequency and 10ns filling time shows a peak power of 430-1040 KW is needed which is too high. Equation 3 shows the relation between peak power (P), gap voltage (V), angular resonant frequency (ω), filling time (τ) and total R/Q factor. To keep the peak power low enough the R/Q factor should be increased then the electrical coupling via beam apertures should be avoided that reduces the R/Q factor. Therefore, a magnetic cell-to-cell coupling was chosen because it has much less influence on the R/Q factor. This selection reduces required RF peak power to 34-82 KW.

$$P = \frac{V^2}{\omega\tau\dfrac{R}{Q}}$$

(3)

Cell design

Figure 3 shows the SHBs cell design layout. The left side shows the cell structure and the right side shows the magnetic coupling hole between cells. Each coupling holes are rotated 90° related to the previous one. The cell is roughly optimized to achieve maximum R/Q according to equation 3 [7]. Coupling hole dimension is chosen to achieve 10ns filling time for a structure with four cells. The R/Q factor in this design reaches to about 500Ω.
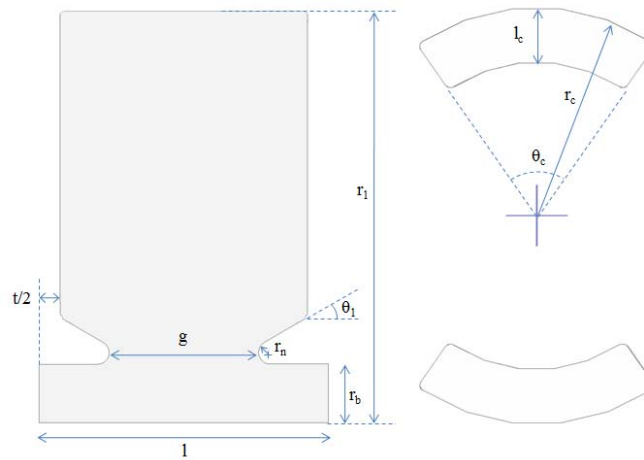
Figure 3: CLIC SHBs cell design layout

Table 1 shows the geometry dimension for the first SHB. For next SHBs, the dimensions can be changed a little to achieve different phase velocity. The difference between phase and beam velocities is needed to compensate beam loading as will be described in the next section.

Table 1: Geometry dimension for first SHB cells

g	50 mm
r_b	45 mm
r_n	4 mm
θ_1	25°
t (disk thickness)	15 mm
Frequency	499.75 MHz
l	100.00 mm
r_1	186.8 mm
r_c	157 mm
l_c	54 mm
θ_c	79.4°
Phase/Beam velocity	0.609c/0.62c
R/Q per cell	123 Ω

2.2.3.4 *Beam Loading Compensation*

Beam loading effect is not negligible for SHBs structures because of high current beam operation (about 5A). It should be mentioned that this kind of beam loading is different from the well-known beam loading in traveling wave structures that bunches travel on the crest. In our case bunches travel near zero crossing. At first glance, there is a similarity between this case and the beam loading in a prebuncher with one cell standing wave structure [8]. But the definition of detuning is not so obvious for a traveling wave structure. It was shown in another paper [9] that by using proper definition for detuning in a traveling wave structure, similar result to a SW case could be reached. Equation 4 shows the relation between detuning ($\Delta\omega$) and phase (v_p), group (v_g) and beam (v_e) velocities when bunches travel on zero crossing. F is the bunch form factor and I is the beam current.

$$\frac{\Delta\omega}{\omega} = \frac{\dfrac{1}{v_e} - \dfrac{1}{v_p}}{\dfrac{1}{v_g} - \dfrac{1}{v_e}} = \frac{1}{2\pi}\frac{V_b}{V}, V_b = -\pi FI\frac{R}{Q}$$

(4)

Table 2 shows these parameters for three SHBs. In our case the group velocity is negative because the structures are backward traveling wave structures. These parameters for the second and third SHBs are not finalized yet then the R/Q factor could be reduced a little to have less detuning so that the required peak power doesn't exceed 100 KW.

Table 2: Geometry dimension for first SHB

	SHB1	SHB2	SHB3
Beam velocity (v_e)	0.62c	0.62c	0.62c
Group velocity (v_g)	-0.13c	-0.13c	-0.13c
I (A)	5	5	5
Average bunch form factor (F)	0.058	0.57	0.73
Total R/Q (Ω)	474	474	474
Frequency (MHz)	499.75	499.75	499.75
Detuning (Δf) (MHz)	1.6	12.1	12.7
V (KV)	22	28	34
V_b (V)	432	4248	5440
Phase velocity (v_p)	0.609c	0.545c	0.542c

2.2.3.5 *Coupler Design*

A high coupling between the structures and RF power source is needed then a waveguide coupling is used. The waveguide coupling has a tapered shape for a smooth transfer to a WR1800 waveguide. Figure 4 shows the entire structure with waveguide couplings. This Figure also shows short-ended waveguides in the opposite side of feeding waveguides. They are used to reach symmetrical field near axis – as much as possible - to reduce the transverse beam kicking.
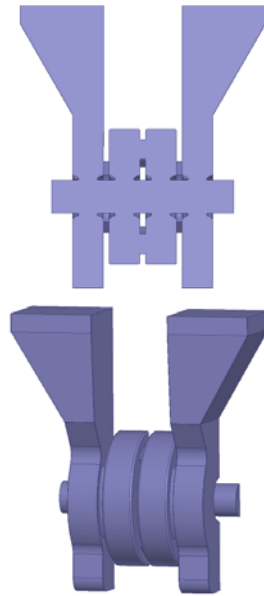
Figure 4: SHB final design.

2.2.3.6 *Coupler Tuning*

To tune the couplers, coupler cell radius and coupling slot length was varied to reduce s_{11} as much as possible. In the same time we should look at on-axis field pattern to be sure there is no local reflections. After each tuning, average phase velocity and asymmetrical field around axis should be checked for the proper magnitude and if is not correct the cell outer radius (r_1 in Fig. 3) and short-ended waveguide lengths should be changed and coupler tuning should be repeated. This time-consuming iteration will

continue to reach the proper magnitudes. Figure 5 shows the final s_{11} result and the on-axis electric field pattern at 499.75MHz.
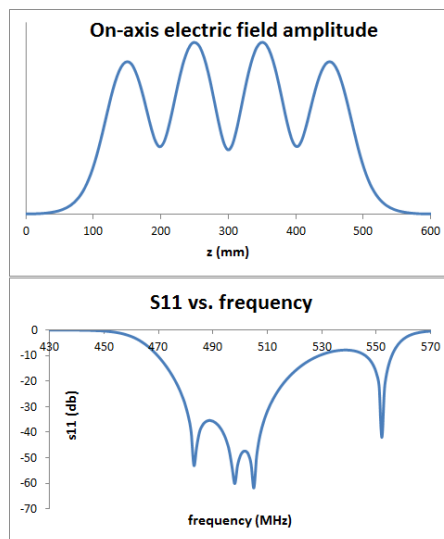
Figure 5: On-axis electric field amplitude and s_{11} with a tuned coupler.

2.2.3.7   *Conclusions*

For CLIC drive beam injector three SHBs are needed with low filling time (10ns) and between 22-34 KV gap voltages. It was showed that wide-band RF sources are needed with 34-82 KW output peak power and about 58 MHz bandwidth. Cell-to-cell magnetic couplings were chosen for higher R/Q factor that results a backward travelling wave structure. Tapered waveguide coupling is chosen for its higher coupling and short-ended waveguides is used to avoid asymmetrical field around axis. Because of high beam current operation, beam loading compensation was required. This compensation was done by cell detuning or in another word by proper difference between phase and beam velocities. Also the Fabrication of a prototype for the first SHB has been launched.

2.2.4   **Drive Beam Injector Electron Source**

The design of the electron source for the drive beam injector is based on the existing CTF3 source [10], a thermionic DC gun at a voltage of 140 kV using a commercial cathode grid assembly. The grid is used to control the emission and shape the electron pulse. The possibility to correct the shape of the electron pulse is essential to fulfill the current stability requirements of the CLIC drive beam. In addition an excellent pulse to pulse stability is needed in the order of 0.1%.

The source has to deliver beam pulses of 140 µs length with an average current of 5A and a repetition rate of 50 Hz. Compared to CTF3 the pulse length increased by a factor of 100 which has several consequences. The high voltage will have to be delivered by a pulsed high voltage modulator instead of the DC power supply with capacitive energy storage. The capacitive energy storage needed to insure a minimal droop along the pulse would be simply too large to be practical. This puts severe constraints on the stability of the modulator.

A Marx generator type modulator is currently under investigation for that purpose. In addition appropriate electronics has to be developed to pulse the grid of the cathode assembly and allow for a correction of the pulse shape.

The cathode assembly currently used in CTF3 (Eimac Y-796) will likely not survive the long pulse length. A larger cathode with a more robust grid has to be used. The dispenser type Eimac model YU-156 has been chosen for the gun design. The actual design of the gun is largely inspired by the design of the CTF3 gun. A ceramic tube is used to insure the high voltage isolation. The cathode assembly is on the high voltage potential such that the power supplies for the bias voltage, heater current and grid pulser all have to be floating on a 140 kV high voltage deck. The cathode is flat and has a 10 mm radius providing sufficiently current for our application. The electrode configuration is a Pierce type focusing electrode and an anode with a 10 mm aperture. The approach for the mechanical design was to have the possibility to easily change electrodes in order to try different shapes and a simple way to adjust the cathode-anode distance. The cathode-anode distance was found in simulations to be the most sensitive parameter to optimize the gun for different currents or voltages. A conceptual design of the gun can be seen in Figure 1.
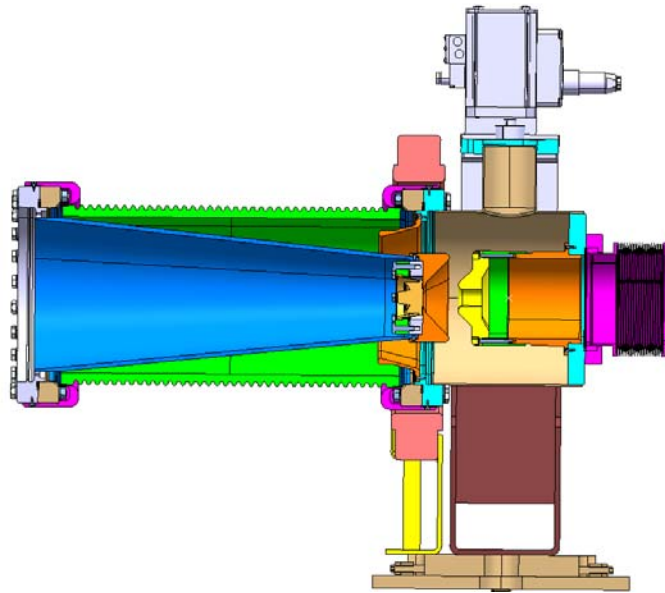
Figure 1: Conceptual design of the drive beam gun. Ceramic isolator (green), Anode (yellow), Focusing electrode (orange), cathode (light orange).

The electrode geometry of the gun has been extensively studied for two different sizes of cathodes and over a wide range of currents and voltages. The simulations have been performed with the codes EGUN and MAGIC. The goal was to understand how to optimize for different operation scenarios and potential different application of the gun. Currents between 5 A and 10 A and voltages between 100 kV and 200 kV have been studied. Figure 2 shows an example of the emittance as a function of current for a fixed electrode configuration.
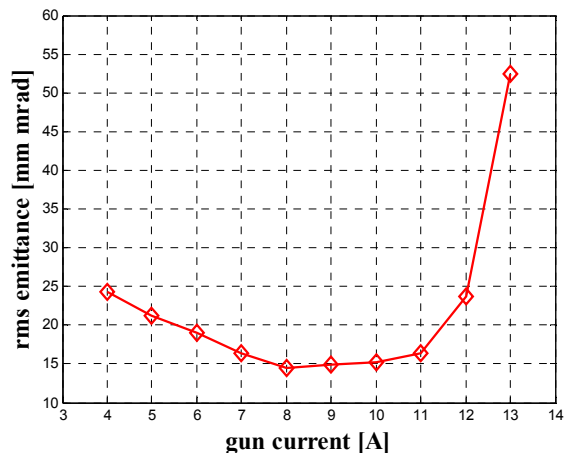
Figure 2: RMS emittance as a function of beam current for a fixed geometry.

It turns out that one can optimize the gun over a wide range of parameter by changing the cathode-anode distance. It is not necessary to optimize each time the shapes of the focusing electrode and anode. One should note here that the drive beam application is not requiring an extremely small emittance. Emittances below 20 mm mrad are perfectly acceptable. The emittance evolution in the drive beam injector will be dominated by the bunching system and not by the initial beam emittance from the electron source.

The injector optimization and the electron source design are still ongoing. The goal is to construct a prototype gun and test it in a test stand at CERN in order to verify the stability of the produced electron beam. The design and test of the drive beam electron source is done in collaboration with CEA/CESTA.

2.2.5   **References**

1. A Multi-TeV linear collider based on CLIC technology: "CLIC Conceptual design report",edited by M. Aicheler, P. Burrows, M. Draper, T. Garvey, P. Lebrun, K. Peach, N. Phinney, H. Schmickler, D. Schulte and N. Toge, CERN-2012-007, CERN, Geneva, 2012
2. Stanford High-Energy Linear Electron accelerator (Mark III), p. 184, M. Chodorow et al, the review of scientific instruments, volume 26, number 2 (1955)
3. Linear Accelerators, edited by Pierre M Lapostolle, Albert L. Septier, North-Holland Publishing Company, Amsterdam, 1970
4. S. Doebert, "Klystron update, Gun ideas", CLIC workshop 2013, Geneva, 28 Jan-1 Feb 2013
5. H. Braun et al., "Sub harmonic buncher at 1.5 GHz for CTF3", CLIC Note 580, 2003
6. S. Sanaye Hajari et al., "Beam Dynamics Study of CLIC Drive Beam Injector," IPAC'13, Shanghai, May 2013, TUPME047
7. J. J. Manca et al., "TM01 mode accelerating cavity optimization, LA-7323, August 1978
8. P. B. Wilson, "High Energy Electron Linacs: Applications to Storage Ring RF Systems and Linear Colliders", SLAC-PUB-2884, Feb 1982
9. H. Shaker, "General Beam Loading Compensation in a Traveling Wave Structure," IPAC'13, Shanghai, May 2013,TUPME053
10. G. Geschonke et al., "CTF3 design report", CERN-PS-2002-008-RF, CERN, Geneva, 2002

2.3 CLIC Beam Delivery System

R. Tomas, H. Garcia, Y.I. Levinsen, M. Modena and E. Marin, CERN, Switzerland

Mail to: Rogelio.Tomas@cern.ch

2.3.1 Introduction

The CLIC Conceptual Design Report [1] presents the machine aspects for a collider with an energy in the center of mass of 3 TeV. Parameters for this option are shown in Table 1. The lower energy machine at 500 GeV was conceived to be operated in a staged approach having a layout fully compatible with that at 3 TeV and at the cost of a compromised performance at the lower energy. In the post-CDR phase the CLIC parameters are under review (including energy stages) with extra emphasis in the performance optimization at lower energies. This article presents the status of the 3 TeV Final Focus System (as it is in the CDR) and the plans to reach an optimum parameter set for the low energy range between 350 and 500 GeV.

Table 1: CLIC Beam Delivery System main parameters at 3 TeV CM.

Parameter	Units	Value
Length (Linac exit to IP distance)/side	m	2750
Maximum Energy/beam	TeV	1.5
Distance from IP to first quad, L*	m	3.5-6
Crossing angle at the IP	mrad	20
Nominal core beam size at IP, σ^*, x/y	nm	45/1
Nominal beam divergence at IP, θ^*, x/y	μrad	7.7/10.3
Nominal beta-function at IP, β^*, x/y	mm	10/0.07
Nominal bunch length, σ_z	μm	44
Nominal disruption paarmeters, x/y		0.15/8.4
Nominal bunch population, N		3.7×10^9
Beam power in each beam	MW	14
Preferred entrance train to train jitter	σ	<0.2
Preferred entrance bunch to bunch jitter	σ	<0.05
Typical nominal collimation aperture, x/y	σ/σ_y	15/55
Vacuum pressure level, near/far from IP	nTorr	1000/1

2.3.2 3 TeV FF

The role of the Final Focus System (FFS) is to demagnify the beam to the required size (σ_x =45 nm and σ_y =1 nm) at the IP. The FFS optics creates a large and almost parallel beam at the entrance to the Final Doublet (FD) of strong quadrupoles. Since particles of different energies have different focal points, even a relatively small energy spread of 0.1% significantly dilutes the beam size, unless adequate corrections are applied. The design of the FFS is thus mainly driven by the need to cancel the chromaticity of the final doublet. The CLIC FFS has a baseline local chromaticity correction [2] using sextupoles next to the final doublets. A bend upstream generates dispersion across the final doublet, which is required for the sextupoles and non-linear elements to cancel the chromaticity. The dispersion at the IP is zero and the angular dispersion is about 1.4 mrad, i.e. small enough that it does not significantly increase the beam divergence. Half of the total horizontal chromaticity of the final focus is generated

upstream of the bend in order for the sextupoles to simultaneously cancel the chromaticity and the second-order dispersion. The horizontal and the vertical sextupoles are interleaved in this design, so they generate third-order geometric aberrations. Additional sextupoles upstream and in proper phases with the final doublet sextupoles partially cancel these third order aberrations. The residual higher order aberrations are further minimized with octupoles and decapoles, see reference [3]. The final focus optics is shown in Fig. 1.
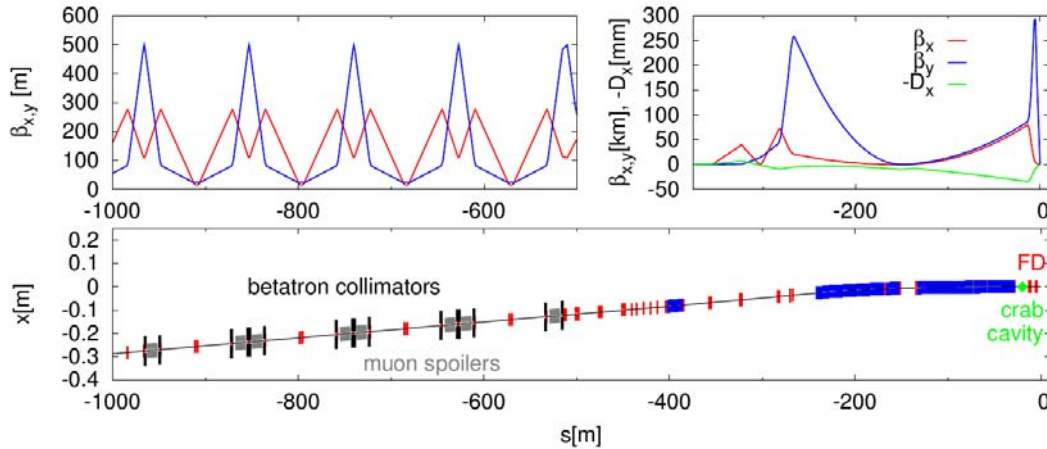
Figure 1: Optics (top) and layout (bottom) of the CLIC betatron collimation and FF sections.

With a 20 mrad crossing angle, crab cavities are required to rotate the bunches so they collide head on. A design of the 12 cell crab cavity is shown in Fig. 2. They apply a z-dependent horizontal deflection to the bunch that zeroes at the center of the bunch. The crab cavity is located prior to the final doublet (FD) as shown in Fig. 1 but sufficiently close to be at 90 degrees phase advance from the IP.
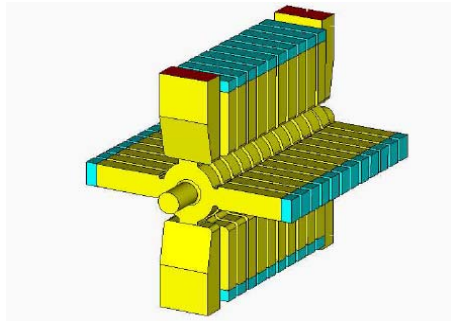
Figure 2: 12 cell crab cavity design including wakefield dampers (length of 300 mm).

In reference [4] it is shown that the small deviation from 90 degrees plus the interference with sextupoles produces a travelling waist at the IP. Therefore the sign of the crossing angle determines the direction of the travelling waist setting a preferred orientation to avoid luminosity loss (travelling waist, unfortunately, cannot significantly increase the luminosity given the CLIC parameters). The baseline crab cavities operate at 12 GHz and require a phase stability of 0.02 deg and an amplitude stability of 2% for a luminosity loss of 2%. Crab cavities also need strong high order mode damping.

Synchrotron radiation from all the Beam Delivery System (BDS) magnets causes a 22% luminosity loss. About 10% comes from the final focus bending magnets and another 10% originates at the final doublet quadrupoles. The CLIC vertical IP beta function is slightly below the theoretical beta function that minimizes the Oide effect [5, 6]. These numbers do not take into account the effect of the detector solenoid as this strongly depends on the final configuration of the interaction region. Recent simulations show that the theoretical minimum luminosity loss due to the current solenoid with anti-solenoid configuration should be 4%. Nevertheless the realization of a lattice actually achieving the 4% loss has not yet been demonstrated. A luminosity loss of about 6-7% has been reached so far in tuning studies. The right adjustments of the length of the anti-solenoid, the L*, the detector solenoid field, the crossing angle together with appropriate coupling corrections should be explored to minimize this luminosity loss.

Table 2: Total luminosity and luminosity in the 1% energy peak for the various L* under consideration

L* [m]	Total Luminosity $[10^{34}\ cm^{-2}\ s^{-1}]$	Peak Luminosity $[10^{34}\ cm^{-2}\ s^{-1}]$
3.5	6.9	2.5
4.3	6.4	2.4
6	5.0	2.1
8	4.0	1.7

In the nominal configuration with L*=3.5 m the last quadrupole of the final doublet, QD0, sits inside the detector. In order to alleviate the engineering and the stabilization of this set-up it has been proposed, as a possible fall-back solution, to move QD0 from the detector to the tunnel, consequently increasing L*. A collection of final focus systems with L* values between 3.5 and 8 m has been studied for CLIC. The performance of these FFS is shown in Table 2. Both the total luminosity and the luminosity in the energy peak degrade as the L* increases. Only the cases with L* of 3.5 and 4.3 m meet the CLIC requirement of a peak luminosity of $2 \times 10^{34}\ cm^{-2}s^{-1}$ with a 20% margin for static and dynamic imperfections. The shortest L* that allows removing QD0 from the detector is 6 m. The FFS with L* =6 m meets the CLIC requirements with a tight margin of 5% for the imperfections. The last case with L* =8 m does not provide sufficient luminosity.

The biggest challenge faced by the beam delivery system is the demonstration of the performance assuming realistic static and dynamic imperfections. The diagnostics and the collimation sections have demonstrated to be robust against misalignments (prealignment of 10 μm over 500 m). Standard orbit correction techniques, such as the dispersion free steering, guarantee the beam transport without blow-up in these regions. However these techniques fail in the Final Focus System. The CLIC FFS is a very non-linear system with a β_y pushed down to 0.07 mm. Many different approaches have been investigated to tune the FFS in presence of realistic misalignments. Currently the two most successful approaches are:

– **Luminosity optimization:** Maximizes the luminosity using all the available parameters in the FFS applying the Simplex algorithm.

– **Orthogonal knobs:** Maximizes the luminosity by scanning pre-computed arrangements of sextupole displacements (knobs), which target the IP beam correlations in an orthogonal fashion.

These approaches are simulated for 100 statistical realizations of the CLIC FFS with misalignments. The final luminosity distribution and the number of iterations are shown in Fig. 3 for these two approaches in black and blue. The number of iterations corresponds to the number of luminosity measurements. A random error up to 3% has been assumed for the luminosity measurement. Neither the Simplex approach, nor the orthogonal knobs reach a satisfactory result in terms of luminosity. However since the orthogonal knobs are much faster it is possible to apply them after the Simplex approach. This corresponds to the magenta curves in Fig. 3, showing 90% probability of reaching 90% of the design luminosity and requiring a maximum of 18000 iterations. The achieved luminosity performance is close enough to the desired 90% probability of reaching 110% of the design luminosity since new approaches or extensions will further improve the final luminosity, e.g., non-linear knobs.

To convert the number of iterations into time it is required to know how long a luminosity measurement will take. A conventional measurement of luminosity takes between 7 and 70 minutes, however faster indicators exist utilising different combinations of beamstrahlung signals and hadronic events [7]. These studies suggest that less than 10 bunch crossings should be enough to obtain accurate signals for tuning. Therefore 18000 iterations would take about an hour, which is reasonable for tuning the BDS from scratch.

During the CLIC technical design phase special focus needs to be put in improved tuning algorithms taking into account realistic errors in all BDS elements (e.g. the solenoid and the crab cavity were excluded in this study). The e− and e+ BDS lines should be optimized simultaneously and more robust final focus designs could be considered.
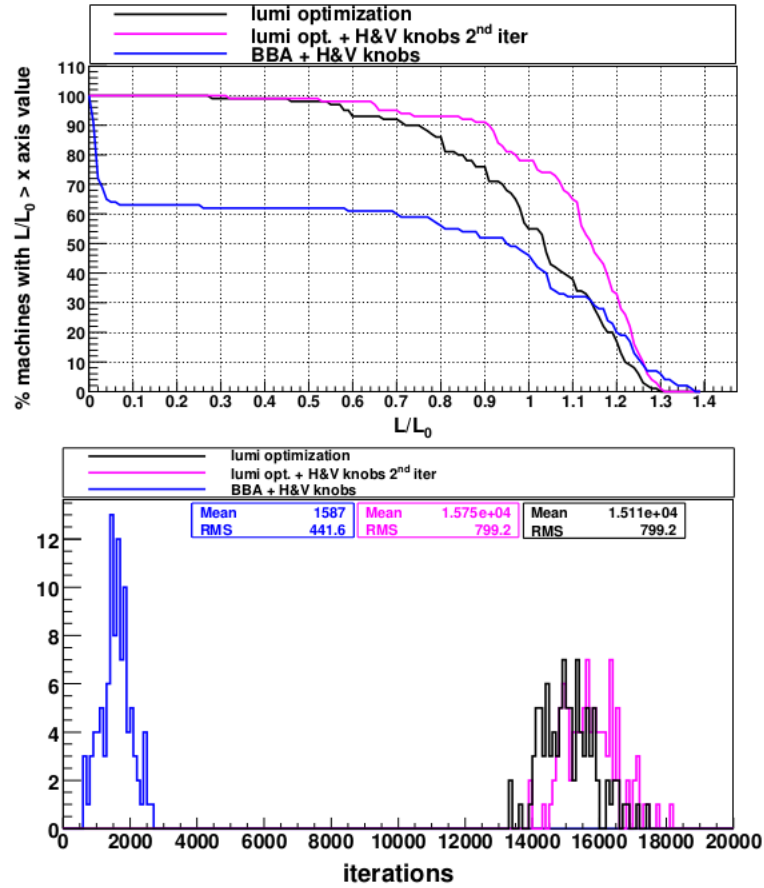
Figure 3: Top: Luminosity performance for 100 statistical realizations of the CLIC FFS after tuning using 3 different approaches. Bottom: Required number of luminosity measurements for the 3 different approaches.

2.3.2.1   *Final Doublet*

Figure 4 shows the tight integration of the QD0 quadrupole with the vacuum pipe of the incoming beam (smaller diameter) and the vacuum pipe of the outgoing beam (larger diameter). The incoming and outgoing beam-lines cross at an angle of 20 mrad and the outgoing (post-collision) vacuum pipe has a conical shape with a half opening angle of 10 mrad.
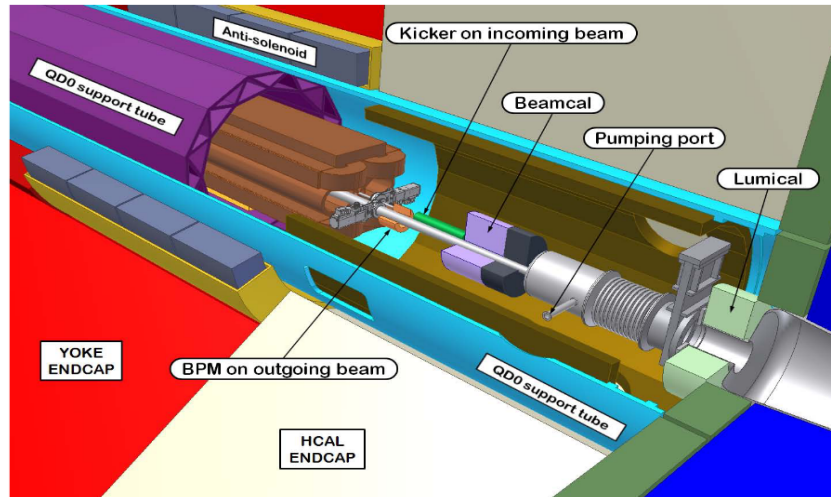
Figure 4: Interaction region showing the QD0 support tube surrounded by the anti-solenoid and all the other elements down to the Lumical.

QD0 is a compact 'hybrid' magnet with permanent magnet inserts and classical electro-magnetic coils. This choice was motivated by: the need for a compact magnet with very high gradient (575 T/m with an aperture radius of 4 mm), the need to tune the gradient (-20% estimation), the mentioned presence of the post-collision beam pipe, and the engineering difficulties in winding superconducting coils with such a small aperture and the impossibility to devise stabilisation techniques of the coils to the subnanometer level. Since the QD0 uses permendur and permanent magnet material, the QD0 must be shielded from external field. In order to both shield the QD0 magnet and reduce the beam distortions, an anti-solenoid design was also developed [8].

The magnets in the final doublet have the tightest tolerances in terms of field quality. Table 3 summarizes the tolerances of the QF1 and QD0 multipolar components at a radius of 1mm for a luminosity loss of 2%. QF1 features tighter tolerances than QD0 reaching 10^{-5} relative field accuracy for the low order skew components.

Table 3: QF1 (left) and QD0 (right) multipolar tolerances in 10^{-4} relative units at a radius of 1 mm for a 2% luminosity loss.

	QF1		*QD0*	
	min	**max**	**min**	**max**
b3	-0.4	2.2	-1.8	0.5
b4	-2.5	3.3	-27	6
b5	-4	18	-220	80
b6	-15	32	-	-
a3	±0.2		±0.7	
a4	±0.5		±8	
a5	±1.7		±130	
a6	±4.8		-	
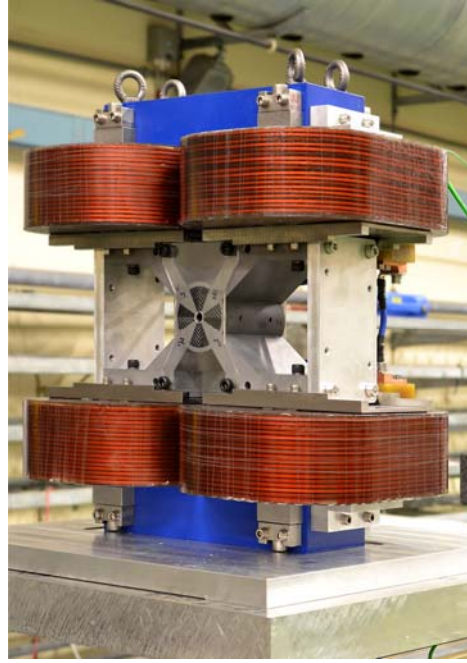
Figure 5: CLIC QD0 prototype.

A CLIC QD0 short prototype has been successfully built [9], see Figure 5. It has achieved 90% of the design gradient with an excellent field quality. Table 4 shows the measured multipolar components at 1 mm. Only the a3 component is out of specification. The origin of this unexpected out of specification and methods to further improve this field quality are under investigation. Nevertheless the adverse effects of the a3 component are easy to mitigate thanks to the nearby SD0 sextupole. SD0 features similar difficulties in terms of magnet design as QD0. As a matter of fact a similar conceptual design [10] has been proposed as shown in Fig. 6.

Table 4: Measured multipolar components of the QD0 prototype in the usual 10^{-4} relative units and at a radius of 1 mm.

b3	0.71	a3	4
b4	3.36	a4	-0.4
b5	-0.31	a5	-0.41
b6	-0.72	a6	0.16
b7	0.02	a7	-0.01
b8	0.00	a8	0.00
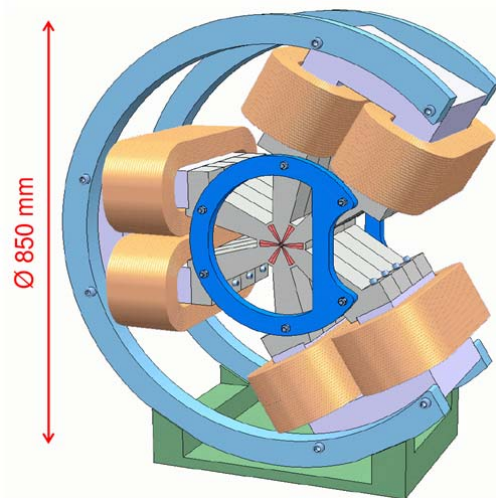
Figure 6: CLIC SD0 design as proposed in [9].

2.3.3 **Lower Energies between 350 and 500 GeV**

The CLIC IP beta functions at low energies are being explored in order to probe the entire machine parameter phase space. Traditional values of the horizontal beta function range between 8 and 10 mm. Lower values give larger total luminosity at the cost of a degradation of the collision energy spectrum. Nevertheless this can be used to reduce the charges per bunch easing the design and operation of the linac and the damping ring.

The current final focus conceptual design with a doublet as a final lens assumes an IP horizontal beta function considerably larger than the vertical one. However limits in the ratio or in the absolute value of the horizontal beta function are not well understood. Three lattices have been designed with the vertical beta function pushed to the hourglass effect limit (0.065 mm) and for horizontal betas of 8, 6, and 4 mm. The dispersion throughout the final focus system has been optimized case-by-case without considering any constraints from the higher energy layout. Figures 7 shows the total and peak luminosities for these lattices together with luminosities from ideal distributions versus number of particles. A clear sign of strong aberrations appears at 4 mm, where the luminosity of the corresponding final focus design only reaches 83% of that from ideal distributions.

Further studies are being carried out to fully understand the limitations and the sources of the higher order aberrations at 4 mm which might lead to cures and even lower beta functions or to establishing lower boundaries for the beta functions.
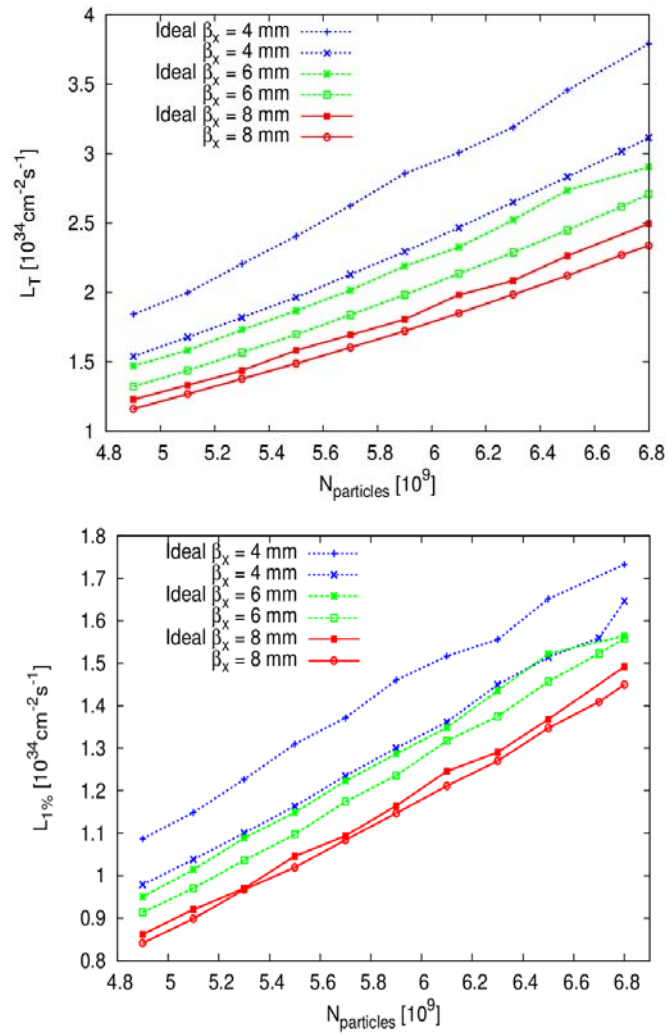
Figure 7: Total (top) and peak (bottom) luminosity versus number of particles per bunch and for 3 different IP horizontal beta functions using ideal distributions and new FFS designs. The vertical beta function has been set to the minimum value allowed by the hourglass effect (0.065mm).
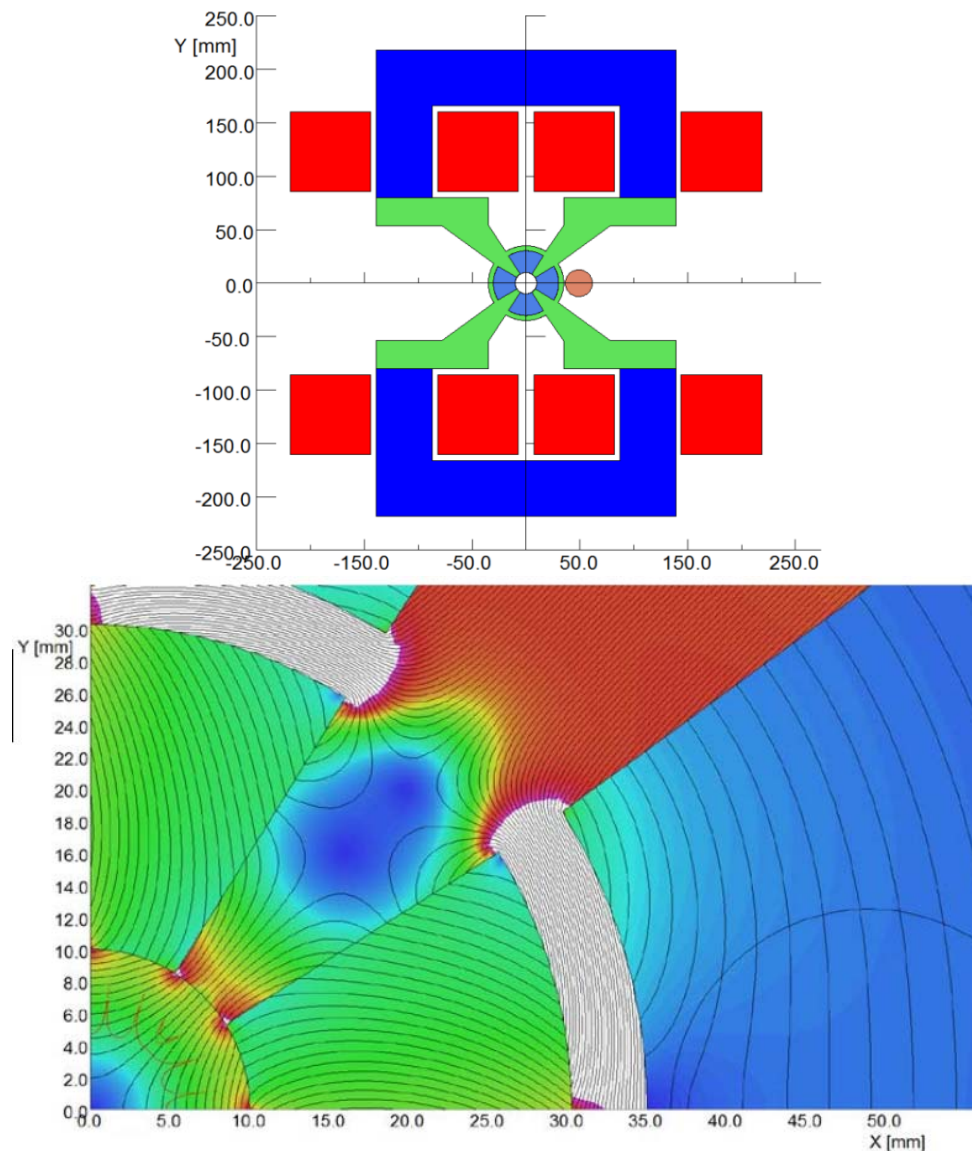
Figure 8: QDO design based on hybrid technology proposed for the ILC FFS [10]. The top figure shows a transverse section of the design and the bottom plot shows the field lines in the main beam pipe and the aperture for the extracted beam.

2.3.4   **500 GeV Final Focus System**

The recent discovery of a Higgs boson like particle with a mass around 125 GeV is pushing forward the interest of running CLIC at lower energies in order to study in detail the properties of this new particle. In the CLIC CDR were added the beam parameters at the IP that this option must have. They are summarized in Table 5. The optics design of the Final Focus System using this parameters has been done following two approaches: the local chromaticity correction scheme and the dedicated chromatic correction scheme.

Table 5: CLIC at 500 GeV and BDS parameters.

Parameter	Unit	CLIC500
Beam energy	GeV	250
Bunches per train		354
Bunch population	10^9	6.8
Repetition rate	Hz	50
Hor. Norm. emittance	μm	2.4
Vert. Norm. emittance	nm	25
Hor. Beta at IP	mm	8.0
Vert. Beta at IP	mm	0.1
Hor. beam size at IP	nm	200
Ver. Beam size at IP	nm	2.26
Bunch length	μm	72
Energy spread (rms)	%	0.3
Luminosity	10^{34} cm^{-2} s^{-1}	2.3

The optics for the traditional chromatic correction scheme consists on two dedicated sections for chromatic compensation, one per plane. In each section we have two pairs of sextupoles to compensate chromaticity and cancel geometric aberrations. Bending magnets are located in these sections to create dispersion at the sextupole positions.

Both lattices are designed according to the CDR parameters present in Table 5. The design based on the local chromatic correction scheme is 553 m long with L*=4.3 m. The design based on the dedicated correction scheme is 660 m long also with L*=4.3 m. The beam size optimization order by order is carried out using MADX and MAPCLASS and the results are shown in Fig. 9. The beam size optimization is approximately the same for both schemes and the aberrations in the vertical plane represent less than 8% of the linear beam size.
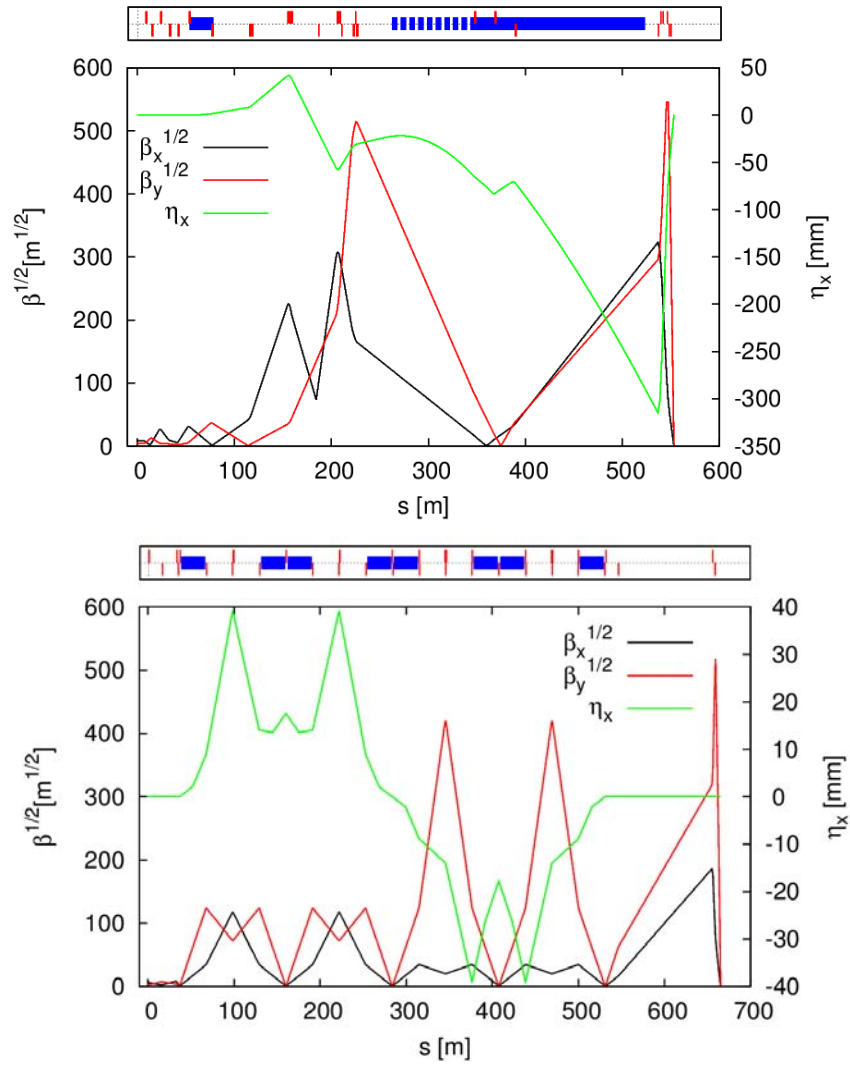
Figure 9: Optics of the CLIC 500 GeV local correction scheme (top) and dedicated correction scheme (bottom) final focus system showing horizontal and vertical beta-functions.
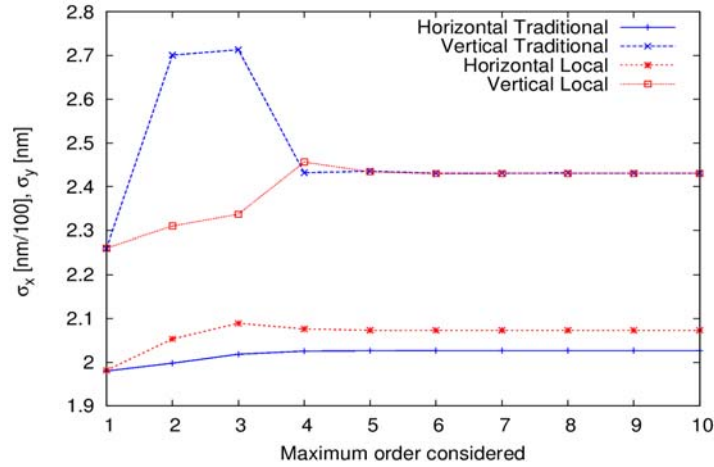
Figure 10: High order optimization using MAPCLASS for CLIC 500 GeV FFS.

Luminosity is calculated using PLACET for tracking the beam through the beam line and GuineaPig for beam-beam simulation. From the simulations we can extract the total luminosity and the peak luminosity given by the collisions with energies within 1% of the energy peak. The results for both lattices are shown in Table 6. The local scheme presents a slightly better performance in terms of luminosity.

Table 6: Total and peak luminosity for CLIC 500 GeV.

Scheme	*Energy*	*L_T [cm⁻²s⁻¹]*	*L_1% [cm⁻²s⁻¹]*
Local	500	2.3	1.4
Traditional	500	2.2	1.3

As in the 3 TeV case, when we consider realistic imperfections such as misalignments of the beamline elements, the performance of the system drops dramatically. Then a proper tuning of the machine is required. The tuning simulation has also been studied applying the same techniques explained above for the 3 TeV case. Concretely for this case we have used beam based alignment techniques like orbit correction and dispersion free steering correction and also tuning knobs based on sextupoles.
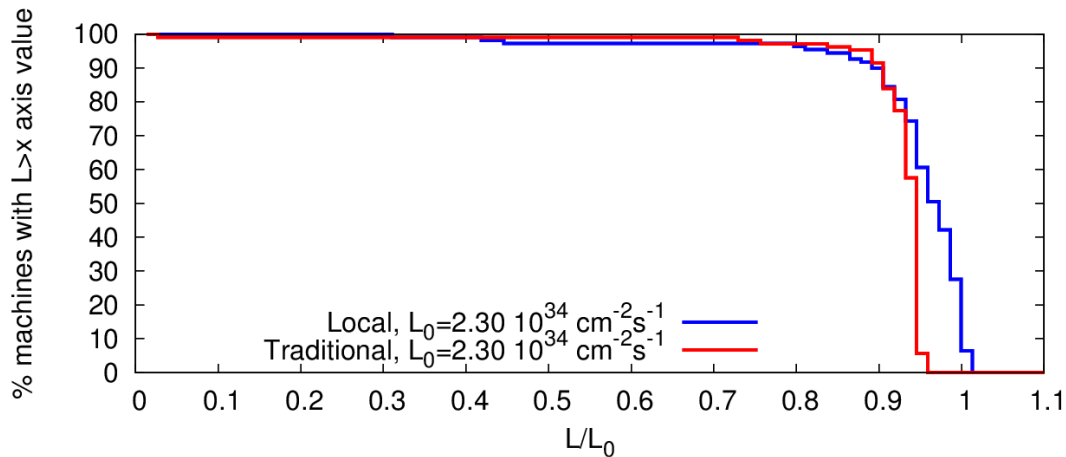
Figure 11: Luminosity distribution of 100 machines after BBA and multiknob algorithm procedure for an initial prealignment of 10 microns

Results of the tuning simulation are shown in Fig. 11 for just one iteration of the algorithm in both cases. We see how the result is quite similar for both systems reaching the goal of 90% of the machines above the 90% of the nominal luminosity. The local correction scheme delivers more total luminosity but the traditional scheme presents a slightly easier tuneability with respect to its best performance. The tuning time is expected to be also around 20-30 minutes in both cases.

2.3.5 A CLIC-Based FFS for ILC

The CLIC and ILC Final Focus Systems are both based in the local chromaticity correction scheme [2]. The optimization procedure is very similar in both schemes in order to correct the nonlinear aberrations and to achieve the maximum luminosity. Table 7 shows a comparison of CLIC 500 GeV and ILC 500 GeV beam and machine parameters at the Final Focus System. There are no parameters deviating more than a factor of four between CLIC and ILC. It is conceivable that a single FFS lattice design could serve both projects. To illustrate this point the CLIC FFS has been used to reproduce the ILC parameters.

As one can see in Table 8, the CLIC-based FFS lattice and ILC FFS lattice present similar performances in terms of IP beam sizes and luminosity. There are many more aspects to consider before claiming a CLIC-based FFS for ILC but this certainly represents a first step towards a common study framework between the two linear collider projects. Having a common FFS lattice would have immediate benefits in the resources needed to maintain the lattice and carry out simulations. Some overhead and compromises might be needed to take into account the particularities of both systems.

Table 7: CLIC and ILC BDS parameters comparison.

Parameter	Unit	CLIC500	ILC500
Beam energy	GeV	250	250
Bunches per train		354	1314
Bunch population	10^9	6.8	20
Repetition rate	Hz	50	5
Hor. Norm. emittance	μm	2.4	10.0
Vert. Norm. emittance	nm	25	35
Hor. Beta at IP	mm	8.0	11.0
Vert. Beta at IP	mm	0.1	0.48
Hor. beam size at IP	nm	200	474
Ver. Beam size at IP	nm	2.26	6.0
Bunch length	μm	72	300
Energy spread (rms)	%	0.3	0.125
Luminosity	10^{34} cm^{-2} s^{-1}	2.3	1.47

Table 8: Performance comparison for ILC and CLIC-based FFS.

Parameter	ILC	CLIC-based
Length [m]	735	553
β_x / β_y [mm]	11/0.48	11/0.48
σ_x [nm]	499.3	483.7
σ_y [nm]	6.03	5.89
Total Luminosity [10^{34} cm^{-2} s^{-1}]	1.39	1.47
Peak Luminosity [10^{34} cm^{-2} s^{-1}]	0.86	0.89

Independently of the lattice design option the technology choice can also be harmonized between CLIC and ILC. For example ILC features a superconducting final doublet while CLIC resorts to hybrid technology as described above. Since a CLIC short prototype has already been successfully built it is natural to explore the possibility of using this hybrid technology for ILC. In [10] a design of a CLIC-like QD0 for ILC is presented. Figure 9 shows the proposed design together with the field lines in a region containing the beam pipe and the aperture for the extracted beam (indicated by the blue circle). The design meets the ILC specifications with some margin that might be used for further optimizations.

2.3.6 Beam Dynamics in the MDI Region

The machine detector interface (MDI) comprises several particular challenges for future linear colliders. For example, the last quadrupole (QD0) might (depending on the chosen L*) be inside the detector, which means it needs to be supported by a cantilever rather than on the cavern floor.

Another particular problem for CLIC, is that the experimental solenoid field could produce significant amount of incoherent synchrotron radiation due to the high beam energy. Studies published so far indicate luminosity loss due to ISR in the solenoid will be between 3 and 25 %. There could be additional losses there are not enough correctors for the optical distortions coming from the solenoid.

The main optical distortions of the solenoid acting on the beam are y-x' coupling and vertical dispersion. The y-x' coupling comes from the fact that there is a relation between the x position of the particles in the last focusing magnet and the x' after this magnet. The vertical dispersion comes from the horizontal crossing angle, which produces a vertical orbit kick through the solenoid.

There are several ways to correct for the optical distortions of the solenoid, and most likely several methods are needed. One method which looks to be very valuable in simulations is an anti-solenoid around the QD0, which minimizes the effect of the solenoid inside this magnet. Several studies both for CLIC and ILC have shown that an anti-solenoid reduces the optical distortions by about 90%. Another tool is to use various magnet movers to correct the last 10 % of the optical distortions.

In Figure 12, we show the difference in the longitudinal field from the solenoid along the beamline, with and without anti-solenoid. In both cases we see a drop in the field in the QD0 region (3.5 m – 6.2 m). This is due to the QD0 itself shielding to some extent.
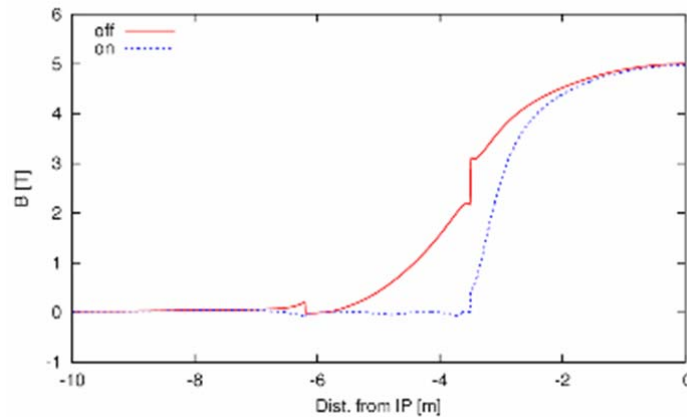
Figure 12: The longitudinal field of the experimental solenoid along the beamline, with and without anti-solenoid.

In Figure 13 an example of a typical vertical orbit distortion due to the solenoid is shown. The orbit distortion is on the order of 10 μm, causing a strong vertical dispersion. In this example, the QD0 has been moved vertically, so as to make the orbit end up at y=0 at the IP.
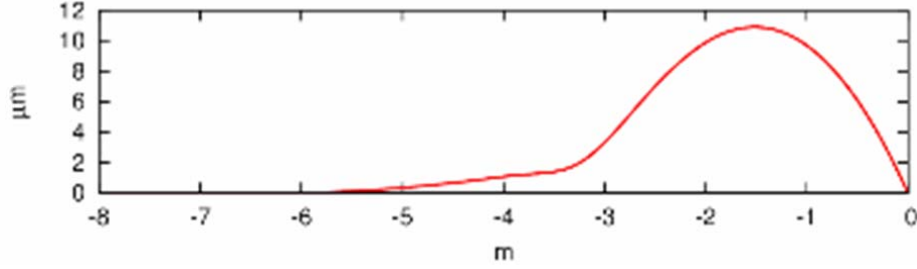
Figure 13: The vertical orbit distortion due to the solenoid field.

2.3.7   Collimation Section

The collimation section follows the diagnostic section in the BDS. It consists of an energy collimation section at around 1800 m before the IP, and a betatron section as shown in Figure 14, at around 1000 – 500 m before the IP. The collimation section serves two main purposes, cleaning off the beam halo, and protecting the BDS against mis-steered beams. The most likely origin of mis-steering is expected to be failure of parts of the RF sectors of the main linac, resulting in lower beam energy. Hence the energy collimation is placed before the betatron collimation for optimal protection of the BDS. Muon spoilers are placed next to the betatron collimators to reduce the flux of muons in the detector.
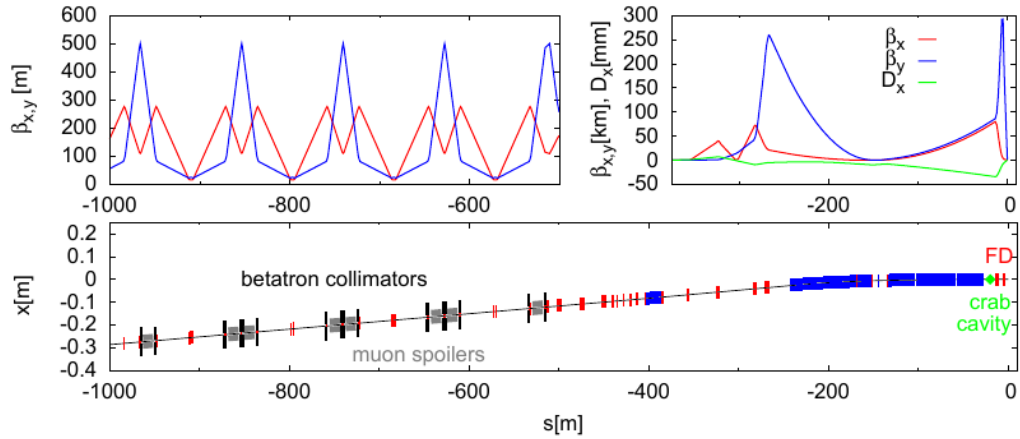
Figure 14: The betatron collimation section, and the following final focus section.

2.3.8   **ATF2 Ultra-low β* Optics**

2.3.8.1   *Motivation*

CLIC is designed to deliver a luminosity above 10^{34} cm^{-2} s^{-1}. To satisfy such a challenging performance, the design horizontal (σ_x^*) and vertical spot size (σ_y^*) at the interaction point (IP) are 45 nm and 1 nm, respectively. This unprecedented vertical beam size can be achieved by focusing the vertical beta function at the IP (β_y^*) down to 69 μm by means of two strong quadrupoles, namely Final Doublet (FD) located a distance L^* upstream the IP. The implication of reducing β_y^* is the increase of the

chromaticity (ξ) of the lattice. The chromatic correction implemented in the Beam Delivery System (BDS) of CLIC is based on the local correction scheme first proposed by P. Raimondi [2], although other alternatives are under investigation. The experimental validation of this novel scheme is currently taking place at the Accelerator Test Facility ATF2 [2]. The nominal lattice of ATF2 features a chromaticity 4 times smaller than the one of CLIC. The ATF2 ultra-low β^* lattice [12] is a proposal for experiencing with a lattice of chromaticity comparable to that of CLIC, and 4 times larger than the ATF2 nominal lattice which is equivalent to the one of ILC [11] in terms of chromaticity. Table 9 summarizes the most relevant parameters of ATF2, CLIC and ILC.

Table 9: Comparison between relevant parameters of ATF2, CLIC and ILC. E is the energy of the beam and $\gamma\varepsilon_y$ is the normalized vertical emittance of the beam.

Project	*E*	$\gamma\varepsilon_y$	σ_y^*	β_y^*	L^*	ξ_y
	[GeV]	[nm]	[nm]	[mm]	[m]	[]
ATF2 Nominal	1.3	30	37	0.1	1.0	10000
ATF2 Ultra-low β^*	1.3	30	23	0.025	1.0	40000
CLIC L^*=3.5 m	1500	20	1	0.069	3.5	50000
ILC	250	35	5.9	0.48	3.5	7000

The impact of realistic error conditions on the performance of the lattice becomes more severe as the chromaticity of the lattice increases. In this sense the design process of the ATF2 ultra-low β_y^* lattice taking into account the multipole content of the ATF2 magnets and the simulation tuning results are given in the following.

2.3.8.2 *ATF2 ultra-low β^* Lattice Design*

Reducing β_y^* by factor 4 increases the beam size at the FD by a factor 2. This also applies throughout the entire FFS, consequently the IP beam becomes more sensitive to magnetic field errors. The tolerances on magnetic field quality are expected to be tighter for the ultra-low β* design.

The values of σ^* presented in Table 9 are evaluated assuming error-free lattices. When the magnetic field errors of the current ATF2 magnets are included in simulations the obtained vertical beam size increases by 35% with respect to the design as shown in Table 9. For comparison, the impact of the same multipole components is less than 3% for the ATF2 nominal lattice. It is patent the severity of the magnetic field errors on higher chromatic lattices. In order to minimize the design spot sizes the inclusion of a pair of octupole lenses permits to reduce the impact to less than 5%, obtaining a final spot size of σ_y^*=24 nm effectively, see [13].

2.3.8.3 *Tuning Performance*

Larger tuning difficulties are expected for lattices with larger chromaticities. In fact the number of iterations required for tuning a lattice was found roughly proportional to the square root of the chromaticity of the lattice, as shown in [14]. Therefore and

increased tuning difficulty is expected for the ultra-low β_y^* lattice with respect to the nominal.

In [15] the tuning performance of the ATF2 nominal lattice using a tuning algorithm based on orthogonal tuning knobs is presented. From the study it is concluded that the vertical beam size can be tuned below 46.8 nm, or equivalently 1.26 times the design spot size, for 84% of the machines considered in simulations. A comparable tuning study was carried out in [16] for the ATF2 ultra-low β^* lattice implementing the same tuning algorithm and assuming similar error conditions. The results showed that only 63% of the simulated machines reached a final vertical spot size below 28 nm which represents 1.2 times the design IP vertical spot size.

2.3.9 References

1. "CLIC Conceptual Design Report", CERN-2012-007.
2. P. Raimondi and A. Seryi, Phys. Rev. Lett. 86, 3779-3782.
3. R. Tomás, ``Nonlinear optimization of beam lines'', Phys. Rev. ST Accel. Beams 9, 081001 (2006).
4. J. Barranco, E. Marin, and R. Tomas, "Luminosity studies in a traveling waist regime in the Compact Linear Collider", Phys. Rev. ST Accel. Beams 16, 041001, Published 4 April 2013
5. K. Oide, Phys. Rev. Lett. 61, 1713 - 1715 (1988).
6. R. Tomás et al, "Summary of the BDS and MDI CLIC08 Working Group", CLIC-Note-776.
7. B. Dalena, J. Barranco, A. Latina, E. Marin, J. Pfingstner, D. Schulte, J. Snuverink, R. Tomas, and G. Zamudio, ``Beam delivery system tuning and luminosity monitoring in the Compact Linear Collider'', Phys. Rev. ST Accel. Beams 15, 051006, Published 30 May 2012.
8. A. Bartalesi, M. Modena, "Design of the anti-solenoid system for the CLIC SiD experiment" TE-MSC Note 2012-11, EDMS N. 1214775
9. M. Modena et al. "Design, assembly and first measurements of a short model for CLIC final focus hybrid quadrupole QD0" Proceedings of IPAC 2012, New Orleans, Louisiana, USA.
10. M. Modena et al, "CLIC QD0 and other BDS and Post-collision line magnets", ECFA LC2013, Hamburg, Germany.
11. C. Adolphsen, et al, "The International Linear Collider Technical Design Report - Volume 3.I: Accelerator R&D in the Technical Design Phase", arXiv:1306.6353, (2013).
12. P. Bambade et al, "ATF2 Ultra-Low IP Betas Proposal", CERN-ATS-2009-092, CLIC-Note-792, (2009).
13. E. Marin, et al, "Design and higher order aberrations of the ATF2 lattices", submitted to Phys. Rev. ST-AB.
11. R. Tomas, et al, "ATF2 ultra-low IP betas proposal", Proc.of PAC'09 Vancouver, (2009).
12. T. Okugi et al., "Linear and 2nd order optics correction of ATF2 final focus beamline", submitted to Phys. Rev. ST-AB.
13. E. Marin, et al, "Design And High Order Optimization Of The ATF2 Lattices", Proc. of NAPAC '13, Pasadena (USA).

2.4   QD0 Design

Michele Modena, CERN, CH 1211 Geneva 23, Switzerland
Mail to: michele.modena@cern.ch

2.4.1   CLIC Final Focus Magnets Design

2.4.1.1   *Introduction*

In a previous ICFA Beam Dynamics Newsletter [1] it was presented the general layout, studies and status for the CLIC Final Focus (FF) system. From the point of view of the magnets system, the layout for a 3 TeV machine is extremely challenging in terms of high gradient required for the magnets like the QD0 and the SD0, the last quadrupole and sextupole of the Beam Delivery System (BDS). Other challenging aspects are: the integration of the QD0 magnet in the detector (focal length L* of 3.5 meter), the tight tolerances required for the alignment and the stabilization (active stabilization in the nanometer range). In this Chapter it will be presented in detail the proposed design for these magnets, highlighting the reasons behind the technical choices proposed and the status of prototypes procured and under procurement. More details about the optical design of the FF system can be found in the previous contribution by R. Tomas, in this Newsletter.

2.4.1.2   *QD0 Conceptual Design*

The CLIC Machine Detector Interface (MDI) layout as presented in the CLIC CDR [2] is shown in Figure 1. The L* value of 3.5 meter means that the defocusing quadrupole QD0, the final element of the BDS, is placed inside the detector, and it is so subjected to very special boundary conditions in terms of integration and operation in the "roll-in" concept proposed for the experiments detectors.
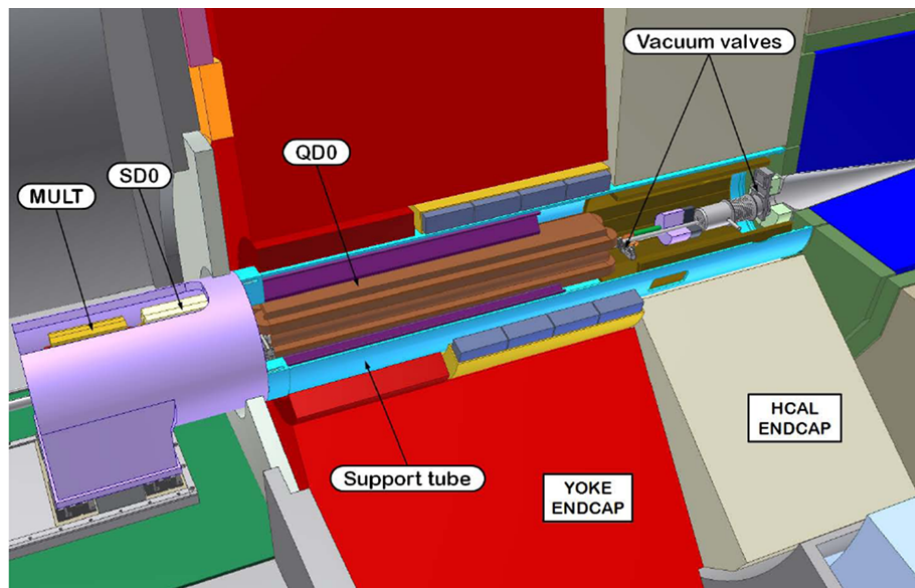
Figure 1: CLIC Machine Detector Interface layout (configuration for 3 TeV machine energy with L* of 3.5 m).

Table 1 resume the most important QD0 parameters. To be highlighted the very high gradient required, and the small aperture, that would require an extremely accurate poles assembly in case of a classical iron dominated EM magnet design assembled by quadrants.

Table 1: CLIC QD0 main parameters.

Main Parameter	*Value*
Required field gradient G	575 T/m
Magnetic length (full size QD0)	2.73 m
Beam required aperture	7.6 mm
Magnet bore diameter	8.25 mm
Good field region(GFR) radius	1 mm
Integrated field gradient error inside GFR	< 0.1%
Gradient adjustment required	+0 to -20%

Besides the challenging magnetic requirements the integration (refer to Figure 1) will also means a list of tight boundary conditions to be fulfilled. They are here resumed:

1. The magnet design must be compatible with the presence of the post collision line. At the inner front end of the QD0 (towards IP), the post collision line wall will be transversally at 35 mm from the incoming beam axis, so the high gradient must be "generated" in a cylinder of 35 mm of radius.
2. The magnet must be actively stabilized in the nanometer range. In order to do that the magnet structure must be as much as possible rigid and sound. Vibrational modes and frequencies of the magnet structure and its supporting system must be easily determined in order to be taken into account by the stabilization system design and development.
3. In case of use of classical electromagnetic coils, the presence of water-cooling system must be checked in terms of a possible source of vibrations that will interfere with the stabilization system functioning.
4. The magnet must have a compact cross section in order to limit the space subtracted to the detectors elements (calorimeters, etc).
5. Magnet will be subjected to an elevate radiation dose (expected dose evaluation is under revision).
6. Due to the experiment "roll-in" concept, the magnets service connections (powering, cooling, etc.) should be minimized and simplified.
7. Due to the extremely tight alignment tolerances required, the magnet design must permit a precise alignment of the magnet "core".
8. In order to guarantee a correct functioning of the magnet, an anti-solenoid, shielding the stray field of the detector main solenoid, is required. This aspect was widely studied and a detailed conceptual design for the anti-solenoid is now available [3].

Nowadays, the standard way to get compact magnet with very strong gradient is the superconducting (SC) one. A first analysis of the above listed boundary conditions make difficult to identify in the SC choice the good one for CLIC QD0:

- It will be not possible to actively stabilize a SC quadrupole since the structure is by definition not sound and rigid (thermal insulation foot, thermal shields, etc) so it will be the cryostat to be stabilized but not the cold mass inside.
- Furthermore the alignment will also be problematic since in a SC assembly will be extremely difficult to know with high precision the position of the cold mass inside the cryostat where the cold mass and other elements move subjected to expansion and contraction consequences of the thermal cycles.
- Another aspect will be the potential impact of the cryogenic cooling on the stability of the cold mass. Also this point could become critical for a correct functioning of the stabilization system.

For these reasons we approached the problem starting from another classical way to provide extremely high gradients in compact magnet design that is by the use of permanent magnets (PM) and mainly with the so called "Halbach" design. In Figure 2 is shown a classical Halbach PM quadrupole scheme (left). The high gradient is generated by the array of PM wedges assembled in a cylindrical shape. Each PM block has a well-defined magnetization direction in order to generate a precise quadrupolar field. On the right it is show a version boosted by the presence of Permendur poles inserts. Permendur is a FeCo alloy characterized by a high magnetic saturation respect to carbon steel. These inserts have two advantages: they increase the performances of the magnet (achievable gradient) concentrating the magnetic flux in the poles, and they ameliorate the field quality since they act as the iron poles in an iron-dominated magnet scheme.
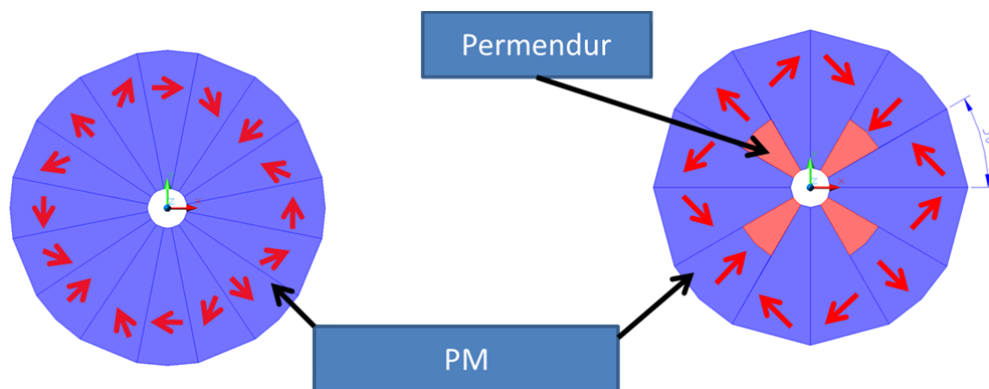
Figure 2: Two classic PM Halbach quadrupole schemes.

The next step was to introduce the tuning capability. This was done developing the concept of hybrid magnet adding the return yoke and EM coils, as shown in Figure 3. The main components and concept of the design are now visible: the presence of the PM blocks (blue), the Permendur poles (green) the return yoke (grey) the EM coils (red). Design is compatibles with the presence of the post-collision line vacuum pipe (the blue hollow cylinder on the right).
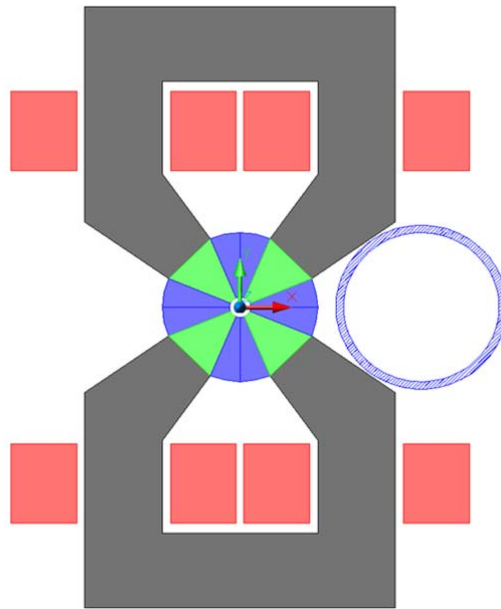
Figure 3: Two PM Halbach tunable quadrupole.

This conceptual design was then developed considering construction and assembly aspects. In order to guarantee the required magnetic field quality, the magnet components must be assembled with very tight tolerances. The conceptual design, as presented in Figure 3, contains a lots of components that would be difficult to assembly precisely on the length of 2.7 m. To be noted as is it possible to procure precise magnetized PM blocks only of limited length of about 80-100 mm maximum. For these reasons we developed the concept of modular monolithic central structures manufactured by Electrical Discharge Machining (EDM) technique. In Figure 4 it is shown a plot of the magnetic calculation of the structure cross-section (2D analysis; the structure is represented only partially due to the main axes symmetries). The introduction of the "ring" structures connecting the poles was not done for magnetic reasons (in fact the quadrupole gradient is slightly decreased due to some flux that is short-circuited by these rings), but the mechanical advantage to have them and consequently creating the monolithic solution are extremely important:

- We have now only one central element and the correct geometry of the quadrupolar configuration is guaranteed by the high precision of the EDM machining.
- The rings and the poles external surface create perfect "alcoves" to insert and position the PM blocks.
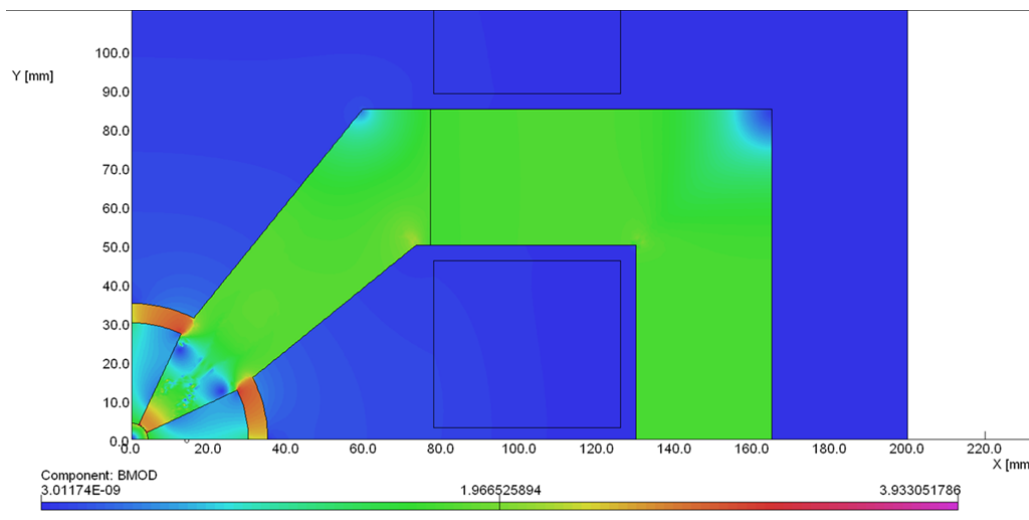
Figure 4: The concept of monolithic central structure.

2.4.1.3 *Prototype Final Design and Procurements of Components*

We then decide to procure a short prototype of the QD0 to validate this hybrid tunable concept [4]. Short prototype means a magnet with the same characteristic in terms of: cross-section dimensions, achievable gradient, current density in the coil, as in the full size magnet, but longitudinally shorter. In fact the procured central part (100 mm of length) will be representative of one module of the many that should be longitudinally assembled to get the central part of the full size magnet (see next Section).

The finalization of the prototype design was then done defining the final dimension of the central components (i.e. the monolithic Permendur and the PM inserts) and the design of the EM coils. The dimension and tolerances of the central components were decide after discussion with the components manufacturer (Vacuumschmelze-D) , while the coils were done at CERN and dimensioned for an operational current density of ~1 A/mm^2. In this way the coils don't need active water cooling that could have a potential impact on the stabilization system (vibrations). Figure 5 shows a complete 3D view and a cross-section of the prototype.
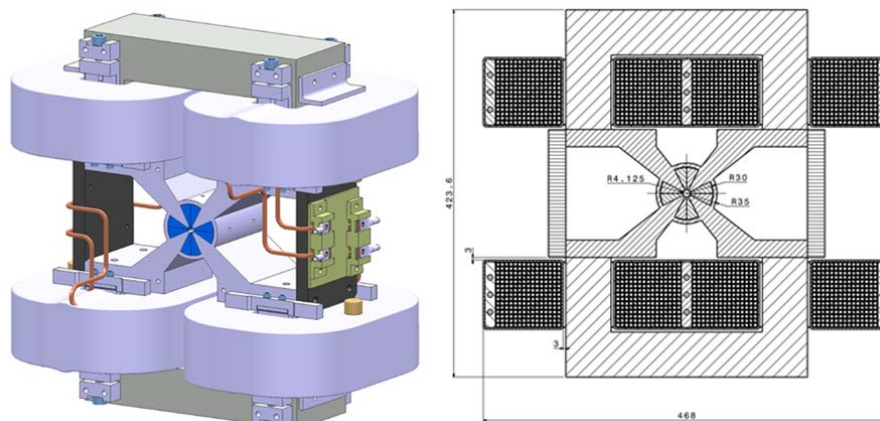
Figure 5: 3D view and cross-section of the procured short prototype.

The Permendur part was machined at Vacuumschmelze premises with achieved tolerances on the most critical dimensions in the range of ±25 µm. Similar values were obtained for the PM block that were procured in two different materials: Sm_2Co_{17} and $Nd_2Fe_{14}B$. To be noted as each of the 4 PM inserts is composed by 4 single PM wedges glued together (azimuthally and longitudinally) Photos of the completed components are shown in Figure 6.

Figure 6: The prototype core elements: the monolithic Permendur structure (left) and a details of the PM wedges inserted in the central part (right). The lines on the PM surface indicate the magnetization directions.

The final assembly and testing was done at CERN. Figure 7 show the completed prototype. Due to minute magnet aperture (8.25 mm diameter), the magnet measurement method utilized was the Vibrating Wire. This method, under development at CERN, permits to measure the gradient, the magnetic axis, and also the field integrated multipole expansion that provide the field quality information [5].
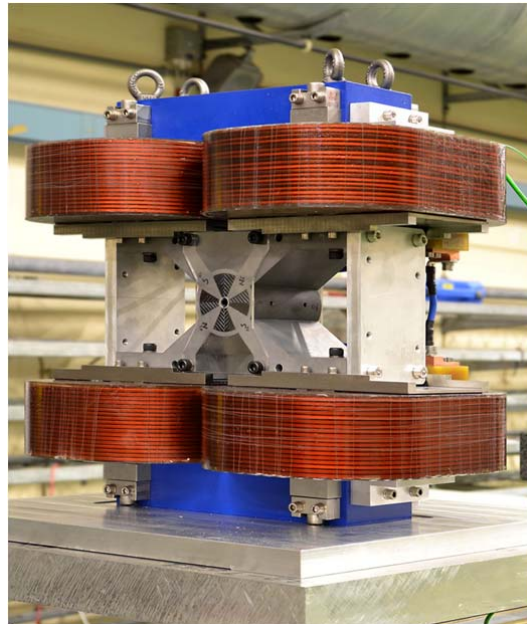
Figure 7: QD0 prototype final assembly.

The powering curves (gradient versus coil ampere-turns) obtained are presented in Figure 8. The red dots show measurement point and the blue line the expected values (from 3D magnetic simulation). The third (black) curve on the right plot shows the expected gradient for a full size magnet (being the prototype quite short, its performances are affected by field decreasing at the extremities). On the left plot are presented the measurements with the magnet equipped with the Sm_2Co_{17} block. On the right plot the case with the $Nd_2Fe_{14}B$ blocks. The correlation is perfect with 1st material, while shows a discrepancy of ~6% with the 2nd material.

These results validate the concept of the design and indicate that there are some non-conformities in the $Nd_2Fe_{14}B$ set of blocks. It could be a problem of magnetization angle or module in one or more wedges. This aspect is under evaluation.

The other information that these two graphs provide are the tuning range of this design that is nominally very wide: -70/80% of the maximum gradient.
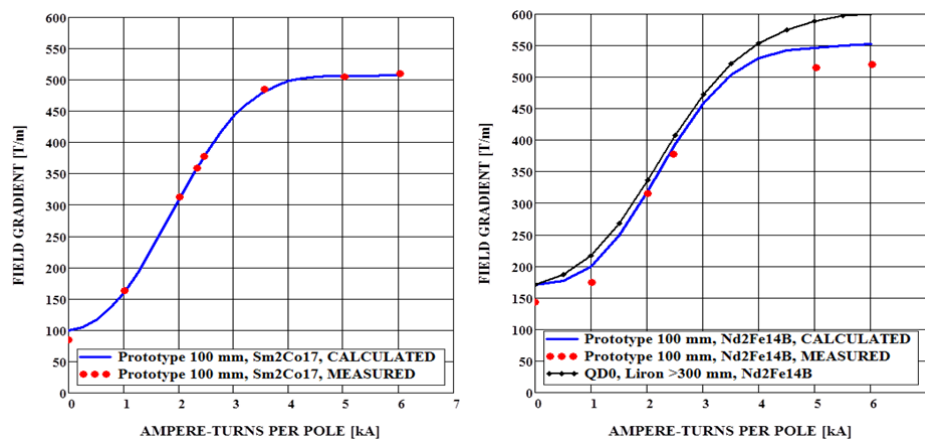
Figure 8: Powering curves measurements.

Concerning the field quality, the two graphs of Figure 9 provide the measurements results obtained by the Vibrating Wire system for different powering (tuning) conditions. The 1st plot applies to the Sm_2Co_{17} case, while the 2nd to the $Nd_2Fe_{14}B$ case. The nominal operating point is 5000 NI (ampere-turns), so identified by the black bars in the 1st plot and red bars in the 2nd plot.

Tests are planned to measure the central structure without PM blocks in order to try to separate the part of multipole components coming from the machining tolerance from the part coming from the PM blocks imperfections. The overall results are anyway quite promising for a so small magnetic design where every mechanical or magnetic error has a relative big impact on the global field quality.
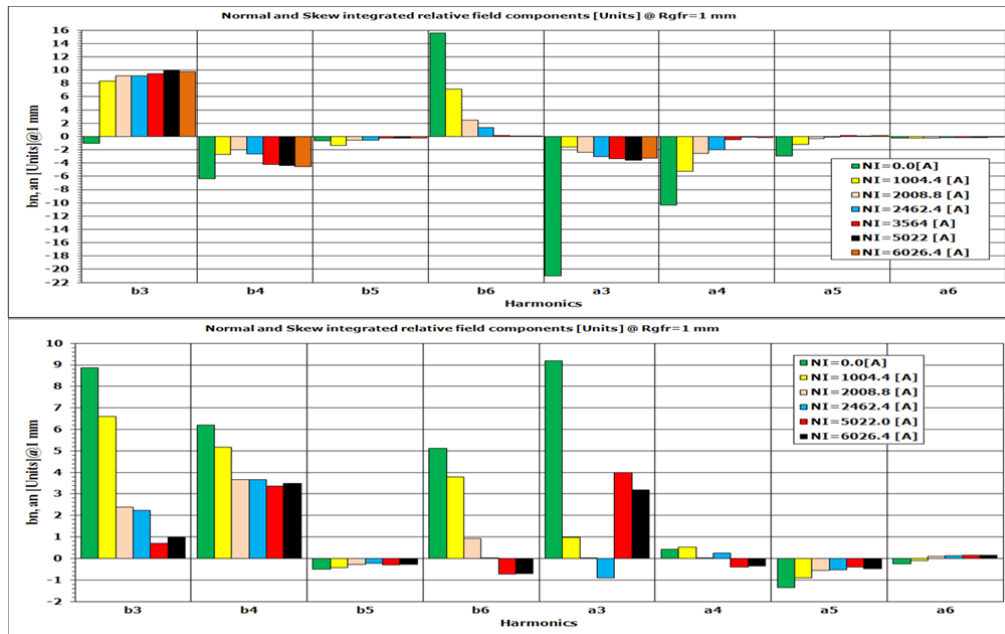
Figure 9: Field quality measurements as multipole content.

2.4.1.4 *From the Short Prototype to a Full Size QD0 Design*

As previously mentioned, the interest to procure a short prototype was that is also representative of the single module that has then to assembled in series to provide a full size magnet.

This assembly solution is obliged for the following reasons:
- It is possible to procure PM blocks only with limited length (max 80-100 mm).
- The EDM precision is dependent from the length (thickness) of the part to be cut. Over a dimension of ~200 mm the precision decrease especially at the centre of the pieces due to the sag of the cutting wire subjected to the Lorentz forces.

For these reasons the full-size magnet will be built by assembly a certain number of sections. In case the section will have the same length as this prototype they should be 27 units to be assembled, but this number can probably be reduced optimizing with the industrial partners the length of the single module. In the full magnet version the return yokes (the grey elements of Figure 5-left) will play the roles of alignment references for the modules and the mating surfaces design for these components will also be optimized to this scope. Figure 10 shows the basic concept of longitudinal modular assembly. The EM coils will be of course covering the full length of the core structure.
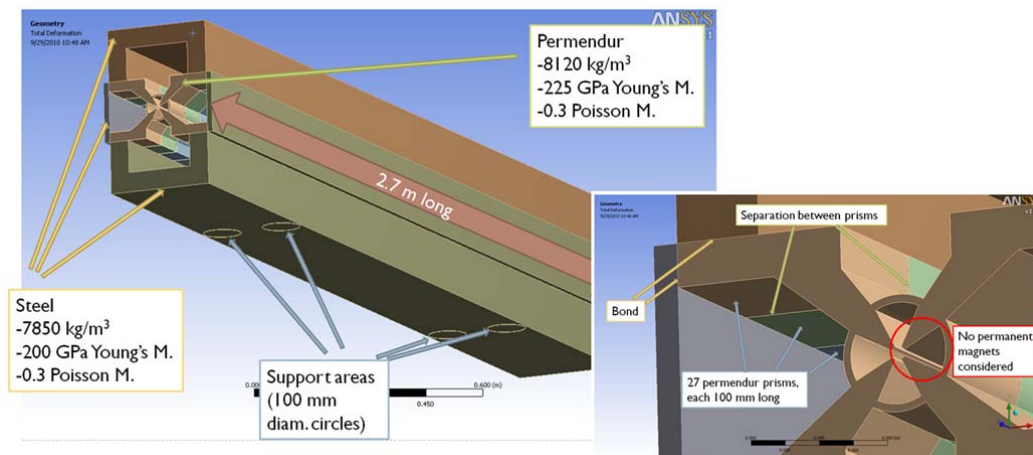
Figure 10: The full-size QD0 as a modular assembly of shorther sections.

For the full-size version, inside the CLIC MDI working group, an integration solution was developed that should permit to support the coils (total weight: ~1100 kg) independently from the central part (total weight: ~1600 kg). This will have a big positive impact on the design and dimensioning of the stabilization system. In Figure 11 it is shown the supporting concept: the coils will be supported by cantilevers (in grey) attached to the supporting tube (in blue). The quadrupole central part will lay on the active (piezoelectric) actuators of the stabilization system through special supporting feet (Figure 6 detail).
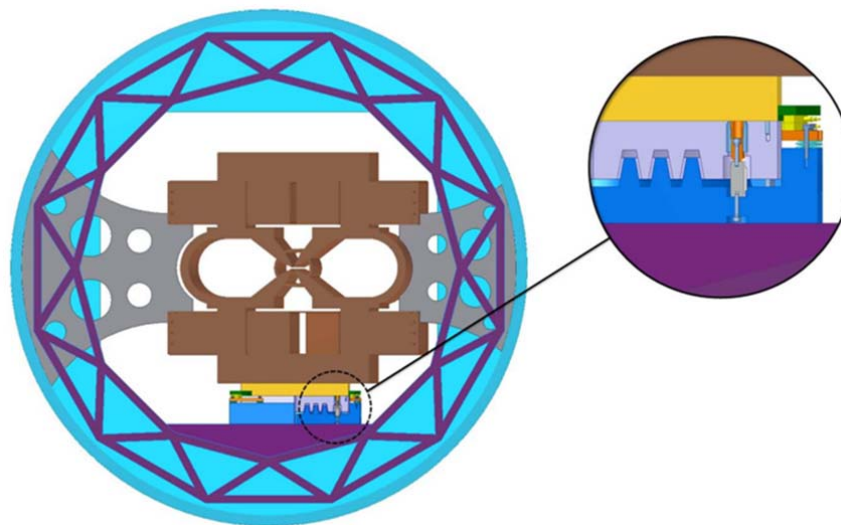
Figure 11: The supporting concept of the full-size QD0 inside the experiment detector.

2.4.1.5 *Next Planned Activities for QD0 and SD0 Design and Procurement*

As mentioned in the previous Sections, the successful procurement of the QD0 short prototype has proven the conceptual magnetic design and the single module assembly solution.

One of the next steps will be the investigation on the $Nd_2Fe_{14}B$ blocks magnetic quality non-conformity that we will do as soon as a 3D Helmholtz coils measuring

systrem under commissioning at the CERN Magnetic Measurement Section will be operational.

The main further step would be to procure a longer prototype in order to investigate the following aspects:

- Check and work on the problem of the longitudinal assembly of several central modules respecting the required tolerances. This is a critical aspect as concerning the mechanics of the assembly where also magnetic forces between blocks (fragile components!) will arise and must be mastered.
- Discuss with the PM suppliers the problem of quality and reproducibility of the PM blocks. Due to the special production method of the PM block (sinterization under a strong magnetic field), the PM block Suppliers cannot guarantee a precision on the magnetization angle better of ±1-2°. This aspect must be discussed and studied since for a full-size magnet, hundreds of block with the same magnetic characteristics are necessary.

We have recently taken the decision to investigate these aspects not choosing to build a longer QD0 prototype but building a full-size SD0 (sextupole) magnet. The SD0 is another element of the CLIC FF system and is placed just behind the QD0 in the MDI layout (refer to Figure 1). Due to the fact that the magnet is not placed inside the experiment detector but just at the border of the accelerator tunnel, the geometric boundary conditions are less stringent, but also for SD0 it is asked to procure a magnet with the highest possible sextupolar gradient and with a design compatible with the integration of the post-collision vacuum line and with an active stabilization system.

For SD0 we propose a design solution very similar to the QD0 one.

In table 2 are listed the main parameters of the sextupole, while in Figure 12 a 3D view of the full-scale prototype under design is shown.

Table 2: CLIC SD0 main parameters.

Main Parameter	*Value*
Inner radius	4.3 mm
Nom. Sext. Gradient	219403 T/m2
Magnetic Length	0.248 m
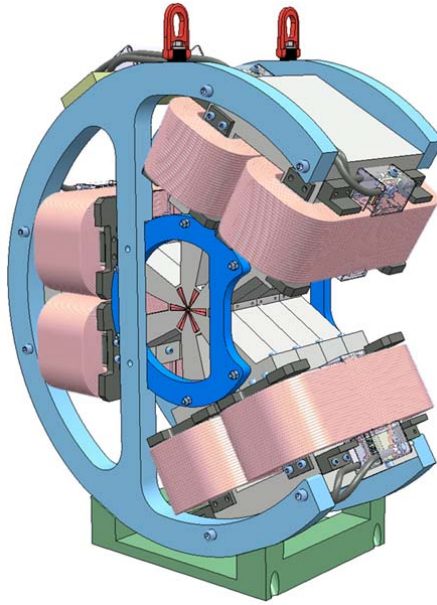
Figure 12: 3D view of the full-scale prototype.

The aperture of the magnet: r=4.3 mm, is very similar of the one of QD0. The length of about 250 mm will permit to assemble longitudinally 4 central modules and we will need at least 24 PM blocks. The key points that we intend to investigate with this prototype are:

- Develop with the PM block Supplier a plan to produce and select the needed block inside tight magnetic tolerances
- Develop with the EDM Manufacturer a plan to get tight tolerances for the four central elements.
- Assembly four complete longitudinal sections using the return yokes as precise alignment and mounting references.
- Develop with the colleagues of the Magnetic Measurements Section a plan of detailed magnetic measurements on the single module (with PM blocks but without coils) and on the full magnet.

Details on the magnet design and procurement will be reported in future Conferences and Journals.

2.4.2 References

1. R. Tomas, H. Garcia, Y.I. Levinsen and M. Modena, "CLIC Final Focus Optics", in "ICFA Beam Dynamics Newsletters No.61"Section: 2.1.3, August 2013. edited by Toshiyuki Okugi (KEK, Japan).
2. "CLIC Conceptual Design Report", CERN-2012-007. Available at http://clic-study.org/accelerator/CLIC-ConceptDesignRep.php
3. A. Bartalesi, M. Modena, "Design of the anti-solenoid system for the CLIC SiD experiment" CLIC-Note-944
4. M. Modena O. Dunkel, J. Garcia Perez, C. Petrone, E. Solodko, P. Thonet, D. Tommasini, A. Vorozhtsov, "Design, assembly and first measurements of a short model for CLIC final focus hybrid quadrupole QD0" Proceedings of IPAC 2012, New Orleans,
5. P. Arpaia, C. Petrone, M. Buzio, S. Russenschuck S, L. Walckiers, "Multipole correction of stretched-wire measurements of field-gradients in quadrupole accelerator magnets" JINST - Journal of Instrumentation, (2013), Ref: 2013 JINST 8 P08010.

2.5 Ring to Main Linac Section

Andrea Latina, CERN, CH 1211 Geneva 23, Switzerland
Mail to: mailto:andrea.latina@cern.ch

2.5.1 Introduction

Primarily the "Ring to Main Linac" (RTML) of CLIC has the function of transporting the beam from the damping ring extraction to the main linac entrance. Two RTML sections are present in CLIC: one for the electron side and one for the positron side of the machine. Each section involves more than 25 km of beamlines and includes specific subsystems to accomplish various tasks and beam manipulations:

1. Matching the requirements of the CLIC geometric layout, transporting the beam from the damping ring extraction located in the center of the site to the entrance of the main linacs located at the two opposite ends of the site; this involves horizontal and vertical doglegs, a turnaround loop, and a long transfer line;
2. Accelerating the beam from 2.86 to 9 GeV while compressing the bunches longitudinally from 1.6 mm to 44 μm bunch length;
3. Controlling the spin of the electrons to achieve any orientation.

These three tasks must be accomplished while: preserving the nanometer transverse emittances, protecting the linac from errant beams and halo particles, measuring the relevant beam parameters for on-line diagnostics.
The presented RTML design is suitable also for different stages of CLIC, because the beam parameters at damping ring extraction and at linac entrance are similar at the different stages. The most significant change regards the long transfer lines, which at 500 GeV are shorter to match the shorter linac length. A detailed description of the entire system can be found in [1].

2.5.2 System Description

The two RTMLs for electrons and positrons have each a total length of approximately 27 km. Their layouts are similar, but there are small differences due to geometric constraints and to the fact that positron polarization is not included in the CLIC baseline. The layout of the RTML is shown in Fig. 1. Not visible in the figure is that the RTML must also descend below the ground level, since the damping rings are located on the site surface whereas the main linac is 100 m underground.

Table 1: Main beam parameters at the entrance and at the exit of the RTML.

Parameter	Entrance	Exit	Unit
Energy	2.86	9	GeV
RMS bunch length	1600	44	μm
RMS energy spread	0.13%	<1.7%	
Normalized horizontal emittance	500	<600	nm
Normalized vertical emittance	5	<10	nm

The RTML is composed by several distinct subsystems, which will be described in the following sections, connected by short matching sections. The beam parameters at

the entrance and at the exit of the RTML are the same for both electrons and positrons, and are listed in Table 1.

2.5.2.1 *Electron Spin Rotator*

A spin rotator is located at the start of the electron RTML. Its design consists in two pairs of solenoid magnets, separated by a bending arc. Between each solenoid pair, a reflector beam line with transfer matrix (I 0 ; 0 –I) is used to cancel the couplings induced by the solenoids. Each solenoid pair can be set independently, allowing a spin rotation from 0 to 90 degrees. The arc in between the solenoid pairs bends the beam by an angle of 13.9 degrees, which corresponds to a spin rotation by 90 degrees. The combination of the two tuneable solenoid pairs with the bending arc allows the achievement of any arbitrary spin orientation. The momentum compaction factor of the arc is small, only 5.9 cm, which limits the bunch lengthening to 2 μm taking into account the small energy spread of the beam, 0.13%. [2,3].
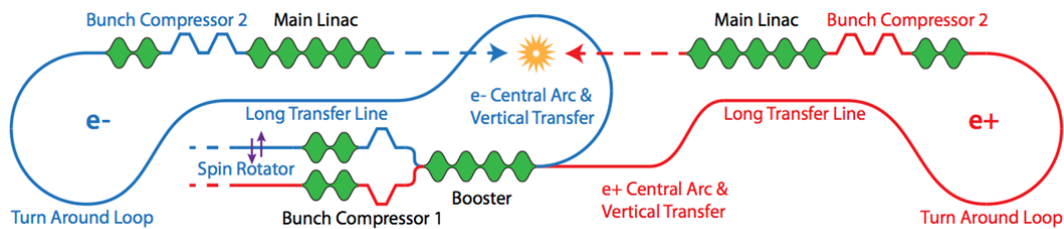
Figure 1: A scheme of the CLIC RTML.

2.5.2.2 *Bunch Compressors and Booster Linac*

To control the longitudinal phase space, both electron and positron lines are equipped with two bunch compressors and a booster linac. Bunch compressor 1 is located at the beginning of the RTML, where the beam has energy 2.86 GeV; bunch compressor 2 is located right before the main linac entrance, at 9 GeV. The beam energy is brought from 2.86 to 9 GeV in the booster linac, right before the central arc and the long transfer line.

The first stage of bunch compression (BC1) compresses the initially 1.6 mm long bunches to a length of 300 μm. Its RF section consists of twenty 2 GHz cavities embedded in a FODO lattice identical to that for the booster linac. Each cavity has a length of 1.5 m and an average gradient of 13.3 MV/m. The beam passes through the cavities at a phase of 90 degrees off-crest, i.e. at zero crossing, so there is in average there is no acceleration but this leads to an almost linear energy which is required to compress the bunches to 300 μm in the chicane that follows, which has R_{56} =-14.5 m.

The setup of the bunch compressors is the result of an optimization process that takes into account effects like coherent synchrotron radiation (CSR) and incoherent synchrotron radiation (ISR) [4], the energy acceptance of the downstream arcs, beam phase stability and RF properties [5,6].

The booster linac accelerates the beam to the main linac injection energy of 9 GeV. The same linac is shared between electrons and positrons. The two incoming bunch trains are shifted in time by 1100 ns, based on RF constraints. The booster linac has the same type of 2 GHz cavities as BC1. There are a total of 276 cavities at an average

gradient of 14.9 MV/m. They are embedded into a FODO lattice with 8 cavities per cell with an average beta function of 16 m. The total length of the booster linac is 538 m.

The second bunch compressor (BC2) compresses the bunch length to 44 μm. It contains an RF section with 78 12 GHz cavities which are 0.23 m long and run 90 degrees off-crest with an average gradient of 94 MV/m. The impact of longitudinal short-range wakefields, that tends to lower the energy chirp, is taken into account. To ensure that the short-range wakefields do not degrade the beam quality, the BC2 lattice is the same as the start of the main linac. To limit the impact of ISR, the required R_{56} is obtained using two chicanes, with R_{56} equal to -1.38 and -0.60 cm respectively. Full bunch compression is achieved, as it increases stability in the main linac.

2.5.2.1 *Central Arc and Turnaround Loop*

The central arcs transport the beams from the booster linac horizontally, and descend 100 m underground to the main linac tunnels. The electrons are bent by 180 degrees in the central arc, and sent toward the linac entrance. The positron beam exits the booster pointing already toward the right direction, thus the central arc is just a dog-leg with the vertical transfer to reach the main linac tunnel. Both lines can compensate for the timing offset between electrons and positrons and implement a feed forward system to counteract incoming transverse beam jitter. Given the shorter length of the positron line, with respect to the electron one, the feed forward correction scheme is more challenging for positrons than for electrons.

The electron central arc has an average radius of 305 m, featuring the same cell design as the turnaround loops. Each cell is 31.9 m long and produces a 6 degrees bend, with five dipoles, seven quadrupoles and four sextupoles. The phase advance is 432 in the horizontal plane and 144 in the vertical plane. It's achromatic, almost isochronous, and optimized for acceptable emittance growth due to incoherent synchrotron radiation (ISR) [1]. Figure 2 shows the optics functions in a single cell, including the dispersion R_{16} and the R_{56}. The central arc is composed by 30 of such cells.
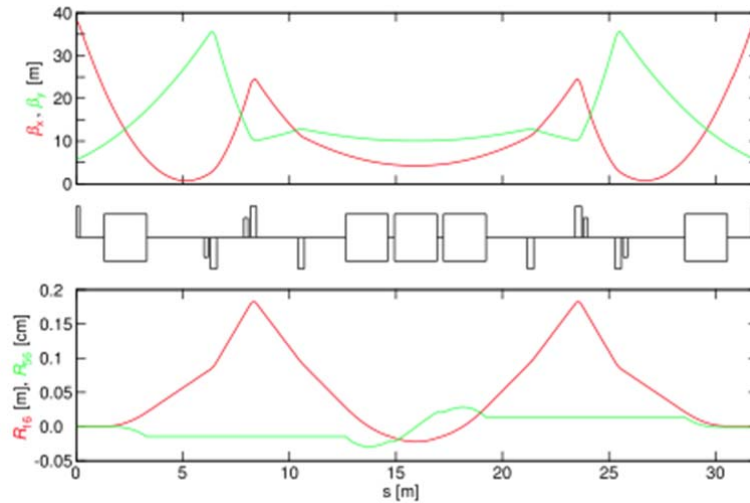
Figure 2: Beta functions (top), dispersion and momentum compaction (bottom) in an arc cell.

The two turnaround loops direct the outgoing beams towards the interaction point (IP). The beams are bent by 180 degrees and the resulting horizontal offsets are

corrected by dog-legs. The choice of two 60 degrees arcs per dog-leg is a compromise between limiting ISR and lattice length. The arcs of each dog-leg are connected by a periodic lattice 354 m long. The average radius of the arcs is again 305 m and the total loop length is 1944 m. Both turnaround loops contain 50 arc cells.

2.5.2.2 *Long Transfer Line*

Long 21 km transfer lines transport the beams from the central region, where the booster is located, to the far ends of the main linac tunnel. They consist of a FODO lattice with very weak quadrupoles, $k_1 = 0.0097$ m^{-2}, resulting in a cell length of 438 m and an average beta function of 620 m. The phase advance is 45 degrees. A beam pipe radius of 6 cm reduces resistive wall wakefields that could cause multi-bunch instability [7,8]. To suppress the fast beam-ion instability, the vacuum must be below 10^{-10} mbar [8]. Studies of emittance preservation showed that a quadrupole pre-alignment of 100 μm is adequate even when only correcting with one-to-one steering [9]. On the other hand, studies show that there are very tight tolerances on the allowed dynamic variation of stray magnetic fields. Periodic stray fields with a wavelength equal to the betatron wavelength must be below 10 nT with a variation of 0.1 nT [5,10].

2.5.3 **Emittance Preservation**

The lengths of the RTML sections are approximately 27 km each. Limiting the emittance growth over this distance is one of the major challenges for the design. Three emittance budgets have been set for the RTML, as they are summarized in Tab. 2: design, static, and dynamic. It is required that the machine remains below the static emittance growth budgets with a probability of 90%. The design budget prescribes that the design emittance growth intrinsic to the design stays below 60 nm in horizontal axis, and below 1 nm in the vertical axis. The static and dynamic budgets account for the impact of the static misalignment of the elements, and for dynamic imperfections such as ground motion, vibrations and stray fields.

Table 2: CLIC RTML emittance growth budgets in nm.

	Design	*Static*	*Dynamic*	*Total*
Horizontal emittance	60	20	20	100
Vertical emittance	1	2	2	5

The effect causing the largest emittance growth even in a perfect system is the emission of incoherent synchrotron radiation (ISR) in the bending magnets. ISR absorbs about 40 nm of the horizontal emittance budget for the electron beam, and about 25 nm for the positron beam (that does not require a central arc). In the vertical plane, where only weak arcs are required in the transfer tunnels, the ISR emittance growth is less than 1 nm. The second largest contribution to the emittance growth is the emission of coherent synchrotron radiation (CSR) in the bunch compressor chicanes. CSR absorbs 20 nm of the total budget in the horizontal plane. The CSR effect can be mitigated shielding the conducting walls of the vacuum chamber. It has been calculated that, for the shielding to be effective, the vertical aperture must be smaller than about 2 cm. The baseline design fulfills the design emittance growth budget, as it is shown in Fig. 3 for the horizontal axis.

2.5.3.1 *Static Misalignments and Beam-based Alignment*

The misalignment of the accelerator components with respect to a reference line, due to imperfect pre-alignment, impacts the beam quality by inducing emittance growth via dispersive and chromatic effects in the quadrupoles, and via short- and long- range wakefields in the accelerating structures. Given the very small vertical emittance, and the tight bu
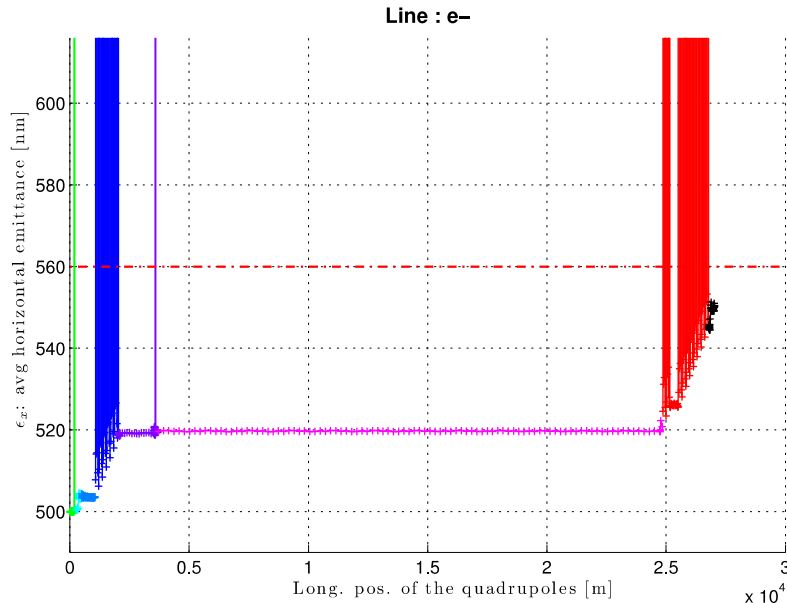
Figure 3: Emittance growth induced by wakefields and synchrotron radiation in the electron RTML.

The effect of static misaligned components is reduced by beam-based alignment (BBA) techniques. Standard BBA algorithms, such as 1:1 correction and dispersion-free steering, have been tested in each subsystem of the RTML, and pre-alignment tolerances have been drawn. Table 3 summarizes the expected RMS pre-alignments that induce 1 nm emittance growth in the vertical axis. Some of the subsystems, like the central arc, the turnaround loop and the bunch compressor 2, are quite tight. Studies are being carried out to relax these tolerances: for instance, finely tuned BBA algorithms, and the usage of more precise beam position monitors (BPMs), already proved to be useful. For example, the simulations have been performed assuming 1 μm BPM resolution: testing a resolution of 0.1 μm has relaxed these tolerances by a factor 1.3 [11].

2.5.4 **Dynamic Imperfections**

Dynamic imperfections such as ground motion, vibrations, stray fields, jitter in the accelerator components and incoming beam jitter can induce emittance growth and ultimately luminosity loss. The RTML, where the bunches travel for more than 25 km and undergo significant transformation of their longitudinal profile through acceleration and bunch length compression, is one of the most critical systems both in the transverse and the longitudinal planes.

Table 3: Average tolerance in µm obtained after applying 1:1 and DFS correction. In brackets the value corresponding to the 90-th percentile curve.

Subsystem	1:1	DFS
Spin Rotator & Bunch compressor 1	17 (11)	55 (24)
Booster	29 (19)	45 (23)
Central arc	7 (5)	14 (7
Long transfer line	153 (88)	280 (150)
Turnaround loop	6 (4)	9 (5)
Bunch compressor 2	1.4 (0.8)	3.5 (2)

2.5.4.1 *Phase Stability*

In the bunch compressors the longitudinal phase space is rotated to achieve compression. This means that energy and phase errors are coupled, with phase errors turning into energy errors and vice versa. This casts stringent requirements on the gradient and phase stability of the RF system of bunch compressor 1 and 2, and of the booster linac [6].

The requirement that luminosity loss due to phase errors must be less than 2% imposes the relative phasing of Main Beam and Drive Beam to be better than 0.2 degrees (at 12 GHz) for coherent errors along the Drive Beam sections, and better than 0.8 degrees (at 12 GHz) for errors incoherent along the Drive Beam sections. The relative phasing of electrons and positrons at the IP has to be better than 0.4 degrees (at 12 GHz). These constraints facilitate the specification of the allowed beam phase errors at ML entrance for the two different phase references under consideration. In case of external phase references (EPR) the beam phase stability in front of the ML has to be better than < 0.2 degrees (at 12 GHz), since any phase error of the Main Beam will remain unchanged along the entire ML and will thus be coherent in all drive-beam sections. In case the outgoing beams are used as reference (OBR) two values need to be specified: since the Main Beam including a possible phase error is used as phase reference for the RF of the second bunch compressor and the Drive Beam the relative phasing will always be correct. Hence, the allowed beam phase error is limited to < 0.4 degrees (at 12 GHz) by the relative phasing of electrons and positrons at the IP. On the other hand, any phase error imposed on the Main Beam behind the phase measurement has to stay below < 0.2 degrees (at 12 GHz) to avoid spoiling the relative phasing of Main Beam and Drive Beam [1]. A feed forward correction scheme to ensure phase stability is being designed based on the experience gained in studies such as [12,13].

2.5.4.2 *Transverse Stability*

Detailed studies of the impact of ground motion, vibrations, stray fields, jitter in the accelerator components on transverse emittance growth and orbit stability are in progress.

To reduce the emittance growth due to incoming beam jitter from the damping ring extraction kicker, a feed forward system is presented in [14]. It consists of two feed forward systems situated across the central arcs (CAs) and turnaround loops (TALs). A beam position monitoring region will be situated upstream of each arc section and a kicker region situated downstream; the feed forward signals will cut across the arc, allowing it to travel a shorter path and arrive earlier than the beam. The beam position

monitor region will be used to determine the position and angle trajectories in both the horizontal and vertical planes. This information is then used to determine the kicker corrections required by the feed forward electronics and the kickers are fired accordingly. The horizontal and vertical feed forward systems are completely independent of each other and use different BPMs and kickers. This is to simplify each feed forward system to a 2-dimensional problem rather than a 4-dimensional one; which reduces the required computing power of each feed forward system. Details on the required electronics and kicker specifications for this system can be found in [14].

Detailed simulations to compare the emittance growth with and without feed forward correction are shown in Fig. 4. In the figure it is visible that the amplitude of the beam jitter at the end of the RTML is reduced by a factor ≈ 10 in the horizontal plane and ≈ 6 in the vertical plane when the feed forward corrections are applied.
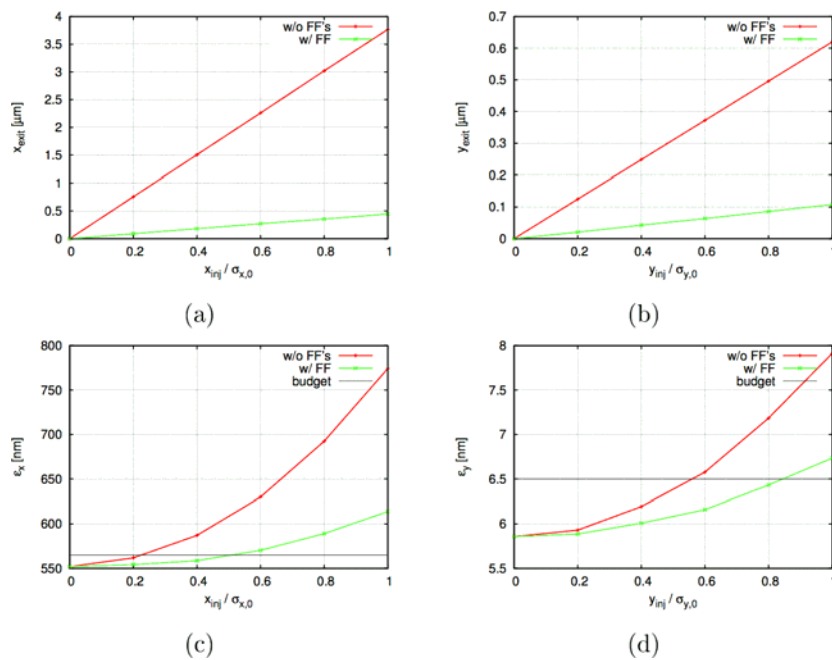
Figure 4: Plots of the orbit jitter (a, b) and normalised emittance (c, d) at the exit of the RTML versus orbit jitter at the entrance of the RTML in the horizontal and vertical planes respectively.

2.5.5 References

1. *CLIC Conceptual Design report*, CERN-2012-007 (CERN, 2012).
2. Emma, P. A spin rotator system for the NLC, NLC-Note-7 (SLAC, Stanford, CA, USA, 1994).
3. Latina, A., Solyak, N. & Schulte, D. in Proc. 1st Int. Particle Accelerator Conf., 23-28 May 2010, Kyoto, Japan (2010), 4608–4610. <http://accelconf.web.cern.ch/accelconf/ IPAC10/papers/thpe040.pdf>.
4. Stulle, F., Adelmann, A. & Pedrozzi, M. Conceptual design of bunch compressors and turn around loops for a multi-TeV linear collider EUROTeV-Report-2008-025 (CERN, 2008).
    <http://www.eurotev.org/sites/site_eurotev/content/e328/e329/e1082/e1500/EUROTeV -Report-2008-025.pdf>.
5. Stulle, F., Schulte, D., Snuverink, J., Latina, A. & Molloy, S. in Proc. XXV Linear

Accelerator Conf., 12-17 September 2010, Tsukuba, Japan (2010), 88–90. <http://accelconf.web. cern.ch/accelconf/LINAC2010/papers/mop019.pdf>.

6. Stulle, F. *Beam phase and energy tolerances in the CLIC RTML* CERN-OPEN-2011-048. CLIC- Note-874 (CERN, 2011). <http://cdsweb.cern.ch/record/1406047/files/ CERN-OPEN-2011-048.pdf >.

7. Jeanneret, J. B. & Braun, H.-H. in *Proc. 11th European Particle Accelerator Conf., 23-27 June 2008, Genoa, Italy* (2008), 3014–3016.
    <http://accelconf.web.cern.ch/accelconf/ e08/papers/thpc017.pdf>.

8. Jeanneret, J. B. *et al.* in *Proc. 11th European Particle Accelerator Conf., 23-27 June 2008, Genoa, Italy* (2008), 3017–3019. <http://accelconf.web.cern.ch/accelconf/e08/ papers/thpc018.pdf>.

9. Stulle, F., Schulte, D., Snuverink, J., Latina, A. & Molloy, S. in *Proc. 1st Int. Particle Accelerator Conf., 23-28 May 2010, Kyoto, Japan* (2010), 3013–3015. <http://accelconf.web. cern.ch/accelconf/IPAC10/papers/wepec054.pdf>.

10. Snuverink, J. *et al.* in *Proc. 1st Int. Particle Accelerator Conf., 23-28 May 2010, Kyoto, Japan* (2010), 3398–3400.
    <http://accelconf.web.cern.ch/accelconf/IPAC10/ papers/wepe023.pdf>.

11. Lienart, T. *Study of pre-alignment tolerances in the RTML* CERN-OPEN-2012-014. CLIC-Note-943. (CERN, 2012). <https://cds.cern.ch/record/1452626/files/CERN-OPEN-2012-014.pdf>

12. Gerbershagen, A. *CLIC Drive Beam Phase Stabilisation*, Phd Thesis (University of Oxford, 2013)

13. Skowronski, P. et al. *Design of Phase Feed Forward System in CTF3 and Performance of Fast Beam Phase Monitors* CERN-ACC-2013-0092 (CERN, 2013) <https://cds.cern.ch/record/1575566/files/CERN-ACC-2013-0092.pdf>

14. Apsimon, R. and Latina, A. *Proposed Feed Forward Correction for the CLIC Ring-To-Main-Linac Transfer Lines* CLIC Note *to be published*

2.6   RF Design of the CLIC Main Linac Accelerating Structure

Alexej Grudiev, CERN, CH 1211 Geneva 23, Switzerland
Mail to: Alexej.Grudiev@cern.ch

2.6.1   Introduction

The parameters of the CLIC main linac accelerating structure have been obtained based on an optimization which includes an improved understanding of high-gradient limits, wakefields related beam dynamics constrains and integrates the performance and cost of CLIC at 3 TeV (see more details in [1,2]). Furthermore, compact couplers have been developed and HOM damping loads have been designed. The rf design has also been made consistent with details of the manufacturing procedure, which is based on bonded asymmetrical disks, and with requirements coming from integration of the accelerating structure in the two-beam module.

2.6.2 Basic Cell Geometry and HOM Damping
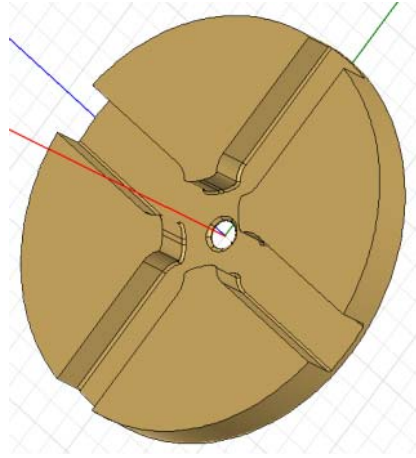
Figure 1: Basic cell geometry of the accelerating structure with strong waveguide HOM damping is shown.

The basic cell geometry is shown in Fig. 1. The cell has an elliptical cross section iris and convex elliptical cross-section outer walls in order to minimize surface fields. There are four damping waveguides incorporated in each cell to provide efficient damping. The Q-factor of the lowest dipole-band is below ten. The cell geometry is adapted to the manufacturing process based on the bonding of disks in which one side of the disks is flat and the other side carries all the cell features. This is the facing side in Fig. 1. Moreover, the geometry of the outer wall and damping waveguides have been optimized to minimize both the pulsed surface heating temperature rise on the outer wall and the penetration distance of the fundamental mode into the damping waveguides while maintaining the same damping efficiency. This has been achieved through reducing both the aperture to the damping waveguide and the damping waveguide width. The smaller penetration distance allows a smaller overall transverse size since the HOM damping loads made of SiC can be placed closer to the axis without affecting the Q-factor of the fundamental mode. The distance from the axis of the structure to the tip of SiC damping load is 50 mm. The geometry of the load placed in the damping waveguide is shown in Fig. 2. It is 30 mm long and is tapered from 1x1 mm cross-section to 5x5 mm over 30mm and a 10 mm long part of the latter cross-section.
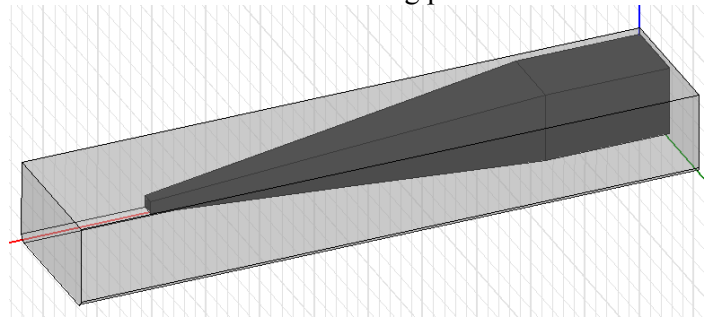
Figure 2: Internal volume of a damping waveguide equipped with HOM load made of SiC is shown.
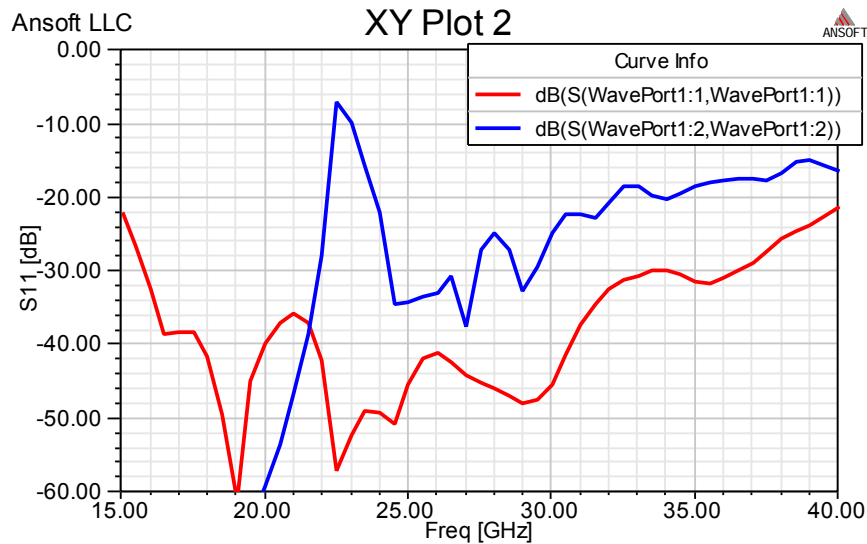
Figure 3: Reflections from SiC load in the damping waveguide are shown both for TE10 (red) and for TE01 (blue) modes.

This load configuration provides very broad band absorption of the wakefields and is used to terminate each damping waveguides of the structure. The reflections of the TE10 and TE01 waveguide modes from the load are calculated using HFSS frequency domain code [3] using measured SiC parameters [4] ($\varepsilon' = 13$, $\tan\delta = 0.16$). The geometry of the load has been optimized to keep the reflections below -30 dB for TE10 mode and below -20 dB for TE01 mode. The final results are presented in Fig. 3. These reflections do not compromise the HOM damping performance primarily determined by the cell to damping waveguide coupling.

2.6.3 Tapering and Couplers
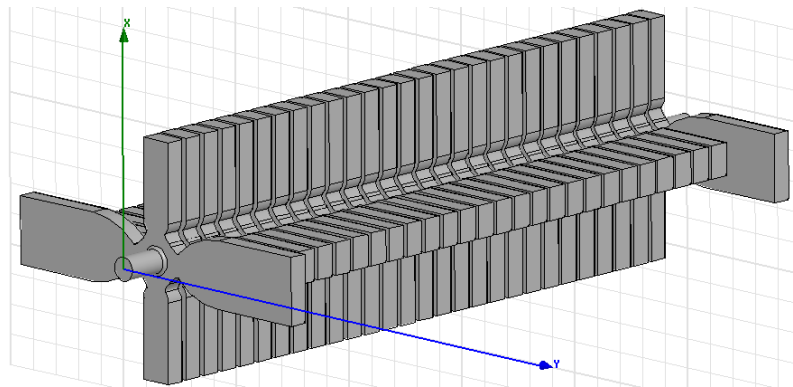
Figure 4: Internal volume of the full structure is shown.

The rf geometry of the full structure is shown in Fig. 4. It has 26 regular cells which are tapered along the length of the structure plus input and output coupler cells. The geometry of a coupler cell is shown in Fig. 5. The coupling is magnetic but the coupler cell geometry is quite different from that traditionally used and resembles very much the regular cell geometry. The only difference is that in the coupler cell, two opposite

waveguides are of the standard WR-90 width forming a double-feed coupler cell. The other two damping waveguides are kept in place to maintain the damping as efficient as in the regular cells. Furthermore, this naturally minimizes the quadrupolar kick, since the geometry is close to the regular cell geometry where the quadrupolar kick is canceled by the symmetry. The coupler provides about the same acceleration as a regular cell and both surface magnetic and electric fields do not exceed maximum values in the rest of the structure. As a double-feed coupler it must be fed in phase from both sides. It is done using a magic-T, in which case, the wakefields coming in opposite direction from the coupler cell into the power waveguides are out of phase for the TE10 mode and in phase for TE01 mode. Under these conditions both modes are guided to the 4th arm of the magic-T which is terminated by a load. This provides efficient HOM damping in both planes in the couplers cells which is not negligible part of the full structure.
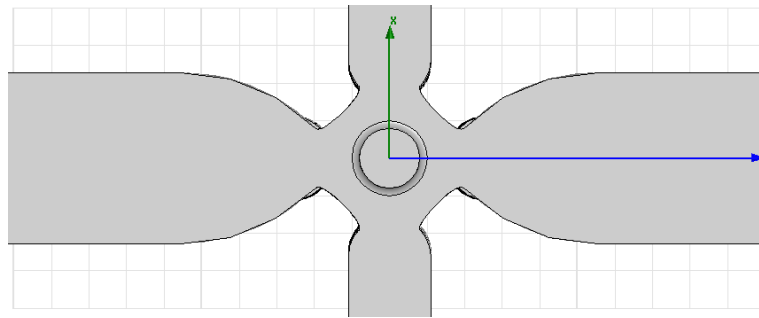
Figure 5: Internal volume of the coupler cell.

The main parameters of the structure are presented in Table 1. Following the beam dynamics requirements, the optimum average aperture radius to wavelength ration is 0.11 resulting in the group velocity reaching in the last cell 0.83 % v_g/c. At this rather low group velocity, the bandwidth of the structure sets a lower limit to the rise time of the field level in a cell in the same way as in a high Q cavity. This rise-time limit is also shown in the Table 1 together with the conventional filling time of a travelling-wave structure. The consequence of the limited bandwidth is that two ramps are necessary at the beginning of the pulse to simultaneously compensate for the structure bandwidth and for the beam loading induced bunch to bunch energy spread. The input pulse shape is shown in Fig. 6.
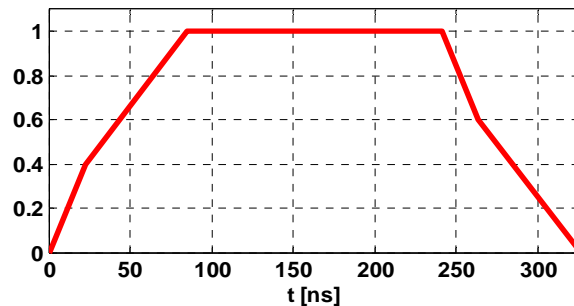
Figure 6: Schematic shape of the input pulse.

Both the iris radius and thickness are tapered linearly in order to provide an optimum distribution of various high-power parameters and to avoid the hot spots along

the structure. Distributions of these parameters are shown in Fig. 7. The unloaded structure gradient, the surface electric field rise and the temperature rise are made to be constant. In Fig. 7, the pink line shows the distribution of a new field quantity Sc [5] which serves as a limit for high gradient performance and to certain extent combines both the power and the surface electric field constraints.
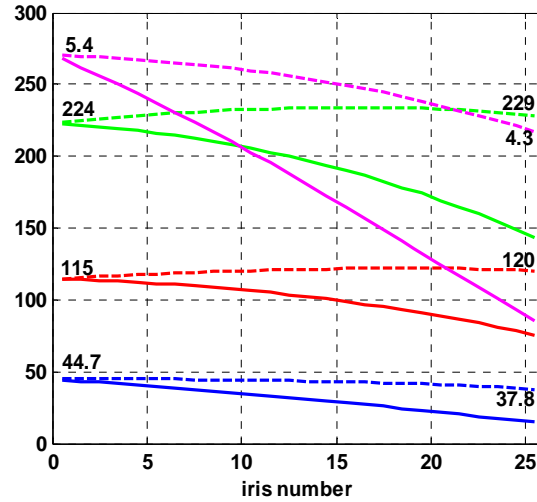
Figure 7: The fundamental mode properties are shown in the regular cells. The traces from top to bottom are: $S_c \cdot 50$ [W/µm²](pink), surface electric field [MV/m](green), accelerating gradient [MV/m](red), pulse surface temperature rise [K](blue). Dashed traces are unloaded and solid are beam loaded conditions.

Table 1: Accelerating Structure Parameters.

Parameter	Unit	Value
Average loaded accelerating gradient	MV/m	100
Frequency	GHz	12
RF phase advance per cell	Rad.	$2\pi/3$
Input, Output iris radii	mm	3.15, 2.35
Input, Output iris thickness	mm	1.67, 1.00
Input, Output group velocity	% of c	1.65, 0.83
First, Last cell Q-factor (Cu)	…	5536, 5738
First, Last cell shunt impedance	MΩ/m	81, 103
Number of regular cells	…	26
Structure active length including couplers	mm	230
Bunch spacing	ns	0.5
Bunch population	…	3.72×10^9
Number of bunches in the train	…	312
Filling time, rise time	ns	67, 21
Total pulse length	ns	244
Peak input power	MW	61.3
RF-to-beam efficiency	%	28.5
Maximum surface electric field	MV/m	230
Maximum pulsed surface heating temperature rise	K	45

2.6.4 **Wakefields**

The tapering also provides detuning of the higher order modes which is an important effect even for heavily damped structures. The relative contributions of the heavy damping and detuning to the transverse wakefields spectrum are illustrated in Fig. 8. Parameters of the lowest dipole-band modes calculated from the fitting to the impedance curves are listed in Table 2. The transverse wake of the full structure including coupler cells was computed in time domain using parallel code GdfidL [6]. The results for both planes are shown in Fig 9. The difference between two planes comes only from the coupler cells and is very small. One can see that both wakes at the position of the second bunch which is 0.15 m are below the 6.6 V/pC/mm/m, as required for beam dynamics.

Table 2: Parameters of the lowest dipole-band modes.

Cell	Unit	First	Middle	Last
Q-factor	…	11.1	8.7	7.1
Amplitude	V/pC/mm/m	125	156	182
Frequency	GHz	16.9	17.4	17.8
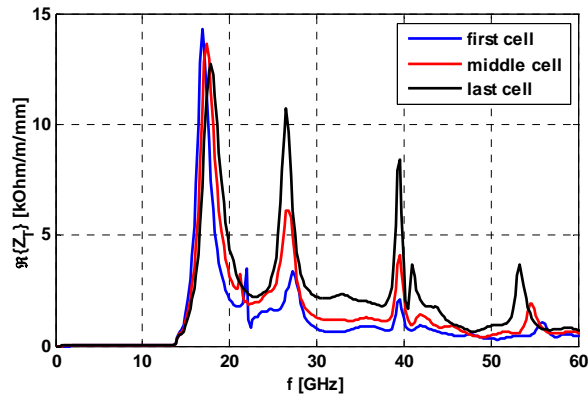
Figure 8: Transverse impedances of the first (blue), middle (red) and last (black) cells.
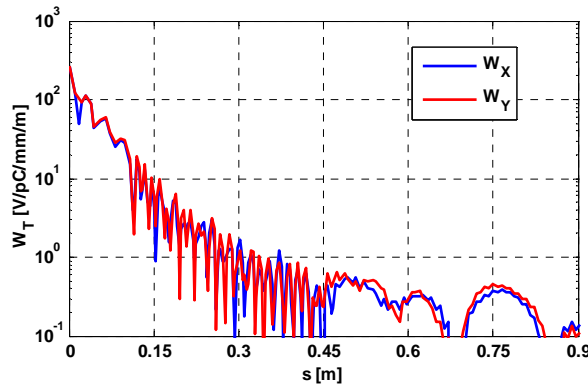
Figure 9: The envelope of the transverse wakefields for both planes is shown. The CLIC bunch spacing is 0.15 m.

2.6.5 **Wakefield Monitor**

To achieve high luminosity in CLIC, the accelerating structures must be aligned to an accuracy of 5 μm with respect to the beam trajectory as specified in section [ref to BD section]. Position detectors called Wakefield Monitors (WFM) are integrated into the first cell of every second structure for a beam based alignment. Its principle is based on the measuring the wake signal excited by the beam and propagating from the cell to the HOM loads through the damping waveguides. In a special cell, the WFM cell four pickups are introduced between the cell and the HOM loads to measure this signal in all four damping waveguides. In Fig. 10 geometry of such a pickup is shown as it is implemented in CTF3 TBTS accelerating structure [7]. The signals from four pickups are combined to provide the measure of the horizontal and vertical displacements of the structure with respect to the beam in the same way as it is done in a cavity BPM.
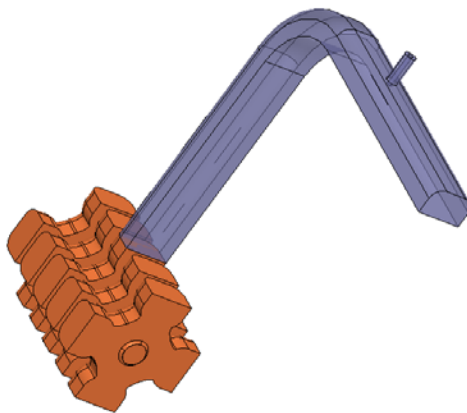
Figure 10: Geometry of one of the four arms of the wakefield monitor. (Courtesy of F. Peauger, CEA, France).

2.6.6 **Fabrication Tolerances**

Due to the very large amount of structures the implementation of tuning in the final design is not suitable, for this reasons the tolerances are defined on the assumption to avoid any possible tuning. A detailed study of the required machining and assembly tolerances has been performed [8] which is summarized below.

• Systematic errors: Inefficiency in acceleration due to rf de-phasing is mainly caused by systematic errors in the cell dimensions since it is a coherent effect. The most sensitive dimension is the transverse size of the cell 2b where 1 micrometer systematic error causes ~2% reduction in the structure acceleration.

• Random errors: Cell to cell frequency error due to random errors in cell dimensions causes mismatch, reflections and appearance of field enhancement due standing wave. Limiting the mismatch to < -40dB results in the same tolerance on the most critical dimension 2b of ~1 micrometer.

• "Bookshelfing": Systematic tilt of the disks introduces the transverse kick which is proportional to the accelerating gradient. Keeping ratio of the transverse kick to the acceleration dVt/dVz <10e-4 (see, BD section) requires the tilt to be below 180 micro-radian.

• WFM: The required WFM accuracy must be below 3.5 micrometers. This sets the limit on the cell shape accuracy such that the transverse alignment of the axis of the

iris aperture (source of the short range wakes) with respect to the axis of the cell and damping waveguides (measuring the wakes) must be at least better than 3.5 micrometers.

In summary, micrometer tolerance level is required in cell disk fabrication and several micrometers in the structure assembly in order to satisfy stringent beam dynamics requirements without additional tuning.

2.6.7 **References**

1. A. Grudiev, H. H. Braun, D. Schulte, W. Wuensch, "Optimum Frequency and Gradient for the Clic Main Linac Accelerating Structure", LINAC08, Victoria, BC, Canada, (2008).
2. A. Grudiev, W. Wuensch, "Design of X-band accelerating structure for the CLIC main linac", LINAC08, Victoria BC, Canada, (2008).
3. ANSYS HFSS, http://www.Ansoft.com
4. M. Luong, I. Wilson, W. Wuensch, "RF Loads for the CLIC Multibunch Structure", PAC'99, New York, 1999.
5. A. Grudiev, S. Calatroni, and W. Wuensch, "New local field quantity describing the high gradient limit of accelerating structures", Phys. Rev. ST Accel. Beams 12, 102001 (2009).
6. W. Bruns, http://www.gdfidl.de
7. F. Peauger, et.al, "Wakefield monitor development for CLIC accelerating structure", LINAC10, Tsukuba, Japan, (2010), CERN-ATS-2010-220.
8. R. Zennaro, "Study of the machining and assembly tolerances for the CLIC accelerating structure", EUROTeV-Report-2008-081, (2008).

2.7 **CLIC Power Extraction and Transfer Structure**

Igor Syratchev, CERN, CH 1211 Geneva 23, Switzerland
Mail to: Igor.Syratchev@cern.ch

The generation of short (250 ns) high peak power (135 MW) RF pulses by decelerating a high current (100 A) bunched (12 GHz) drive beam is one of the key components in the CLIC two beam acceleration scheme. The CLIC PETS is a low impedance, high group velocity iris loaded 0.213 m long structure with a relatively large ($2\, a/\lambda = 0.92$) beam aperture. Each PETS is comprised of eight octants separated by damping slots. Each slot is equipped with damping loads in order to provide the strong damping of the transverse higher order modes [1]. In operation, the high peak power RF pulses (135 MW × 240 ns) are generated in the PETS via interaction with a high current (100 A) bunched (12 GHz) drive beam. These pulses are extracted at the downstream end of the PETS using a special high power coupler and are distributed to the two CLIC accelerating structures using an RF waveguide network. The snapshot of such a process simulated with computer code T3P [2] is shown in Fig. 1.
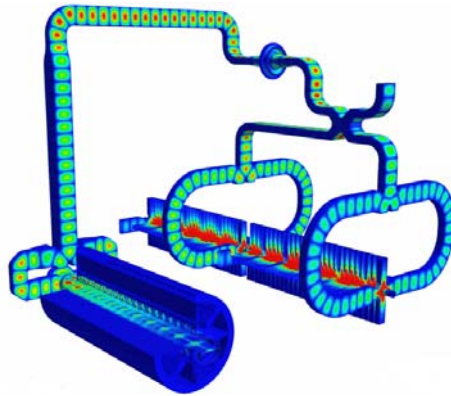
Figure 1: Electric filed plot in the CLIC two-beam accelerator unit. Here the PETS (shown left) is driven by the steady state drive beam current (courtesy SLAC).

During the period of 2008-2012, a thorough high RF power testing program was conducted at CERN in order to demonstrate experimentally the feasibility of all the issues associated with high RF power generation using the drive beam. In parallel, complimentary tests using X-band high power klystrons as a RF power source were done at ASTA (SLAC). Operated at a repetition rate of 60 Hz, such experiments provided high enough statistics to quantify the RF breakdown trip rate. To do these tests, an 11.424 GHz scaled version of the 12 GHz PETS was designed and fabricated, see Fig. 2. The feasibility of the PETS operation at a peak RF power level ~7% higher and with RF pulses ~10% longer compared to CLIC requirements was successfully demonstrated in these experiments [3]. The tests at a fixed power level (see Fig. 3) were ended when the measured breakdown trip rate was close enough to the CLIC specification of 1.0E-7/pulse/m. In the ASTA test, it occurred after 80 hours of operation without breakdown (BDR <2.4E-7/pulse/m).
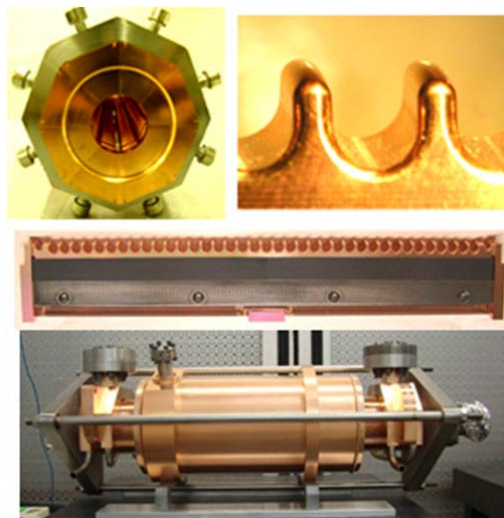
Figure 2: The front view of the assembled PETS body (top left), zoom of the PETS single bar period (top right), the single bar equipped with damping loads (centre) and fully assembled structure (bottom).
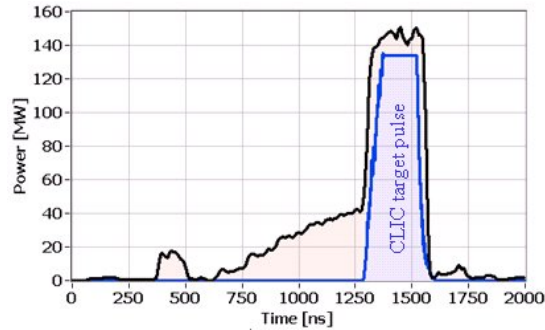
Figure 3: Typical RF pulse shape in ASTA. Here, for convenience, we also have plotted the shape of the CLIC target pulse.

2.7.1 PETS Testing Program in CTF3

2.7.1.1 *PETS Operation at Two Beam Test Stand*

The generation in the PETS of 12 GHz RF power from the drive beam was demonstrated in the CLIC experimental area (CLEX), which is a part of the CLIC Test Facility (CTF3) [4]. The CLEX is equipped with a number of experiments. One of them is the Two Beam Test Stand (TBTS). The TBTS is a unique and versatile facility where the two-beam acceleration experiments are conducted. It comprises two beam lines equipped with various types of beam diagnostics. One line is for the drive beam, which is generated in the CTF3 complex and then delivered to the TBTS via a beam transfer line, the other is dedicated to the probe beam, which is prepared in the CALIFES accelerator complex. As it is shown in Fig. 4, CTF3 will allow for different scenarios of the drive beam generation in terms of the beam current and pulse length.
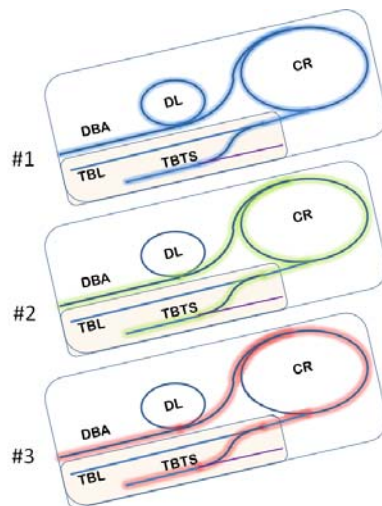
Figure 4: The drive beam generation modes in CTF3: 1– with full recombination (×8), 2 – with partial recombination (×4), and 3 – without recombination.

Because the drive beam current available in CTF3, even with full recombination, will be about four times lower than the CLIC design, the TBTS PETS design was

modified to be able to generate the nominal CLIC RF power. To recover the lack of current, the active PETS length was significantly increased from original 0.213 m to 1m. The fully assembled, 1 meter TBTS PETS equipped with water cooling channels and power couplers on its girder and ready for the installation into the vacuum tank is shown in Fig. 5. The TBTS PETS power production capability for the different CTF3 modes of operation (assuming the single bunch form factor =1) is summarized in a Table 1. Mode 1 of the PETS operation provides power levels well above CLIC nominal values; unfortunately, the pulse length of 140 ns is rather short compared to the CLIC nominal pulse of 240 ns. To improve this, it was decided to implement a different configuration – PETS with external re-circulation [5]. In this case, the PETS operates in an amplification mode, similar to that in the classical resonant rings. The only difference is that now we have a beam as an internal source of RF power.

Table 1: The TBTS PETS power production modes

Operation mode	#1	#2	#3
Current, A	<30	14	4
Pulse length, ns	140	<280	<1200
Bunch Frequency, GHz	12	12	3
PETS power (12 GHz), MW	<280	61	5
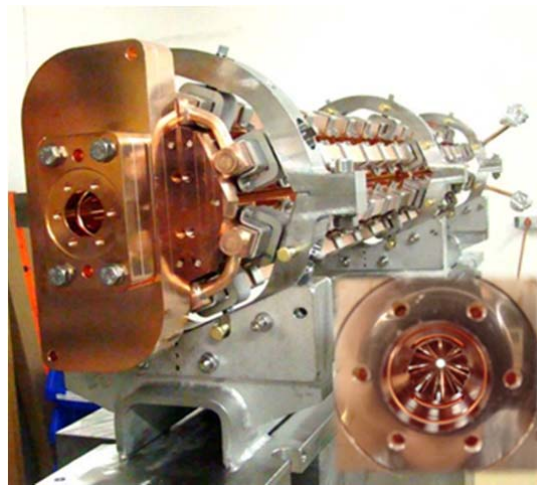
Figure 5: The TBTS PETS general view.

The implementation of re-circulation required development of several special RF components. High RF power variable splitter and variable (2π) RF phase shifter were ordered and received from industry (GYCOM, Russia) [6]. In 2008, a PETS tank equipped with all the RF components was installed into the drive beam line in the TBTS experimental area, as is shown in Fig. 6. With re-circulation, the power gain of the system in a steady can be written as:

$$P_G = \frac{1}{1 - 2g\,\cos(\phi) + g^2}$$
$$g = \sqrt{S\eta_{loop}}$$

(1),

where S is fractional power delivered back to the PETS input, ϕ is RF phase advance in the loop and η_{loop} is total round trip efficiency. Following (1), in a phased loop (ϕ=0) with 50% re-circulation (S=0.5) and 75% measured ohmic efficiency (η_{loop}=0.75), the steady state power gain is about 6.5. Thus, driven with only 8.6 A drive beam current, the PETS generates the required CLIC RF peak power. At the same time, the RF power extracted from the re-circulating loop (50%) and received by the single accelerating structure would also be as high as required. Providing enough margin in drive beam current and pulse length, the PETS operation mode 2, together with ~50% re-circulation was chosen as a working point for the PETS power production and two-beam acceleration program. In this configuration, the TBTS PETS was operated until September 2011. After start up and initial conditioning, it was reliably generating RF peak power well in excess of the CLIC nominal value. In Fig. 7 the example of a typical pulse generated at the PETS output is shown. One can see clearly the expected stair-case nature of the RF power build-up, where the duration of each step corresponds to the round-trip delay in the re-cycling loop.
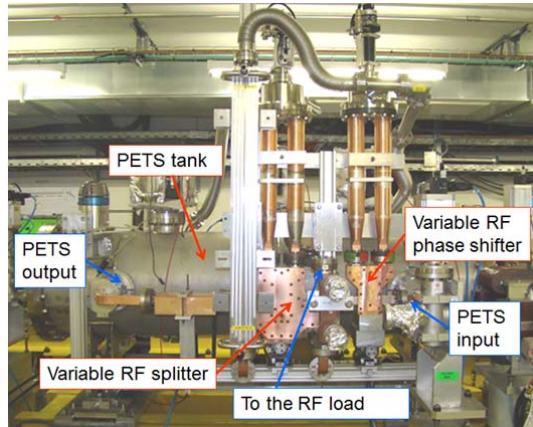
Figure 6: The PETS tank installed in the TBTS test area.
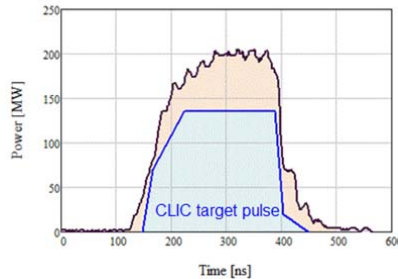
Figure 7: Typical RF pulse shape measured at the PETS output. Here, for convenience, we also plotted the shape of the CLIC target pulse.

We have developed a number of computer models of varying complexity which accurately reconstruct and predict the processes in the system with re-circulation [7-9].

In order to illustrate this, in Fig. 8 and Fig. 9, the simulated results are compared to measurements. In this example, we used a rather simple model [9] based on the known settings of re-circulation (ϕ and g) and measured profile of the drive beam current. One can see good agreement between the simulations and experiments.
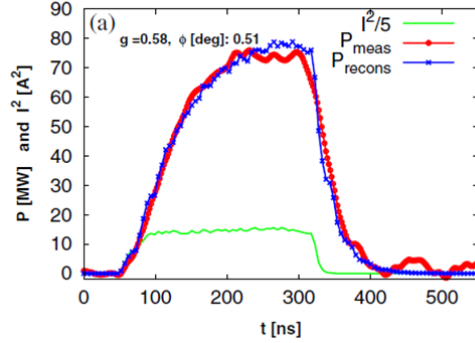
Figure 8: Measured RF pulse (red line) and reconstructed signal (blue line) are shown together with the current pulse used as an input for reconstruction (green line).
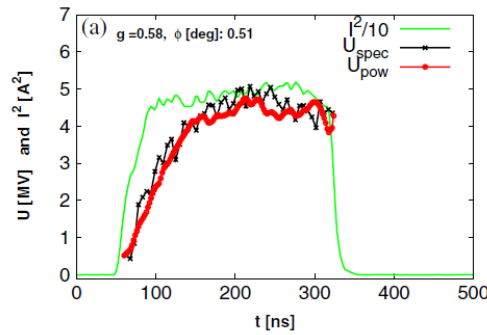
Figure 9: Measured with the spectrometer the drive beam deceleration (black line) and the one calculated from power measurements (red line) are shown together with the pulse current (green line). It shows the same pulse as in Fig. 8.
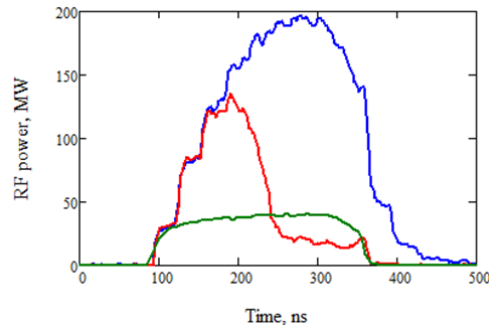
Figure 10: The normal RF pulse (blue line) followed by the RF pulse with breakdown (red line). Here the expected direct (without re-circulation) RF power production (green line) is shown for the reference.

Here we cannot give a firm conclusion about the breakdown trip rate in our experiments in the TBTS, because of insufficient statistics (CTF3 operates at 1 Hz

repetition rate) and some difficulties with providing stable drive beam generation during long enough periods. Nevertheless, an important observation concerning the pulse shape modifications due to the RF breakdown was made: power production is normally quenched just after the RF breakdown happens. This may be explained by the fact that the RF breakdown products modify the gain and phase advance in the loop. In most of the cases (>90%), the PETS continued to generate RF power at a much lower level, which is close to the direct power production level, see Fig. 10. This indicates that most probably, the breakdown happened in the re-cycling waveguide loop and not the PETS itself. Relying on this "self-protecting" effect, a quite aggressive operational procedure was implemented, where the control system followed up the integrated level of residual gas pressure in the PETS tank, rather than reacting on each individual breakdown event.

2.7.1.2 *Demonstration of the PETS ON/OFF Operation*

One of the feasibility issues of the CLIC two-beam scheme, is the possibility of rapidly switching off the RF power production in an individual PETS in case of breakdowns, which can occur either in the PETS or one of the main beam accelerating structures. The proposed solution is to use a variable external reflector connected to the PETS. When activated, this scheme allows us to continuously manipulate the RF power transfer to the accelerating structure and to reduce the RF power production in the PETS itself by a factor of 4 [10].
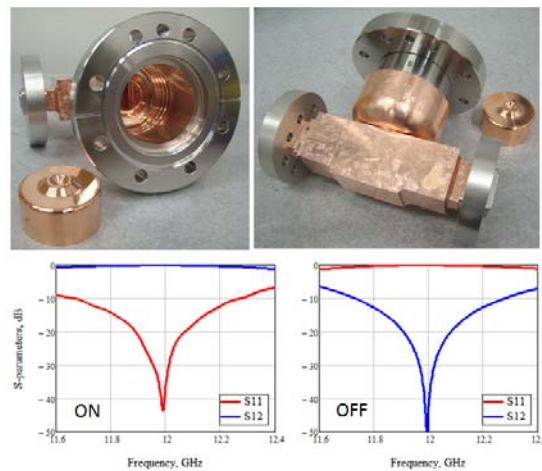
Figure 11: The general view of the variable reflector body and movable piston (up). S-parameters measured at two extreme positions of the piston.

An external high power variable RF reflector is the key component of the system [11]. Providing the whole range of reflections from 0 to 1, it can fully or partially terminate the RF power transfer from the PETS to the accelerating structure. In general, the reflected RF power will be returned back to the PETS. In order to mitigate this effect, a fixed RF reflector is placed at the upstream end of the PETS, in order to establish re-circulation of the RF power inside the PETS. If, at the operating frequency, the electric length of such an RF circuit is tuned to $L=\lambda_0(n+1/4)$, then a destructive interference with the RF power generated by the drive beam is achieved. A prototype of the new high RF power variable reflector was fabricated and low RF power measurements were in good agreement with HFSS [13] simulations, see Fig. 11. We

also built a separate variable RF short circuit to enable the tuning of RF phase advance in the system. In 2011, these new components replaced the external re-circulation circuit on the TBTS PETS tank as shown in Fig. 12.
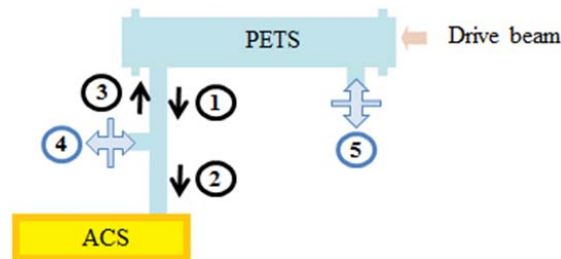
Figure 12: Layout of the PETS ON/OF setup in TBTS. The black arrows show RF power flows in the system: 1) RF power extracted from the PETS; 2) RF power transmitted to the accelerating structure; 3) RF power reflected back into the PETS. The new components are: 4) variable RF reflector; 5) variable RF short circuit.
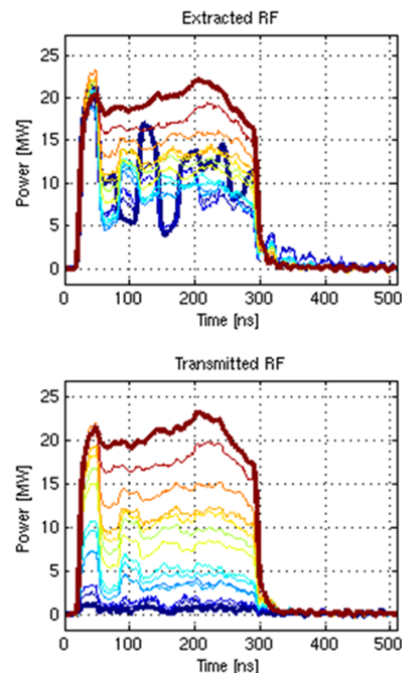
Figure 13: TBTS PETS ON/OFF demonstration with the beam. Here the line colors correspond to different settings of variable reflection. The colors are gradually changed from red (ON) to blue (OFF).

During experiments with the beam, the variable reflector settings were changed gradually from full reflection to full transmission. The RF powers produced by PETS and delivered to accelerating structure were measured at different intermediate piston positions. The results of one of the tests are shown in Fig. 13. These results were in a good agreement with the system computer modeling, where measured S-parameters of all components were used as an input [12].

At the time of the experiment, the available drive beam current in CTF3 made it impossible for us to run the system at the nominal CLIC RF power level in direct RF

power production mode. To demonstrate the power capability of the new RF components used in the ON/OFF RF circuit, we set the recirculation loop parameters to their amplification mode, similar to the setup that was routinely used in the TBTS PETS with external recirculation. The processing of the PETS with ON/OFF circuit went rather fast. In about 100 hours ($2x10^5$ pulses) the system was conditioned up to 150 MW × 200 ns. The PETS processing and operation history is summarized in Fig. 14 and Fig. 15.
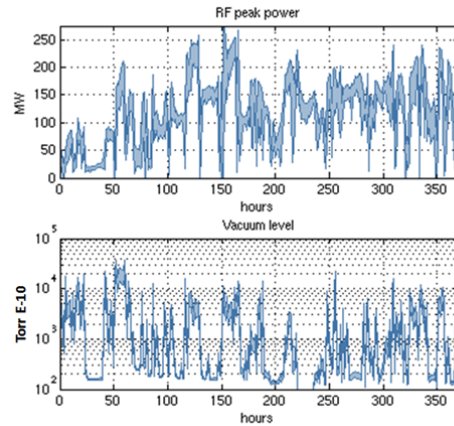
Figure 14: The PETS ON/OFF operation history: peak RF power (top) and vacuum level (bottom).
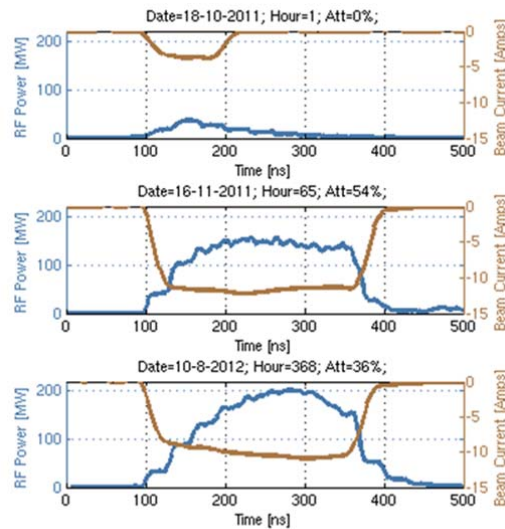
Figure 15: Typical drive beam current (brown lines) and RF power (blue lines) pulses at the different stages of operation.

2.7.2 Summary

The feasibility of all the issues associated with high RF power generation using the drive beam was successfully demonstrated in the dedicated testing program that was conducted at CERN during the period of 2008-2012.

The scaled, 1 m long, PETS was installed and operated in beam driven mode with external RF re-circulation in order to compensate for the lack of drive beam current and pulse length. The PETS routinely produced RF power with peak levels well in excess of the CLIC specifications.

The new high RF power variable RF reflector and variable RF short circuit were designed and fabricated. These devices have replaced the external recirculation in the special, 1 m long PETS installed in CTF3. The PETS ON/OFF operational principle and high peak RF power capability were successfully demonstrated in experiments with the CTF3 drive beam.

2.7.3   References

1. I. Syratchev *et al.,* 'High RF Power Production for CLIC', Proceedings of PAC 2007, Albuquerque, New Mexico, USA.
2. A. Candel *et al.,* "Numerical verification of the power transport and Wakefield coupling in the CLIC Two-Beam accelerator", SLAC-PUB-14439.
3. A. Cappelletti *et al.,* "Demonstration of the high RF power production feasibility in the CLIC power extraction and transfer structure [PETS]", NIMA, Vol. 667, Issue 1, pp. 78-81, 2011.
4. P. Skowronski *et al*., "The CLIC feasibility demonstration in CTF3", CERN-ATS-2011-117.
5. I. Syratchev *et al.,* 'CLIC RF High Power Production Testing Program', Proceedings of EPAC 2008, Genoa, Italy.
6. S. Kuzikov *et al.*, "A 12 GHz Pulse Compressor and Components for CLIC Test Stand", Proceedings of RuPAC-2010, Protvino, Russia.
7. R. Ruber and V. Ziemann, CERN CTF3 Note Report No. 092, 2009.
8. E. Adli, CERN CTF3 Note Report No. 096, 2009.
9. E. Adli *et al*., "*X*-band RF power production and deceleration in the two-beam test stand of the Compact Linear Collider test facility", PRST Accelerators and Beams, 14, 081001, 2011.
10. I. Syratchev, 'On-Off option and operation', 2nd CLIC Workshop 2008, Geneva, CERN.
11. I. Syratchev *et al*., "High Power Operation with Beam of a CLIC PETS Equipped with ON/OFF Mechanism", Proceedings of IPAC-2012, New Orleans, USA.
12. I. Syratchev, "The high power demonstration of the PETS ON/OFF operation", 5th High Gradient Workshop, KEK, Tsukuba, Japan, 2012.
13. Ansoft Corporation – HFSS: http://www.ansoft.com/

2.8   PACMAN (Particle Accelerator Components Metrology and Alignment to the Nanometer scale)

Nuria Catalán Lasheras, Helene Mainaud Durand, Michele Modena
CERN, CH 1211 Geneva 23, Switzerland
Mail to: helene.mainaud.durand@cern.ch

2.8.1   Introduction

The alignment of passive and active components along the CLIC accelerator shall reach unprecedented small values at micrometer level and with nanometer resolution. Indeed, this is a common requirement for the next generation of accelerators. Whether for producing a high number of collisions at the highest energy, or for producing the

brightest light from light sources, the tolerance concerning the position of the beam inside an accelerator is becoming increasingly tight. In practice, the static alignment of three fundamental components must be included within a few micrometers with respect to a reference line over several hundreds of meters. These components are quadrupole magnets, accelerating structures, and beam position monitors. They are heavy objects sometimes weighting more than a hundred kilograms and measuring one meter long or more. Still, their reference axis must be aligned within a few micrometers.

Nowadays, the current alignment strategy used in most accelerators consists of three steps: first to measure for each component the position of its reference axis w.r.t external targets named fiducials (fiducialisation process), then to align the components on a common support, and finally to align this support in the accelerator tunnel using alignment sensors. First tests concerning this strategy have shown that the precision and accuracy required for linear colliders and other future accelerators of 10 micrometres cannot be reached with this serial process. Additionally, accelerators are logically built out of modular elements built as mechanical supports on which the components are assembled. These modules constitute the backbone of sometimes several kilometres of accelerator and are industrially produced in large numbers, typically in the order of thousands of units. The requirement of tighter tolerances in the alignment inside these modules shall thus be fulfilled at the manufacturing premises.

A group of scientists at CERN have put together an EC-funded Initial Training Network composed by private companies, universities and research institutions interested in metrology under the name of PACMAN (a study on Particle Accelerator Components Metrology and Alignment to the Nanometer scale). The partners of the network are listed in Table 1. They will supervise a group of ten doctoral students working on electromagnetism, mathematics, precision mechanics, microwave technologies, electronics, mechatronics, nano-positioning, controls engineering and computing.

The main objective of the network is the training of young researchers on a multicultural, multidisciplinary environment. The students will be trained through research, and on the job through secondments in the partner private companies. They will follow academic training and supervision towards the completion of a PhD. The PACMAN network will also embark on outreach activities addressed to the general public, young children and female scientist in particular to increase awareness of the importance of research in society and also of the Marie Curie actions.

Table 1: Partners of the PACMAN network

Coordinating organization	Country
CERN	CH
Universities	
ETH Zurich	CH
Universita' del Sannio	IT
Cranfield University	UK
TU Delft	NL
IFIC (Universidad de Valencia)	ES
Research institutions	
LAPP	FR
SYMME	FR
TNO	NL
Private sector companies	
Hexagone	DE
Etalon AG	DE
Metrolab	CH
SigmaPhi	FR
Eltos	IT
DMP	ES
National Instruments	HU

The scientific objective of the PACMAN network is to propose and develop an alternative solution integrating all the alignment steps and a large number of technologies at the same time and location, in order to gain the required precision and accuracy. The solution proposed by the PACMAN network needs to be robust and also work reliably in an industrial environment. By the end of the program, a prototype alignment bench will be built in which the final demonstration of the PACMAN system (methods, alignment sequence and algorithms) will be implemented.

A number of issues need to be tackled previously. In practice we have to:

• optimize the manufacturing of the mechanical components of magnets and monitors and their assembly by applying ultra-high precision engineering and accurate machining techniques,

• refine methods for magnetic measurements that will deliver the functional axis of magnets with very small aperture and with the required accuracy by using vibrating wire techniques and printed circuit boards rotating search coils,

• refine and propose new measurements for finding the electromagnetic center of microwave cavities to nanometer resolution. Investigate laser and wire excitation and capacitive measurements,

• design new methods of absolute alignment between all the components inside the CLIC modules and their associated fiducials using a stretched wire as reference,

• develop portable methods of absolute alignment based on a combination of new techniques like micro triangulation and Frequency Scanning Interferometry (FSI),

• improve the commercial apparatus and seismic detectors to work in harsh environment and in magnetic fields by reviewing their mechanical and electronic design as well as the integrated feedback,

• study ground motion and other environmental noise to be able to filter it accordingly using seismic sensors,

• position the quadrupole and the attached beam position monitor with the help of actuators to the nanometer level,

- build a prototype alignment bench integrating all the metrology and electromagnetic measurements plus active nano-positioning and background monitoring,
- automatize this test bench,

The network delegates onto four science and research work packages. They will be described in the following sections.

2.8.2 WP1. Metrology and Alignment

This work package concentrates mostly on metrology, mechanics, electronics, optics, image analysis and magnetism. Three students will integrate this package together with Hexagon metrology, Cranfield University, ETH-Zürich and Etalon AG.

The monitoring at micrometric precision of large structures like bridges or buildings or the precise control of machining tools in industry is becoming ever more standard. However, both applications are interested only in relative measurements performed with respect to a given reference time. Only Coordinate Measuring Machines (CMM) have ever achieved micrometric precision and accuracy in absolute measurements. Within this work package, we aim to develop new methods of absolute metrology in the micrometer range and make them portable. We plan to bring the already existing CMM technology to our required accuracy and resolution.

In the field of CMM, a new optical sensor has been developed by Hexagon Metrology for the Leitz PMM-c Infinity LSP4 measurement head, allowing very high precision rugosimetry measurements [1]. To be used for targets as a vibrating stretched wire it would require further upgrading from one axis to 3D measurements. Micrometric portable means exist, e.g. measurement arm, but they do not perform measurements at the required accuracy and precision. Two methods under development are proposed to be tested, validated and implemented as portable means: Frequency Scanning Interferometry (FSI) and Micro-Triangulation. The SME Etalon AG has introduced FSI to the market recently: thanks to optical fibers and corner cubes, very precise measurements of distances are already performed. This is a relative measurement system, planned to be used for monitoring applications as the control of systematic deviations of CMM machines. The next step, going beyond the state-of-the-art, is to develop an absolute measurement method, based on FSI. Finally, alignment using micro-triangulation performs angle measurements on illuminated targets, by automatic image recognition. This system is currently under development by the university of ETH Zürich [1].

We intend to develop an optical sensor to be plugged in the Leitz CMM measurement head for high precision positioning of objects such as ceramic balls and vibrating stretched wires. The sensor must provide absolute measurements in the local coordinate system of the CMM and provide the most accurate and repeatable measurements without relying on a similar external reference in order to establish a proportional relationship. Different sensors types (cWPS, oWPS, opto-coupler) must be studied including their mechanical, electronic and optical parts.

In parallel, we will develop an absolute portable metrology method based on Frequency Scanning Interferometry. In collaboration with Etalon AG, we intend to develop the fiducials allowing the centering of optical fiber in order to perform absolute measurements of distance.

We intend to adapt Micro-triangulation for high accuracy on short range measurements of dynamic objects. In other to do this, it is necessary to increase the frequency of acquisition up to 50 Hz, synchronize the CCD camera and develop the detection algorithm for a vibrating stretched wire and targets. Prior simulation of the different configurations and verification on the experimental model will be part of the required research.

2.8.3 **WP2. Magnetism**

Disciplines directly related to this work package are magnetism, mechatronics, signal processing, numerical analysis and optimization, and partial differential equations. Two doctoral students will join this work package together with Eltos, Metrolab, Sigmaphi and the University of Sannio

The standard technique to measure the field quality in accelerator magnets is the rotating search coil. The magnetic axes of a quadrupole can be determined to a precision of micrometres which is indeed the required accuracy for new accelerators. However, for small-aperture accelerator magnets like the ones used in the future linear colliders, the sensitivity of search coils is difficult to maintain as for smaller coils, the coil cross section is not point like with respect to the surface spanned by the probe. Recently, the oscillating wire technique has been extended to field quality measurements by exciting the wire with a sinusoidal excitation current. The vibrations of the wire can be used to reconstitute the integrated transversal field components. The aim of this work package is to develop very accurate magnetic measurement techniques capable of measuring integral fields and magnetic axes of small aperture magnets at the micrometre scale. As a single method may not fulfil all the requirements of precision and portability, both the rotating coil and the stretched wire will be investigated, cross-checked and brought to their intrinsic limitations.

Rotating search coils wound on an epoxy-glass spacer have been used for magnetic measurements of normal and superconducting magnets of large aperture. They have routinely been used at CERN and in industry and reach a precision of 2 micrometres for the magnetic axes measurement [3]. Smaller coils have been produced recently with the printed circuit board technology and used at CERN for the measurement of magnets for the CLIC study. However, the accuracy of the coil positioning is not of the same order compared to the classical coils. In parallel, oscillating wire measurements of magnetic fields have been developed in recent years by the University of Sannio in collaboration with CERN [4]. The achieved accuracy of the alignment between the wire and the magnetic axis is of 10 micrometres. This work package aims for an alignment accuracy of 1-2 micrometres when using an oscillating wire which will be common to all the other work packages.

We will develop a magnetic measurement system based on the oscillating wire field-measuring technique for small aperture magnets integrating metrological techniques: measurement of vibrations, tension, opto-couplers, data acquisition, digital integrators with methods of potential theory and the solution of the wave equation on vibrating strings.

In parallel PACMAN will also build a magnetic measurement system based on rotating search coil with printed circuit board technology. This method will be used for direct comparison with the oscillating wire technique and for acceptance of the quadrupole magnets coming from industry.

A cross check of the results of both instruments is essential as only the oscillating wired method can be integrated in the prototype alignment bench whereas the rotating search coil is potentially more accurate.

2.8.4 WP3. Precision Mechanics and Nano-Positioning

The work package 3 exploits and develops the disciplines of mechanical and manufacturing engineering; nanotechnology; metrology and measurement; mechatronics; material science; seismology; control engineering; numerical analysis, simulation and optimization; and signal processing. Three students will join the research with the support of DMP, TNO, SYMME, LAPP, Cranfield University and TU Delft

The initial position of the magnetic centre and its relative alignment to the beam position monitor is guaranteed by ultra-high precision engineering of the quadrupole magnet itself. Active mechanical stabilization is required to limit the vibrations of the magnetic axis to the sub-nanometre level in a frequency range from 1 to 100 Hz. A stabilization system isolates the quadrupole from ground motion for up to six degrees of freedom using seismic sensors and actuators performing nano-positioning. The aim of this work package is to reach and maintain statically and dynamically the position of the main beam quadrupole axis at nanometre level.

Ultra high precision engineering is responsible for many of the latest technology developments in medical diagnostics, aerospace, optoelectronics, etc. The integration of the manufacturing procedures with metrology is however a new field with rare examples as the Cranfield BoX [5]. The stabilization of structures at the nanometre scale is a concern in various fields of precision engineering like integrated circuit lithography, interferometers, microscopes, or in manufacturing [6]. CLIC stabilization has proven to reduce the integrated displacements of ground motion by a factor of the order of 10 above 1 Hz with a reduction of transmissibility going up to a factor 500. Displacements are reduced to the sub-nanometre level in a laboratory environment. This was done with stiff actuating supports to be robust against external forces that otherwise would upset the alignment. The solution needs to be adapted to the component chosen for the project and confronted with other technical systems involved as micrometric alignment. Seismic sensors currently available in industry can measure in the sub-nanometre range and at low frequency [7]; however, they have not been designed to work in an accelerator environment where radiation and magnetic fields play a determinant role.

As part of the PACMAN research, we will re-engineer the quadrupole magnets assembly from the point of view of ultra-high precision engineering including the yokes quadrant mating surfaces, Beam Position Monitor support and the assembly procedure to guarantee an initial co-alignment at the micrometre level. The same attention will be paid to the mechanical integration of the prototype alignment bench

We will upgrade or develop sensors with a large bandwidth covering the whole frequency region of interest (0.1-100Hz) and presenting sufficiently low noise to measure quiet Ground Motion in the presence of radiation and stray magnetic fields. The sensors also need to be compact to fit in the crowded space of the prototype alignment bench and light-weight (typically less than a few kg) to avoid disturbing the measured structures.

At last, we will upgrade the first prototype of nano-positioning to be used for the test setup. We will also study the possibility of using long range actuators in flexural guides

for the combination of alignment and stabilization with sub nanometre resolution in a millimetre range.

2.8.5 WP4. Microwave Technology

This last work package focuses on microwave technology. It exploits metrology, ground motion, automation and general electromagnetism. Two doctoral students will form the core team of the work package with National Instruments and IFIC (University of Valencia) as partners.

There are two main Radio Frequency components being produced for CLIC. Besides the 12GHz accelerating cavities, the CLIC beam position monitor has been designed like a resonant device operating at microwave frequencies (15 GHz) [8] to achieve the very high spatial (50 nm) and temporal (50 ns) resolution required. For the absolute alignment of both components we rely on ultra-high precision mechanics both for the accelerating cavity as for the BPM cavity rigidly attached to the quadrupole. Still, the spatial resolution limit of the BPM system, is expected to be 1 nm or below for longer integration times. This work package aims to use RF excitation in a microwave cavity to measure accuracy to the micrometre level and resolution to the nanometre level. Qualifying the cavities at these extreme limits requires the monitoring and correlation of environmental data, e.g. ground motion, temperature, etc.

State of the art: The use of a stretched wire for determining the alignment between a beam position monitor and a quadrupole has been previously exploited in DESY for the Tesla Test Facility (now FLASH) [9]. However, the use of the system at smaller resolution and higher frequencies necessitates understanding of environmental noise and multiple corrections. Similar experimental set-ups have been studied recently for monitoring the displacement of test cryo-modules during cool-down with a precision of a few micrometres [10]. Concerning the accelerating cavities, alignment is done up to now by ultra-high precision machining and bonding of the disks that form the structure [11]. The only means to verify the alignment is from the outside diameter of the structure using classical metrology methods. This provides only an indirect measurement of the internal manufacturing precision and disregards any internal deformation due to the bonding process. Other alignment techniques based on the excitation of an RF signal by the beam itself when passing through the structure are being currently studied [12].

We aim to demonstrate the nanometre resolution of the beam position monitor by using a RF excitation on the stretched wire. The measurement should prove sub-micrometre spatial resolution as well as calibration; absolute alignment and long-term stability of a few micrometre or better, as well as high temporal resolution Essential parts of the read-out and control system are based on National Instruments hard- and software.

In parallel, we will investigate an independent measure of the axis of RF accelerating cavities to cross check against the mechanical alignment and provide laboratory, non-destructive tests. We will investigate the limits of the classical techniques and compare them to lasers excitation and stretched wire. We shall consider the use of the RF input ports and/or the damping waveguides as transmission lines.

2.8.6 **Conclusion**

PACMAN project (EC-funded Initial Training Network) has started on the 1st of September 2013, for a duration of 4 years. The "kick-off" Meeting with participation of all Partners has just taken place (20 November 2013). The recruitment of the 10 PhD students is under way and the work on the project will really start beginning of next year with a first period of intensive training of the students, followed by a period of secondment in industry, combined with study at CERN and trainings at universities, towards a common goal: the validation of the developed methods on the prototype alignment bench. More details about the program and the Partners involved in the project can be found at the PACMAN web site: http://pacman.web.cern.ch

2.8.7 **References**

1. http://hexagonmetrology.com/Press_86.htm?id=3799
2. S. Guillaume et al. "QDaedalus : Augmentation of Total Stations by CCD Sensor for Automated Contactless High-Precision Metrology" FIG Working week 2012 Proceedings ISBN 97887-90907-98-3.
3. L. Bottura et al. "Measurement of magnetic axis in accelerator magnets: critical comparison of methods and instruments", Instrumentation and Measurement Technology Conference, 2006. IMTC 2006. Proceedings of the IEEE
4. P. Arpaia et al. "Measuring field multipoles in accelerator magnets with small-apertures by an oscillating wire moved on a circular trajectory". JINST 7 P05003
5. http://www.cranfield.ac.uk/sas/clientservices/facilities/page5332.html
6. Carter, A. et al. Applied Optics 46, 421–427 (2007); Stochino, A. et al. Nucl. Instr. and Meth. A 598, 737–753 (2009). Furutani, K., Suzuki, M. & Kudoh, R. 15, 467–474 (2004).
7. B. Bolzon, "Etude des vibrations et de la stabilisation a l'echelle sous-nanometrique des doublets finaux d'un collisionneur linéaire" Thesis : Lab. Annecy Phys. Part. : 2007
8. H. Schmickler et al. Submicron multi-bunch BPM for CLIC, 1st IPAC, Kyoto, Japan, 23 - 28 May 2010
9. G. Priebe et al. Precision Alignments of Stripline BPMs with Quadrupole Magnets for TTF2 22nd International Linear Accelerator Conference, Lubeck, Germany, 16 - 20 Aug 2004
10. N. Eddy et al. A Wire Position Monitor System for the 1.3 GHZ Tesla-Style Cryomodule at the Fermilab new-Muon-Lab Accelerator. 15th SRF2011. 25-29 Jul 2011. Chicago, Illinois, USA
11. M. Dehler et al. *Fabrication of the CERN/PSI/ST X-Band accelerating structures* 2nd IPAC, San Sebastian, Spain, 4 - 9 Sep 2011,
12. M. Dehler et al. *X-band rf structure with integrated alignment monitors* Phys. Rev. ST Accel. Beams, 12, 062001 (2009)

2.9 Status of the CLIC Beam Instrumentation

T. Lefevre, CERN, CH 1211 Geneva 23, Switzerland
on the behalf of the CLIC BI collaboration
Mail to: Thibaut.lefevre@cern.ch

2.9.1 Introduction

For the Compact Linear Collider (CLIC) study [1], achieving high luminosity requires colliding beams with nanometer spot size and short bunch length [2] and this puts a high demand on the performance of most of the beam instrumentation systems. The extremely small emittance beams are generated in the Damping Rings. These emittances must be conserved over more than 40km, first through long transfer lines and then all along the main linac and the beam delivery system, which requires a precise control of the beam position. The bunch length is shortened from 2ps down to 150fs sigma in two consecutive stages, the last compression stage being located just before the main linac. At the interaction point, the beam is finally focused to only a few nanometers in size. After the collision highly disrupted beams need to be dumped in clean conditions, making sure that the 14 megawatts of power carried by the particles are safely absorbed.

The Drive Beam complex produces a series of 2.4GeV electron beams with high current (100 A) and high bunch frequency (12 GHz) using a bunch frequency multiplication scheme where bunched beams are interleaved by means of transverse RF deflectors [3]. These drive beams are thus distributed all along the CLIC main beam accelerator to produce the required 12GHz RF power locally, being decelerated over several hundreds of meters to an energy of 250MeV.

Table 1: Drive beam instruments

Instruments	DB surface	DB Tunnel	DB Total
Intensity	38	240	278
Position	1834	44220	46054
Beam Size	32	768	800
Energy	18	192	210
Energy Spread	18	192	210
Bunch Length	24	288	312
Beam Loss /Halo	1730	44220	45950

Table 2: Main beam instruments

Instruments	MB surface	MB Tunnel	MB Total
Intensity	86	98	184
Position	1539	5648	7187
Beam Size	34	114	148
Energy	19	54	73
Energy Spread	19	4	23
Bunch Length	17	58	75
Beam Loss /Halo	1936	5854	7790
Beam Polarization	11	6	17
Tune	4	0	4
Luminosity		2	2

An overall description of the CLIC beam instrumentation has been presented as a part of the CLIC conceptual design report [4] published in 2012. In this document, the beam instrumentation requirements have been reviewed in detail for the whole accelerator complex and an appropriate instrument technology was discussed and proposed to cover every specific needs. The number of instruments foreseen for the Drive and the Main beams is reported in Tables 1 and 2 respectively. In some cases, some R&D was still required to match the expected monitor's performances but no showstopper was identified. Alternative techniques or technologies were already mentioned in the conceptual design report as possible solutions with the aim to reduce cost or complexity. It was also clear that, in many areas, a lot of engineering work is still required to bring the state of the art developments to the level of reliability and availability expected for this kind of machine. The CLIC beam instrument experts have been working along these lines during the last few years and the status of some of our current developments is presented in the paper.

2.9.2 Beam Position Monitors

The beam position monitor (BPM) system for CLIC is extensive; the complex for the luminosity beams contains about 7200 BPMs while that for the drive beams requires about 46000 monitors. There is a wide variety of different types of BPM with differing beam pipe apertures and performance requirements, but we focus our developments on two cases, the Main Beam linac and beam delivery system RF cavity BPMs and the Drive beam decelerator BPMs.

2.9.2.1 *Main Beam Cavity BPMs*

The 4196 beam position monitors throughout the CLIC main linac and beam delivery system must routinely operate at 50 nm resolution and be able to make multiple position measurements within a single 156 ns long bunch train. Single-bunch spatial resolution better than these requirements has already been demonstrated using cavity BPMs [5]. Even if this is not expected to be a major problem, the required temporal resolution implies a BPM design with a bandwidth of 20MHz, much broader than that of existing systems [6].

A prototype cavity BPM has been designed [7], manufactured and installed in the main beam of the Two Beam Test Stand (TBTS) [8] at CTF3, as depicted on Figure 1. The BPM consists of a stainless steel 15GHz cylindrical pillbox position cavity with waveguides, which strongly coupled to the two polarisations of the first order dipole mode (TM110) and a second 15GHz pillbox cavity coupling to the first monopole mode (TM010) for charge normalization and phase reference.
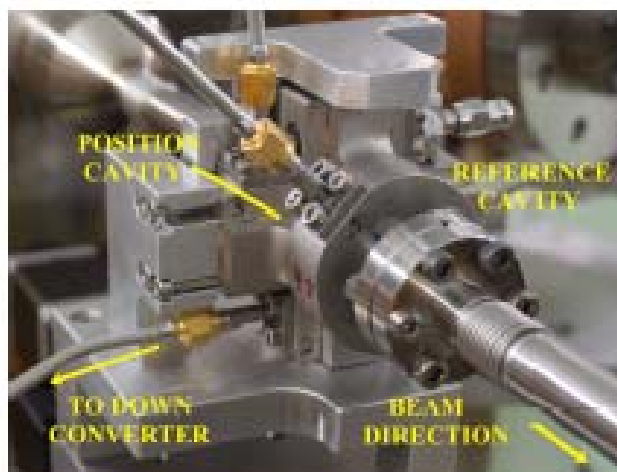
Figure 1:. Prototype cavity BPM installed in TBTS.

The signals from each cavity are filtered and then mixed down to an intermediate frequency (IF) with downconverter electronics near the pick-up, which also include a gain stage after the downconversion. Currently, the IF is set to about 200 MHz and the signals are digitised with a 2 GS s−1 with a 10-bit digitiser located outside the tunnel. Typical beam signals are presented in Figure 2.
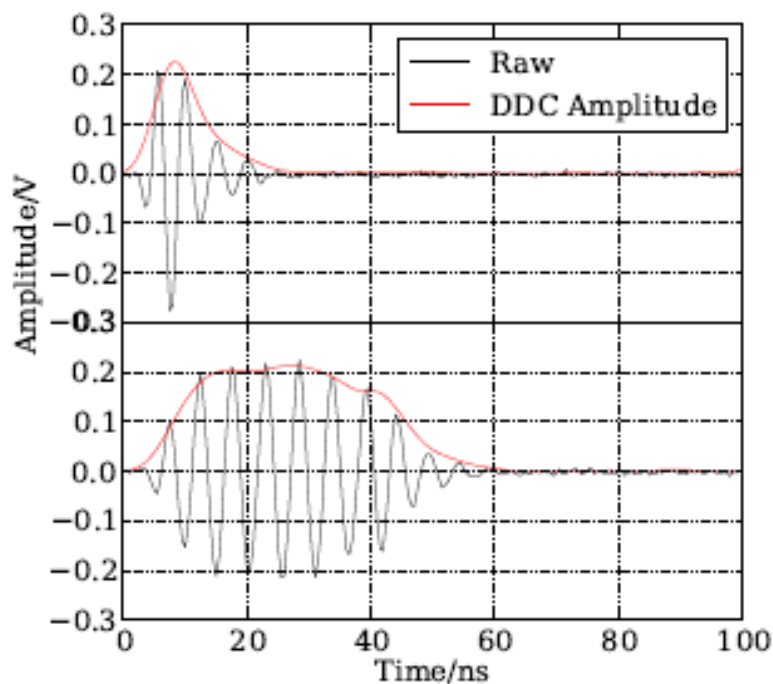
Figure 2: Example of digitised signals from the cavity BPM as excited by a short beam pulse (top) and long beam pulse (bottom) with the amplitude as measured using digital down-conversion.

The sensitivity of the position cavity has been measured [9] to 16.5 V.nC^{-1}.mm^{-1} close to the predicted value of 17.1. The time response of the cavity output signals was

also measured experimentally with about 25ns to decay down to zero (with 1%) after the stimulus. Based on these experimental results, an optimization of the design has been worked out with the aim to improve the mechanical tolerances on the waveguide to coaxial transition with a new geometry of the coupling antenna as visible in Figure 3. The BPM sensitivity and time response have also been intensively simulated and has led to a new design [10] based on a copper cavity with a larger loaded quality factor of 520. Three of such cavity BPMs will be manufactured and installed in 2014 on the beam line to assess the BPM resolution.
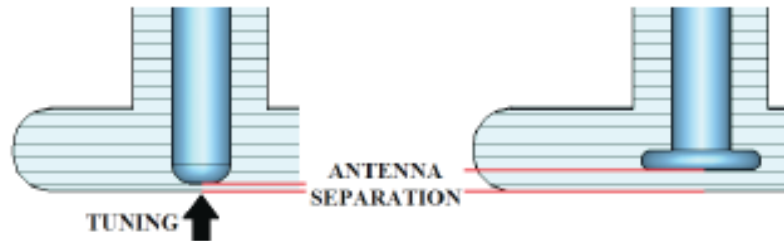
Figure 3: Waveguide to coaxial transition in the first prototype (left) and the new design with a bead on the antenna tip (right).

2.9.2.2 *Drive Beam Decelerator BPMs*

The Drive Beam Decelerator BPMs face several challenges, as they will be operated in close proximity to the Power Extraction and Transfer Structures (PETS), while the accuracy requirements are demanding (20μm). They have to be compact to fit with the tight mechanical layout of the decelerator and inexpensive as they need to be mass-produced with more than 40000 monitors. The high beam current in the Drive Beam also puts strong constraints to prevent wakefields, and to keep the longitudinal impedance as low as possible.

The first proposed solution [11] was a compact, downstream shortened stripline BPM utilizing a low-frequency (<40MHz) signal processing scheme operating in the accelerator tunnel. The system has been recently tested with beam in the CLIC Test Facility 3 (CTF3) [12], in presence of 12GHz RF signals from the PETS. The beam measurements have been performed for two different settings of the PETS RF power, 6MW (BEAM 6) and 60MW (BEAM 60). For both PETS settings the measured BPM parameters are very similar, indicating only little from the effect of the PETS RF power on the beam position measurement. Figures 4 displays the measured data along with linear fits, showing the change in the electrical offset (EOS) for the two power settings. The data also indicates a tilt between quadrupole QDR0800 and our BPM in the order of 5mrad for the horizontal plane and 7mrad for the vertical plane
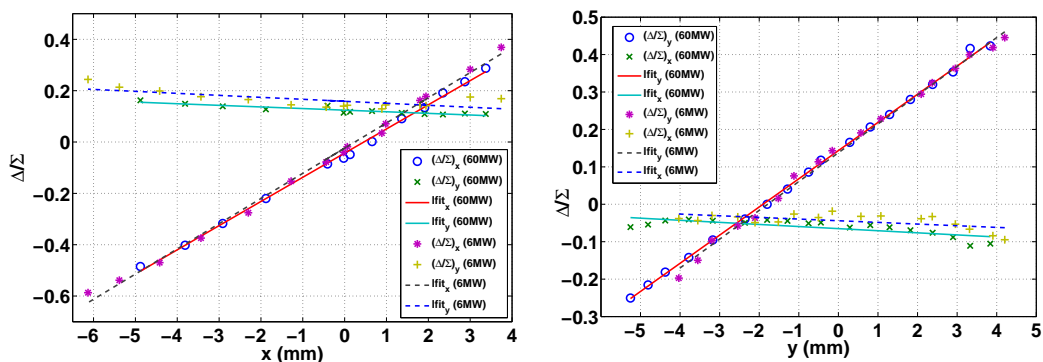
Figure 4: Dependency of the difference-over-sum ratio on the beam displacement in the horizontal (Left) and vertical (Right) plane for PETS RF power values of 6 MW (dashed lines) and 60 MW (solid lines).

Currently the prototype electronics have not been integrated into the control and timing system of CTF3 yet, so we were unable to synchronise shot-by-shot data to the other 16 BPMs [13] in the beam-line, thus to entangle beam motion from the residual noise systematics of the BPM. Simply analysing the RMS value of 85 consecutive beam shots gives an upper resolution limit of 43.3μm and 54.9μm for the horizontal and vertical planes, respectively. These values are consistent with the analysis of the neighbouring BPMs: BPS0850, 64.2μm (H) and 80.9μm (V), and BPS0910, 73.3μm (H) and 66.9μm (V).

In parallel, a second prototype stripline BPM, with improved notch-filtering properties at 12GHz, has been simulated. Similarly as in the first version, it is necessary to damp a strong resonance peak of the transverse wake impedance observed in EM simulations around 12GHz. A ring of SiC has been placed at each end of the striplines, separated from their rounded end by a narrow gap (Fig. 5, right). However, while successfully damping higher order modes (HOMs), the dielectric ring also increases the electrical length the stripline electrodes, thus shifts the notches to lower frequencies. Therefore, to obtain the desired frequency behaviour with electrodes of 37.5mm physical length, the distance between the upstream and downstream port pins was reduced to 36.6mm, which compensated the lengthening effect of the SiC dampers.
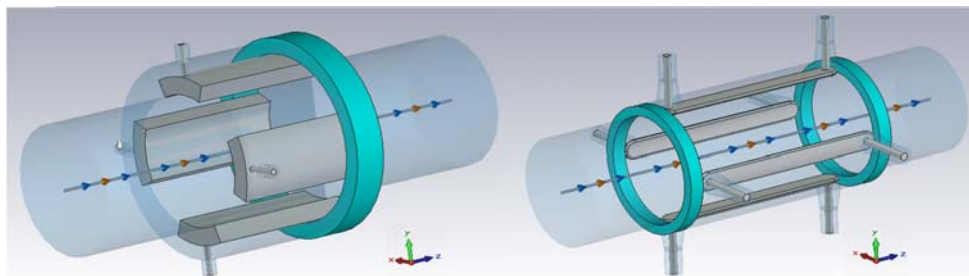
Figure 5: Initial (left) and modified (right) stripline BPM prototypes for CLIC DB.

As shown in Figure 5, the stripline electrodes of the terminated design are less wide (20^0 vs. 45^0 coverage) to ensure a TEM-like field propagation, which reduces unwanted spurious resonances and results in an improved transfer response. Evidently, the coupling of these narrow striplines to the beam is reduced by ~8dB, which is not an

issue as of the high beam current in the drive beam. In contrast to the prototype with shortened electrodes, the frequency response of the modified pick-up (Fig. 6) resembles that of an ideal stripline BPM up to higher frequencies (~8GHz). An unavoidable resonance appears around 10GHz, which seems to be caused by the TM_{01} waveguide mode of the vacuum chamber [14]. However, a substantial notch effect at 12GHz is still present, and should improve the suppression to the PETS high power RF fields.
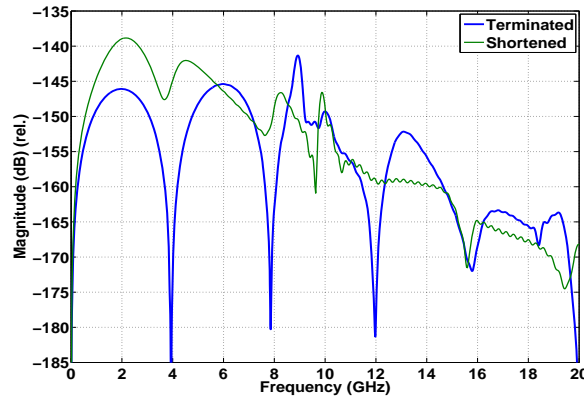
Figure 6: Initial (left) and modified (right) stripline BPM prototypes for CLIC DB.

2.9.3 Beam Profile Monitors

With a total number of requested monitors exceeding one thousand, the transverse and longitudinal profile measurement system for CLIC will be 3 times larger than the current total number of such devices actually in use at CERN. Whilst the Drive and the Main beams have very different parameters, their charge densities can reach levels well beyond the damage threshold of any physically interceptive monitor. For this reason the choice of instrument technology has favored non-intercepting devices wherever possible. Spatial resolution higher than 20microns, as requested in the Main Beam injector and in the Drive Beam complex, can be easily achieved using Optical Transition Radiation screens [15]. However, beam induced thermal loads will limit the use of such devices for beam sizes smaller than 500um for the MB and 3mm for the DB. This implies working with a reduced beam charge or pulse length, or using non-interceptive devices for high charge beams. Thus, in order to cover all the operational needs, a profile monitor may actually require two instruments based on different technologies.

The beam emittance is significantly reduced in the damping rings and requires monitoring with a 1micron resolution. In the CLIC complex, this concerns more than 80km of beam line and a total of more than 100 devices. In the rings and turn-arounds, imaging systems based on synchrotron radiation are being developed in the X-ray regime [16,17] to push this spatial resolution to the micron range. Alternatively, an innovative technique has been successfully developed and tested in PSI [18] to measure the very small vertical beam size by observing the visibility of the Point spread function of vertically polarized synchrotron radiation. In the transfer lines, main linac and beam delivery system, electron beam sizes down to one micron must be measured. The corresponding profile monitor is based on Laser Wire Scanners (LWS) [19] that have recently shown their capability to measure sub-micron beam spot sizes at the ATF2 [20]. LWS are also envisaged as non-intercepting transverse profile monitors for the

Drive Beam wherever necessary. However, they remain expensive and complicated devices and several studies have been initiated in order to find a possible alternative. Diffraction Radiation (DR) is currently being investigated for non-invasive beam size monitors as described in more detail in the article by Lorraine Bobb published in this newsletter. In the next paragraphs, we describe two R&D activities currently pursued on high resolution Optical Transition Monitor imaging system for low emittance beams and on non-invasive undulator-based off-axis synchrotron radiation imaging system for high charge Drive Beams.

2.9.3.1   *High Resolution OTR System*

The resolution of transition radiation imaging systems has been extensively studied both experimentally and theoretically using diffraction laws [21,22]. It is normally defined as the root-mean-square size of the Point Spread Function (PSF), which corresponds to the image of the field generated by a single particle. Therefore, the PSF contains information about both, the actual source distribution at the target surface and imperfections of the optical system. An example of the horizontal projection of the OTR electric field distribution at the source, calculated for different beam energies, is shown in Figure 7 with its typical spatial distribution, null in the centre and with two main lobes.
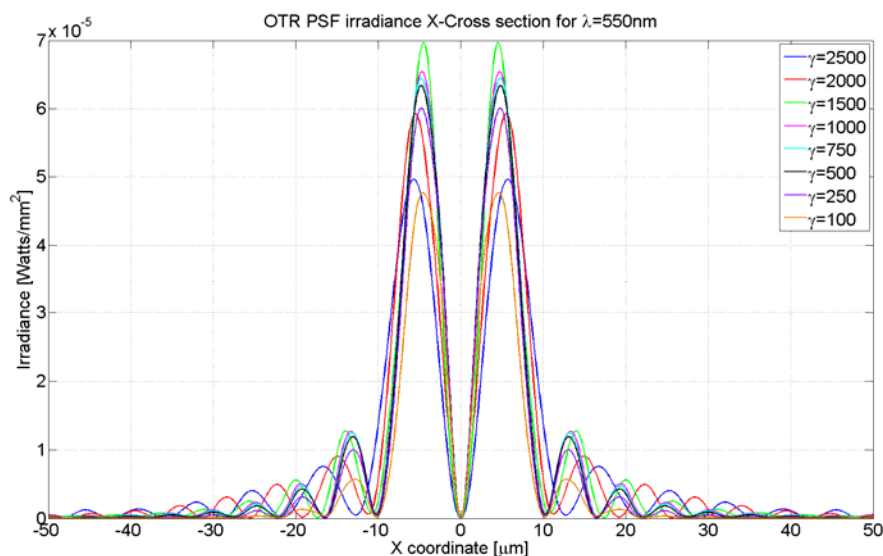
Figure 7: Horizontal cross-section of the OTR electric field distribution calculated for different beam energies.

In optical wavelength range the resolution of conventional OTR monitors is diffraction limited down to a few micrometers [23]. When the beam size is comparable or smaller than the OTR PSF, it is then possible to extract the beam size from a visibility measurement of the PSF. An experimental validation of this principle was recently performed on the ATF2 using a 1.28GeV electrons beam with an extremely small vertical beam emittance [24]. An example of the OTR PSF images obtained on ATF2 is shown in Figure 8.
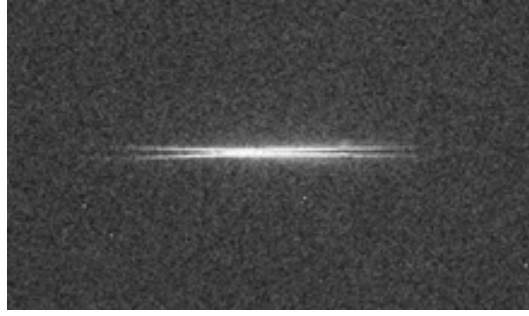
Figure 8: Image of the OTR PSF measured at ATF2 using vertically polarised photons.

The most advanced analytical calculations developed to study the PSF propagate the spatial distribution of radiation sources for a single particle or for a perfect Gaussian beam through ideal lenses up to the image plane. Main sources of errors are not correctly taken into account in these models and the PSF can thus not be calculated precisely. In 2012, simulation tool based on the physical optics propagation mode of ZEMAX [25] has been developed and is now capable to provide accurate estimate of the properties of OTR PSF of any optical system. It was used to study the limitation of the monitor under development at KEK, which turned out to be limited by chromatic and spherical aberrations, as observed experimentally. A new design was proposed and tested earlier this year and has shown an excellent agreement between measurements and predictions. For example, as presented on Figure 9.
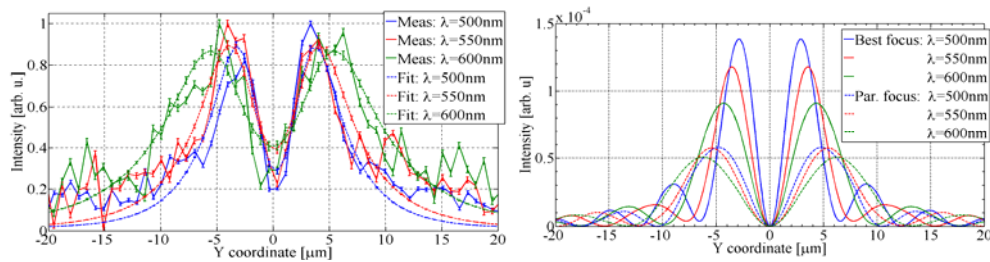
Figure 9: A comparison between the measured (left) and simulated (right) PSF for 500nm, 550nm and 600nm wavelengths.

Measurements are always performed with 40nm bandwidth optical filters at best focus conditions, which correspond to a position of the lens providing the smallest distance between peaks. In simulations, best focus conditions are typically obtained for a position of the lens being displaced by some 100 microns with respect to the paraxial focus condition. During the last beam test campaign [26], the minimum measured vertical beam size was 0.75micron, which improves by a factor 5 the resolution of conventional OTR monitors.

2.9.3.2 *Non-invasive Beam Imaging System for the CLIC Drive Beam Injector*

The CLIC Drive Beam accelerator will provide an intense electron beam up to 2.4 GeV [1]. The transverse beam profile should be measured at various points along the

linac and non-invasive profile monitors are being developed for this purpose. Parameters for the CLIC Drive Beam are shown in table 3.

Table 3: Relevant parameters for the CLIC Drive Beam Accelerator

Bunch population	5×10^{10} e-
Transverse Emittance	100 nm rad
Bunch length / spacing	13 ps / 2 ns
Pulse length	140 μs
Pulse Population	3×10^{15} e-
Repetition Frequency	50 Hz

A small permanent-magnet undulator, as shown in Figure 10, can be used to generate synchrotron radiation (SR) from the CLIC drive beam, which can be used for transverse profile measurements. SR is an attractive option for beam diagnostics since it is non-destructive and carries both transverse and longitudinal beam information. In this case, SR emitted in the forward direction is extracted out of the beam pipe using a ring mirror.
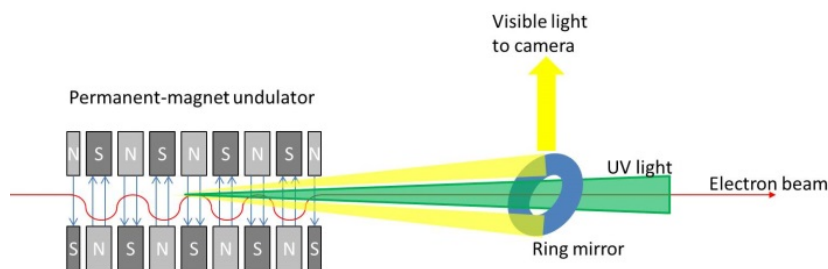
Figure 10: Schematic of off-axis SR observation.

For an electron beam at a given energy, various combinations of undulator period and strength may produce visible light with the required opening angle. Figure 11 shows the combinations which would produce 500 nm light with a 2.5 mrad opening angle using a pure permanent magnet undulator made of NdFeB (B_r=1.15 T) with pole gap $g \geq 10$ cm and $g/\lambda_u \leq 1$. It can be seen that the constraints can be fulfilled for all energies above 300 MeV.
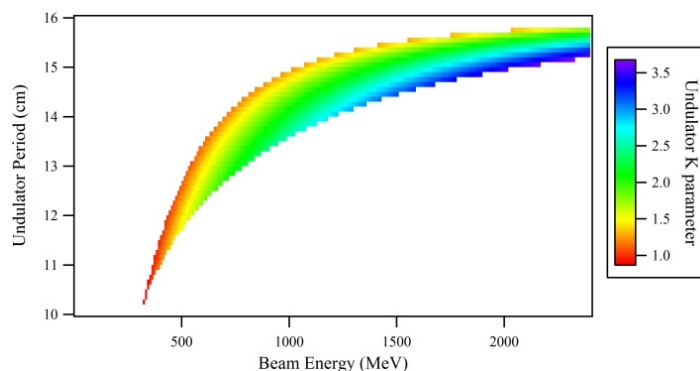
Figure 11: Undulator period and K parameter needed to produce 500 nm light at an opening angle of 2.5 mrad for different beam energies.

In order to determine the amount of light that could be gathered on the ring-shaped extraction mirror, simulations were performed with SRW [27]. As an example, Figure 12 shows the total SR and visible synchrotron light produced by 500 MeV electron beam passing through an undulator with K=1.3 and 3 periods of 12 cm. If the ring mirror is located so as to capture light emitted with opening angle between 2 and 3 mrad, approximately 5% of the SR power will hit the mirror. The spectrum of SR on the mirror is very broad, as shown in Figure 13.
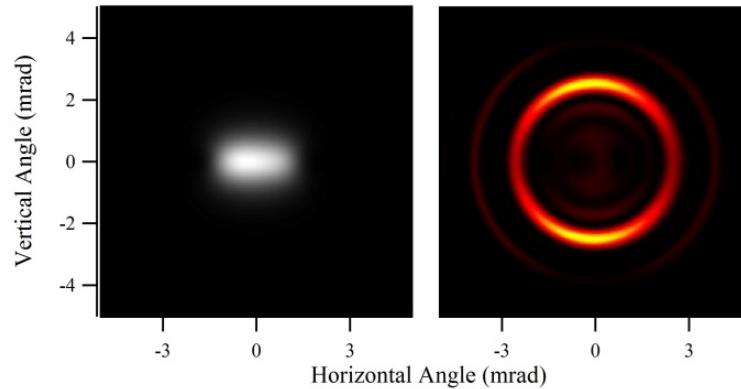
Figure 12: Total SR (left) and visible SR (right) from a 500 MeV electron beam crossing an undulator with 3 periods, K=1.3, λ_u=12 cm. Simulated with SRW.
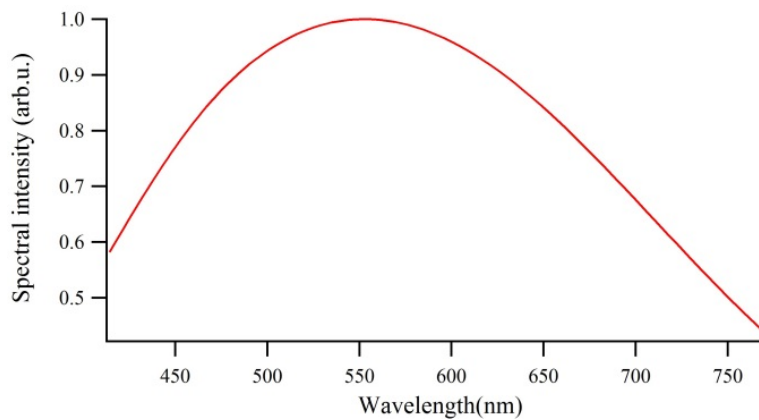
Figure 13: Spectrum of SR emitted with angle 2-3 mrad from a 500 MeV electron beam crossing an undulator with 3 periods, K=1.3, λ_u=12 cm. Simulated with SRW.

For any beam energy, the light yield on the mirror can vary considerably for different K, λ_u combinations giving the same opening angle. Thus the undulators, for which the yield has been calculated in table 4 are only examples. The power radiated from an undulator scales with γ^2. However, most of the radiation is contained in a cone with half-angle $1/\gamma$, so that as the beam energy increases, the fraction of SR reaching the ring mirror is reduced. These effects roughly cancel. At higher beam energies the SR power radiated on-axis can be considerable and shall be taken into account in the engineering design of the monitor.

Table 4: Examples of K, λ_u combinations which fulfil the conditions for visible light at 2.5 mrad opening angle and $g/\lambda_u \leq 1$. The yield has been calculated in SRW for undulators with 3 periods, assuming the mirror captures all light with 400-750 nm wavelength and 2-3 mrad opening angle.

Beam Energy	Undulator Period (cm)	K	Light yield (photons / e⁻)
300 MeV	10	0.7	2×10^{-3}
500 MeV	12	1.3	4.4×10^{-3}
1 GeV	14.5	1.6	2.8×10^{-3}
2.4 GeV	15.7	1.7	7×10^{-4}

The light yield could be increased by increasing the number of undulator periods However, increasing the length of the undulator makes the resolution worse due to depth-of-field effect as well as increasing the cost and space requirement of the undulator. The effect of the undulator on the beam optics is relatively small with a transverse movement of the electron beam inside the undulator of only 100 μm for the 300 MeV case, and less at higher beam energies.

A number of factors will affect the resolution of the profile monitor. The undulator represents an extended source so if the optical system is focused on the centre of the undulator, the entrance and exit will be slightly out of focus. Usually a narrow aperture is used to increase the depth of field of the optical system, but the large diameter of the ring-shaped extraction mirror makes this difficult. In order to investigate the effect on the profile monitor resolution, a simple optical simulation was carried out in ZEMAX [28]. The SR wavefront calculated in SRW was written to a ZEMAX beam. The ZEMAX Physical Optics mode was then used to propagate the wavefront through a simplified optical system with 1:1 imaging. The undulator in this simulation had K=1.3, λ_u=12 cm as in figure 4 above. The 500 MeV electrons are defined as a filament beam i.e. a point source. Since ZEMAX physical optics only deals with one wavelength at a time, only SR at 500nm was simulated. Transverse resolutions better than 200microns are possible for 2periods long undulator [29], but would degrade if using longer undulators.

Synchrotron light from undulators could be used as a source for beam-imaging monitors along the Drive Beam Linac and in the long transfer lines for beam energies higher than 300MeV. It could provide an online monitoring of the evolution of the transverse beam size all along the 140 microseconds of the Drive Beam pulse duration. Its limited resolution would imply to locate the monitor at a position where the optic lattice offers large β values with beam sizes larger than 1mm.

2.9.4 Beam Loss Monitors

As an integral part of the CLIC machine protection system [30], the CLIC Beam Loss Monitors (BLM) [31] should detect potentially dangerous beam losses and prevent subsequent injection into the main beam linac and the drive beam decelerators. The system should also assist in beam diagnostics, localizing and characterizing the beam loss distribution. This includes the ability to measure the time structure of the loss, which can indicate the origin of beam perturbations.

The CLIC BLM system requires a very large number of devices. Compared to other existing large BLM systems [32], one challenge of the CLIC BLM system is the requirement to identify structure specific beam losses along the CLIC modules where

both beams propagate simultaneously and in parallel. At this stage the proposed detector uses standard and robust ionization chambers but the use of Cherenkov optical fibres is under investigation [33].

A Monte Carlo study of beam losses has been performed to help with the commissioning of the Test Beam Line at CTF3, which is a small-scale version of Drive beam decelerator [34]. A simple model for the estimation of beam losses is based on the numerical integration of Gaussian beams. Following this approach, the misalignment of the beam shows bigger impact than its size growth throughout the TBL. Several Monte Carlo simulations have been performed to study the effect of detector location, impact angle, beam energy and loss scenario on the energy depositions and particle fluences at detector locations. The uncertainties found range between 10% and 70%, the detector location and the impact angle being the most relevant. Finally, the electron fluences at detector locations are used as an estimator for the BLM signals. The fraction of losses and the electron fluences expected at a detector for particles lost on a given azimuthal region on the beam pipe are combined to produce a realistic estimation of the BLM signals. Despite the relatively large differences of the expected BLM signals for the different azimuthal cases, the estimation of the BLM signals is dominated by the total fraction of beam loss irrespective of the direction of the loss in the transverse plane.

2.9.5 References

1. H.H. Braun *et al*, "CLIC 2008 parameters", CLIC note 764 (2008)
2. J.P. Delahaye *et al*, "Scaling Laws for Normal Conducting e$^+$ e$^-$ Linear Colliders", Proceeding of LINAC, Chicago, USA, 1998 pp.13
3. R. Corsini and J.P. Delahaye, "The CLIC Multi Drive Beam Scheme", CLIC Note 331 (1998)
4. CLIC Conceptual Design Report, "A Multi-TeV Linear Collider Based on the CLIC Technology", CERN-2012-007
5. S. Walston *et al*, "Performance of a High Resolution Cavity Beam Position Monitor System", Nucl. Instrum. Methods Phys. Res A578, 2007, 1-22.
6. S.R. Smith *et al*, PAC Vancouver (2009) pp754; A. Heo *et al*, PAC Vancouver, Canada (2009) pp3603
7. F.J. Cullinan *et al*, "A Prototype Cavity Beam Position Monitor for the CLIC Main Beam", Proceeding of IBIC, Tsukuba, Japan, 2012 pp.95
8. R. Ruber *et al*, Nucl. Instrum. Methods Phys. Res. A 729 (2013) 546-553
9. F.J. Cullinan *et al*, "First Beam Tests of a Prototype Cavity Beam Position Monitor for the CLIC Main Beam", Proceeding of IBIC, Oxford, UK, 2013 pp. 469
10. J.R. Towler *et al,* "Technologies and R&D for a High Resolution Cavity BPM for the CLIC Main Beam", Proceeding of IBIC, Oxford, UK, 2013 pp.476
11. S. Smith, *et al*, "CLIC Drive Beam Position Monitor", Proceeding of DIPAC, Hamburg, Germany, 2011 pp.326
12. A. Benot-Morell *et al*, "Status of the Stripline Beam Position Monitor Development for the CLIC Drive Beam", Proceeding of IBIC, Oxford, UK, 2013 pp.418
13. M. Gasior, "A Current Mode Inductive Pick-Up for Beam Position and Current Measurement", Proceeding of DIPAC, Lyon, France, 2005 pp.175
14. A. Benot-Morell *et al*, "Design and Characterization of a Prototype Stripline Beam Position Monitor for the CLIC Drive Beam", Proceeding of IBIC, Tsukuba, Japan, 2012 pp.87
15. K. Honkavaara *et al*, "Design of OTR Beam Profile Monitors for the TESLA Test Facility, Phase 2 (TTF2)", Proceeding of PAC, Portland USA, 2003 pp.2476
16. K. Ida *et al*, "Measurement of an Electron-Beam Size with a Beam Profile Monitor

using Fresnel Zone Plates", Nucl. Instrum. Methods Phys. Res A 506 (2003) 41; S. Takano *et al*, "X-ray Imaging of a Small Electron Beam in a Low Emittance Synchrotron Light Source", Nucl. Instrum. Methods Phys. Res A 556 (2006) 357

17. M. Kocsis and A. Snigirev, "Imaging using Synchrotron Radiation", Nucl. Instrum. Methods Phys. Res A 525 (2004) 79

18. A. Andersson *et al*, "Electron Beam Profile Measurements with Visible and X-ray Synchrotron Radiation at the Swiss Light Source", Proceeding of EPAC, Edinburgh, UK, 2006 pp.1223

19. S.T. Boogert *et al*, "Micro-scale Laser-Wire Scanner for the KEK Accelerator Test Facility Extraction Line", Phys. Rev. ST Accel. Beams 13, 122801 (2010)

20. L. Nevay *et al*, "Sub-micrometer Resolution Laserwire Transverse Beam Size Measurement System", Proceeding of IBIC, Oxford, UK, 2013 pp.26

21. M. Castellano *et al*, "Spatial Resolution in Optical Transition Radiation Beam Diagnostics", Phys. Rev. ST Accel. Beams 1, 062801 (1998)

22. A.P. Potylitsyn, Adv. Rad. Sources and App., Vol. 199, (2006) 149-163

23. M. Ross *et al*, "A Very High Resolution Optical Transition Radiation Beam Profile Monitor", SLAC Pub 9280, 2002

24. P. Karataev *et al*, "First Observation of the Point Spread Function of Optical Transition Radiation", Physical Review Letters 107, 174801, 2011

25. B. Bolzon *et al*, "Results of the High Resolution OTR Measurements at KEK and Comparison with Simlations", Proceeding of IBIC, Oxford, UK, 2013 pp.60

26. K. Kruchinin *et al*, "Extremely Low Emittance Beam Size Diagnostics with Sub-micrometer Resolution Using Optical Transition Radiation", Proceeding of IBIC, Oxford, UK, 2013 pp.615

27. O. Chubar and P. Elleaume, "Accurate and efficient computation of synchrotron radiation in the near field region", Proceeding of EPAC, Stockholm, Sweden, 1998 pp.1177

28. ZEMAX, www.zemax.com

29. A. Jeff *et al*, "Off-Axis Undulator Radiation for the CLIC Drive Beam Diagnostics", Proceeding of IBIC, Oxford, UK, 2013 pp.106

30. M. Jonker *et al*, "The CLIC Machine Protection System", Proceeding of IPAC, Kyoto, Japan, 2010 pp.2860

31. M. Sapinski *et al*, "Requirements of the CLIC Beam Loss Monitoring System", Proceeding of IPAC, Kyoto, Japan, 2010 pp.2869

32. B. Dehning *et al*, "The LHC Beam Loss Monitoring System's Surface Building Installation", CERN-AB-2006-009 BI

33. L.J. Devlin *et al*, "Update on Beam Loss Monitoring at CTF3 for CLIC", Proceeding of IBIC, Oxford, UK, 2013 pp.898

34. E. Nebot del Busto *et al*, "Monte-Carlo Simulations of Beam Losses in the Test Beam Line of CTF3", Proceeding of IBIC, Oxford, UK, 2013 pp.299

2.10 Development of a Diffraction Radiation Monitor for Non-invasive Transverse Beam Size Measurements at CesrTA

L. Bobb, E. Bravin, T. Lefevre and S. Mazzoni, CERN, Switzerland
T. Aumeyr and P. Karataev, Royal Holloway, U. of London, Egham, Surrey, UK
M. Billing and J. Conway, Cornell University, Ithaca, New York, USA
Mail to: Lorraine.Bobb@cern.ch

2.10.1 Introduction

Future accelerators such as the Compact Linear Collider (CLIC) [1] will typically operate using high charge density beams. For these beams, invasive diagnostic systems cannot be used without risking damage to the instrumentation. Laser-wire scanners are the primary candidate for non-invasive transverse beam size measurements. However, for future accelerators the quantity required could become costly and require extensive maintenance. For these reasons Diffraction Radiation (DR) monitors are being investigated as an alternative [2] [3].

When a relativistic charged particle moves in the vicinity of a medium DR is emitted. The spatial-spectral properties of DR are sensitive to a range of beam parameters. Furthermore, the energy loss due to DR is so small that the beam parameters remain unchanged. The horizontal and vertical beam sizes (σ_x, σ_y) can be measured using direct target imaging [4] and the angular distribution of DR [3] [5] respectively for a target aperture of size a in the vertical direction. At ATF2 the achieved beam size sensitivity using angular distribution measurements was as small as 14 μm [6].

For beam size measurements with micron-scale resolution DR in the UV and X-ray spectral range must be investigated. Experimental validation of such a scheme using 0.5 and 1 mm target apertures, 2.1 GeV beam energy and 400 nm wavelength is ongoing at CesrTA at Cornell University, USA. The DR experiment will run in two phases. In Phase 1 DR is measured in the near optical to UV regime. In Phase 2 the optical system must be redesigned such that DR at X-ray wavelengths can be measured. Over the last year, the first phase of the experimental program has been implemented whereby hardware has been installed and data acquisition is ongoing.

2.10.2 CesrTA Overview

CesrTA with beam parameters as shown in Table 1 was primarily reconfigured as a test accelerator [7] for the investigation of beam physics of the International Linear Collider damping rings. CesrTA provides a high energy 2-5 GeV electron or positron beam and the possibility to measure small beam sizes ($\sigma_y < 10$ μm). At CesrTA we are conducting the first DR beam size measurement experiment on a circular machine. This allows the study of wakefields and synchrotron radiation (SR) associated with DR monitors on circular machines. Here we can test the applicability of DR monitors for machines other than CLIC such as the LHC which has a comparable Lorentz factor.

Table 1: Phase 1 experiment parameters for CesrTA and comparison with the CLIC damping ring complex [1].

	E [GeV]	σ_x [μm]	σ_y [μm]
CesrTA	2.1	320	~9.2
	5.3	2500	~65
CLIC	2.86	~10-200	~1-50

2.10.3 Experiment Setup

The DR experiment is located in the L3 straight section of CesrTA (Fig. 1). Directly attached to the DR vacuum chamber is a 4-button beam position monitor (BPM). This BPM is located approximately 30 cm upstream of the DR target. Another BPM is located 30 cm downstream of the target in the electron beam direction. The X-ray beam size monitor (xBSM) [9] is used to measure the vertical beam size is located at the CHESS synchrotron radiation station (see bottom-left of Fig. 1). The visible beam size monitor (vBSM) [10] is used to measure the horizontal beam size and is located in L3 approximately 10 m upstream of the DR target.
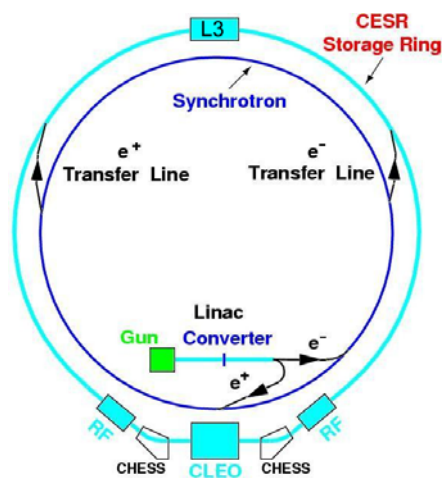
Figure 1: Layout of CesrTA [8].

An overview of the DR tank is shown in Fig. 2. Inside the vacuum chamber there is a section of beam pipe, which is moved out of the way during DR experimental sessions and reinserted for high current operations of CesrTA to minimize the higher order mode loss for the stored beams. On the opposite side of the chamber the target is attached to a mechanism with two degrees of freedom: translation IN/OUT and rotation about this axis. The compact optical system shown in Fig. 3 consists of an achromat for target imaging, a biconvex lens for imaging the angular distribution in the prewave zone [11], a bandpass filter, a Glan-Laser polariser and an intensified CCD (ICCD) camera.
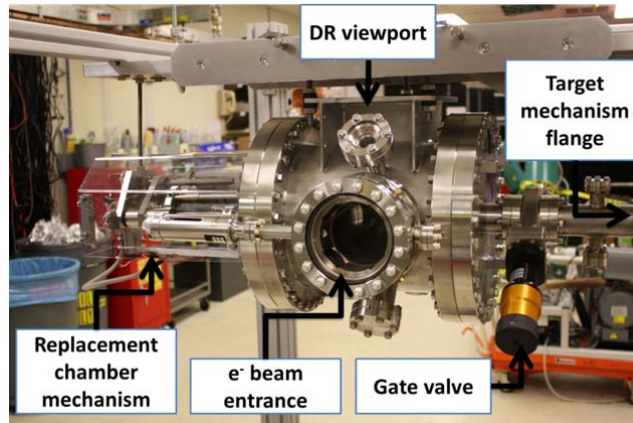
Figure 2: View of the DR target vacuum chamber from the upstream direction.
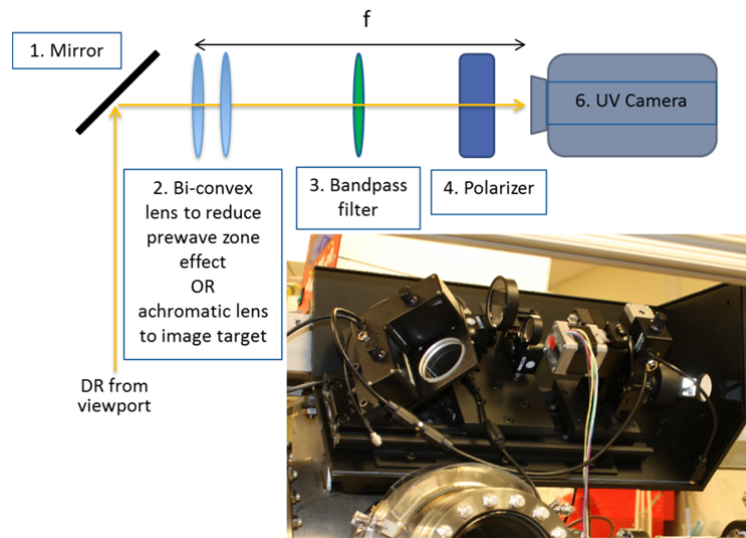
Figure 3: Schematic and image of the optical system.

2.10.4 **Diffraction Radiation Tests**

The first step at CesrTA was to install and test the vacuum chamber, optical system and controls and also to pass a single bunch electron beam through a target aperture. A dummy target was machined from unpolished stainless steel with aperture sizes of 0.5 and 1 mm (see Fig. 4). The apertures were etched. The reflectivity of this target was relatively poor therefore beam size measurements were not possible. However, the aim was to establish a method of beam alignment to pass through the apertures and to observe the beam lifetime.

Figure 4: Dummy target in the vacuum chamber viewed from the downstream direction.

The beam energy was 2.1 GeV and approximately 1 mA single-bunch beam current. The observation wavelength was 400 nm and the vertical polarisation was selected. The vertical polarisation is preferable to reduce background from SR which is predominantly horizontally polarised. To align the beam with the target aperture a combination of diagnostic instruments are required, these include: beam loss monitors (BLMs) positioned downstream of the target, beam position monitors (BPMs), beam current/lifetime monitors and direct imaging of the target using the ICCD camera in the DR optical system.

To determine the coarse vertical position of the target aperture the target was rotated such that the incident beam was perpendicular to the target thickness i.e. the largest target surface was parallel to the horizontal plane. A vertical bump was used to pass the beam above the target. The beam was gradually lowered to approach the target. The position at which significant losses were detected on the BLMs was recorded. The target was then retracted and the process repeated from below the target. The centre of rotation of the target is at the aperture centre. Therefore taking the average of these two vertical positions gave a coarse estimate of the vertical position of the target aperture.

The fine vertical position of the target aperture was found by inserting the target to a position at which losses could be detected on the BLMs. The beam was then swept vertically. The vertical position at which the minimum scraping was observed was the central position of the target aperture.

The beam lifetime in the dummy target was 2-3 minutes for the single-bunch beam with both aperture sizes. A 10-bunch train with 1 mA beam current was also tested but no improvement in the beam lifetime was observed indicating the lifetime was not determined by a charge-per-bunch dependent process.

$$
E_{y_i}^i = \frac{ic}{2\pi\lambda M\nu} \int d\theta \, d\phi_i \, \theta \, \exp\left[-ik\,\frac{x_i\theta\cos\phi_i + y_i\theta\sin\phi_i}{M}\right]
$$
$$
\times \left[\frac{e^{-kt_1\left(\sqrt{(\theta\cos\phi_i)^2-\gamma^{-2}}-i\theta\sin\phi_i\right)}}{\sqrt{(\theta\cos\phi_i)^2+\gamma^{-2}}-i\theta\sin\phi_i} - \frac{e^{-kt_2\left(\sqrt{(\theta\cos\phi_i)^2+\gamma^{-2}}-i\theta\sin\phi_i\right)}}{\sqrt{(\theta\cos\phi_i)^2+\gamma^{-2}}+i\theta\sin\phi_i}\right] \quad (1)
$$

A profile was selected and plotted against the expected intensity distribution using the vertical polarisation component of the electric field defined in Eq. 1 where x_i, y_i are the horizontal and vertical beam positions on the detector respectively,

$-\frac{ie}{2\pi\lambda M\gamma} = \text{constant}$, t_1 and t_2 are the distances of the particle to each aperture edge, using the integration ranges $[0, \theta_m]$ where θ_m is the maximum acceptance angle of the lens in the optical system and $[0, 2\pi]$, where ϕ_l is the lens polar angle, M is the magnification factor, k is the wavenumber and γ is the Lorentz factor. The intensity is calculated as $I_y(x_i, y_i) \propto \left|E_{y_i}^i\right|^2$ [4].
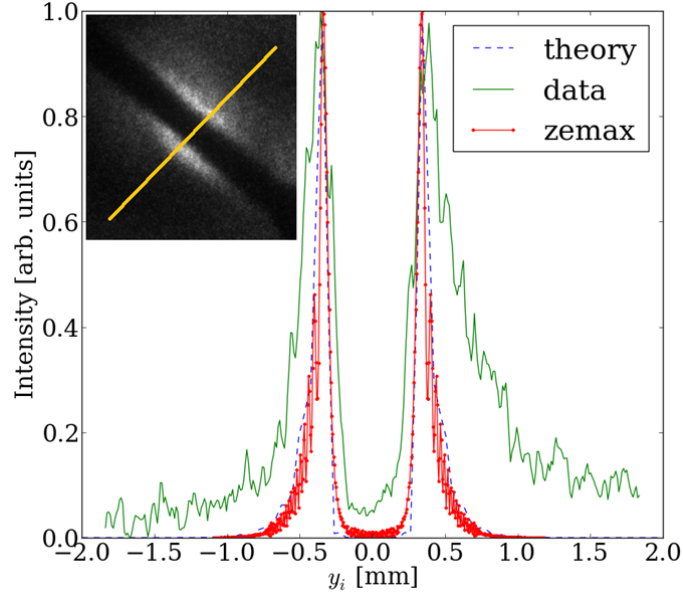
Figure 5: A plot of the intensity profile (solid line) and expected distribution from Eq. 1 (dashed line) and Zemax (dash-dot line).

In Fig. 5 the amplitudes of the data peaks are symmetric indicating that the beam was well centred in the aperture. The data is observed to be much broader than expected from the theory. This broadening could be due to the finite beam size used to acquire the data rather than a single particle used in the theoretical model, misalignment of the polariser allowing some horizontal contribution and parasitic light from SR background. The data and theory were also compared to the simulated Zemax output for a single electron which suggests that the broadening observed is not due to aberrations from the optical system [12]. The exposure time of the camera was 15 ms (CesrTA revolution period $T = 2.56\,\mu s$), therefore beam jitter although not observed on the BPMs could also contribute. In addition, the bandwidth of the filter was $10 \pm 2\,nm$ which could lead to some smearing of the data from light with wavelength $\lambda \neq 400\,nm$ although this effect is presumed to be small. The principle cause is thought to be due to the diffusive surface of the dummy target.

Two fabrication techniques have been used for the targets: chemical etching and molecular adhesion. The targets are made of polished silicon. In addition to the aperture size, a crucial property of these targets is the coplanarity between the upper and lower tines. The coplanarity δ should be within a fraction of the wavelength λ at which DR is observed i.e. $\delta = 0.1\lambda$. For $\lambda = 400\,nm$, the coplanarity should be $\leq 40\,nm$. The tines of the target must also be etched such that given a target tilt angle $\theta_u = 70°$, the

effective aperture size should not be further reduced by the 0.3 mm thickness of the target.
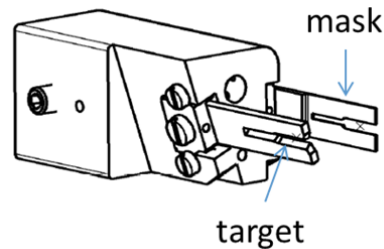
Figure 6: Target holder with mask and target mounted.

Chemical etching is a process where silicon wafers are dipped into an etchant which is traditionally an acidic mixture [13]. Although the 0.5 and 1 mm apertures could be fabricated within tolerance the coplanarity of the tines could not be guaranteed. Therefore an alternative fabrication technique was also investigated.

Bonding by molecular adhesion is a technique that enables two substrates having polished surfaces to adhere to one another, without the application of adhesive [15]. The upper and lower tines of the target are machined separately in sets. The tines are then paired together in all variations to identify which upper/lower pairs result in the best coplanarity. The aperture size was 1 mm only.
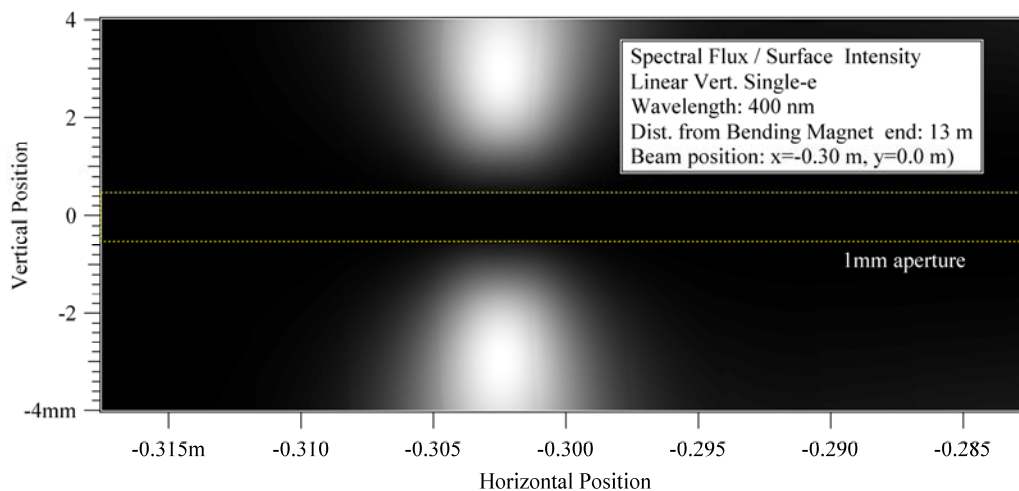
Figure 7: Simulated SR distribution on target.

Metrology was conducted at CERN to measure the coplanarity of the chemically etched targets. The molecular adhesion targets were measured during manufacture. The coplanarity of the four chemically etched targets showed a wide variation from $< 0.1\ \mu m$ to $10\ \mu m$. The coplanarity of the best chemically etched target ranged from $0.1\ \mu m$ at the innermost (0.5 mm) part of the aperture to $0.75\ \mu m$ at the ends of the tines [14]. The coplanarity of the molecular adhesion target was smaller than the chemically etched target as expected at approximately 60 nm with an rms 20 nm. Although these coplanarity measurements do not meet our requirements for $\lambda = 400\ nm$ they can be accounted for in the data analysis.

A silicon carbide mask is used to reduce the contribution of SR to background and is mounted upstream of the target as shown in Fig. 6. The mask is not etched since it is orientated perpendicular to the beam. The mask aperture size is 4 times larger than the target aperture size to minimise interference effects [3].

Simulations were made using the Synchrotron Radiation Workshop (SRW) [16]. In Fig. 7 the simulated vertically polarised SR distribution on the target surface is shown. The 1 mm target aperture is marked by the dashed lines. It is seen that the most intense areas of SR do not occur at the slit edges. Therefore light emitted at the slit edge (see inset Fig. 5 and 8) is from DR, possibly with a small contribution from transition radiation (TR). To verify the signal in the images is DR the intensity profile from the target edge is taken and fitted to an exponential curve. It is known that the DR intensity should decrease exponentially with distance from the slit edge whereas SR is relatively uniform over small regions [4]. Using simulations the DR intensity is found to be approximately 50 times brighter than SR at 400 nm wavelength considering vertically polarised photons only. This difference was found to be a factor of approximately 25 from the chemically etched target images.
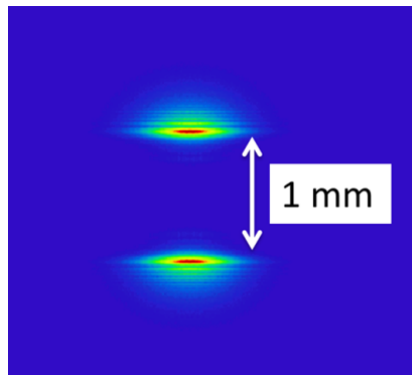
Figure 8: Simulated 400 nm vertically polarised DR distribution on the target using Zemax [12].

From the preliminary test it was noted that 5-10 minutes was lost for each beam injection and manual beam alignment. A program was developed to automate this task, reducing the time taken between data acquisition to a couple of minutes. Initially the same manual beam alignment methods previously described were used to establish the route (vertical bump setting and target insertion position) into the target aperture. This route was then used as an input file for the program.

The beam lifetime with the target/mask assembly inserted was 2-3 minutes. This lifetime was the same for the chemically etched and molecular adhesion targets. The vertical beam size was varied from $13 - 52\ \mu m$. The horizontal beam size was approx. $490\ \mu m$. The beam lifetime was not affected by the vertical beam size until $\sigma_y = 50\ \mu m$ where it could then be regained by manually adjusting the vertical beam position in the slit. It is thought that the beam lifetime is primarily dependent on the roll of the beam and the aspect ratio $(\sigma_x : \sigma_y)$ which for this test was 1:38.

2.10.5 **Conclusion and Outlook**

Over the last year the hardware and instrumentation for the first phase of the DR experimental program have been installed and tested in CesrTA. A method of beam alignment in the target aperture has been established and the typical beam lifetime was 2-3 minutes. DR signals have been identified from SR background in target images.

Recently, improvements were made to the optical system. A plano-convex lens with 500 mm focal length will be used for improved angular resolution. All optical components were also changed for 50 mm clear aperture versions to avoid clipping. The whole system was also dismantled and realigned. As part of the preparations for the next test in the winter of 2013 a trigger system has been put in place for the possibility of acquiring single-turn images.

2.10.6 **References**

1. H. Schmickler, et al., "CLIC CDR", CERN-2012-007.
2. M. Castellano, "A New Non-Intercepting Beam Size Diagnostics Using Diffraction Radiation from a Slit", Nucl. Inst. And Meth. A 394(1997), 275-280.
3. R.B. Fiorito, D.W. Rule, "Diffraction Radiation Diagnostics for Moderate to High Energy Charged Particle Beams", Nucl. Instr. and Meth. B 173 (2001) 67.
4. D. Xiang, et al.,"Imaging of High-Energy Electron Beam Profile with Optical Diffraction Radiation", Phys.Rev.ST Accel.Beams, 10 (2007) 062801.
5. L. Bobb, et al., "UV/X-ray Diffraction Radiation for Nonintercepting Micron-scale Beam Size Measurement", Proceedings of IBIC2012, Tsukuba, Japan, MOCC01, p. 24.
6. P. Karataev, et al., "Beam-Size Measurement with Optical Diffraction Radiation at KEK Accelerator Test Facility", Phys. Rev. Lett. 93 (2004) 244802.
7. D. Rubin, et al., "CesrTA Layout and Optics", Proc. of PAC2009, Vancouver, Canada, WE6PFP103, p. 2751.
8. Cornell Electron Storage Ring, LEPP, Cornell University, http://www.lepp.cornell.edu/Research/AP/CESR/
9. N.T. Rider, et al., "Operation of a Single Pass, Bunch-by-Bunch X-ray Beam Size Monitor for the CESR Test Accelerator Research Program", IBIC2012, Tsukuba, Japan, WECD01, p. 585.
10. S. Wang, et al., "A Turn-by-turn Beam Profile Monitor using Visible Synchrotron Radiation at CESR-TA", IPAC2013, Shanghai, China, MOPWA073, p. 849.
11. P. Karataev, "Pre-Wave Zone Effect in Transition and Diffraction Radiation: Problems and Solutions", Phys. Lett. A 345, 2005, 428.
12. T. Aumeyr, et al.,"Zemax Simulations of Diffraction and Transition Radiation", IBIC2013, WEPF18.
13. M.S. Kulkarni, H.F. Erk, "Acid-Based Etching of Silicon Wafers: Mass-Transfer and Kinetic Effects", Journal of The Electrochemical Soc., 147 (1) 176-188 (2000).
14. L. Remandet, CERN internal report, EDMS.1274854
15. S. Kerdiles, et al., Patent US 8158013 B2
16. Synchrotron Radiation Workshop, ESRF, http://www.esrf.eu/Accelerators/Groups/InsertionDevices/Software/SRW

2.11   Status of the CLIC Damping Rings Design

Yannis Papaphilippou, CERN, CH 1211 Geneva 23, Switzerland
for the CLIC damping rings design team
Mail to: yannis@cern.ch

2.11.1 Generation of Ultra-low Emittances

The high luminosity of a linear collider, at the lowest power, requires the generation of ultra-low emittance high-intensity bunches, with remarkable stability. Although conventional electron sources and positron production schemes provide the intensity required but with emittances that are several orders of magnitude larger than the ones needed. The natural synchrotron radiation damping of the beam when circulating in rings is the cooling mechanism enabling to reach these small emittances.

Table 1: CLIC versus ILC and NLC parameters driving the DRs design.

Parameter [unit]	ILC	NLC	CLIC
Bunch population [10^9]	20	7.5	4.1
Bunch spacing [ns]	369	1.4	0.5
Number of bunches/train	2625	192	312
Number of trains	1	3	1
Repetition rate [Hz]	5	120	50
Horizontal normalized emittance [nm.rad]	4400	2400	500
Vertical normalized emittance [nm.rad]	20	30	5
Longitudinal normalized emittance [keV.m]	38	11	6

The performance challenges of these damping rings (DRs) are driven by the key performance parameters of the collider and the requirements of the upstream and downstream systems, and principally the efficiency of the main linac RF. The parameters guiding the design of ILC [1], NLC [2] and CLIC damping rings are presented in Table 1. The technological choice of super-conducting over copper RF cavities for the main linacs, clearly diversifies the design of damping rings, although a number of design issues and challenges still remain common. In the one flavour of the damping rings as CLIC or NLC, the bunch trains are relatively short with even shorter bunch spacing and with a high repetition rate. The ILC bunch train is much longer necessitating a much longer ring circumference where the train is compressed and uncompressed in a bunch-by-bunch beam transfer scheme. For getting the high luminosity in the ILC, the bunch charge is much higher whereas CLIC targets for much smaller emittances, orders of magnitude lower in all three dimensions (500nm.rad horizontal, 5nm.rad vertical and 6keV.m longitudinal). Although these emittances are unprecedented, modern X-ray storage rings in operation or construction phase are rapidly approaching these regimes. Especially for the vertical emittance, requiring challenging magnet alignment tolerances and stringent control of the optics and orbit, X-ray rings hold the current record, at the level of below 1pm.rad [3-4], thereby reaching the CLIC DR target. Figure 1 presents the horizontal and vertical normalized emittance in a number of low emittance rings, including test facilities, DRs, B-factories and synchrotron light sources, under operation (red) or in the design phase (blue). Whereas

the future light source projects are aggressively pushing the limits of horizontal emittance below 100pm, and some operating ones reach a very low vertical one, CLIC DRs are unique for being in the cross section of both challenges.
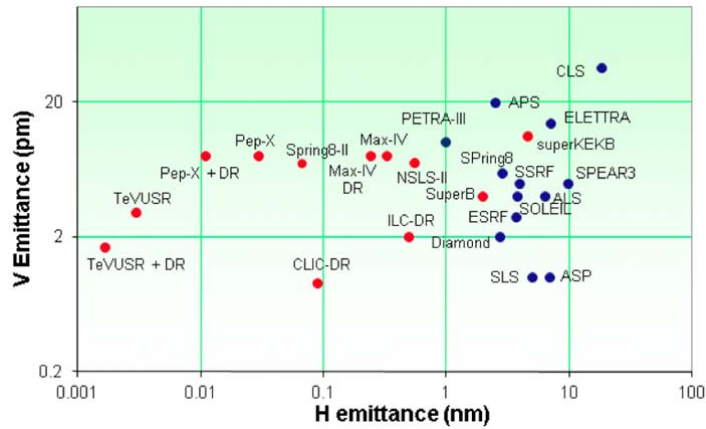
Figure 1: Horizontal versus vertical normalized emittance for low emittance rings in operation (blue) and in the design phase (red) (from R. Nadolski [3]).

2.11.2 The CLIC Damping Rings Complex

A schematic layout of the CLIC damping ring complex is shown in Fig. 2 comprising of two pre-damping rings, two damping rings and a delay loop. Two pre-damping rings (PDRs) are needed due to the large input emittance especially coming from the positron source and the high repetition rate of 50Hz. The electron pre-damping ring could become obsolete provided that the delivered electron normalised emittance from the linac can be below 50μm (the horizontal emittance achieved in the PDR).

At every machine cycle, two trains are injected in the damping rings with twice the nominal bunch separation (1 vs 0.5ns), in order to reduce the transient beam loading effects in the RF cavities. The head of each train is separated by half of the damping rings circumference. The two trains are damped simultaneously and then extracted in a single turn from the main damping rings. A delay and recombination loop, downstream of the main rings, is used in order to provide a unique train with the required 2GHz bunch structure.

Standard transport lines transfer the beam between the injector linac, the damping rings, the delay loop and the booster linac. As the train recombination is provided by the same loop for both species, the time delay between the e^+ and e^- trains is recovered in the downstream systems.

2.11.3 Damping Ring Challenges and Parameter Choice

The goals guiding the design of the damping rings are driven by the main parameters of the collider and the requirements of the upstream and downstream systems.

The large energy spread of the positron beam reduces the capture efficiency in the pre-damping rings and explains the much larger bunch population needed at their entrance. Note also that the transverse emittances for the two particle species differ by almost three orders of magnitude. For electrons before and after the pre-damping rings, the bunch population contains roughly a 10% overhead for ring and transfer losses.
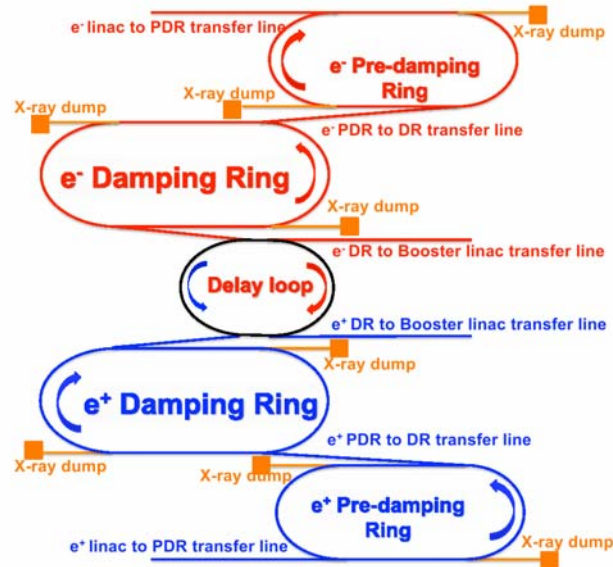
Figure 2: The damping ring complex layout including two pre-damping rings, two damping rings and a single delay loop.

For the pre-damping rings, the main challenge is the huge positrons emittance to be captured, necessitating large dynamic transverse and momentum acceptance [6].

The design challenges of the CLIC main DRs are driven from the extremely high bunch density, i.e. the ratio between bunch charge and the 3-dimensional beam volume, and the collective effects associated with it. In this respect, the CLIC DR parameters shown in Table 2 are carefully chosen and optimised in order to mitigate these effects. In addition, these parameters drive the technology of a number of components such as wigglers, RF system, kickers, vacuum, instrumentation and feedback.

After the adaptation of the latest main linac RF systems parameters, which drive the design of most CLIC accelerator systems, the damping rings presented a final emittance with a blow-up of a factor of 5 in the horizontal emittance due to the effect of IBS [7]. The design strategy followed was to raise the ring energy, change the optics, adapt the wiggler parameters and increase slightly the longitudinal emittance in order to mitigate as much as possible the IBS effect, down to a factor of 1.5, with respect to the equilibrium horizontal emittance. In particular, the scaling of the ratio between the steady state and zero current emittances with the energy is shown in the left part of Fig. 3. The IBS effect is reduced for higher energies as expected. The dependence of the steady state emittances to the energy is displayed on the right part of Fig.3. A broad minimum is observed around 2.0 GeV for the horizontal and vertical emittances, where the IBS effect also becomes weaker. Although higher energies may be also interesting for reducing further collective effects, the output emittance is strongly increased due to the domination of quantum excitation. In this respect, the energy of 2.86 GeV was chosen for the CLIC DR, which is close to a steady state emittance minimum but also reduces the IBS impact [7,8].

Table 2: CLIC Damping Rings' design parameters.

DR Parameters [unit]	Value
Energy [GeV]	2.86
Circumference [m]	427.5
Energy loss/turn [MeV]	4.0
RF voltage [MV]	5.1
Compaction factor	1.3×10^{-4}
Damping time transverse / longitudinal [ms]	2.0/1.0
Number of arc cells/wigglers	100/52
Dipole/wiggler field [T]	1.0/2.5

The lattice including the number of cells, the bending magnet characteristics, the wiggler field and period are chosen such that the target emittance is reached within the high repetition rate of 50Hz, in a compact ring. In particular, the wigglers have to reach peak fields that only super-conducting materials can provide them. The vertical emittance at "zero current" is dominated more by vertical dispersion and less by coupling, so in order to achieve it, apart from tight alignment tolerances, a very good correction and control of the orbit is necessary. In any case, the geometrical target emittance of less than 1pm.rad is the present achieved record in synchrotron light source storage rings for similar energies and bunch currents [4].

Due to the very small beam size especially in the vertical plane, the space charge tune-shift can be quite important. For reducing it, and apart from the short ring circumference, the bunch length had to be increased to the maximum acceptable level imposed by the RTML, by tuning the TME cell to an increased momentum compaction factor.
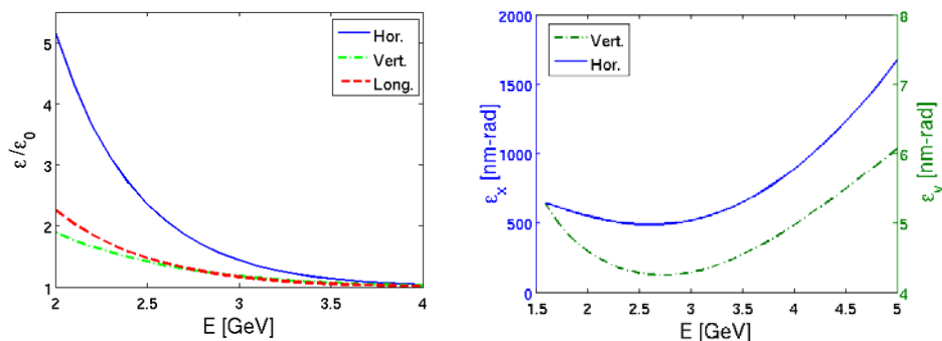
Figure 3: Dependence of the IBS growth factor, i.e. ratio between steady state and equilibrium emittances (left) and steady state emittances (right) with energy.

The beam loading transients in the RF cavities can be reduced by halving the RF frequency, which indeed imposes injection of two trains with a subsequent recombination in a delay loop. In order to reduce the stationary phase and linearise the bucket, the voltage cannot be raised without shortening the bunch. Instead, the energy loss per turn was increased in a way that it does not affect the fast damping, by reducing the bending field.

High bunch density in combination with the short bunch spacing triggers two stream instabilities. In the electron ring, the fast ion instability can be avoided with ultra-low

vacuum pressure. This necessitates coating of vacuum chambers with getters like NEG for increasing pumping in addition to vacuum conditioning.

In order for the electron cloud build up to be reduced and the instability not to occur in the positron ring, it is necessary that the vacuum chambers present a low secondary electron and photo-emission yield (SEY and PEY). The low SEY can be achieved with special chamber coatings, whereas the low PEY is already imposed by the required absorption efficiency to reduce the heat deposition in the super-conducting magnets. In addition, the increased bunch spacing with the two trains scheme, indeed relaxes the above requirements.

The stringent beam stability requirement of typically 10% of the beam size, imposes tight jitter tolerances for the damping ring extraction kicker (a few 10^{-4}). An ILC type beam extraction experiment using a proto-type strip-line kicker has been carried out at KEK-ATF [13] with quite encouraging results, approaching the stability requirements of CLIC.

2.11.4 Optics Design

The optics functions for a quarter of the ring, are shown in Fig. 4. Each arc is filled with 48 TME cells and 2 half cells at either side for the dispersion suppression. The original TME cell was designed as compact as possible but presented several weaknesses with respect to space and magnet strength constraints. A series of optimisation steps was followed in order to rationalise it and, at the same time, to reduce the effect of IBS [9]. The major contribution of IBS is associated to locations where the beam sizes, i.e. beta functions and dispersions, reach their minima. In the TME cell, both horizontal and vertical beam sizes become minimum at the centre of the arc cells and it is exactly at this location where IBS growth rates are maximum. However, the low emittance condition requires only small horizontal betatron function in the bending magnets while the vertical one can be large.

A defocusing gradient in the bending magnet can reduce further the emittance but also reverses the behaviour of the vertical beta at the centre of the dipole (Fig.4) , hence reducing the IBS growth rate, while the resulting output emittance is almost the same [9].

As the final emittance of the ring can be further reduced by the use of damping wigglers in the straight sections, which provide also the fast damping, a detuned TME cell was designed, which is more flexible, easier to achieve and has lower chromaticity. The horizontal and vertical phase advances are μ_x = 0.408 and μ_y = 0.005. The horizontal phase advance allows a higher value of the momentum compaction factor, while keeping the final emittance within the budget. The vertical one is the smallest possible in order to increase the vertical beta functions and reduce IBS kicks while keeping the beam acceptance large enough. The bending radius of the dipole (determining its field of 1 T and length of 0.58 m) was chosen such that the energy loss per turn becomes smaller and the bunch length as large as possible.
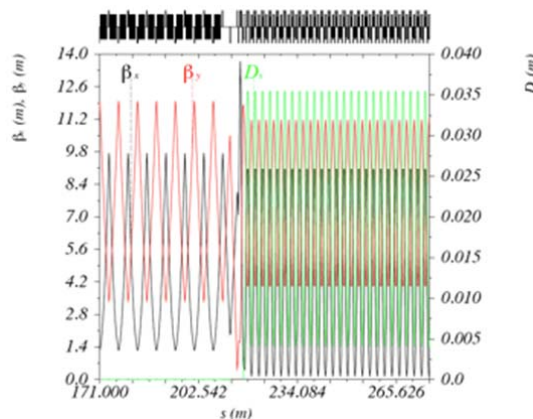
Figure 4: Horizontal (black) vertical (red) beta functions and horizontal dispersion (green) of the for a quarter of the CLIC DR.

The long straight sections (LSS) are filled with FODO cells and accommodate the damping wigglers. There are 13 FODO cells per straight section with two wigglers per cell. Further emittance minimisation can be made by properly choosing the lattice functions in the wigglers [9]. For a FODO cell, the minimum emittance is reached for horizontal phase advance $\mu_x = 0.31$ and for the vertical one tending to zero. The vertical phase advance can then be set as low as possible ($\mu_y = 0.12$) in order for the chromaticity to be minimized. Another possible choice is $\mu_y = 0.25$ corresponding to minimum vertical betas and thus, maximum vertical acceptance.

The lattice functions between the arcs and the straight sections are matched with the dispersion suppressors and matching sections. The first part is a half TME cell, with different quadrupole strengths. These two quads are used as knobs in order to minimise the length of the suppressor. A dipole is then used for the suppression of the dispersion and four more quads as knobs for matching all the optics functions at the entrance of the LSS. Space is reserved in the dispersion free region for injection/extraction and RF cavities. This lattice including sextupoles, magnet fringe fields and linear imperfections was proved to provide an adequate dynamic aperture [11] and good low emittance tuning characteristics [12].

2.11.5 Wiggler Specifications and Performance

Producing the ultra-low horizontal emittance in a compact ring within the machine pulse of 20 ms necessitates the use of damping wigglers. The highest field and relatively short period is needed in order to reach the target emittances. Pure permanent magnets are not able to reach high field (the maximum is around 1.2 T for Sm_2Co_{17}), so pole concentrators are used (e.g. vanadium permendur) to enhance the field to a maximum value of 2.3 T. This maximum field of 2.3T can be reached for a relatively large period of around 140 mm. In that case, the horizontal emittance gets more than doubled and far above the required 500 nm. In order to achieve the target DR performance, the number of wigglers has to be more than doubled, which results to a 40% increase of ring circumference. In this respect, the only way to reach the very small emittance while keeping the ring compact, is the use of high field for high gap/period ratio, necessitating superconducting damping wigglers.

130
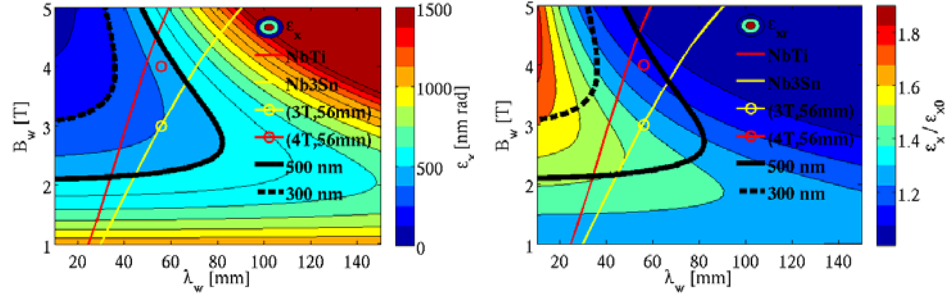
Figure 5: Dependence of the steady state emittance (left) and its ratio with the equilibrium emittance (right) as a function of the wiggler peak field and period. The blue color denote smaller emittances or ratios, whereas the red ones bigger. The black curve traces the horizontal emittance target barrier of 500nm.

In order to explore the dependence of wiggler characteristics on the output horizontal emittance with respect to IBS, a simulation was performed by varying the wiggler peak field and period, while keeping the final vertical and longitudinal ones fixed. The results are shown in Fig. 5. The left plot is colour-coded with the horizontal steady state emittance while the right one with the ratio between the steady-state and the zero-current one. The black curve corresponds to the target emittance of 500 nm and defines the area for which the output emittance is within the budget. The highest field and the shortest period is necessary for reaching the smallest emittance possible. On the other hand, the effect of IBS in that case becomes extremely strong. For reducing the blow-up due to IBS, still the highest fields are interesting but for moderate periods.

In each DR, it is foreseen to install 52 wigglers of peak field 2.5 T and 50 mm period, based on NbTi technology. A short prototype with these characteristics was developed and measured at Budker Institute achieving the field requirements. Another mock-up with more challenging design (2.8 T field, with 40 mm period) wound with Nb$_3$Sn wire is also under testing at CERN [13].

Around 9kW of total power is produced by each wiggler and an absorption system is necessary and critical to protect machine components and wigglers against quench, but also to lower the photo emission yield for reducing the e-cloud effect in the positron ring. The power limit is set between 1 and 10 W/m, depending the wire technology and the vacuum chamber cooling. A series of horizontal and vertical absorbers are placed downstream of the wigglers. A terminal absorber at the end of the long straight section is absorbing the remaining 100kW of photon power [14].

Full wiggler prototypes with similar magnetic characteristics are expected to be built at BINP and installed at a straight section of the ANKA synchrotron for tests under beam conditions, during 2014. Of particular interest would be the validation of cooling concept and the resistance of the wiggler to heat load under real beam conditions.

2.11.6 Longitudinal and RF Parameters

The very high peak and average current corresponding to the full train of 312 bunches spaced by 0.5 ns presents a big challenge due to the transient beam loading, especially for a 2 GHz RF system. In this respect, it was decided to consider two bunch trains with 1ns bunch spacing. The RF system with frequency of 1 GHz is more

conventional and an extrapolation from existing designs is possible. Nevertheless, the trains have to be recombined in a delay loop downstream the DRs with an RF deflector.

This choice has a positive impact in both the PDRs and the main DRs. Doubling the bunch spacing halves the harmonic number increasing the momentum acceptance. The extraction kicker rise time becomes shorter but it is still long enough (560 ns). The 2-train structure may require two separate extraction kicker systems or one kicker with longer flat top (1 μs). The beam loading is significantly reduced, as the larger bunch spacing reduces peak current and power by a factor of 2. Several beam dynamics issues are also eased due to double bunch spacing. The e-cloud production and instability is reduced, while the fast ion instability will be less pronounced by doubling the critical mass above which particles get trapped. The reduced number of bunches per train reduces the central ion density, the induced tune-shift and the rise time of the instability is getting doubled, thus relaxing the feedback system requirements. Finally, a bunch-by-bunch feedback system is more conventional at 1 than at 2 GHz.

For both frequencies, and in order for the RF bucket to become more linear, the stationary phase has to be kept low. This could be achieved be increasing the RF voltage but this shortens the bunch and increases the impact of collective effects. In order to lower the stationary phase, the dipole field was lowered for reducing the energy loss per turn. At the same time, the momentum compaction is increased and so does the bunch length, leaving some margin for the increase of the voltage.

2.11.7 Collective Effects

2.11.7.1 *Intrabeam Scattering*

One of the main limitations of the CLIC DRs is the effect of intrabeam scattering (IBS) which increases the output emittances in all three dimensions. IBS is a small angle multiple Coulomb scattering effect which depends on the lattice characteristics and the beam dimensions. It is described by a series of theories and approximations [15-18]. Multi-particle tracking codes were developped [19,20] was developed for evaluating the IBS effect in the emittance, including damping and quantum excitation. These codes were compared with classical IBS theories and approximations and the results are presented in Fig.6. for the horizontal emittance evolution over one turn of the ring. The results seem to be in very good agreement with the Piwinski theory, while all other theories are very close to the simulations. In addition, the trend of the emittance evolution is the same. Due to this identical behaviour of the theories and simulations in the arcs and straight sections of the DR, and taking into account that the simulations are quite lengthy, it is convenient to use one of the analytical approaches for understanding and minimising the IBS effect. Thus, the Piwinski theory is used for this purpose, as it seems to be the closest to the simulation results [8].

A measurement campaign in CESRTA [21] and SLS [22] has been initiated for evaluating IBS effect and benchmark theories and simulation codes.
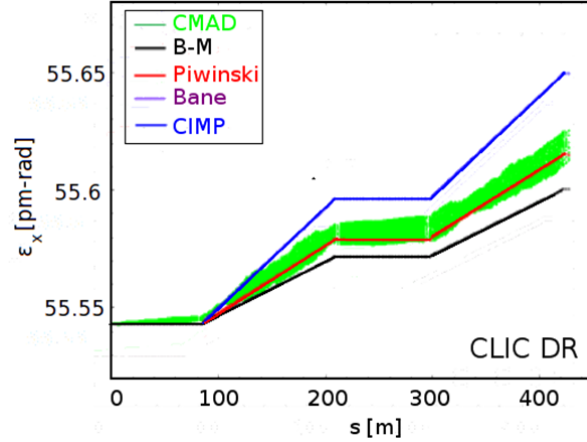
Figure 6: The one turn behaviour of the horizontal emittance starting from the zero current values, as computed by CMAD-IBSTrack (green), BM (black), modified Piwinski (red), Bane (purple) and CIMP (blue) formalisms.

2.11.7.2 *Space Charge*

Due to the very small beam size especially in the vertical plane, the space charge tune-shift can be quite large, and an effort was undertaken in order to reduce the vertical tune-shift to around 0.1. In this respect, the bunch charge and the beam sizes cannot be changed without affecting the collider's performance and the energy was already optimised for reducing the relative impact of IBS, while reaching the required steady state emittances. Consequently, in order for the space charge to be reduced, the ring has to become as compact as possible. At the same time, the bunch length has to be increased without affecting the performance of the downstream bunch compressors. This was achieved by increasing the equilibrium bunch length through combined reduction of the circumference (removing wiggler cells), lowering the harmonic number by reducing the RF frequency and increasing the momentum compaction factor. Note finally that the space charge tune-shift grows to its final large value during the first few ms of damping to the steady state emittance thus forcing the beam core to traverse resonances. Fast pulsing quadrupoles may be necessary, in order to control the coherent tune-shift in order to avoid emittance growth or beam loss.

2.11.7.3 *Electron Cloud Effect and Mitigation*

The positron DR accumulates many densely populated bunches with a narrow spacing. Therefore, electron cloud could be an issue as the positron beam emits synchrotron radiation photons, which create a large number of photoelectrons at the inner chamber wall surface which get scattered inside the vacuum chamber and they can multiply through secondary emission. This causes electrons to be accumulated in the chamber in large amounts with a possible destabilising effect on the circulating beam.

The electron cloud build up was simulated with Factor2 code [23], for elliptical beam pipes. In the dipoles, the electron cloud formation appeared to be largely dominated by the photoemission up to maximum secondary emission yields of 1.8 with central densities between 10^{11} to 10^{13} m^{-3}.

In the wigglers, the situation is more critical because of the smaller pipe radius. The electron cloud build up starts to be dominated by secondary emission for maximum

SEY's around 1.5. Fig. 7 show the electron central densities for three different values of photoemission yield of 90, 99% or 99.9% and maximum SEY of 1.3, 1.5 and 1.8. These studies show that, independently of the initial seed of photoelectrons, extremely high central densities of electrons can be reached for SEY of 1.8. For SEY of 1.3, the electron central density would still be very high if the absorber absorbs less than 99.9% of the emitted synchrotron radiation. Therefore, for maximum SEY below 1.3, the photoelectrons can still be present in large numbers in the wiggler beam pipe, if the absorption is not sufficiently efficient to remove a high fraction of them.
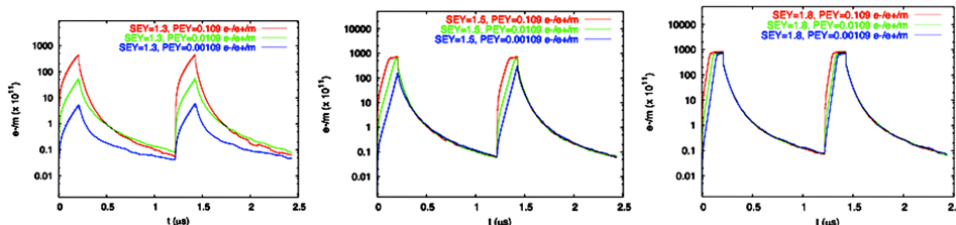
Figure 7: Electron central densities in the wiggler chamber of the CLIC DRs for photoemission yields of 90 (red), 99 (green) or 99.9\% (blue) and secondary electron yield of 1.3 (left), 1.5 (center) and 1.8 (right).

The single bunch electron cloud instability has been studied with an intense simulation campaign showing that the threshold value for the e-cloud density lies at about $5x10^{13} m^{-3}$ in the wigglers, independently of the electron density value in the dipoles. This means that countermeasures are needed to prevent electron accumulation in the wigglers, because when the electron cloud forms it reaches very quickly the critical values to make the beam unstable.

Conventional feedback systems cannot damp the e-cloud instability, as a very wide band is needed. Several mitigation techniques are presently under study[3], including low impedance clearing electrodes, solenoids (only usable in field free regions), low SEY surfaces, grooved surfaces and coatings with NEG and TiN. In particular, an amorphous carbon coating has been extensively tested at SPS [24] and later at CESRTA [25], with promising results, with respect to SEY and photo emission.

It has to be noted that some techniques such as surface coatings, non smooth surfaces or clearing electrodes to fight electron cloud do not come for free and can be serious high frequency impedance sources [26].

2.11.7.4 *Ion Effects*

In the electron DR, the ion oscillation frequency inside the bunch train during the store is in the range of 300 MHz (horizontal plane) to about 1 GHz (vertical plane), to be divided by the the square root of the mass number of the ion However, not all ion types will be trapped in the bunch train and the ones trapped around the beam are those having a mass number above a critcal value, which depends on the location in the ring (due to the different beam sizes). Molecules like N_2 and CO can be trapped almost along the full ring and will accumulate around the electron beam, potentially becoming a source of fast ion instability. The critical masses for trapping are twice as large, reducing the fraction of the ring over which ions like H_2O can be trapped. With the pressure of 1nTorr, the induced tune shift introduced by the ion cloud at the end of the train is moderate. The exponential rise time of the fast ion instability is quite large and equal to a few turns for both options. It would therefore require a very demanding

multi-bunch feedback system to be controlled and/or an even lower vacuum pressure through coatings with getters (NEG) or conditioning. The train gaps have also proved to provide a natural cleaning mechanism for the trapped ions.

2.11.7.5 *Instabilities and Impedance Budget*

The broad-band model is used as a first approximation to model the whole ring in order to scan over different impedance values and define the instability threshold and the impedance budget. In these model, the impedance source is assumed to be identical in the horizontal and vertical planes.

In the transverse plane, a strong head-tail instability or Transverse Mode Coupling Instability (TMCI) can occur and cause rapid beam loss. In the case of a round beam and axisymmetric geometry for a short bunch an analytical criterion can be used to predict the TMCI threshold of around 10.7 MΩ/m for the transverse broad-band resonator in the vertical plane.

Simulating the evolution of the bunch centroid for zero chromaticity over several turns for different impedance values, it was found that modes 0 and -1 are observed to move and couple for impedance values of 15 MΩ/m and 4 MΩ/m in the horizontal and vertical plane respectively, causing a TMCI.

Chromaticity is believed to raise the TMCI threshold thanks to the tune spread that it causes and because it locks the coherent modes to their low intensity values, making mode merging weaker. For this reason, a simulation was done for different positive and negative values of chromaticity. As expected, the presence of chromaticity causes the modes to move less and not to merge and by consequence to avoid a TMCI, but another type of instability, the head-tail instability, is occurring. The TMCI quickly becomes very fast above the threshold for the onset, but for the case of head-tail instability the calculation of its rise time is needed and the damping time of 2 ms defines an instability threshold at 2MΩ/m.

The resistive wall in the wiggler sections with 6 mm vertical half aperture is expected to be a strong source of impedance. Because of the small aperture, compared to 9 mm for other parts of the ring, the contribution of the wigglers is expected to take a significant fraction of the available impedance budget. Moreover, layers of coating materials, which are necessary for e-cloud mitigation or good vacuum, can significantly increase the resistive wall impedance especially in the high frequency regime. The materials used in these simulations are stainless steel (ss) and copper for the pipe of the wigglers, which is assumed to be flat. Amorphous carbon (aC), used for e-cloud mitigation, and non-evaporated getter (NEG), used for good vacuum, were chosen as coating materials. Different material and coating combinations were tried, in order to study the effect of coating on the threshold. For the case of copper, the thresholds are higher compared to those of stainless steel making it a better choice in terms of instabilities but also a more expensive material. Adding a layer of coating material on the beam pipe reduces the intensity thresholds and in fact the thicker the coating is, the more the threshold is reduced, corresponding to an extra 1MΩ/m reduction in the impedance budget.This budget is expected to be further reduced if all the different contributions from the DR are taken into account.

The rise time of the coupled bunch modes caused by resistive wall are estimated to be 0.3 ms corresponding to about 210 turns and can be damped with a transverse feedback. The rise time was simulated to be quite larger than the calculated one (by a factor 5-10), as the simulation takes into account the real wiggler and the train length.

2.11.8 Injection/Extraction

The injection and extraction process is quite simple with only one pulse stored in the damping ring per cycle. This pulse contains two trains of 156 bunches with 1GHz structure. Each train which is supposed to be symmetrically spaced in the DR, covers a small fraction of the circumference of only 11%. The injection and extraction system is located at symmetric locations, at the end of the arc, after the dispersion suppressor and upstream of the super-conducting wigglers to avoid that synchrotron radiation damages the sensitive injection/extraction elements. The kickers can be placed at maximum horizontal beta functions for minimising the deflection angle. For the same reason, the phase advance between injection (extraction) septa and kickers are set to around $\pi/2$. Additional space can be added in order to install longer elements thus reducing the available voltage needed and accommodate protection systems.

An extraction kicker ripple produces a beam size jitter which is propagated up to the collider IP. On the other hand, injection kicker jitter is translated to reduction of the beam stay clear, during the injection process. For both processes, a typical tolerance of 10\% of the beam size at extraction or injection is considered, although in the case of injection, it can be relaxed to even higher values (e.g. 20-30%). Taking into account that the extracted beam size for the required normalised emittance of 500~nm corresponds to a few tens of microns, the kicker stability tolerance is around 10^{-4}.

A similar tolerance can be established for the kicker roll, which will induce a vertical beam size jitter. The extracted vertical beam size is of the order of a few μm and to keep the distortion to the order of a few hundred nm, the kicker alignment should be better than a few tens of μrad. Future refinement in the lattice of the damping rings will not change significantly the kicker specifications, especially the stringent required stability.

To ease this very tight requirement, a 2nd identical kicker powered by the same pulser can be installed in the extraction line, at a phase advance of π for jitter compensation. This solution was already proposed in the case of the NLC damping rings [1], which required similar stability tolerances. A double strip-line kicker system was at ATF with similar stability requirements but for shorter rise/fall times and flat top [27]. A prototype stripline kicker was built in collaboration with IFIC-Valencia and TRINOS and it is currently tested magentically at CERN [28]. There are plans on testing this stripline including the pulser in existing storage rings.

2.11.9 Delay Loop

The two trains of the CLIC DR have to be recombined in a single delay loop for both species, using RF deflectors. A unique α-shape loop, as in CTF3, is considered, for both species with a circumference of 263m, i.e. half of the damping rings. The optics is tuned to achieve high-order iso-chronism and is based on TME cells and sextupole tuning. The emittance growth due to synchrotron radiation is negligible due to the low energy and relatively short length of the loop. The path length correction is very critical and a wiggler, orbit correctors or a chicane may be considered in order to control it down to a few mm. The systematic energy loss is roughly half of the DR and can be corrected with RF cavities of a few hundred kV. As the beam stability requirement is quite low, this imposes tight jitter tolerances for the RF deflector (around 10^{-3} . This tolerance is within the capability of modern klystrons. It will necessitate a demonstration

through measurements in CTF3 which are equipped with similar RF deflectors for the drive beam recombination and frequency multiplication [29].

2.11.10 Acknowledgements

The author would like to thank all the members of the CLIC damping ring design team and the Low Emittance Rings collaborators for their numerous contributions to this work and in particular F. Antoniou, M. Barnes, S. Calatroni, P. Chiggiatto, R. Corsini, A. Grudiev, E. Koukovini-Platia, T. Lefevre, N. Mounet, G. Rumolo, S. Russenchuck, H. Schmickler, D. Schoerling, D. Schulte, M. Taborelli, G. Vandoni, M. Wendt, F. Zimmermann, P. Zisopoulos (CERN), Y.M. Boland, R. Dowd, R. Rassool, E. Tan, K. Wooton (ACAS, Melbourne, Australia), A. Bragin, E. Levichev, D. Shatilov, S. Siniatkin, S. Piminov, P. Vobbly, K. Zolotarev (BINP), M. Billing, J. Calvey, J. Crittenden, G. Dugan, D. Rubin, J. Shanks (Cornell), M. Palmer (FNAL), F. Torral (CIEMAT), M. Korostelev (Cockroft), C. Belver-Aguilar, A. Faus-Golfe (IFIC-Valencia), D. Alesini, M. Biagini, S. Guiducci, S. Liuzzo (INFN-LNF), P. Raimondi (ESRF), R. Bartolini (DIAMOND), K. Kubo, T. Naito, N. Terunuma, J. Urakawa (KEK-ATF), A. Bernard, A.S. Muller (KIT-ANKA), E. Wallen, A. Anderson (Maxlab), M. Aiba, M. Boege, N. Milas, L.Rivkin, A. Streun (PSI-SLS).

2.11.11 References

1. N. Phinney, N. Toge, N. Walker, ILC Reference Design Report Vol. 3 -Accelerator, arXiv:0712.2361, http://arxiv.org/pdf/0712.2361.pdf.
2. Next Linear Collider Zeroth-Order design report, SLAC-R-474, 2002.
3. 3rd Low Emittance Rings Workshop 2013, http://www.physics.ox.ac.uk/lowemittance13/index.asp
4. M. Aiba et al., Nuclear Instruments and Methods in Physics Research, 694, 2012.
5. F. Antoniou and Y. Papaphilippou, "Design considerations for the CLIC pre-damping rings", PAC'09, Vancouver, May 2009.
6. H. Braun et al., CLIC 2008 parameters, CLIC-Note-764.
7. Y. Papaphilippou, H.H. Braun and M. Korostelev, "Parameter scan for the CLIC damping rings", EPAC'08, Genova, June 2008, p.679.
8. F. Antoniou, M. Martini, Y. Papaphilippou and A. Vivoli, "Parameter scan for the CLIC Damping Rings under the influence of intrabeam scattering", IPAC'10, Kyoto, 2010.
9. Y. Papaphilippou et al., "Lattice options for the CLIC damping rings", PAC'09, Vancouver, May 2009.
10. Y. Papaphilippou et al., "Design Optimization for the CLIC Damping Rings", IPAC2010, Kyoto, Japan, 2010.
11. Y. Renier et al. Proc. of IPAC 2011, p. 2205, San Sebastian, Spain, 2011.
12. K.P. Wooton, et al., Proc. of IPAC 2011, p. 1102, San Sebastian, Spain, 2011.
13. D. Schoerling et al, Design and System Integration of the Superconducting Wiggler Magnets for the CLIC Damping Rings, PRST-AB, 2012, (in press).
14. K. Zolotarev, et al., CLIC Note, 2009, in preparation.
15. A. Piwinski, Handbook of Accelerator Physics, World Scientific (1999) 125.
16. M. Martini, Tech. Rep. PS/84-9(A4), CERN, 1984.
17. J. Bjorken and S. Mtingwa, Part. Accel., 13 (1983) 115.
18. K. Bane, SLAC-PUB-9226, June 2002.
19. A. Vivoli and M. Martini, Proc. of IPAC 2010, p. , Kyoto, Japan, 2010.
20. M. Pivi et al, Proc. of IPAC 2012, p. 3147, New Orleans, USA, 2012.
21. M. Ehrichman et al, Proc. of IPAC 2012, p. 2970, New Orleans, USA, 2012.

22. F. Antoniou et al, Proc. of IPAC 2012, p. 1951, New Orleans, USA, 2012.
23. G. Rumolo, et al., "Electron Cloud Build Up and Instability in the CLIC Damping Rings", EPAC'08, Genova, June 2008.
24. E. Shaposhnikova, et al., "Experimental studies of carbon coatings as possible means of supressing beam induced electron multi-pacting in the CERN SPS", PAC'09, Vancouver, May 2009.
25. M. Palmer et al., "Electron Cloud at Low Emittance in CesrTA", IPAC'10, Kyoto, Japan, 2010.
26. N. Mounet and E. Metral, Proc. of IPAC 2011, p. 778, San Sebastian, Spain, 2011.
27. T. Naito et al, "Multi-bunch Beam Extraction by using Strip-line Kicker at KEK-ATF", IPAC'10, Kyoto, Japan, 2010.
28. C. Belver-Aguilar et al, IPAC 2013, 2013.
29. D. Alesini and F. Marcellini, "RF deflector design of the CLIC test facility CTF3 delay loop and beam loading effect analysis", PRSTAB12 031301, 2009.

2.12 High Frequency Studies for the CLIC Damping Rings

Eirini Koukovini-Platia, Giovanni Rumolo
CERN, CH 1211 Geneva 23, Switzerland; EPF Lausanne, Switzerland
Mail to: eirini.koukovini.platia@cern.ch

2.12.1 Introduction

Due to the unprecedented brilliance of the beams, the performance of the Compact Linear Collider (CLIC) damping rings (DR) is affected by collective effects. Single bunch instability thresholds and the associated coherent tune shifts have been evaluated with a multi-kick version of the HEADTAIL code in order to define the available transverse impedance budget. The study on the strip-line kickers and the electromagnetic material properties characterization at high frequencies will also be presented.

2.12.1.1 *HEADTAIL Simulations*

The interaction of charged particle beams with the surroundings, and therefore energy loss and transverse kick due to a particular machine element or the vacuum chamber, is expressed in terms of impedance in the frequency domain. The full ring is modeled with a total impedance made of two main components: resistive wall and one broad-band resonator. These interactions need to be known in order to estimate the thresholds of coherent instabilities which may limit the achievable beam current.

Single bunch instability thresholds and the associated coherent tune shifts have been evaluated with the HEADTAIL [1] code in the case where different impedance contributions are taken into account such as the broadband resonator in combination with the resistive wall contribution from the arc and the wigglers of the DR assuming the worst case scenario (in terms of impedance) of stainless steel (StSt) pipe coated with 2 μm of NEG. The DR parameters used for the simulations can be found in the CLIC DR twiki page [2].

2.12.1.2 *Impedance Budget for Zero Chromaticity*

The HEADTAIL code gives the evolution of the bunch centroid over several turns for different impedance values. The goal is to scan over different transverse shunt impedance values, in order to define the impedance budget by observing the transverse mode coupling instability (TMCI) threshold. By applying the Sussix algorithm [3] on the coherent bunch motion, the spectrum of the bunch modes can be obtained. The relative tune shift $(Q - Q_{x,y})/Q_s$ with respect to the zero-current tune $Q_{x,y}$ is normalized to the synchrotron tune Q_s to identify each of the azimuthal modes. The mode spectrum represents the natural coherent oscillation frequencies of the bunch. The tune shift is plotted, for the case of zero chromaticity, as a function of the transverse shunt impedance in Fig. 1 and 2.
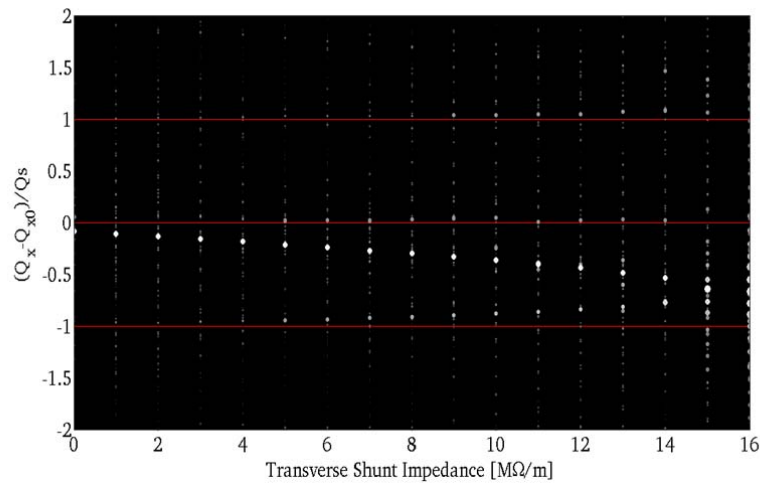
Figure 1: Mode spectrum of the horizontal coherent motion for zero chromaticity.
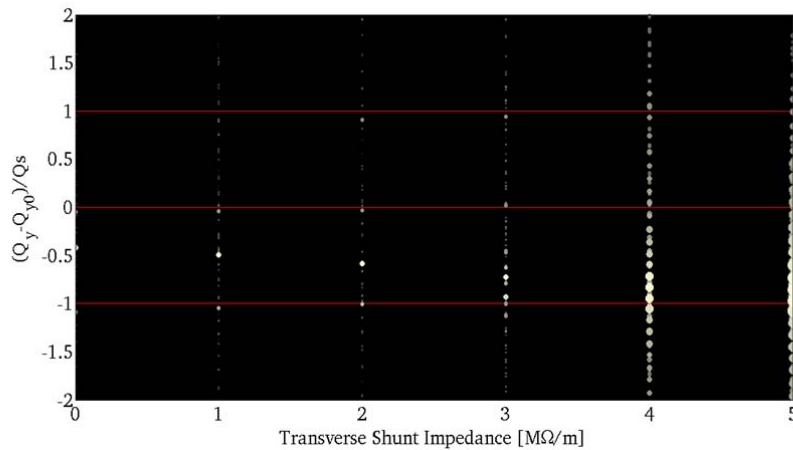
Figure 2: Mode spectrum of the vertical coherent motion for zero chromaticity.

Modes 0 and -1 are observed to move and couple for impedance values of 15 MΩ/m and 4 MΩ/m in the horizontal and vertical plane respectively, causing a TMCI. Considering the most critical plane (the vertical), the remaining impedance budget is estimated at 4 MΩ/m.

2.12.1.3 *Budget for Positive Chromaticity*

Chromaticity is believed to raise the TMCI threshold thanks to the tune spread that it causes making mode merging weaker. As expected, the presence of chromaticity causes the modes to move less and not to merge and by consequence to avoid a TMCI, but another type of instability, the head-tail instability, is occurring. In Fig. 3 and 4, it is observed that in the case of positive chromaticity, ξ_x equal to 0.055 and ξ_y equal to 0.057, higher order modes get excited whereas $m = 0$ is damped, showing that while a TMCI can be avoided, a head-tail instability develops on a single mode.
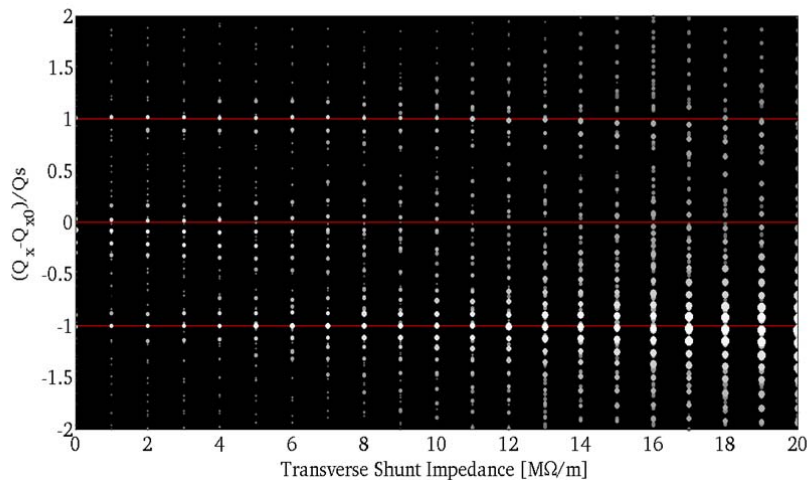
Figure 3: Mode spectrum of the horizontal coherent motion for positive chromaticity.
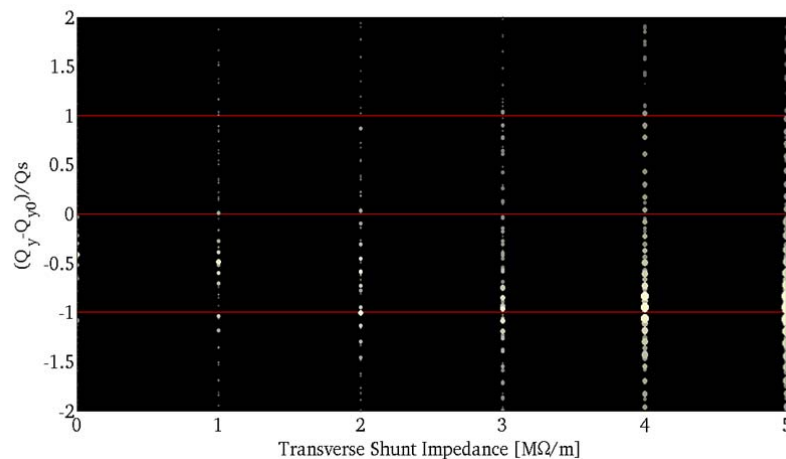
Figure 4: Mode spectrum of the vertical coherent motion for positive chromaticity.

The TMCI quickly becomes very fast above the threshold for the onset, but for the case of head-tail instability the calculation of its rise time is needed and the comparison with the damping time given by the design parameters. If the rise time is lower than the damping time, the instability is faster than the damping mechanism. The damping time of 2 ms given by the DR design parameters [2], defines an instability threshold at 1 MΩ/m in the vertical plane. Presence of some positive chromaticity should be expected in real operation of the machine, therefore the budget is considered to be 1 MΩ/m, and a

detailed impedance budget calculation should be carried out including contributions of other components of the DR to ensure safe operation.

2.12.2 Study on the Strip-line Kickers

Preliminary studies on the impact of the strip-line kickers have been carried out. In order to add their contribution to the total CLIC DR impedance budget, it is necessary to calculate the wake function required for the macroparticles simulations in HEADTAIL. For the calculation of the wake function a very short bunch excitation of 0.2 mm is needed for the 3D simulation of the kicker with the CST Microwave Studio (CST MWS) [4]. This requirement explodes the number of meshcells to around 700 billion, a number that might not be possible to simulate even with the use of a cluster. Currently, simulations are being done for a higher bunch length of 20 mm to simulate the wake potential before attempting to go at higher frequencies.

2.12.3 Characterization of NEG Conductivity at High Frequencies

Coating will be used in both electron (EDR) and positron damping rings (PDR) to suppress effects like electron cloud formation or ion instabilities. In particular, NEG coating is necessary to suppress fast beam ion instabilities in the EDR. The impedance modeling of the chambers for the instabilities studies must also include the contribution from the coating materials. This advocates for a correct characterization of this impedance in a high frequency range, which is still widely unexplored. The electrical conductivity of NEG in the frequency range of 9 - 12 GHz is determined with the waveguide method, based on a combination of experimental measurements of the complex transmission coefficient S_{21} and 3D electromagnetic (EM) simulations with CST MWS.

2.12.3.1 Waveguide Method

An X-band NEG-coated copper (Cu) and a stainless steel (StSt) waveguide of 50 cm length are the devices under study. Using a network analyzer, the transmission coefficient is measured over a frequency range from 9 - 12 GHz. The S_{21} coefficient is related to the attenuation due to the finite conductivity of the material.

Figure 5: Measurements setup: network analyzer, the transmission coefficient S_{21} of an X-band waveguide is measured.

2.12.3.2 *3D CST Simulations*

The CST MWS is used to simulate the NEG coated waveguides with the same dimensions as the real ones. With the Transient Solver of CST, the experimental setup used for the measurements can be simulated in real time domain. For each frequency from 9 - 12 GHz the output of the 3D EM simulations is the S_{21} parameter as a function of conductivity. The relative permittivity ε_r and permeability μ_r of the material are assumed to be equal to one while the conductivity σ is the unknown parameter which is scanned. For CST simulations, the coating thickness is assumed to be uniform and equal to a certain expected value or infinite to simulate the case where the skin depth is much smaller than the thickness (upper limit for the NEG conductivity). The intersection at each frequency of the measured S_{21} with the CST output obtained numerically, determines the unknown electrical conductivity as a function of frequency. Repeating this method for all the frequency range the material conductivity is obtained as a function of frequency.

2.12.3.3 *Results for NEG Conductivity*

From the intersection of measured data with CST results, the conductivity is plotted as a function of frequency. The plot displayed in Fig. 6 show an upper limit for the NEG conductivity assuming that the NEG thickness is infinite in the simulation. The case of 9 μm thickness is also plotted in the same figure.
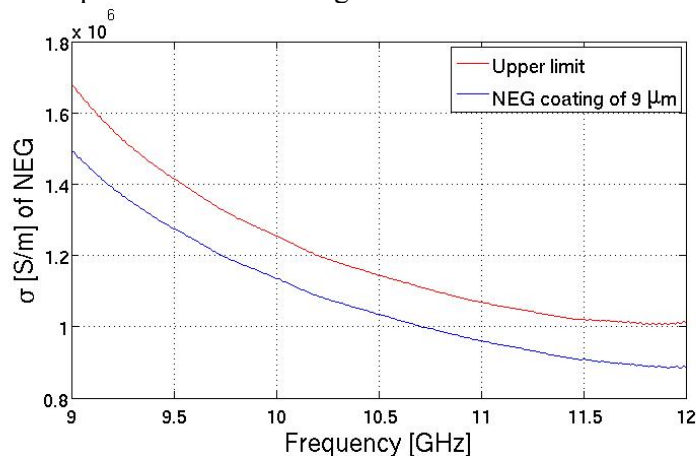
Figure 6: Conductivity of NEG as a function of frequency.

This waveguide was later cut in order to measure the NEG thickness with the X-ray fluorescence method. The x-rays revealed a non-uniform coating profile, Fig. 7, with an average value of 9 μm. This non-uniformity though is neglected in the CST simulations where uniform coating is considered, something that could introduce errors in the final results.
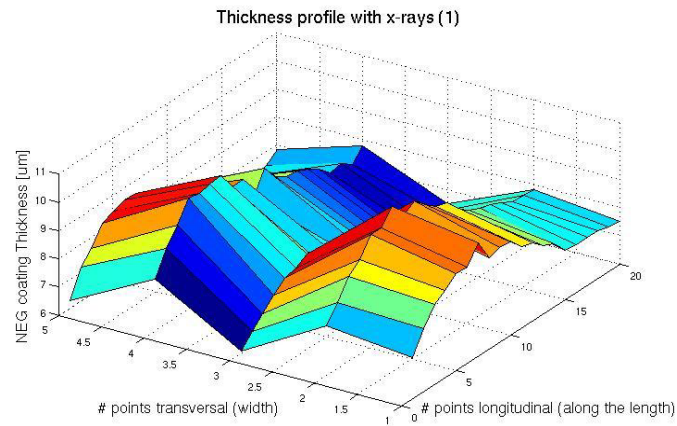
Figure 7: NEG coating profile of the Cu waveguide with x-rays fluorescence.

2.12.3.4   *Results for StSt Conductivity*

An X-band StSt waveguide was used as another benchmark of the method due to the well known DC conductivity of the material. The procedure followed was the same as described above and the results of the StSt conductivity as a function of frequency are presented in Fig. 8.
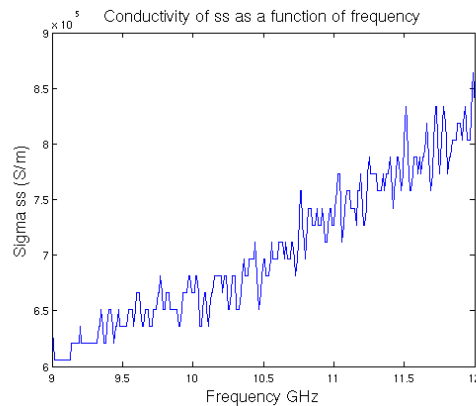
Figure 8: StSt conductivity as a function of frequency.

The average value of conductivity measured is $\sigma_{StSt} = 0.75 \; 10^6$ S/m, lower than the expected DC value of 1.3 10^6 S/m. The same procedure was repeated 3 times in different days and by re-calibrating the network analyzer to check the reproducibility of the measurements. Indeed, the results shown in Fig. 9, were almost identical each time indicating that the measurements cannot be the reason of deviation in the conductivity characterization.
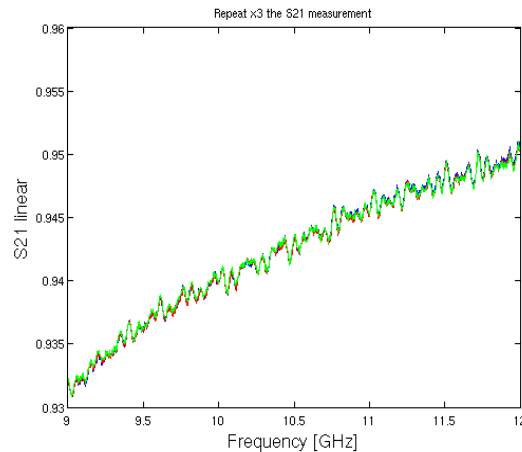
Figure 9: Different measurements of S_{21} as function of frequency.

One possible explanation could be the surface roughness that can affect the conductivity measurement but this needs further investigation.

2.12.4 Acknowledgements

I would like to thank Carlo Zannini and Giovanni De Michele for their help and contribution in the material characterization studies, Pedro Costa Pinto for the coating of the waveguides, Marina Malabaila and Anité Pérez Fontenla for the thickness profile measurements.

2.12.5 References

1. G. Rumolo, F. Zimmermann, CERN-SL-Note-2002-036 (2002).
2. CLIC DR parameters, reference page:
   https://twiki.cern.ch/twiki/bin/view/CLIC/DampingRings.
3. R. Bartolini, F. Schmidt, CERN-SL-Note-98-017-AP (1998).
4. CST Microwave Studio- Getting Started (2003).

2.13 Superconducting Wiggler Prototype for the CLIC Damping Rings

Axel Bernhard[1], Paolo Ferracin[2], Konstantin Zolotarev[3]
[1]Karlsruhe Institute of Technology (KIT), Karlsruhe, Germany
[2]CERN, CH 1211 Geneva 23, Switzerland
[3]Budker Instititute for Nuclear Physics, Novosibirsk, Russia
Mail to: axel.bernhard@kit.edu

2.13.1 Introduction

The design of the CLIC damping rings presupposes a strong radiative damping achieved by 104 meters of damping wigglers [1]. The target parameter range of these wigglers in terms of magnetic flux density amplitude and period length calls for an

advanced superconducting magnet technology. In 2011, a collaboration between the Karlsruhe Institute of Technology (KIT), the European Center for Nuclear Research (CERN) and the Budker Institute of Nuclear Physics (BINP) started to study CLIC damping wiggler prototypes under real operation conditions in the ANKA storage ring in a two-step approach. In the first step, a full-scale prototype based on state-of-the-art Nb-Ti superconducting wiggler technology is developed, manufactured and tested. The design of this wiggler prototype, regarded as baseline design for the CLIC damping wigglers, involves an advanced cooling concept suitable for the operation conditions expected in the CLIC damping rings. In parallel, fundamental research on the potentially significantly more powerful, but so far not fully developed Nb_3Sn superconducting wiggler technology is performed. In case of a success in both of these branches, the realization and test of a full-scale Nb_3Sn wiggler prototype is foreseen in the second project step.

2.13.2 **Technological Options**

In the conceptual design phase of CLIC a number of technological options for the CLIC damping wigglers was considered regarding the choice of the superconducting material, the wiggler coil geometry, the cooling concept and the properties of the (cold) beam pipe surfaces in terms of impedance and secondary electron yield. All of these points will also be addressed in the experimental program of the technical feasibility studies during the technical design phase of the CLIC project.

2.13.2.1 *Niobium-Titanium versus Niobium-Tin*

The most prominent criterion for choosing the appropriate damping wiggler technology is the achievable damping efficiency which is directly related to the magnetic performance of the wigglers in terms of period length and field amplitude. The wigglers increase the radiative power loss per turn and thereby reduce the damping time in the damping rings. The damping time as a function of the power dissipation in the wigglers scales like

$$\tau \propto \frac{1}{1 + F_W},$$

where

$$F_W = I_{2w}/I_{2a}$$

is the ratio of the second synchrotron radiation integrals over the wigglers and the arcs, respectively [2]. The integral radiated power of the wiggler radiation that is represented by I_{2w}, depends on the magnetic length of the damping wigglers L_w and their flux density amplitude $\widetilde{B_w}$ like

$$I_{2w} \propto L_w \widetilde{B_w^2},$$

i.e. for a given magnetic length of the wigglers it is favorable to maximize the flux density amplitude in order to minimize the damping time. On the other hand, the wigglers also introduce an additional source of quantum excitation and therefore make an additive contribution to the equilibrium emittance, scaling like

$$\gamma \epsilon_w \propto \widetilde{B_w^3} \lambda_w^2.$$

Consequently, while the maximization of the damping rate calls for a maximization of the damping wigglers' flux density amplitude, it is desirable to minimize at the same time the period length in order to keep the contribution of the wigglers to the equilibrium emittance low. This requirement, in the first place, motivates the employment of superconducting wigglers for the CLIC damping rings.
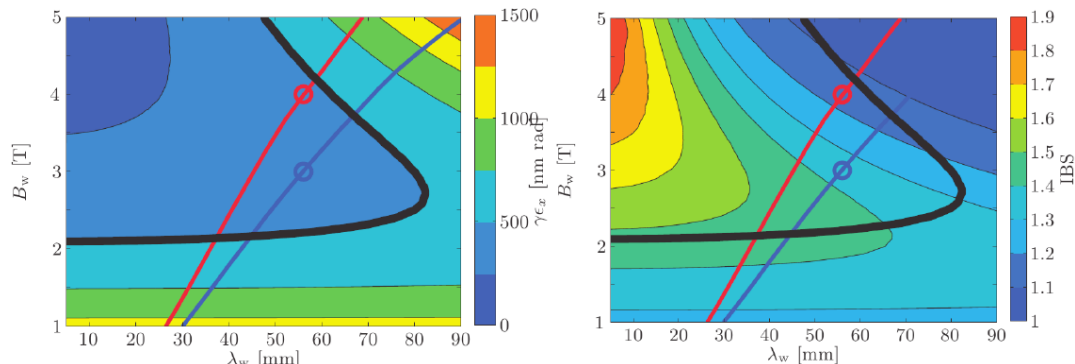
Figure 1: (a) Normalized equilibrium horizontal emittance as a function of wiggler period lenght and flux density amplitude. The solid black line indicates the target normalized emittance for the CLIC damping rings. The blue and red line indicate the maximum achievable operational flux density amplitude as a function of period length for a magnetic gap of 18 mm for Nb-Ti and Nb$_3$Sn technology, repectively. (b) Ratio of normalized emittance including intra beam scattering (IBS) and zero-current emittance, graphics from [3].

Figure 1(a) shows a contour plot of the equilibrium normalized horizontal emittance achieved with the current CLIC damping ring optics with a fixed overall magnetic length of the damping wigglers $L_w = 104m$ as a function of period length and magnetic flux density [3]. The target normalized horizontal emittance $\gamma\epsilon_x \leq 500nm\,rad$ is indicated by the thick black line. The blue and the red solid line indicate the maximum achievable operational flux density amplitude for a magnetic gap of 18 mm (the design value for the CLIC damping wigglers) as a function of period length for Nb-Ti and Nb$_3$Sn, respectively. The plot illustrates the statement on the optimal range for $\widetilde{B_w}$ and λ_w made before and shows that both technologies under consideration, Nb-Ti and Nb$_3$Sn, provide sufficient magnetic performance for reaching the target emittance.

The Niobium-Titanium superconducting wiggler technology has been developed and improved over more than 30 years [4] and has proven a reliable technique in a number of synchrotron radiation facilities all over the world. Therefore it is appropriate to regard Nb-Ti technology as the baseline technology for the CLIC damping wigglers.

Figure 1 (b), however, illustrates why the Nb$_3$Sn-option, although technically much more challenging, might still be favorable: The contour plot shows the intra beam scattering (IBS) contribution to the normalized equilibrium horizontal emittance in the CLIC damping rings $\epsilon_x/\epsilon_{x,I=0}$, again as a function of wiggler period and flux density amplitude. By employing Nb$_3$Sn wigglers an extended parameter range gets accessible, allowing for a substantial reduction of the IBS contribution to the equilibrium emittance, i.e. for reaching the target emittance under much more relaxed conditions in terms of beam dynamics.

Another potential advantage of the Nb$_3$Sn technology is the increased heat load budget as compared to Nb-Ti. In the CLIC damping rings, the cold beam pipes of the wigglers are subject to heat load mainly from synchrotron radiation emitted by the upstream wigglers (up to 40 W) and from image currents (2 W) [3]. Depending on the

efficiency of the thermal insulation between the beam pipe and the superconducting coils, a fraction of this heat load is transferred to the coils, resulting in an increase in operating temperature. For Nb-Ti the tolerable margin for this increase is in the order of 1 K (see section 2.13.4 below). Nb_3Sn, due to its by roughly a factor of two higher transition temperature, provides a larger temperature and also a larger enthalpy margin. However, there is obviously a trade-off between heat load tolerance on the one hand and magnetic performance on the other. One aim of the experimental study with the CLIC damping wiggler prototype in the ANKA storage ring will therefore be to define proper criteria for the parameter optimization for a potential Nb_3Sn damping wiggler.

The advantages of using Nb_3Sn for superconducting insertion devices were realized and discussed early in the development of superconducting short-period undulators for 3rd generation synchrotron radiation sources. The studies on short undulator prototypes at three different labs in the US [5,6,7], although in principle successful, exhibited also the particular difficulties using this material for superconducting insertion devices which may be summarized under the keyword of – mechanical, thermo-mechanical and thermo-magnetic – instabilities [8]. For full-scale superconducting insertion devices these difficulties have not been resolved so far [9]. Consequently, fundamental R&D is mandatory if one intends to exploit the potential advantages of Nb_3Sn for the CLIC damping wigglers.

2.13.2.2 *Vertical versus Horizontal Racetrack Coils*

Two established solutions for the winding geometry of superconducting insertion devices exist, schematically shown in Fig. 2. The horizontal racetrack geometry has been used for high-field superconducting multi-pole wigglers for a long time. In this scheme each single coil enveloping one iron pole is individually wound and the coils are afterwards interconnected by low resistance splices. This technique facilitates the mass production of the superconducting coils and an exchange of individual coils in case of a failure. Since the splices usually are normal conducting and therefore a heat source distributed along the magnet, the horizontal racetrack geometry on the other hand requires a splicing technique reliably providing interconnections with very low resistance. For Nb-Ti, cold welding of the Nb-Ti filaments is the state of the art, providing resistances of $10^{-10}\ldots10^{-12}\Omega$[4]. For Nb_3Sn, joints with resistances of several $n\Omega$ can be achieved by galvanic copper plating or electromagnetic pulse welding [16,17], resulting in a heat load in the order of a few tenths of a Watt per meter which can be a significant fraction of the available cooling power budget.
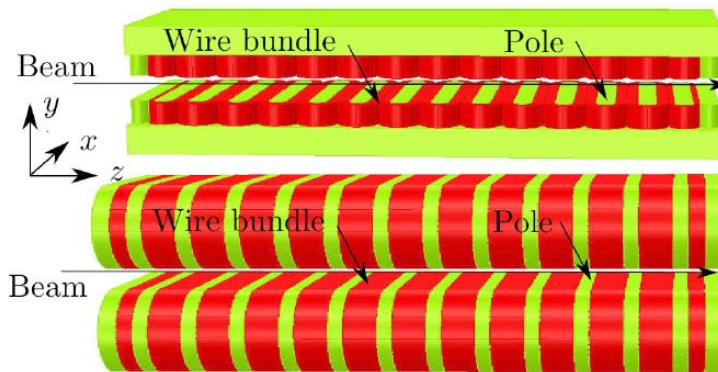
Figure 2: Possible winding geometries for a superconducting wiggler magnet, top: horizontal racetrack (HR) geometry, bottom: vertical racetrack (VR) geometry (graphics from [3])

The lowest period lengths achievable with the horizontal racetrack geometry are limited by the tensile Lorentz force acting on the wire bundles [3]. Using the vertical racetrack scheme this limitation does not exist. The racetrack arc radius can be chosen such that the forces acting on the wire bundles are compressive or zero. Superconducting undulators are usually optimized for short radiation wavelengths and thus typically laid out as short-period vertical racetrack coils. Vertical racetrack coils in most cases consist of one or a few multi-period sectors wound with a single wire. Consequently only a limited number of joints is required. On the other hand, due to the larger volume of the coil former the stored magnetic energy, which is dissipated in case of a quench, is somewhat higher in vertical racetrack than in horizontal racetrack coil assemblies.

For the CLIC damping wigglers with a target period length between 40 and 60 mm in general both winding schemes seem appropriate. The lower number of splices and the lower tensile forces acting on the wire seem to favor the vertical racetrack design for the Nb_3Sn case. However, there is no compelling indication for either of the two alternatives.

2.13.2.3 *Bath Cooling versus Conduction Cooling*

One of the most crucial questions in the conceptual design phase of the CLIC damping wigglers was that of the appropriate cooling scheme. Accordingly the test of the cooling concept of choice under real operation conditions is among the primary objectives for the experimental tests to be performed at ANKA.

The standard cooling technique for superconducting wigglers applied so far is bath-cooling. In this scheme the superconducting coil assembly as a whole is submerged in a liquid Helium bath. The beam pipe is fed through the Helium bath and shielded from the beam by a liner with high electrical conductance which is placed concentrically inside the beam pipe and thermally insulated from it by a vacuum layer (see e.g. [10]).

For the CLIC damping wigglers, a different cooling scheme based on conduction cooling will be applied. In this scheme the superconducting coil assemblies and the beam pipe are placed in vacuum. The liquid Helium is contained in heat exchangers attached to the cold mass. The heat exchangers will be cooled by continous liquid Helium flow. Indirect cooling was chosen for several reasons: (1) In a bath cryostat the gap between the superconducting coils and the beam pipe is filled with liquid Helium. A

quench of the magnet causes a steep increase of the ambient pressure by the evaporation of liquid Helium which the beam pipe has to be able to withstand. This demand is absent in an indirect cooling scheme, relaxing the mechanical requirements for the beam pipe and thereby allowing for a smaller magnetic gap and thus better magnetic performance. (2) The Helium mass required for cooling the wiggler is reduced which is obviously advantageous for operating a large number of superconducting insertion devices in one cryogenic line as intended in the CLIC damping rings. (3) The heat load on the beam pipe may be directly extracted by an independent cooling circuit either driven by gaseous Helium or, in case of a sufficient thermal insulation between the superconducting coils and the beam pipe, by liquid Nitrogen – which obviously would be beneficial particularly from the economical point of view. (4) The indirect cooling scheme enables a modular cryostat design keeping all components accessible and exchangeable and thereby facilitating maintenance and repair of the devices. An additional advantage of the modular cryostat design for the planned experiments at ANKA is that different options for the key components like the superconducting coils or the beam pipes can be tested with the same cryostat.

2.13.2.4 *Beam Vacuum Chamber Coatings*

There are two aspects regarding interaction of the particle beams in the CLIC damping rings with the (cold) beam vacuum chambers of the wigglers which require consideration and experimental research: Impedance and electron cloud mitigation. Resistive wall impedance as well as electron cloud build-up are an issue, both for the beam dynamics in the damping rings and for the heat load on the superconducting wigglers. A beam pipe made of or coated with a low-resistance material reduces the heat load due to image currents [11] and increases the intensity threshold for coherent single bunch instabilities [12], which makes e.g. OFHC copper a good choice for the electron damping ring.

For the positron damping ring, however, ECLOUD simulations show that electron cloud mitigation becomes a crucial requirement [3]. The mitigation of electron cloud build-up can be achieved by coating the beam pipe surface with materials exhibiting a low secondary electron yield like e.g. with non-evaporated getter (NEG) or amorphous carbon (aC),. Such a coating on the other hand increases the resistive wall impedance of the wiggler beam pipes. Simulations with the HEADTAIL code so far indicate that in case of the CLIC damping rings this increase is tolerable in terms of beam stability [12]. Nonetheless experimental data for different vacuum chamber coatings and shapes under realistic operation conditions are highly desirable.

2.13.3 Feasibility Study: Objectives of the Two-Step Test Program

Most of the objectives of the experimental program on the CLIC damping wiggler prototypes at ANKA arise directly from the above discussion of technological options:
- long-term reliability test of the indirect cooling scheme under normal operation conditions in the ANKA storage ring, including the long-term reliability of the magnet and particularly its quench detection and magnet protection system
- test of the cooling scheme under special conditions simulating the heat load expected in the CLIC damping rings
- validation of the magnetic field quality of the wiggler in terms of integrated higher order multipole components and their impact on beam dynamics

- system test of a full-scale Nb_3Sn wiggler prototype
- investigation of beam vacuum chamber shapes and coatings and their impact on beam dynamics and heat load to the wigglers

Above that, dedicated experiments on beam dynamics under special conditions are desired which allow to draw conclusions on the beam dynamics in the CLIC damping rings, e.g. experiments in an operational regime of the storage ring where significant collective effects are present.

Of course, the experimental program has to account for the fact that ANKA is a user facility in the way that it must not disturb or, in the best case, should benefit the ANKA user operation. Therefore, the program was split into two successive steps with the aim of minimizing the technological risk and at the same time maximizing the experimental outcome and the benefit for the ANKA users.

In the first step, a baseline damping wiggler prototype based on Nb-Ti magnet technology and employing an indirect cooling scheme is built and tested in the ANKA storage ring. This device will be equipped with an uncoated copper beam pipe. Regarding the magnetic parameters this prototype turns out to be well suited to serve as a light source for the ANKA IMAGE beamline. The design of the wiggler was specified in a joint effort of CERN and KIT and elaborated and implemented by BINP. The experimental program at ANKA will be prepared by KIT and carried out jointly by the three parties involved.

Parallel to the fabrication and test of this prototype the Nb_3Sn wiggler technology is further advanced through design, fabrication and bath-test of short prototype wiggler magnets. This R&D program is conducted at CERN.

If both the test of the indirectly cooled Nb-Ti prototype in ANKA and the development of one or more short Nb_3Sn prototypes are successful, in the second step a second cryostat and one or more full-scale Nb_3Sn wiggler coils will be built. The availability of two identical, modularly designed cryostats will then allow for a relatively quick exchange of devices and thereby for a successive test of different magnet coils and beam pipes without interfering with the ANKA user operation schedule. Thus, in the success-related second step of the experimental program it is foreseen to carry out the beam test of a full-scale Nb_3Sn wiggler and to evaluate the impact of different vacuum chamber coatings on heat load and beam dynamics.

2.13.4 Technical Design and Status of the Nb-Ti Damping Wiggler Prototype

2.13.4.1 *Magnetic Layout*

The primary objective of building and testing the first damping wiggler prototype is to validate the non-standard cooling scheme under operation conditions resembling those to be expected for the CLIC damping rings as far as possible. Accordingly the *magnetic* design of the prototype complies with the current state of the art. Table 1 lists the basic parameters of the magnet.

Table 1: Magnetic design parameters of the Nb-Ti CLIC damping wiggler prototype

Basic parameters	
Wiggler period λ_w	$51mm$
Magnetic gap	$18mm$
Flux density amplitude on axis $\widetilde{B_y}$	$3T$
I/I_c on load line @ $T = 4.2K$	86%
T_{quench}@$\widetilde{B_y} = 3T$	$4.8K$
Number of main poles	68
Winding scheme	
1/4 coil, $N_1 I_1$	$62 \times 487A$
3/4 coil, $N_2 I_2$	$124 \times 487A$
Main, inner, $N_1 I_1$	$62 \times 487A$
Main, outer, $N_1(I_1 + I_2)$	$62 \times 974A$
Wire parameters	
Diameter (bare)	$0.85mm$
Nb-Ti:Cu ratio	1.1:1
Filaments	312
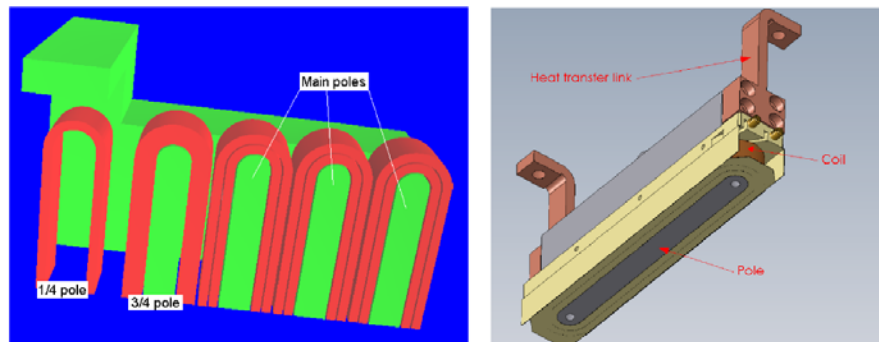
Figure 3: Octant of a short wiggler model (left), main poles with two coil sections each and 3/4-1/4 matching poles; 3D model of a single coil with extended iron core and heat transfer links (right), graphics from [13]

The coils are laid out as horizontal racetrack coils. A partial schematic view of the coil assembly is shown in Figure 3 (left). The main coils consist of two sections, an inner section close to the iron poles and therefore subject to a high external magnetic flux density and an outer section subject to a low external magnetic flux density. The outer coil sections can be operated at about a twice as high current as the inner sections, as can be concluded from the load lines shown in Figure 4. By this arrangement the number of Ampère-turns per pole and thereby the magnetic flux density amplitude on axis is maximized.
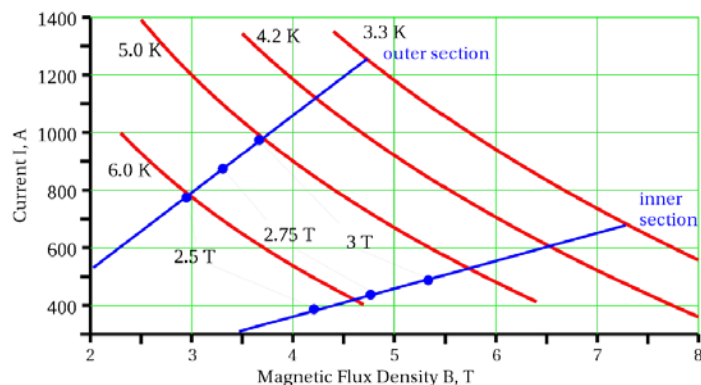
Figure 4: Load lines of the inner and outer coil sections (blue) and critical current as a function of magnetic flux density and temperature (red)

The right-hand part of Figure 3 shows a 3D-model of a single coil. The iron cores of the coils are extended on the back side and connected via copper links to a heat exchanger plate extended over the whole coil array. In this way the indirect cooling of the coils is effected.

The field configuration of the wiggler is anti-symmetric with a 1/4-3/4 termination providing zero field integrals in first approximation. A detailed compensation of the field integrals is achieved by powering subsets of the coils/coil sections by individual power supplies (see middle part of Table 2).

2.13.4.2 *Cryogenic Design*

A likely scenario for cooling the wiggler magnets in the CLIC damping rings is a forced-flow liquid Helium circuit supplying all wigglers in a line, connected to a central cryoplant. A similar circuit for gaseous Helium or potentially liquid Nitrogen could be employed for cooling the beam vacuum chambers. Since such an arrangement is not appropriate for cooling a single device in the ANKA storage ring, the damping wiggler prototype to be installed in ANKA will instead be equipped with an internal liquid Helium reservoir and two cryocoolers (Sumitomo SRDK-415D) recondensing the evaporated Helium. Since the equilibrium vapor pressure in the Helium reservoir is reduced due to the slightly overdimensioned cooling power of the reconsder, the equilibrium temperature of the liquid Helium is expected to be slightly below 4*K* The first stages of the recondenser cryocoolers will be used to cool the HTSC current leads. The continous flow of liquid Helium through the heat exchanger on the back side of the magnet assembly is effected through a thermosiphon arrangement adopted from a very similar design for the APS superconducting undulator [14].

For cooling the beam pipe and two radiation shields (20 and 60 K) two further cryocoolers (Sumitomo SRDK-408S2) will be used. Figure 5 shows a cross section of the cryostat.
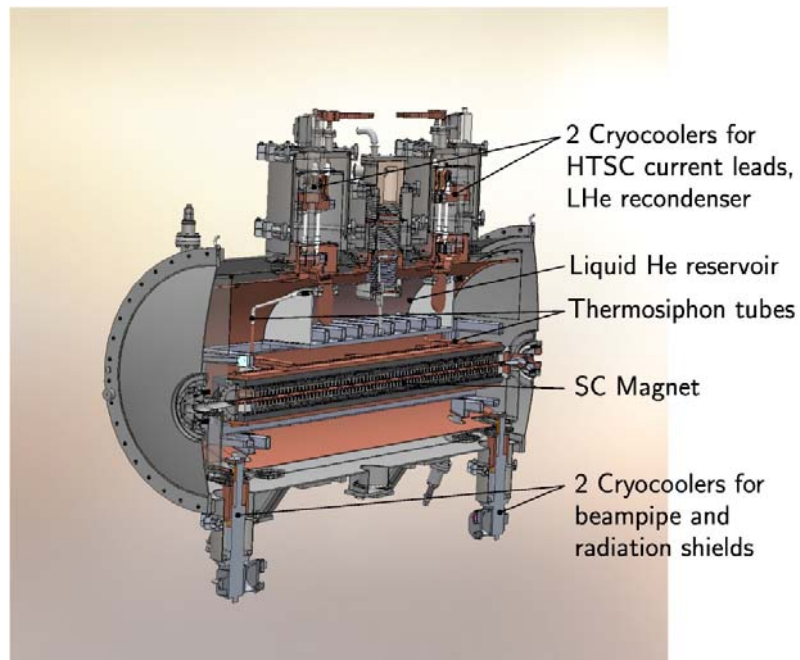
Figure 5: Cross section of the CLIC damping wiggler prototype (graphics from [13])

Under regular operation conditions at ANKA, the heat input to the beam pipe will not exceed $4W$. Under these conditions the beam pipe temperature will be $10K$. In the CLIC damping rings the situation will be largely different. 26 wigglers will be placed in a row in the straights of the damping rings, each wiggler emitting about $14kW$ of synchrotron radiation. Most heat load will be taken by vertical and horizontal absorbers placed between the wigglers and a radiation dump in forward direction. However, the wigglers placed behind the horizontal absorbers still receive an integrated heat load of about $40W$ from the respective nearest upstream wiggler. This load is mainly deposited on the top and bottom surfaces at the downstream end of the beam pipe. In the CLIC damping wiggler prototype, heaters will be placed in this region in order to simulate the heat load distribution expected for the operation in the CLIC damping rings.

For operating the superconducting wigglers under these conditions it is crucial that the heat is efficiently extracted from the beam pipe and that coils and beam pipe are effectively thermally decoupled. This thermal decoupling in the first place is achieved by the vacuum insulation. The remaining dominant and inevitable heat leak is the support of the beam pipe which is attached to the cold mass. The design of this support minimizes the heat transfer through minimized contact surfaces and minimized heat conductivities of the employed materials. The heat transport from the beam pipe to the coils has been estimated by finite element calculations under conservative assumptions. According to these calculations the expected temperature gradient over the cold mass does not exceed 0.12 K. This value is, as will be discussed in the next section, within the tolerable range.

2.13.4.3 *Short Model Test*

The magnetic performance and particularly the indirect cooling scheme were tested using a ten-pole short model magnet. The model assembly including two arrays of ten

coils thermally linked to the heat exchanger plates, gap spacers and soft magnetic housing was fully representative for the full-scale magnet. No liquid Helium was applied but a cryocooler with 1 W cooling capacity at 4.2 K was directly attached to one of the heat exchanger plates, while the other was cooled by conduction through copper links connecting the two heat exchanger plates. Photographs of the coil assembly and of the complete test set-up prepared for the installation in a test vacuum recipient are shown in Figure 6.

Figure 6: Short model coil assembly (left) and experimental set-up for the quench and cooling performance tests (right), photographs from [13]

During the test the current in the coils was ramped up to a quench several times with different ramp rates. A full quench training of the coils, however, was not performed. In Table 2 an excerpt of the quench history is given.

Table 2: Quench history of the short model (excerpt)

Quench no.	$I_1[A]$	$I_2[A]$	$\widetilde{B_y}[T]$	$T_{max}[K]$
1	550	547	3.31	3.70
5	484	484	3.00	4.83
6	387	387	2.50	5.75
7	436	436	2.75	5.33

In steady state operation, the temperatures measured at the pole faces did not exceed 3.8 K, the temperature difference between the two halves of the magnet was lower than 0.1 K. The quench currents achieved at the $T \sim 3.8K$ temperature level were about 90% of the theoretical critical current on the load line, corresponding an on-axis flux density amplitude of 3.3 T.

The quenches 5-7 were triggered by increasing the temperature at fixed current corresponding on-axis flux density amplitudes of 3, 2.5 and 2.75 T, respectively. At the

target magnetic flux density of 3 T the magnet is operable at temperatures up to 4.8 K. The full-scale wiggler cold mass with no beam-induced heat load is expected to reach the same temperature level as the short model, i.e. $T \sim 3.8K$. The acceptable margin for temperature differences over the coils due to beam-related heat input is therefore about 1 K which is well above the estimated value. The short model test therefore provided confidence that the cooling scheme for the full-scale wiggler prototype is feasible.

2.13.5 Research on Nb_3Sn

Prior to winding the first short Nb_3Sn wiggler prototype detailed investigations on the manufacturing methods involved were carried out [15], addressing strand and ground insulation, winding and potting techniques and implications of the heat treatment necessary for reacting the precursor material to Nb_3Sn. Based on the results of these studies both a vertical racetrack and a horizontal racetrack Nb_3Sn trial coil were built.

Considering in particular the horizontal racetrack design, but also vertical racetrack coils built up from short modules, the availability of a reliable splicing technique is crucial. Therefore also splicing methods for Nb_3Sn strands were studied [16,17]. It was found that it is possible to achieve stable interconnections with resistances of $4n\Omega < R_{splice} < 10n\Omega$ by using a galvanic copper plating or an electromagnetic pulse welding technique. The latter has the advantage of being more easily applicable to a large number of splices.

The two trial coils mentioned above were quench-tested in liquid Helium. Both coils reached quench currents corresponding the short sample values.

Subsequently, a two-period short model magnet with 40 mm period length and vertical racetrack geometry was built according to the manufacturing process used for the trial coil, and tested in liquid Helium [18]. In these tests the thermo-magnetic instabilities (i.e. flux jumps) appearing particularly at low ambient magnetic fields and getting increasingly likely with increasing strand length turned out to be a major challenge for the quench detection system as well as for the power supply controller and thereby for the stable and safe operation of the magnet. Within four quenches the magnet reached about 75% of the short sample limit.

At the fourth quench an insulation failure occurred, rendering the magnet inoperable. In order to localize the points of failure, the short model was analyzed post mortem at room temperature. From this analysis it was concluded that the insulation between the wire bundles and the iron former as well as that of the single wire in the turnaround loops should be improved. The analysis of a vertical racetrack coil built according to a revised design showed that such an improvement can be achieved by inserting a fibreglass insulation layer.

Notwithstanding the need for improvements, the basic feasibility of Nb_3Sn wiggler magnets was shown by the short model test. A second vertical racetrack short model, with the same two-period configuration as the first one, is currently under development at CERN. The new design will include modifications to the parts to accommodate a more robust insulation scheme and an improved set-up of the splice region. The complete engineering design and fabrication of the model is expected in 2014, followed by a test to verify its performance at cryogenic temperature. It is expected that the test results will provide fundamental information which will help defining the next steps, in particular regarding the possibility of developing a longer prototype and of exploring the horizontal design option.

2.13.6 Conclusions

To study the technical feasibility of the CLIC damping wigglers as well as possible effects of the real devices on the beam dynamics in the CLIC damping rings, full-scale wiggler prototypes are developed, built and tested in the ANKA storage ring in a two step approach. In the first step, a Nb-Ti wiggler magnet meeting the magnetic requirements of the CLIC damping rings, is built and tested, while in parallel a reliable and scalable design for Nb_3Sn wigglers is developed.

The Nb-Ti damping wiggler prototype involves a cooling technique not applied so far to wiggler magnets, based on conduction cooling using heat exchangers cooled by liquid Helium in a thermosiphon flow arrangement. The test of a conduction cooled short model magnet combined with finite element simulations of the heat transport from the beam pipe to the cold mass provided confidence that heat extraction and thermal insulation will be sufficient for operating the wiggler even under the high radiative heat input to the beam pipe expected for the CLIC damping rings.

The Nb-Ti wiggler is currently being manufactured at BINP and is foreseen to be installed in the ANKA storage ring in summer 2014. Above a long-term reliability test, dedicated experiments on heat load tolerance and on beam dynamics will be carried out with this insertion device.

The application of Nb_3Sn superconductor technology is expected to significantly extend the accessible region of magnetic performance parameters for the damping wigglers which in particular would allow for operating the CLIC damping rings under relaxed conditions in terms of collective effects. This advantage, however, comes at the cost of a much more challenging magnet design and manufacturing process. The basic feasibility of Nb_3Sn wiggler magnets with the desired magnetic design parameters has been proven in a short model test. A robust Nb_3Sn wiggler design suitable for series production and reliable operation of roughly 100 devices in the CLIC damping rings is still a matter of research. To build and to test a full-scale Nb_3Sn wiggler in the ANKA storage ring, which is the aim of the second step of the CLIC damping wiggler feasibility study, would be a major achievement in the development of superconducting insertion devices.

2.13.7 References

1. Y. Papaphilippou et al., "Conceptual design of the CLIC damping rings", Proceedings of the IPAC 2012, TUPPC086 (2012)
2. P. Emma and T. Raubenhemier, "Systematic approach to damping ring design", Phys.Rev.STAB **4**, 021001 (2001)
3. D. Schoerling et al., "Design and system integration of the superconducting wiggler magnets for the Compact Linear Collider damping rings", Phys.Rev.STAB **15**, 042401 (2012)
4. see e.g. N. Mezentsev and E. Wallén, "Superconducting Wigglers", Synchrotron Radiation News **24**, 3 (2011) and references therein
5. S.H. Kim et al., "Development of short-period Nb_3Sn superconducting undulators for the APS", IEEE Trans.Appl.Supercond. **18**, 431 (2008)
6. D. Dietderich et al., "Fabrication of a short-period Nb_3Sn superconducting undulator", IEEE Trans.Appl.Supercond. **17**, 1243 (2007)
7. H.W. Weijers et al. "A short-period high-field Nb_3Sn undulator study", IEEE Trans.Appl.Supercond. **16**, 311 (2006)
8. P. Lee, Ed., "Engineering Superconductivity", Wiley-Interscience, New York, 2001

9. Yu. Ivanyushenkov and Elizabeth Moog, "Development of Superconducting Undulators at the Advanced Photon Source", Synchrotron Radiation News **24**, 20 (2011)

10. E. Bekhtenev et al., "The main test results of the 3.5 Tesla 49-pole superconducting wiggler for DLS", Proceedings of RuPAC 2006, 404 (2006)

11. B. Poldobedov, "Resistive wall wakefields in the extreme anomalous skin effect regime", Phys.Rev.Stab **12**, 044401 (2009)

12. E. Koukovini-Platia et al., "Impedance Effects in the CLIC Damping Rings", Proceedings of IPAC2011, TUPC050 (2011)

13. N. Mezentsev et al., "Final Design Report on Superconducting CLIC Damping Wiggler Test Device", Technical Report, Budker Institute of Nuclear Physics, Novosibirsk, 2012

14. J. Fuerst et al., "", AIP Conference Proceedings **1434**, 901 (2012)

15. D. Schoerling, "Superconducting Wiggler Magnets for Beam-Emittance Damping Rings", Dissertation, Technische Universität Bergakademie Freiberg, 2011

16. C. Scheuerlein et al., "Electrical interconnection of superconducting strands by electrolytic Cu deposition", IEEE Trans.Appl.Supercond. **21**, 1791 (2011)

17. D. Schoerling et al., "Electrical resistance of Nb_3Sn/Cu splices produced by electromagnetic pulse technology and soft soldering", Supercond.Sci.Technol. **25**, 025006 (2011)

18. D. Schoerling et al., "First magnetic test of a superconducting Nb_3Sn wiggler magnet for CLIC", Proceedings of IPAC2012, TUPPR061 (2012)

2.14 Stripline Kicker Design for Beam Extraction from the CLIC Damping Rings

C. Belver-Aguilar, A. Faus-Golfe, Instituto de Física Corpuscular, Valencia

F. Toral, Centro de Investigaciones Energéticas, Medioambientales y Tecnológicas

M.J. Barnes, CERN, CH 1211 Geneva 23, Switzerland

Mail to: cbelver@ific.uv.es, afaus@ific.uv.es

2.14.1 Introduction

The injection and extraction systems of the CLIC PDRs and DRs consist of a FODO cell with kicker and septum magnets in the drift spaces to deflect the beam. The injection and extraction kickers are located at symmetric locations, after the dispersion suppressor and upstream of the super-conducting wigglers, to avoid damage from synchrotron radiation [1]. The main kicker parameters are shown in Table 1.

Table 1: Kicker specifications for the PDRs and DRs for electrons [2].

Kicker parameters	Symbol	PDRs 1/2 GHz	DRs 1/2 GHz
Deflection angle (mrad)	α	2.0	1.5
Aperture (mm)	a	40	20
Effective length (m)	L	3.4	1.7
Field rise and fall time (ns)		428/1000	560/1000
Pulse flat top (ns)		900/160	900/160
Flat top reproducibility		$\pm 1 \times 10^{-4}$	$\pm 1 \times 10^{-4}$
Injection stability		$\pm 2 \times 10^{-2}$	$\pm 2 \times 10^{-3}$
Extraction stability		$\pm 2 \times 10^{-3}$	$\pm 2 \times 10^{-4}$
Injection uniformity (%)		$\pm$ 0.1[a]	$\pm$ 0.1[a]
Extraction uniformity (%)		0.1[a]	0.01[b]
Repetition rate (Hz)	f_{rep}	50	50
Vacuum (mbar)		10^{-10}	10^{-10}
Stripline voltage (kV)	V_k	$\pm$ 17.0	12.5
Stripline current (A)	I_k	340	250
Longitudinal beam impedance (Ω/n) [3]	$Z_{\parallel}$	0.05	0.05
Transverse beam impedance (kΩ) [3]	$Z_{\perp}$	200	200

[a]over 3.5 mm radius
[b]over 1 mm radius

2.14.2 Stripline Kicker Operation

A stripline-type kicker has been proposed for the extraction kicker of the CLIC DRs. It consists of two parallel electrodes housed in a conducting cylinder: each of the electrodes is driven by an equal but opposite polarity pulse. A 3D model of the stripline kicker prototype is shown in Fig. 1.
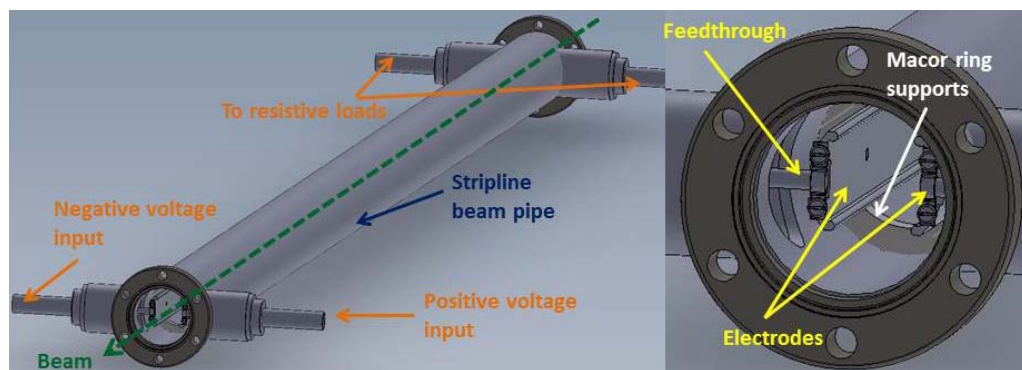
Figure 1: 3D model of a stripline kicker.

The stripline kicker operates as two coupled transmission lines with two operating modes: odd and even mode. When the electrodes are excited with equal magnitude but opposite polarity voltages, the current flow is in opposite directions in each stripline

electrode and an electromagnetic field is created between the electrodes, giving a transverse kick to the beam: this is the odd mode. When unkicked circulating beam passes through the aperture of the striplines, it induces image currents in the electrodes: the direction of current flow is the same in both electrodes - this is the even mode. The induced current generates an electromagnetic field, which gives a longitudinal kick to the beam and can produce beam instabilities.

2.14.3 Design of the Stripline Geometry

2.14.3.1 *Characteristic Impedance and Field Homogeneity Optimization*

The electrode cross section was selected by studying several shapes for the striplines and optimizing each shape to achieve 50 Ω even mode characteristic impedance, in order to minimize impedance mismatches seen by the beam, and ±0.01% field inhomogeneity over a circle of 1 mm radius at the centre of the aperture. The odd mode impedance of each optimized shape was also calculated. Ensuring that the odd mode characteristic impedance of each electrode is close to 50 Ω will avoid large mismatches to the characteristic impedance of feedthroughs, coaxial cables and the inductive adder.

The most common electrode shapes for striplines, used in injection/extraction kickers, are flat and curved electrodes [4-6]. Flat electrodes show good field homogeneity, whereas curved electrodes may allow for a better impedance matching between the two operation modes, but with poorer field homogeneity. Hence a new geometry was proposed: the half-moon electrode. This new electrode shape allows for both features, i.e. good field homogeneity and suitable impedance matching. The geometric parameters used to optimize the shape of the electrodes are shown in Fig. 2.
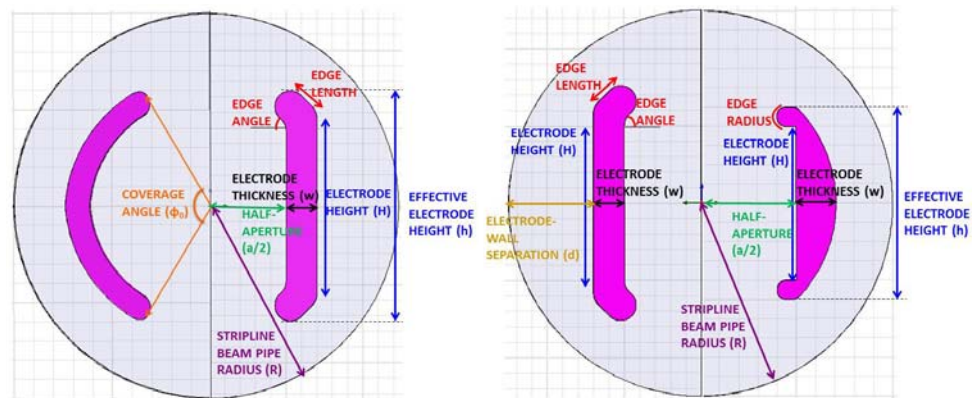
Figure 2: Schematic of the geometric parameters, for a curved and a flat electrode (left), and t for a flat and a half-moon electrode (right).

Only with flat electrodes and half-moon electrodes it is possible to achieve the required field homogeneity. For flat electrodes with 50 Ω even mode characteristic impedance, an odd mode characteristic impedance of 36.8 Ω was achieved with a stripline beam pipe radius of 25 mm. For the half-moon electrodes the odd mode characteristic impedance is 40.9 Ω. The higher odd mode impedance for the half-moon electrodes is due to the fact that the distance between the electrode and the stripline beam pipe, optimized for field homogeneity, is smaller than for the flat electrodes,

which leads to a closer values for the odd mode and even mode characteristic impedances. Therefore, flat and half-moon electrodes have been studied further and, in the following sections, the features of both electrode shapes are compared, which allows the final geometric design of the striplines to be chosen.

2.14.3.2 *Power Transmission through the Striplines*

The coaxial feedthroughs have 50 Ω characteristic impedance outside of the beam pipe, however, the characteristic impedance of the connection to the electrode is not 50Ω. Furthermore, during the kicker operation, the electrode (odd mode) characteristic impedance is lower than 50 Ω. These impedance mismatches will result in power being reflected. HFSS has been used to study the S_{11} parameter, and the results are shown in Fig. 3.
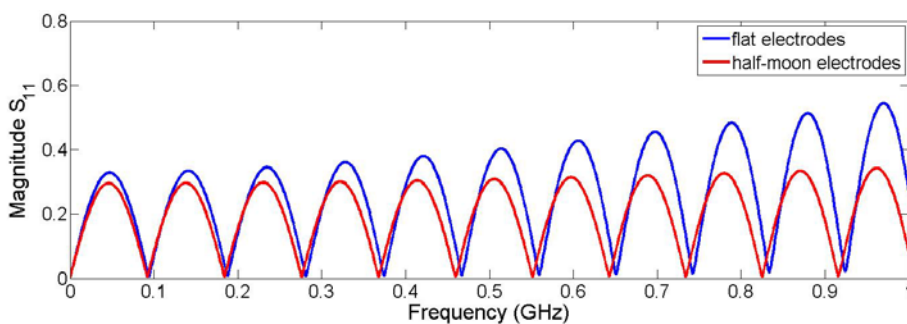
Figure 3: S_{11} for flat electrodes (blue) and half-moon electrodes (red), for a frequency range from DC to 1 GHz.

The peaks of S_{11} increase with frequency, with more impact for the flat electrode. The shape of the curves depends on the coaxial feedthrough to electrode transition, and the frequency difference between peaks is related to the electrode length as $\Delta f = \frac{c}{2L} \approx$ 90 MHz. The half-moon electrode has a reflection magnitude below 0.35 over the whole frequency range analyzed (up to 1 GHz), whereas the flat electrode shape has a reflection parameter consistently below 0.35 only up to approximately 350 MHz.

2.14.3.3 *Settling Time*

Impedance mismatches create reflections and thus ripple of the driving pulse. The time for the ripple to reduce within specification (± 0.02 %) is called the settling time: settling time is measured from the end of the rise time. An inductive adder will be used to power each stripline electrode [7]. From the inductive adder point of view, settling time should be as low as possible; settling time increases the required pulse width, thus increasing power dissipation and cross-sectional area of magnetic material. Hence the aim is to limit settling time (T_s) such that is no more than 100 ns.

Figure 4 shows the predicted settling time versus odd mode characteristic impedance of the electrodes, for different 0% to 100% rise times of the output pulse of the inductive adder. For flat electrodes, an odd mode characteristic impedance of 36.8 Ω results in a settling time of 113 ns for a rise-time of the output pulse, from the inductive adder, of 100 ns. For the same rise-time, a settling time of 78 ns will result when the odd mode characteristic impedance is 40.9 Ω, which is the case for the half-moon electrodes.

Therefore, half-moon electrodes allow for a reduced settling time, which is beneficial for the design of the inductive adder.
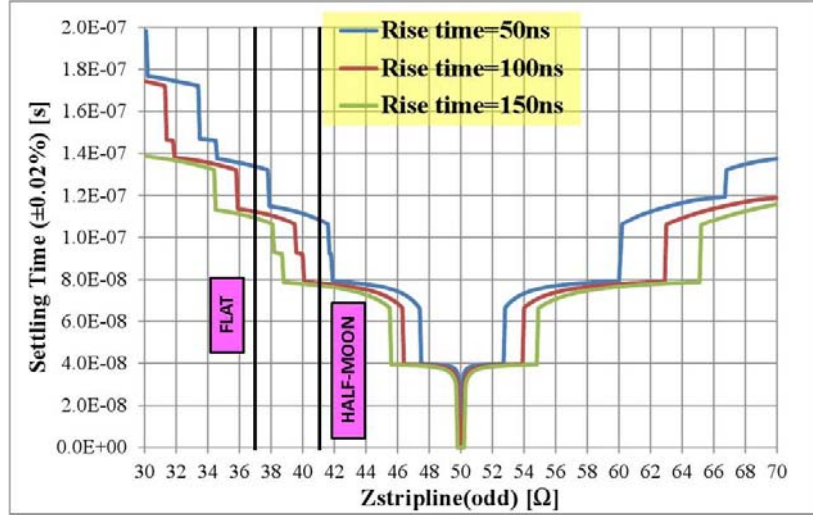
Figure 4: Settling time of the stripline voltage pulse as a function of stripline impedance for different 0% to 100% rise times of the output pulse of the inductive adder. The inductive adder, transmission line and terminating resistor impedances are 50 Ω.

2.14.3.4 *Beam Coupling Impedance*

The permissible beam coupling impedances, per kicker system, are assumed to be 5% of the longitudinal impedance allowance, i.e. 0.05 Ω/n, and 2% of the transverse impedance allowance, i.e. 200 kΩ/m [3].

At low frequencies, analytical equations for the longitudinal and transverse coupling impedance, Z_L and $Z_\perp$, respectively, for untapered stripline beam position monitors, are shown in [8]:

$$Z_{\square} = 2Z_{even} \left(\frac{\phi_0}{2\pi} \right)^2 \left[2\sin^2\left(\frac{\omega L}{c} \right) - i\sin\left(\frac{2\omega L}{c} \right) \right] \qquad (1)$$

$$Z_\perp = \left[\frac{Z_{\square}}{\omega} \right]_{pair} \left[\frac{c}{R^2} \right] \left[\frac{4}{\phi_0} \right]^2 \left[\sin^2\left(\frac{\phi_0}{2} \right) \right] \qquad (2)$$

where ϕ_0 is the coverage angle of a single electrode, ω is the angular frequency, L the striplines length and R the stripline beam-pipe radius. For the proposed striplines of approximately 1.7 m length, the even mode characteristic impedance (Z_{even}) is 50 Ω and the coverage angle ϕ_0, for each stripline, is 2.0 and 1.8 radians, for a flat electrode and a half-moon electrode, respectively.

By using the code CST Particle Studio (PS), the beam coupling impedance has been studied and compared with the analytical equtions. Results for untapered striplines are shown in Fig. 5 and Fig. 6, for longitudinal and transverse beam coupling impedance, respectively. The results show good agreement between analytical calculations and predictions from simulations. The magnitude of the low frequency peak for the longitudinal beam coupling impedance is lower in the case of half-moon electrodes. The reason for this can be understood from Eq. 1: longitudinal beam coupling impedance is

proportional to the square of the coverage angle. Transverse beam coupling impedance is initially lower in the case of flat electrodes, since the stripline beam pipe radius is larger in this case (Eq. 2).
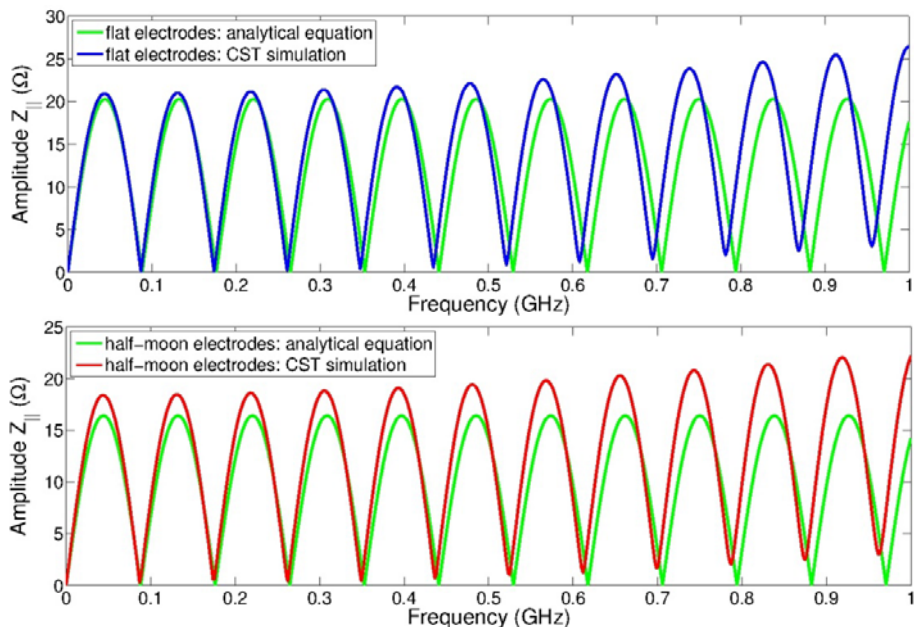
Figure 5: Longitudinal beam coupling impedance results for untapered striplines from both Eq.1 (green) and CST PS simulations for flat electrodes (blue) and half-moon electrodes (red).
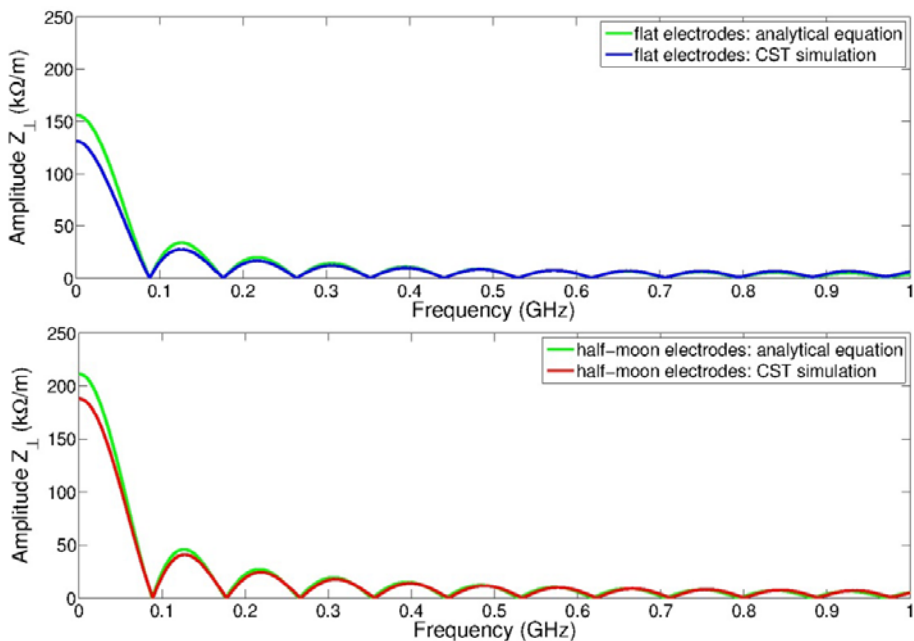
Figure 6: Transverse beam coupling impedance results for untapered striplines from both Eq. 2 (green) and CST PS simulations for flat electrodes (blue) and half-moon electrodes (red).

2.14.3.5 *Discussion and Choices of the Stripline Geometry*

Studies of the cross-section of the striplines for the extraction kicker of the CLIC DRs have shown that for a 50 Ω even mode characteristic impedance of the striplines and the field homogeneity required, the half-moon electrode shape results in an odd mode characteristic impedance closer to 50 Ω than the flat electrodes. Furthermore, the reflection coefficient predicted looking into the input port, with 50 Ω on each output port, shows that the transmission is slightly better in the case of half-moon electrodes (Fig. 3), hence the settling time (Fig. 4) is reduced. Finally, simulations of beam coupling impedance show that the longitudinal beam coupling impedance is lower for the half-moon electrode (Fig. 5), whereas the flat electrode shape is better from the transverse beam coupling impedance point of view (Fig. 6).

Overall, the half-moon electrodes are considered as the best choice for the cross-section of the striplines for the extraction kicker of the CLIC DRs.

2.14.4 **Stripline Kicker Components**

2.14.4.1 *Study and Optimization of the Electrode Supports*

The electrodes have a total length of 1.639 m and, ideally, must be perfectly aligned along their entire length. In order to ensure the alignment, the electrodes are fixed outside the aperture by using four equally-spaced Macor rings, of 10 mm length each. Once the electrodes are aligned and fixed to the Macor rings, this assembly will be placed inside the stainless steel tube.
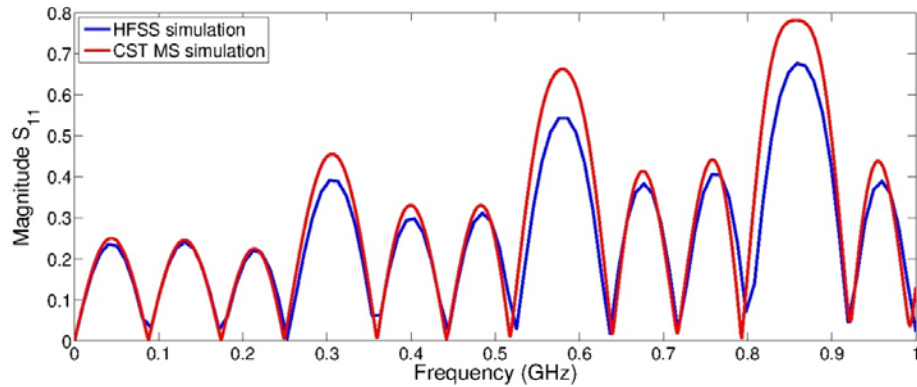
Figure 7: Magnitude of S_{11} predicted by HFSS and CST Microwave Studio (MS), for striplines with four equally-spaced Macor ring supports, and ideal 50 Ω feedthroughs.

Figure 7 shows that the Macor rings increase the magnitude of the reflection parameter S11, starting from 300 MHz, of every third peak. The separation between these maxima corresponds to the distance, there and back, between the equally-spaced Macor rings (510 mm). However, the frequency content of the driving pulse from the inductive adder will only extend up to approximately $f = 0.35/T_r \approx 7$ MHz, where the pulse rise time considered is $T_r = 50$ ns. Thus, since the Macor rings mainly affect the S11 above 300 MHz, they are not expected to significantly influence the ripple of the driving pulse.
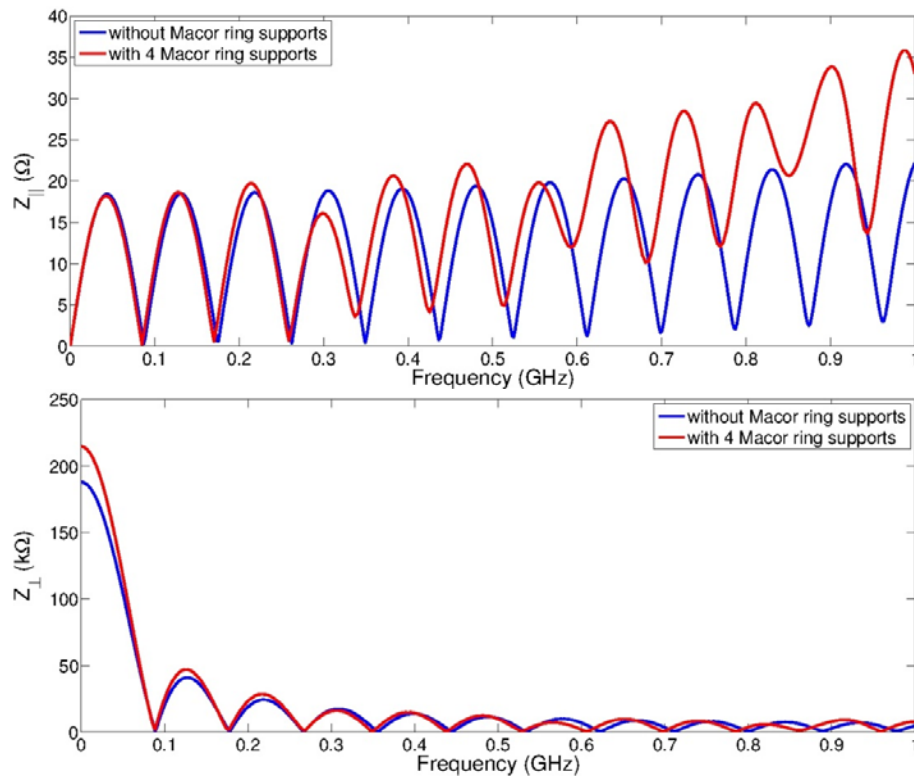
Figure 8: Longitudinal (top) and transverse (bottom) beam coupling impedance for striplines with and without Macor rings, simulated with CST PS, for ideal 50 Ω feedthroughs.

From the beam coupling impedance point of view, the presence of the Macor rings increases the energy lost by the beam particles when passing through the aperture. Hence there is an increase of the longitudinal beam coupling impedance above $\approx$ 330MHz (Fig. 8, top), whereas the transverse beam coupling impedance (Fig. 8, bottom) is not significantly affected because the Macor rings do not change the cross-section of the striplines.

2.14.4.2 *Feedthroughs Study and Optimization*

To study the effects of the feedthroughs upon the power reflected, a model with ideal coaxial feedthroughs was first used. Once we chose the Kyocera 15kV-F-UHV feedthroughs [9], they were simulated and results are shown in Fig. 9.
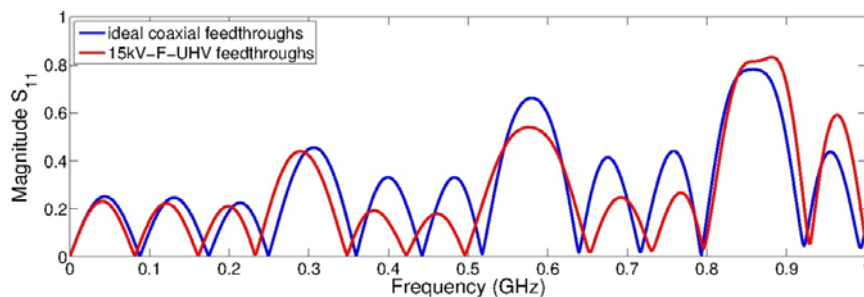
Figure 9: Predicted magnitude of S_{11} for striplines with ideal coaxial feedthroughs and with Kyocera 15kV-F-UHV feedthroughs.

Figure 9 shows that up to $\approx$800 MHz the magnitude of the S_{11} parameter is generally lower with the commercial feedthroughs than with the ideal feedthroughs. This is due to the impedance of the connection between the feedthrough and the striplines being lower than 50 Ω up to 800 MHz. Furthermore, a frequency shift is observed in the maxima and minima pattern for the two models. This is due to the change in the dielectric from only vacuum for both the ideal coaxial feedthrough and the transition to the electrode, to Al_2O_3 for the Kyocera coaxial feedthrough and back to vacuum for the transition: the different dielectric constant results in a change in the velocity of the pulse signal, and therefore a frequency shift.

In addition, simulations of beam coupling impedance have been carried out: preliminary results from the model with the Kyocera feedthroughs do not show any difference compared to the model simulated using ideal 50 Ω feedthroughs. Changes in the beam coupling impedance could occur at high frequencies; however, it has not been possible to run CST PS simulations at higher frequencies than 5 GHz.

2.14.5 **Conclusions**

The electromagnetic design of the striplines, including a detailed study of the electrode supports and the feedthroughs, has been carried out. The stripline design provides the performance specified for the extraction kicker of the CLIC DRs: excellent field homogeneity, good power transmission and low broadband beam coupling impedance. A first prototype of the extraction stripline kicker for the CLIC DR has been manufactured by Trinos Vacuum Projects (Valencia, Spain), and will be tested with and without beam, as well as with and without the inductive adder, in the near future.

2.14.6 **References**

1. R. Apsimon, B. Balhan, M.J. Barnes, J. Borburgh, B. Goddard, Y. Papaphilippou, J. Uythoven, "Optics and protection of the injection and extraction regions of the CLIC damping rings", proceedings of the 4th International Particle Accelerator Conference (IPAC, 2013).
2. A multi-TeV linear collider based on CLIC technology: CLIC Conceptual Design Report (CDR, 2012).
3. G. Rumolo, private communication.
4. T. Naito, H. Hayano, M. Kuriki, N. Terunuma, J. Urakawa, "Development of a 3 ns rise and fall time strip-line kicker for the International Linear Collider", Nuclear Instruments and Methods in Physics Research A 571 (2007).
5. I. Rodríguez, "Calculation methodology and fabrication procedures for particle accelerator strip-line kickers: application to the CTF3 combiner ring extraction kicker and TL2 tail clippers", PhD thesis, Universidad Politécnica de Madrid (2009).
6. D. Alesini, S. Guiducci, F. Marcellini, P. Raimondi, "Design, test and operation of new tapered stripline injection kickers for the e$^+$e$^-$ collider DAΦNE", Physical Review Special Topics –Accelerators and Beams, 13, 111002 (2010).
7. J. Holma, M.J. Barnes, S.J. Ovaska, "Modelling of parasitic inductances of a high precision inductive adder for CLIC", proceedings of the 4th International Particle Accelerator Conference (IPAC, 2013).
8. W. Chao, Handbook of Accelerator Physics and Engineering, 3rd Edition (2006).
9. http://global.kyocera.com
10. Transfer Lines CLIC Note to be published

2.15 CTF3 Status, Progress and Plans

R. Corsini, P. Skowroński, F. Tecker, CERN, CH-1211 Geneva 23, Switzerland
Mail to: Roberto.Corsini@cern.ch

2.15.1 Introduction

The aim of the CLIC Test Facility CTF3 (see Fig. 1.1), built at CERN by the CLIC International Collaboration, is to prove the main feasibility issues of the two-beam acceleration technology [1]. CTF3 consists of a 150 MeV electron linac followed by a 42 m long Delay Loop and a 84 m Combiner Ring. The beam current from the linac is first doubled in the delay loop and then multiplied again by a factor of four in the combiner ring by interleaving bunches using transverse RF deflecting cavities. The high current beam can then be sent in the CLIC experimental area (CLEX) where it can be decelerated to extract 12 GHz RF power to be used for high gradient acceleration. In the same area a 200 MeV injector (CALIFES) generates a Probe Beam for two-beam experiments.
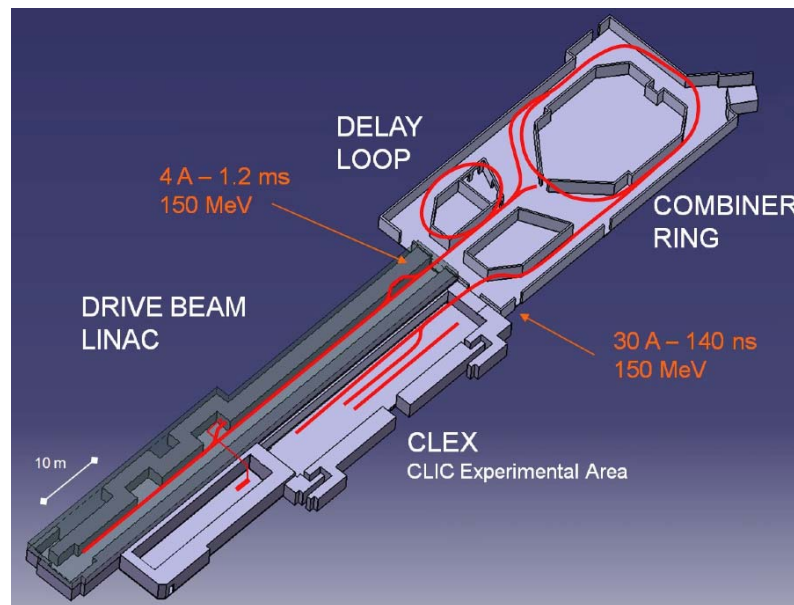
Figure 1.1: CTF3 overall layout.

CTF3 was built in order to demonstrate the following two main issues [2]:
1. Drive Beam Generation: efficient generation of a high-current electron beam with the time structure needed to generate 12 GHz RF power. CLIC relies on a novel scheme of fully loaded acceleration in normal conducting travelling wave structures, followed by beam current and bunch frequency multiplication by funneling techniques in a series of delay lines and rings, using injection by RF deflectors. CTF3 is meant to use such a technique to produce a 30 A Drive Beam with 12 GHz bunch repetition frequency. The Drive Beam can be sent to an experimental area (CLEX) to be used for deceleration and two-beam experiments.

2. RF power production and two-beam acceleration: in CLIC the needed 12 GHz high power RF is obtained by decelerating the high-current Drive Beam in travelling wave resonant structures called PETS (Power Extraction and Transfer Structures). Such power is transferred efficiently to high gradient accelerating structures, operated at 100 MV/m. In the CTF3 experimental area (CLEX) one line (Test Beam Line, TBL) is used to decelerate the Drive Beam in a string of PETS. The Drive Beam can alternatively be sent to another beam line (Two-Beam Test Stand, TBTS), where a PETS is used to power one or more structures, used to further accelerate a 200 MeV electron beam provided by a dedicated injector, CALIFES.

CTF3 has been installed and commissioned in stages since 2003. Delay loop running-in was basically completed in 2006. The Combiner Ring and the connecting transfer line were installed and put in operation in 2007, while the transfer line to CLEX was installed in 2008. In 2009 this last beam-line and the various Drive Beam lines in CLEX were commissioned, together with the CALIFES Drive Beam injector. During the autumn of 2009, recombination with the DL and CR together was achieved, yielding up to 28 A of beam current. In 2010 the nominal power production from the PETS was obtained, and the first two-beam test was performed, reaching a measured gradient of 100 MV/m. In 2011 a gradient of 145 MV/m was reached in two-beam tests and the PETS ON/OFF mechanism was successfully tested. In 2012 and 2013 the Drive Beam stability and the overall performances of the facility were improved and a 23 A Drive Beam was decelerated by 35% of its initial energy in a string of 12 PETS structures.

2.15.2 The Injector: Beam Current and Time Structure

The CTF3 Drive Beam injector consists of a high current thermionic gun, three 1.5 GHz sub-harmonic bunchers, and a 3 GHz system composed of a pre-buncher, a buncher and the first two accelerating structures in the linac [3].

The sub-harmonic bunchers (SHBs) are used to give the first energy-time modulation to the beam and to perform the phase coding by means of fast 180° RF phase switches. The SHBs have six 2.6 cm long cells each, and their nominal power is 40 kW. To compensate the growing beam loading, different in each one of the structures, they are tuned in a different way. Downstream of this system, a 3 GHz single-cell pre-buncher and a traveling wave buncher are installed to create the final bucket structure and to accelerate the beam up to about 6 MeV. The 2 cm long pre-buncher nominal power is 100 kW, while the TW buncher is about half a meter long and is fed a maximum power of 40 MW.

The first two accelerating cavities follow this system to bring the beam to an energy of about 20 MeV. These cavities are of the same type as those installed in the rest of the linac and described later. Exhaustive simulations have been performed using PARMELA to optimize the bunch length, the satellite population and the transverse emittance. The magnetic field distribution has been optimized to keep the emittance at the exit of the injector below 50 μm. Measurements in the CTF3 linac gave emittances in agreement with the predicted ones [4]. A bunch length of 1 mm at the end of the linac and less than 2 mm has been measured in the combiner ring by means of streak camera measurements [5].

The sub-harmonic bunchers perform 180° phase jumps to create the correct bunch train structure. Some particles captured by the 3 GHz system form satellites in between the 1.5 GHz buckets. The measured fraction of the satellites is about 8% to be compared with the 7% of the design. Figure 1.2, a projection of a streak camera image, shows the bunch population vs. time during the 180° phase switch. The measured phase switch time is less than 6 ns, which corresponds to eight 1.5 GHz periods, well below the target time of 10 ns [6].
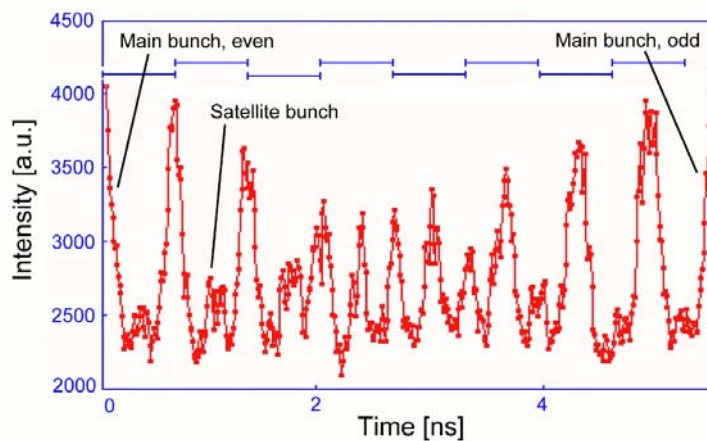
Figure 1.2: Fast bunch phase switch, measured in CTF3 by a streak camera.

2.15.3 The Linac: Full Beam-Loading Acceleration

As the overall efficiency is paramount for a linear collider, a very efficient energy transfer to the Drive Beam is crucial. An essential ingredient of the Drive Beam linac is full beam-loading operation. The high pulse current of both CLIC and CTF3 (about 4 A in both cases), in conjunction with the use of short travelling-wave accelerating structures with relatively low gradient, results in an extremely high energy transfer efficiency to the beam, as depicted in Figure 1.3. No RF power is transmitted to the load when the beam is present, and the resistive losses in the cavity walls are minimal. In this condition, an overall transfer efficiency of about 98% is expected for CLIC. However, an energy transient is present at the beginning of the pulse, where the first bunches have twice the energy of the steady-state part, reached after the filling time. This mode of operation also strongly couples beam current fluctuations to the beam energy. One of the main goals of CTF3 is the validation of the CLIC Drive Beam generation scheme with fully loaded linac operation.
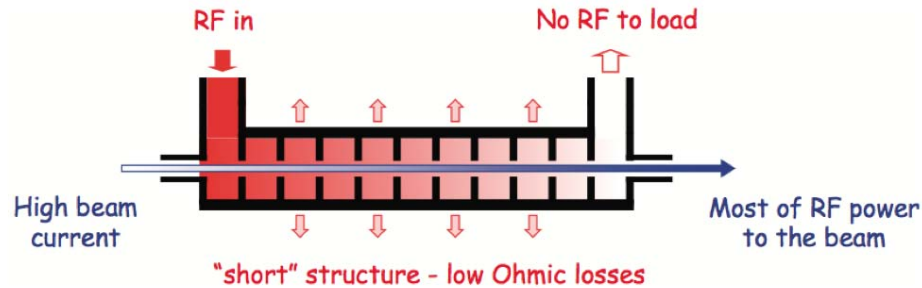
Figure 1.3: Acceleration of a beam in a travelling wave structure. Under full beam loading operation no RF power is leaving the structure.

The 3 GHz travelling wave accelerating structures designed and built for CTF3 [7] work in the $2\pi/3$ mode, have a total length of 1.22 m and operate at a loaded gradient (nominal current) of 6.5 MV/m. The large average current also implies that transverse higher order modes (HOMs) must be damped in order to prevent transverse beam instability and control emittance growth to the desired level. A Slotted Iris — Constant Aperture structure (SICA) has been designed to be used in the Drive Beam linac. Irises are radially slotted to guide dipole and quadrupole modes into SiC loads situated outside the cells. In this approach the selection of the damped modes is obtained through their field distribution, so that all dipole modes are strongly damped (Q typically below 20), while monopole modes are not influenced due to the symmetry. In addition to strong damping, SICA uses detuning of the dipole modes along the structure; this improves the suppression of HOMs and allows one to change group velocity along the structure, so providing the desired gradient profile. The HOM detuning is obtained by nose cones of variable geometry. The aperture can therefore be kept constant along the structure, which helps in reducing the short-range wake-fields.

The RF power is supplied by klystrons with power ranging from 35 MW to 45 MW and compressed by a factor of two to provide 1.3 μs pulses with over 30 MW at each structure input. The pulse compression system uses a programmed phase ramp to produce a constant RF power.

Beam commissioning started in June 2003. The design beam current and pulse length were rapidly reached, successfully demonstrating the operation under nominal working conditions of the structures with their novel damping scheme [8]. The main result obtained was the first proof of stable operation under full beam loading. The beam was remarkably stable and no sign of beam break-up was observed at high current. The measured normalized emittance at the end of the CTF3 linac was routinely about $\varepsilon_{x,y} \approx$ 50 μm. This confirms that the Drive Beam accelerator wake-field effects are small, as predicted by simulations.

The energy spread during the initial beam transient (about 100 ns) could be reduced to a few percent by partial RF filling of the structures at beam injection. The observation of the RF signals at the structures' output coupler was particularly useful. It allowed one to easily adjust the beam-to-RF phase by maximizing the beam loading and to determine the phase errors between structures.
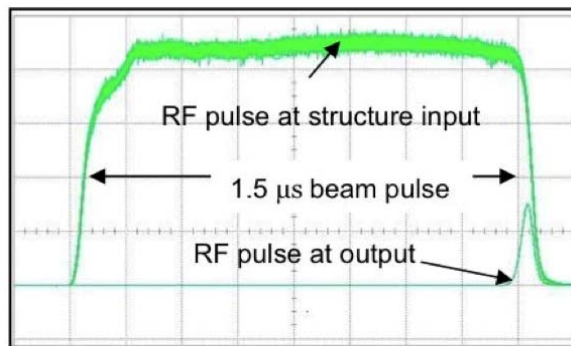
Figure 1.4: RF power measured at the accelerating structure input and output with beam.

The efficiency of the acceleration was demonstrated in a dedicated experiment [9]. After careful calibration of beam current and RF power measurements, the energy gain of the beam was calculated and compared to spectrometer energy measurements. Figure 1.3 shows an example of the RF power measured at the structure input and output, showing that the RF power is almost fully absorbed by the beam. The measurements were in excellent agreement with the theoretical energy gain. Including the ohmic losses, the obtained RF-to-beam transfer efficiency yielded 95.3%.

In summary, CTF3 has been stably operated over several years with fully loaded structures. The highly efficient acceleration of the Drive Beam has been successfully demonstrated.

2.15.4 The Delay Loop and Combiner Ring: Isochronicity Requirements and Bunch Combination Process

Beam recombination is done in two stages. First, using the Delay Loop (DL) a 1120 ns long bunch train with a current of 4 A is converted into 4 pulses of 140 ns and 7.5 A (taking into account the satellite bunches content). Later, the pulses are interleaved in the Combiner Ring (CR) to produce a single 140 ns long pulse with a maximum current of 30 A.

The first RF deflector, operating at 1.5 GHz, sends odd and even phase-coded sub-pulses either straight to the CR or into the DL, whose length is equal to the sub-pulse length. The sub-pulses circulating in the DL come back in the deflector at half a wavelength distance, and their orbits are merged with the following ones to obtain 140 ns long pulses with twice the initial current and twice the bunch repetition frequency. The pulses are combined again in the CR. A pair of RF deflectors is employed to create a time-dependent closed bump at injection, which can be used to interleave the bunches. The combination process must preserve transverse and longitudinal beam emittances: isochronous lattices, smooth linear optics, low impedance vacuum chambers and diagnostics, HOM free RF active elements are all needed to accomplish this task. CTF3 routinely provides a recombined beam of 28 A, slightly lower than the expected value [10] (see Fig. 1.5).
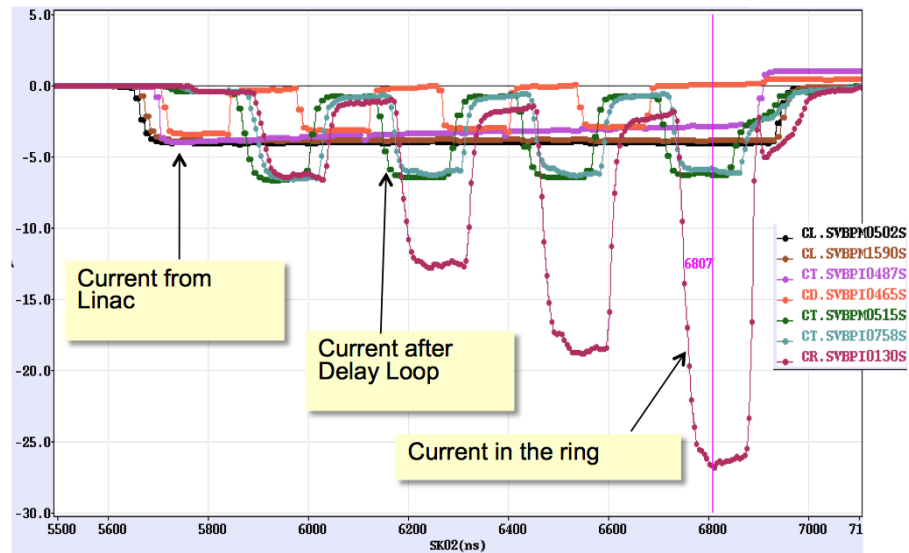
Figure 1.5: Beam current multiplication in CTF3.

Initially, the recombined current was limited by losses. In 2011, several improvements reduced drastically the losses, but the satellite content increased due to the unavailability of one of the three 1.5 GHz RF sources used in the bunching system, such that the DL recombined beam had a current of 7.2 A.

2.15.4.1 *Isochronicity and Other Lattice Requirements*

A short bunch length is fundamental for efficient RF power production in the PETS. Bunch length preservation requires the use of isochronous optics (which implies R_{56}=0) in the DL, the CR and the transfer line connecting them. The DL and CR arcs are based on the use of three-dipole isochronous cells. The isochronicity requirement is $|R_{56}| \leq$ ±1 cm. The range of tunability of such a cell with three independent quadrupole families fits well the requirements. It is envisaged, but not yet implemented, to correct with sextupoles also the second-order matrix term R_{566}. Bunch length control to < 1 mm r.m.s. was shown in the past after the linac. No time was then dedicated to get such a bunch length in CLEX as well, since the present value (< 2 mm r.m.s.), estimated from RF power production in CLEX and by direct streak camera measurements in the ring is entirely sufficient for CTF3 operation and in agreement with expectations.

Emittance preservation requires good control of the optics, a very good closure of the DL and CR orbits and that the beam from the linac is properly matched. The RF bump in the combiner ring must not introduce any distortion. Therefore the phase advance between the RF deflectors in the horizontal plane must be 180°, so that any distortion introduced by the first RF deflector is corrected by the second one. CTF3 has not yet reached the target emittances for the Drive Beam after combination, 150 μm in both planes. Although 50 μm is routinely obtained in the linac, measurements on the fully recombined beam typically give values two to four times larger than the target. Better results are obtained for the factor 4 beam combination, where the goal has been reached. The main source of emittance growth was identified as orbit mismatch between delay loop and combiner ring, and non-perfect orbit closure in the ring itself. Several correcting measures are now being put in place.

Damping and detuning is used in the RF deflectors of the ring in order to minimize wake-fields in the vertical plane, which are not extracted from the output coupler [11]. The lowest order horizontal dipole mode is the operational one, therefore it cannot be damped or detuned. However, the fill-time of the travelling wave deflectors is short enough to avoid turn-by-turn direct build-up. In order to avoid any residual amplification of the orbit errors from RF deflector induced wake-fields, the fractional tune of the Combiner Ring is set to be about 0.6 in both planes. Also, the β function in the deflectors should be as small as possible.

2.15.4.2 *Recombination Process Setting-up*

Besides demonstrating the feasibility of the CLIC bunch combination principle, CTF3 has allowed us to develop an optimized setting-up procedure of such a process, validating also the special diagnostics needed. For instance, to set-up the Delay Loop, initially the 1.5 GHz RF deflector is not used and magnetic correctors are employed to inject the beam on the DL design orbit. The design injection orbit is established, adjusting septa and main bend current. If needed, the injected beam is then matched to the DL closed solution: the Twiss parameters of the beam are measured using the quadrupole-scan technique, in two Optical Transition Radiation (OTR) screens, located upstream and downstream of the DL injection and the optics of the transfer line from the linac is re-adjusted based on the results obtained.

In order to define the proper phase and amplitude in the RF deflector, the beam is sent straight past the DL into a dump. The RF deflector is powered, and its phase adjusted at zero crossing so it does not affect the beam trajectory. Afterwards, the phase is moved by 90° and the magnetic correctors used for injection are disabled. If the bunches don't follow exactly the reference orbit, the amplitude needs to be adjusted, and the procedure is repeated. The recombination with RF deflectors requires the length of the DL and the CR to be precisely adjusted such that the bunches, going again through the RF deflectors, see the proper RF phase with an accuracy of a few degrees. The length of both DL and CR can be tuned in a maximum range of 9 mm using 4-pole wigglers, and can be precisely measured with 3 GHz phase monitors (BPRs), which compare the bunch phase with a 3 GHz reference signal. In the last step, phase switching is introduced in the sub-harmonic bunching system, and the sub-pulses are recombined.

The Combiner Ring setup also starts with RF deflectors disabled. A static magnetic corrector is used to inject the beam on a good orbit through the first half of the ring. As in the DL case, we need to find precisely the correct amplitude and phase of the RF deflectors. The pulse is shortened to less than the CR circumference (280 ns) and only the first RF deflector after injection is powered. The zero-crossing phase is determined as the phase that leaves the beam orbit unchanged. This is done for different RF amplitude values, thus measuring the phase dependence on the amplitude. In the next step the RF deflector phase is moved by 90° so bunches arrive at the crest and the corrector is disabled. The amplitude is adjusted in order to inject on the reference orbit, with the phase following according to the dependence found in the previous step. The timing of the klystron that feeds the deflectors is adjusted such that it stops just after the last bunch is injected. Since the RF deflectors are travelling wave structures with very short filling time, the train can thus make tens of thousands of turns in the ring. At this stage the orbit in the whole ring is corrected, as well as the ring length. The ring length

must be (N $\pm$ 1/N_f) λ_{RF}, where N is an integer number, N_f the combination factor (here 4), and λ_{RF} is the RF wavelength. The fractional part λ_{RF}/N_f, can be determined precisely from Fourier transform of the BPR phase monitor of the coasting beam. To adjust the ring length the 4-pole wiggler is used. In the next step the phase and amplitude of the second RF deflector are adjusted. The RF pulse for the deflectors is extended by 280 ns such that the field is present when the train makes the second turn. This should not change the orbit since the ring length was adjusted before. Attenuation of the second deflector is removed and phase adjusted such that the orbit stays unchanged. The RF pulse is extended by another 280 ns and the amplitude of the second deflector is fine tuned to keep beam position unaltered. If all is done properly, extending the RF pulse to the 4th turn will not affect the orbit. Putting back the beam pulse length to the nominal value gives the recombined beam.

2.15.5 Stability Issues

The two-beam acceleration scheme puts tight constraints on the Drive Beam current, energy and phase stability. The CLIC Main Beam should experience the correct RF phase and amplitude within tight tolerances in order to avoid energy fluctuations, causing luminosity reduction mainly due to emittance increase in the main linac and through the limited energy bandwidth of the Beam Delivery. The stability of the Drive Beam used to produce the RF power is therefore of crucial importance, since both bunch charge and phase jitter contribute quadratically to the luminosity loss [12].

The main concern is that energy jitter generated in the Drive Beam accelerator would be transformed into beam phase jitter during the final bunch compression. The tolerances on the linac RF are therefore extremely tight: the r.m.s. RF phase jitter tolerance is 0.05◦ for a constant error along the whole Drive Beam train and 0.2% for the RF amplitude. A CTF3 klystron was used to measure the short-term RF stability over 500 consecutive RF pulses ($\approx$ 10 min). The mean pulse-to-pulse phase jitter measured with respect to the external reference is 0.035°. The pulse-to-pulse phase jitter for a fixed 10 ns time slice is 0.07° (3 GHz). The relative pulse-to-pulse power jitter has been 0.21% [12]. The measurements show that the RF stability of the klystron is very close to the CLIC requirements.

Due to the fully loaded acceleration, any current variation will also result in an energy variation of about the same relative amplitude, even if any high frequency variation will be averaged over the fill time of the Drive Beam accelerating structure. Taking this into account, a maximum variation of 0.75×10^{-3} for the Drive Beam current and 0.2° at 1 GHz for the Drive Beam bunch phase after combination are allowed. Such tolerances are evaluated for a maximum contribution of 1% to the luminosity loss per parameter and assuming a feed-forward system (discussed below) capable of reducing the Drive Beam phase jitter by the factor of 10 (from 0.2° to 0.02° at 1 GHz). The pulse-to-pulse current variations in the CTF3 linac were measured using the current measurements of the beam position monitors. Initially, the stability was only of the order of $\Delta I/I = 2 \times 10^{-3}$ but it could be improved by replacing the gun heater power supply with a more stable one. A slow drift was still present that could be reduced by a feedback. Finally, a variation on a single BPM as low as $\Delta I/I = 0.54 \times 10^{-3}$ was measured [13] (see Fig. 1.6). This is already better than the required current stability for CLIC of $\Delta I/I = 0.75 \times 10^{-3}$. A correlation analysis of different BPMs

showed also that the BPM noise level was of the order of $\Delta I/I = 0.3 \times 10^{-3}$, indicating that the real current variation is even lower, well below the CLIC target.
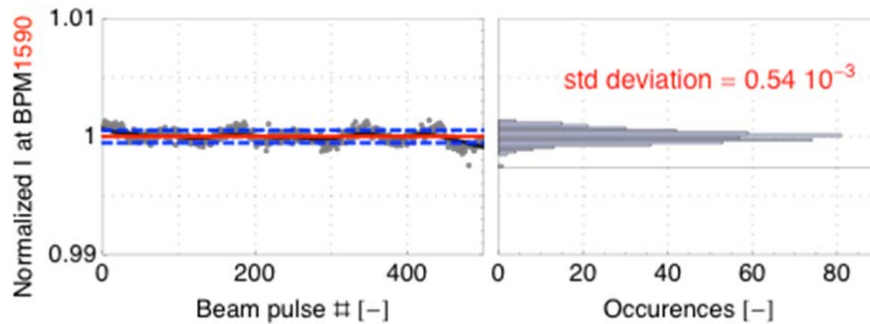
Figure 1.6: Beam current fluctuations measured at the end of the CTF3 linac.

The current stability after the recombination process is not as good as in the linac. The main source of variations and jitter is the RF system. While at least part of the klystrons have very good amplitude and phase stability, as discussed above, the RF pulse compression system is very sensitive to temperature fluctuations, which lead to a changing beam energy. Through dispersion, energy fluctuations lead in turn to fractional losses of the beam current. In order to improve the beam performances, a feedback has been developed that takes into account the ambient temperature around the compression cavities, as the thermal isolation of these cavities is not perfect. The set point of the temperature stabilization system is corrected according to the variations in the ambient temperature. This system works well and significantly suppresses the RF variations [14]. A further feedback acts in addition to this on the setup of the RF pulse compression and keeps the RF power constant along the beam pulse [15] (see Figure 1.7).
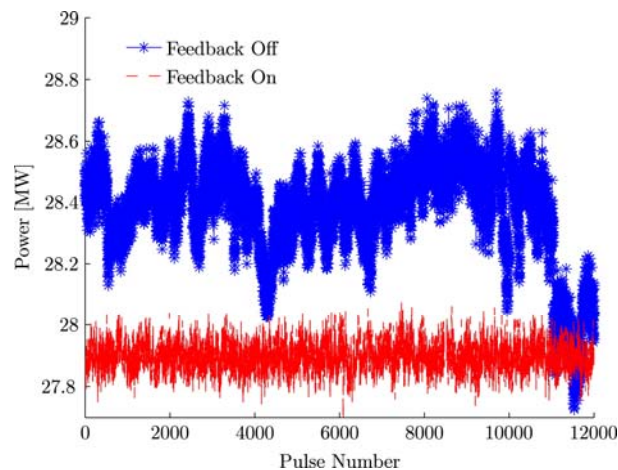
Figure 1.7: Average compressed RF power time evolution measured in one of the CTF3 klystrons, with and without the RF amplitude feedback.

It must however be noted that RF pulse compression is specific to CTF3 and will not be used in CLIC. Still another feedback stabilizes the input RF phase of the different

linac accelerating structures at a given phase reference by adjusting the low-level RF phase.

After a factor of four combination in the Combiner Ring, a current stability of 1×10^{-3} was measured. The beam current variation increases after extraction from the Combiner Ring. This increase is probably due to an emittance increase during the combination together with the aperture limitation for the extraction channel. As the operation for the full factor 8 recombination is more complex, the beam becomes more sensitive to deviations from the nominal parameters. For the factor eight combination with Delay Loop and Combiner Ring, a stability of the order of 1% has been reached up to now.

As mentioned before, in CLIC a drive beam phase feed-forward system is foreseen in order to reduce the phase jitter by about a factor ten [2], from is specified value at the exit of the ring complex (2° at 12 GHz) to the level needed at injection in the decelerator sections (0.2° at 12 GHz). The CLIC feed-forward for CLIC will utilize a four bend C-shaped chicane after each turnaround. The phase of the drive beam bunches is measured prior to the turnaround. Based on this measurement the orbit of the beam through the chicane is change by altering a series of four fast kickers. Early bunches will take longer paths through the chicane and late ones shorter paths, thus correcting their longitudinal position (phase) back to nominal. As the distance the beam travels between the phase monitor and the chicane is much greater than the cable lengths between the monitor and the kickers, the same bunches that was originally measured can be corrected, which makes the system a real feed-forward.

The installation of a proof-of-principle experiment and R&D ground for the proposed CLIC drive beam phase feed-forward scheme at CTF3 is currently in progress [16]. Due to space constraints the system installed at CTF3 utilizes the existing four bend dog-leg chicane in the transfer line TL2, linking the ring area to CLEX, as opposed to a four bend C-chicane like in the CLIC scheme. One of the main challenges is the bandwidth of the whole system, whose overall bandwidth should be at least 30 MHz. This includes the amplifiers, which need to deliver a peak power of 65 kW at a bandwidth of 50 MHz. Three phase monitors are installed in the transfer line between the Stretching Chicane and the Delay Loop, prior to TL2, and after TL2 at the beginning of the TBL. The first monitor provides the input to the digital processor which calculates the voltage applied to the kickers to perform the correction. The second monitor, placed just before the first kicker, is used to assess any phase variation occurring between the first phase monitor and where the correction is made. Finally, the last monitor measures the corrected beam. The two kickers are placed prior to the first and last dipoles of the TL2 chicane. At a maximal voltage of ±1.2 kV the kickers will be able to deflect the drive beam by ±1 mrad. The feed-forward system will be tested using an uncombined beam, i.e. a Drive Beam pulse bypassing the delay loop and making only half a turn in the combiner ring, in order to prove the principle. In a second stage the system may be implemented for the combined beam, to enhance phase stability for the beam users in CLEX. The beam time of flight between the first phase monitor and the first kicker is 380 ns, which defines the maximum latency of the feed-forward system. The estimated total latency of the components (phase monitor, digital processor and amplifier) is around 150 ns, with cable delays adding an additional 120 ns. This gives a total of 270 ns, well within requirements. It is also possible to store the beam in the combiner ring for additional turns to relax the latency demands.

Beam phase errors within ±15° at 12 GHz and 30 MHz bandwidth can be corrected. It was recently confirmed [17] that the main source of phase jitter in CTF3 is energy jitter of the beam (from RF phase and power jitter of klystrons in the injector) transformed into phase jitter and amplified when passing through a magnetic chicane, for non-zero momentum compaction factor. When the chicane is set to low momentum compaction (R_{56}=0), the beam phase jitter is reduced below 2° at 12 GHz, which will allow a full demonstration of CLIC requirements if the expected factor ten gain will be reached (see Figure 1.8).
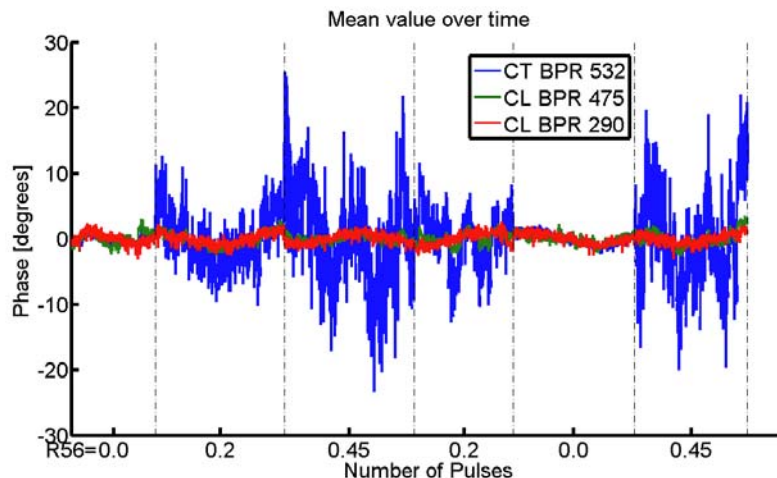
Figure 1.8: Mean phase value vs. time measured before the stretching chicane red and green traces) and after it (blue trace). The phase is measured in 12 GHz degrees, and the different R_{56} values used in the chicane during the measurement are indicated on the horizontal axis. For R_{56}= 0 the phase jitter is very close in all positions, and its rms is below 2°.

2.15.6 The Two-Beam Test Stand: Power Production

The RF power for the Main Beams is produced by the Drive Beam interacting with a periodically-loaded constant impedance structure, the Power Extraction and Transfer Structure (PETS). The Drive Beam excites preferentially the synchronous mode with frequency $\omega_{RF} = 2\pi \times 11.994$ GHz. Extensive studies have been performed to arrive at the current CLIC PETS design, including studies of high-power behavior and higher-order mode behavior [18]. In CLIC each of the 140000 PETS will generate 240 ns RF pulses of 135 MW. High-power testing of the PETS using a klystron has been performed at the ASTA test stand at SLAC [19] demonstrating satisfactory high-power performance with a breakdown rate less than 2.4×10^{-7} per pulse per meter at nominal PETS power and pulse length.

Figure 1.9: Photo of the TBTS test area with vacuum tanks for the PETS (to the right) and accelerating structure (at the left).

In CTF3, PETS prototypes are tested with beam in the Test Beam Line (TBL) and the Two-Beam Test Stand (TBTS). The TBTS consists of two parallel beam lines, fed respectively with the Drive Beam from TL2 and the Probe Beam from CALIFES (see Figure 1.9). In the TBTS a PETS extracts RF power from the Drive Beam, which is then fed to an accelerating structure in the Probe Beam line. The TBTS PETS (see Figure 1.10) is a 1 m long 12 GHz RF structure in eight octants separated by damping slots in order to provide strong damping of transverse modes. The downstream end of the PETS is equipped with an output coupler. The initial configuration had an external waveguide loop, allowing for recirculation and resonant build up of RF power in order to amplify it. Towards the end of the 2011 run the external recirculation circuit was replaced by an On/Off mechanism including external RF reflectors at both ends of the PETS. The recycling loop was equipped with a variable power splitter and RF phase shifter. With feedback coupling above zero the PETS operates in the amplification mode, and depending on the settings (feedback coupling and circuit phase advance) the PETS peak power can reach levels more than 10 times higher than in the case without recirculation. The extracted RF power can then be amplified by about a factor four. This gives greater flexibility in handling the RF power level delivered to the accelerating structure and in particular it gives the possibility to generate a CLIC parameter PETS RF pulse (135 MW, 240 ns) from the CTF3 factor four combined Drive Beam [20, 21].

The commissioning of the TBTS PETS with recirculation started in November 2008 with power levels up to 30 MW. The power level produced in the PETS was then gradually increased. Using a Drive Beam current of more than 15 A the PETS power routinely reached levels of more than 300 MW in the recirculation loop, twice the nominal PETS power.
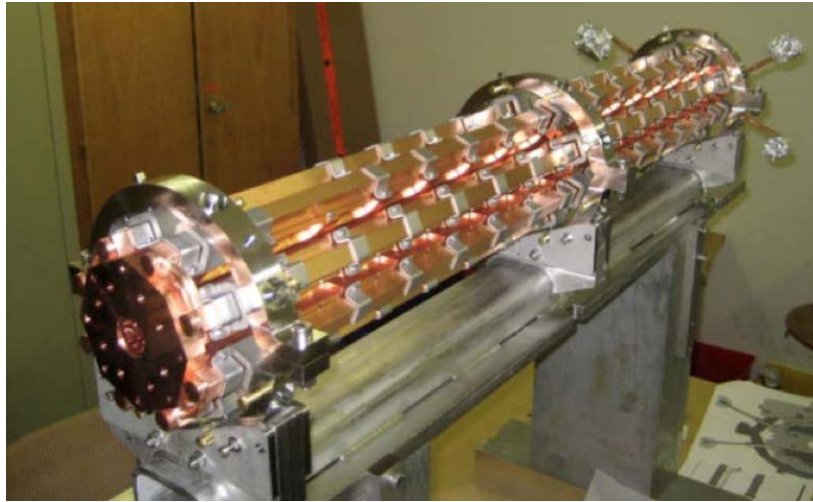
Figure 1.10: The 12 GHz PETS prototype installed in the TBTS. The PETS is based on the CLIC baseline design but longer (one meter as opposed to 0.21 m for CLIC) in order to reach and exceed the CLIC nominal power in spite of the lower CTF3 Drive Beam current (30 A maximum, as opposed to 100 A for CLIC).
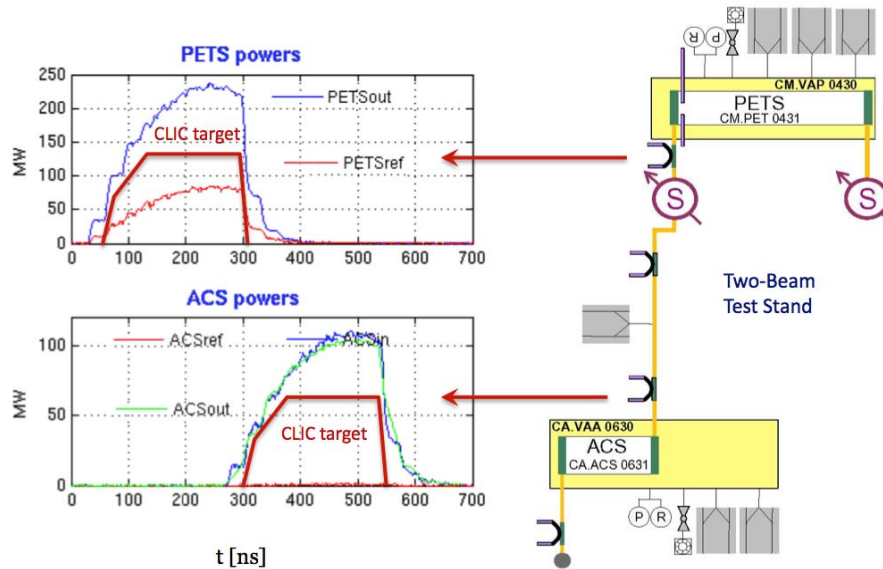
Figure 1.11: RF signals measured in different locations of the TBTS. The use of recirculation allowed to reach in the PETS (above) and in the accelerating structure (below) RF power levels and pulse lengths well beyond the CLIC nominal value.

The PETS was operated with power levels at and above the nominal CLIC power (see Figure 1.11) for long periods, showing very small vacuum activity and a relatively low breakdown rate. The analysis of the structure of the RF pulses during breakdown events showed evidence that in most of the cases, the activity was associated with waveguide components in the recirculation loop and not the PETS itself.

2.15.6.1 *PETS On/Off Mechanism*

The PETS On/Off mechanism is required in CLIC in order to be able to switch on and off individual PETS whenever localized breakdowns threaten the normal machine operation. The system should also provide a gradual ramp-up of the generated power in order to reprocess either the main accelerating structure and/or the PETS itself. Therefore a suitable mechanism has been developed, based on an external high-power variable RF reflector [22]. The reflector can be tuned to stop any power transfer to the accelerating structures, effectively preventing any further break-down in the structures. The reflected RF power is sent back to the PETS, where internal power recirculation is established by another reflector placed at its upstream end. The reflector positions are chosen such that the back-propagating power is in anti-phase with the forward one, achieving partial cancellation of the beam generated power inside the PETS as well. For the CLIC case, the RF power extracted from the Drive Beam in the PETS is suppressed down to 25% of its original value, which is expected to be enough to prevent or to reduce dramatically the probability of RF breakdown in the PETS itself.

To test a prototype with beam in CTF3, a variable RF reflector and a variable RF short circuit were installed on the TBTS PETS tank, substituting the external recirculator. At the beginning the variable short circuit was set at the position that provided destructive phase advance in the loop for the case of full reflection in variable reflector. During experiments with beam, the variable reflector settings were changed gradually from full reflection to full transmission. The RF power produced by PETS and delivered to the accelerating structure was measured at different intermediate positions. The results are summarized in Figure 1.12.
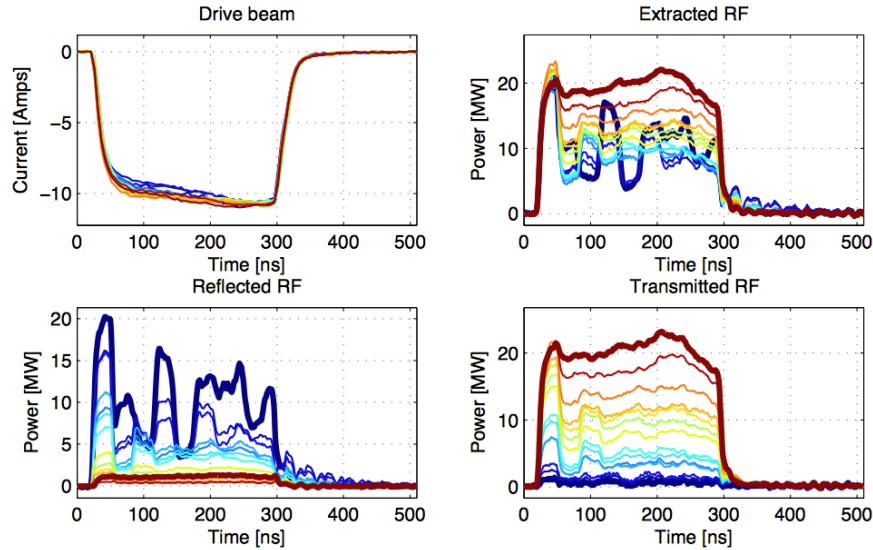
Figure 1.12: PETS On/Off demonstration with beam. Here the coloured lines correspond to different setting of variable reflection. The colours are gradually changed from red (On) to blue (Off).

These experiments successfully demonstrated the PETS On/Off operational principle [23]. They were in good agreement with computer simulations based on the low RF power measurements of all the RF components and the measured Drive Beam current pulse shape (see Figure 1.13).

However, the Drive Beam current limitation in CTF3 made it impractical to run the system at nominal CLIC RF power level. To demonstrate the power capability of the On/Off RF circuit, we set the recirculation parameters to their amplification mode, as was routinely done in the TBTS PETS when it was equipped with external recirculation. The processing of the PETS with the On/Off circuit went rather fast. In about five days $(2 \times 10^5$ pulses) the system was conditioned up to 130 MW $\times$ 200 ns. In conclusion, the PETS On/Off capability was successfully demonstrated in experiments with the Drive Beam in CTF3. Currently the system is used to provide RF power for the two-beam experiments in the TBTS.
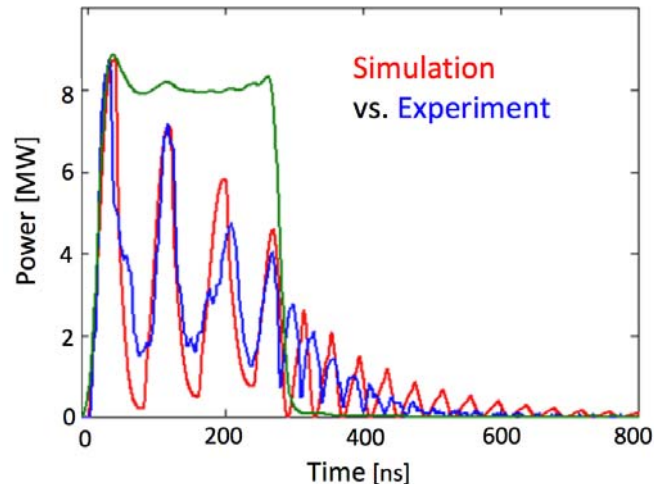
Figure 1.13: The simulated (red) and measured (blue) RF pulses generated by PETS in the Off state. The direct power production (On state) is shown in green.

2.15.7 The Two-Beam Test Stand: Two-Beam Acceleration

One of the key purposes of CTF3 is to demonstrate the CLIC two-beam acceleration scheme, i.e., the production of RF power from the Drive Beam and its transfer to high-gradient structures to accelerate the Main Beam (represented by the Probe Beam in CTF3). This is done in the Two-Beam Test Stand (TBTS), used for an extensive program to investigate both the PETS power production structures and high gradient accelerating structures.

The Probe Beam is provided by the 24 m long injector linac CALIFES (Concept d'Accélérateur Linéaire pour Faisceaux d'Electrons Sondes) [24], situated in CLEX like the TBTS. It has been developed by CEA Saclay, LAL Orsay and CERN to deliver single bunches and bunch trains at 1.5 GHz bunch repetition rate and energies up to 200 MeV. The beam is generated in a photo-injector. A Nd:YLF laser produces 1047 nm infra-red pulses at 1.5 GHz repetition rate, which are converted to green and then to ultra-violet before impinging on the photocathode. The bunches have an energy of about 5 MeV at the exit of the photo-injector and are further accelerated in three 3 GHz accelerating structures recuperated from the LEP Injector Linac (LIL). The three LIL accelerating structures and the photoinjector are powered by a single 3 GHz klystron which delivers 45 MW RF pulses during 5.5 μs to an RF pulse compressor.

The nominal bunch charge produced by the photo-injector is 0.6 nC, however for trains longer than 32 bunches the total beam charge is limited to 19.2 nC due to the

beam loading in the LIL structures. CALIFES is usually operated with bunch charges of around 0.1 nC which can also be used for long bunch trains. A new laser system is being developed to provide UV pulses with energy over 1 µ J, far beyond the present 220 nJ, to ease operation at higher charges. A normalized beam emittance of 10 µ m has been achieved.

As mentioned, the TBTS consists of two parallel beam lines, fed respectively with the Drive Beam from TL2 and the Probe Beam from CALIFES. In the central part of the TBTS large vacuum tanks contain a PETS and one accelerating structure (two since 2012). The TBTS PETS has been fully described in the previous section. During the 2010 and 2011 runs, the accelerating structure installed in the TBTS Probe Beam line was of the type TD24_vg1.8, a 24+2 cell detuned and damped design with a 2 π /3 phase advance and an active length of 20 cm. It was designed to reach an accelerating gradient of 100 MV/m at an input power of approximately 45 MW (unloaded) [2].

During the 2009 run, the PETS produced over 170 MW peak in full RF re-circulation mode, well above the nominal 135 MW foreseen in CLIC, but in the presence of pulse shortening due to RF break-down in the recirculation components (high power splitter and phase shifter). These parts were repaired and improved for the 2010 run, when RF power levels in the 300 MW range were reached at the nominal pulse length. During the 2010 run the first two-beam acceleration of the Probe Beam was achieved. The Probe Beam energy with two-beam acceleration can be measured in the spectrometer line as a function of the Probe Beam 3 GHz RF phase, which is phase-locked to the laser pulse timing. A phase scan is then used to adjust the relative phase between Probe and Drive Beam for maximum acceleration. The nominal CLIC accelerating gradient of 100 MV/m corresponds to an energy gain of $\Delta E = 21.4$ MeV.
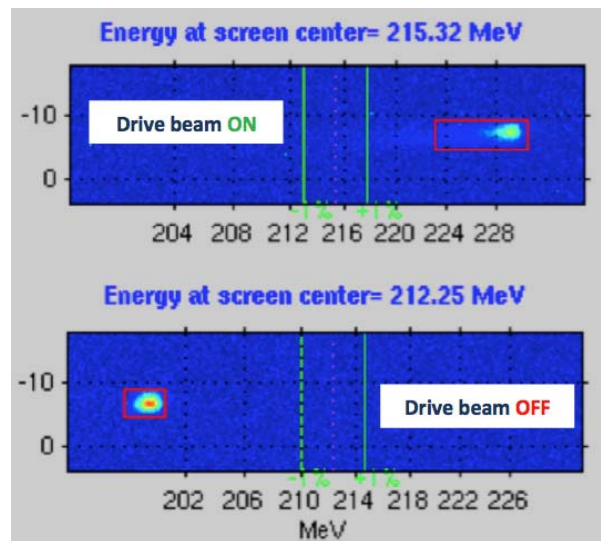
Figure 1.14: Probe Beam observed in the TBTS spectrometer screen with the 12 GHz RF power from the drive beam on (top) and off (bottom). The energy gain is about 31 MeV which corresponds to a gradient of 145 MV/m in the accelerating structure.

Due to an extensive conditioning campaign during the 2011 run, energy gains of up to $\Delta E = 32$ MeV were achieved [25] in the last month of operation with relatively low

breakdown rate. Accelerating gradients up to 165 MV/m were achieved during periods with higher breakdown rate.

Figure 1.14 shows an example of ΔE = 31 MeV Probe Beam acceleration measured on the spectrometer screen, corresponding to an accelerating gradient of 145 MV/m. The accelerating gradient and energy gain as function of the RF input power is shown in Fig. 1.15, and compared to the expectations for this structure (red line).
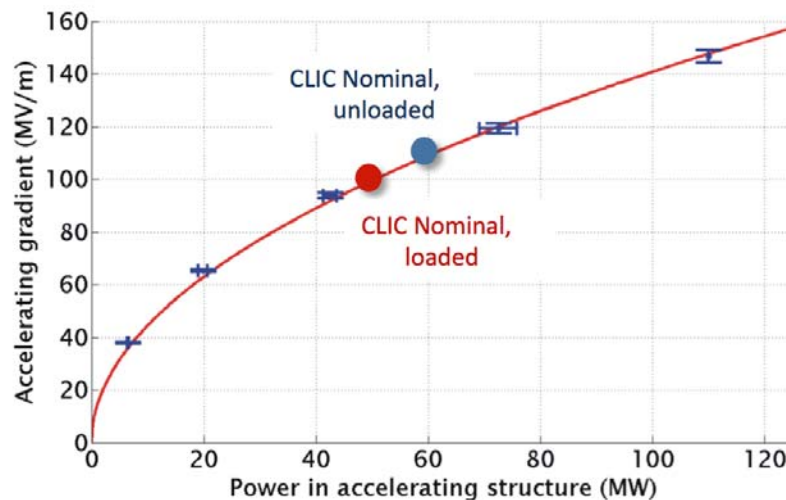
Figure 1.15: Measured (crosses) and expected (red line) accelerating gradient as function of the RF input power for accelerating structure TD24_vg1.8 used in the 2011 run. The Nominal CLIC conditions (100 MV/m loaded and 110 MV/m unloaded) are also reported.

2.15.8 The Test Beam Line (TBL): Drive Beam Deceleration.

The test beam line (TBL) was installed in the CLEX building of CTF3 to study the CLIC decelerator beam dynamics and 12 GHz power production. The beam line consists of a FODO lattice with high precision BPM's and quadrupoles on movers for precise beam alignment as shown in the schematic of Figure 1.16.
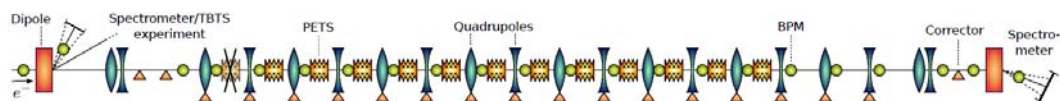
Figure 1.16: Schematics of the Test Beam Line showing the F0D0-lattice with the PETS structures in the drift spaces and the diagnostic section before and after.

Vacuum tanks containing a Power Extraction and Transfer Structures (PETS) each are installed in the drift space between the quadrupoles to extract 12 GHz power from the Drive Beam coming in CLEX from the ring area of CTF3. The PETS in TBL have the same RF design as the CLIC PETS but their active length is a factor 4 longer compared to CLIC to compensate for the lower Drive Beam current. Therefore the end of the structure as well as the coupler will see the full nominal power of CLIC, 135 MW

when the fully combined Drive Beam with a bunch-train length of 140 ns and an average current over the train of 28 A is injected into the TBL.

The TBL lattice and the available diagnostics are comparable to the CLIC decelerator. The beam will fill 2/3 of the aperture after deceleration in TBL due to the much lower Drive Beam energy. Therefore the beam transport of the high energy spread beam is considered more challenging than in CLIC. On the other hand the effect of the wake-fields will be smaller in TBL due to the much shorter decelerator. The quadrupoles have been installed on moving tables developed by CIEMAT [26] which allows positioning in the micrometer range. Beam based alignment studies are foreseen using the precision BPM's developed by IFIC Valencia and UPC Barcelona [27]. Due to the lower initial beam energy the maximum amount of beam energy which can be extracted in TBL is 54% compared to the 90% envisaged in CLIC.

The emphasis for the experimental program of TBL is on 12 GHz power production and the transport of the decelerated beam. The final goal of TBL is to decelerate the Drive Beam by at least 50% of its initial energy of 120 MeV at the end of the beam line. In this case the beam will contain particles with energies between 60 MeV and 120 MeV.

The commissioning of the beam line started at the end of 2009 with nine PETS tanks installed, all constructed by CIEMAT [28] and CERN. Other tanks were installed in the next years, bringing the present total to 13. The maximum power produced so far was about 80 MW per PETS, limited by the maximum transported beam current of 22 A. No sign of breakdown has been observed so far in the PETS. The beam was decelerated from 120 MeV by more than 40 MeV corresponding to about 35% of the beam energy extracted. The 12 GHz power produced by the beam agrees well with the theoretical predictions. To check the consistency of the power production and beam deceleration we can measure a time resolved beam spectrum at the end of the TBL line using a novel segmented dump [29].
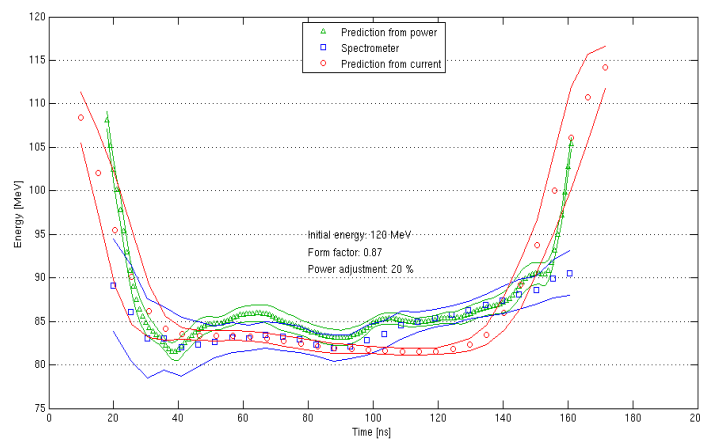
Figure 1.17: Comparison between the measured time resolved energy profile of the beam along the pulse with a segmented beam dump and the predictions from beam current and power production measurements. The data points shown are the average of 48 consecutive pulse and the shaded areas indicate the standard deviation for the measurement over this pulses.

Figure 1.17 shows a comparison of the time resolved energy measurement along the 140 ns long bunch train with the predicted energy profile from the 12 GHz power measurements and the beam current measurements. The three independent

measurements are consistent assuming a bunch form factor of 0.87 for the prediction from the beam current and power measurements and a 20% calibration error in the 12 GHz power measurements. The form factor has been confirmed by bunch length measurements using a streak camera.

It is essential for CLIC that the 12 GHz power production is efficient and stable. The current stability after Drive Beam generation as well as the stability of the 12 GHz power produced in terms of amplitude and phase can be measured directly. For a beam of 12 A obtained by a factor 4 combination in the combiner ring only, a current stability around 1% has been obtained regularly [30], the corresponding amplitude stability of the 12 GHz power scales roughly with the current squared. The phase stability along the pulse has been measured to be within 2° and the phase jitter pulse to pulse to ±5° total. The pulse phase jitter likely comes from a timing jitter of the incoming beam in the ps range.

A first measurement of the BPM resolution measuring the trajectory of the beam in three consecutive BPMs to take out the effects of beam jitter has been performed. For a beam with 13 A average current, 9 μm resolution was measured corresponding well to the specified resolution of 5 μm for the nominal beam current of 28 A. Beam based alignment studies have been started using the micrometric quadrupole movers. The beam could be aligned with a residual misalignment of 250 μm r.m.s. limited to date by beam jitter and residual dispersion coming from upstream of the beam line.

Two more PETS tanks will be installed during the shutdowns in 2014 and 2015 to bring the total of installed PETS to 15. These last PETS will have input and output couplers and will be equipped with internal recirculation systems, based on the PETS On/Off mechanism. This will allow more flexibility in power production and will make easier to reach the 50% deceleration goal with moderate currents.

2.15.9 Conclusions, Ongoing Activities and Outlook.

All identified feasibility issues of the CLIC two-beam scheme, from drive beam generation to its deceleration to produce RF power, and to the use of such power for high gradient acceleration of a second beam have been successfully addressed in CTF3 and were documented in the CLIC CDR [2].

CTF3 will continue its experimental program until 2016 in order to give further indications on cost and performance issues, to act as a test bed for the CLIC technology, and to conduct beam experiments aimed at mitigating technological risks. Additional improvements in beam quality and stability are expected in the near future, in particular from a number of additional feedbacks, meant to stabilize further beam energy and injector phases. The TBTS activities are now concentrating on the full characterization of the wake-field monitors, essential tools for emittance preservation in the CLIC linac. In particular, it is important to assess their resolution in presence of the full power RF pulse and the electromagnetic noise generated by the Drive Beam running in parallel. Also breakdown kicks studies [31] are continuing.

A new experiment studying the breakdown effect is now being implemented [32]. Indeed, the breakdowns limits of accelerating structures have been studied so far without a beam. The presence of the beam modifies the distribution of the electrical and magnetic field, which determine the breakdown rate. Therefore a dedicated experiment was designed: a special beam line allows extracting a beam with nominal CLIC beam current and duration from the CTF3 linac and send it into a structure, powered by an X-

band klystron. It will then be possible to measure the breakdown rate in the presence of beam-loading and in its absence, and to compare them. The beamline installation has been completed, the beam transport through the structure has been established and the RF signal acquisition system has been set up. In 2014 the structure will be connected to the klystron and conditioned, and in the second half of 2014 the measurements should start.

The Drive Beam deceleration studies in TBL are ongoing at present, with the aim of reaching soon 40% with the present set-up and eventually 50% with the installation of the two new PETS tanks. The new tanks would also allow for the installation close to them of accelerating structure for RF conditioning and high-power testing.

A central role in the CTF3 experimental program in the next years will be played by the Drive Beam phase feed-forward experiment described before, and by the test of a full-fledged two-beam module in CLEX. The module program should cover the following points: a) test of the RF behavior of the module (system conditioning, breakdown rate and potential PETS/structures cross talk), b) two-beam acceleration tests (energy gain, set-up with beam and two-beam phasing), c) test of the active alignment system and of the stabilization system, in presence of radiation and electromagnetic noise, d) verification with beam of alignment and fiducialization using wake-filed monitors and high resolution BPMs and e) phase drift studies.

In parallel with CTF3 operation, we are also planning to build a new test facility, the Drive Beam front-end, in order to help the CLIC study advance towards a project implementation plan. Such a facility will consist of a 10-20 MeV Drive Beam injector and will be a first step towards the CLIC0 facility. It will drive the technology development of modulators, klystrons, and accelerating structures for the CLIC Drive Beam linac at the correct CLIC parameters and will address the issues related to high average power and long-pulse beam handling. An active R&D program on the essential components of the front-end has started, and from 2016 we should have all components to start assembling the test accelerator.

2.15.10 **References**

1. G. Geschonke and A. Ghigo Eds, "CTF3 Design Report", CERN/PS 2002-008 (RF).
2. M. Aicheler et al., "A Multi-TeV Linear Collider Based on CLIC Technology : CLIC Conceptual Design Report", CERN-2012-007; SLAC-R-985; KEK-Report-2012-1; PSI-12-01; JAI-2012-001.
3. Y. Thiery, J. Gao, J. LeDuff, "CTF3 Drive-Beam Injector Design", in Proc. XX Int.l Linac Conf., 21-25 August 2000, Monterey, CA, USA (2000), 95–97.
4. P. Urschuetz et al., "Beam Dynamics Studies and Emittance Optimization in the CTF3 Linac at CERN", Proceedings of EPAC 2006, Edinburgh, UK (2006), 798–800.
5. A. Dabrowski et al. "Measuring the Bunch Frequency Multiplication at CTF3" in Proc. 1st Int. Particle Accelerator Conf., 23-28 May 2010, Kyoto, Japan (2010), 1107–1109.
6. P. Urschütz et al., "Beam Dynamics and First Operation of the Sub-Harmonic Bunching System in the CTF3 Injector", Proceeding of EPAC 2006, Edinburgh, UK (2006), 771–773.
7. E. Jensen, "CTF3 Drive Beam Accelerating Structures", in Proc. XXI Int. Linear Accelerator Conf., 19-23 August 2002, Gyeongju, Korea (2002), 34–36.
8. R. Corsini et al. "First Full Beam Loading Operation with the CTF3 Linac" in Proc. 9th European Particle Accelerator Conf., 5-9 July 2004, Lucerne, Switzerland (2004), 39–41.
9. P. Urschuetz et al. "Efficient Long-Pulse Fully Loaded CTF3 Linac Operation" in Proc.

2006 Linear Accelerator Conf., 20-25 August 2006, Knoxville, Tennessee, USA (2006), 31–33.

10. P.K. Skowroński et al., "Progress Towards The CLIC Feasibility Demonstration In CTF3", in Proceedings of IPAC'10, Kyoto, Japan (2010) 3410–3412.

11. D. Alesini et al., "Beam instability induced by RF deflectors in the combiner ring of the CLIC test facility and mitigation by damped deflecting structures", Phys. Rev. ST Accel. Beams 14, 022001 (2011).

12. D. Schulte et al., "Status Of The CLIC Phase and Amplitude Stabilisation Concept", in Proc. XXV Linear Accelerator Conf., 12-17 September 2010, Tsukuba, Japan (2010), 103–105.

13. G.Sterbini, "Beam current stability in CTF3, international Workshop on Future Linear Colliders, 2010, Geneva, Switzerland (2010).

14. A. Dubrovskiy, F. Tecker, "RF Pulse Compression Stabilization at the CTF3 CLIC Test Facility", in Proc. 1st Int. Particle Accelerator Conf., 23-28 May 2010, Kyoto, Japan (2010), 3774–3776.

15. T. Persson, "Drive beam stability studies and stabilization algorithms in CLIC Test Facility 3", Nucl. Instrum. Methods Phys. Res. A, Volume 735, 21 January 2014, Pages 152–156.

16. P.K. Skowroński et al., "Design of Phase Feed-Forward System in CTF3 and Performance of Fast Beam Phase Monitors", in Proc. of IPAC'13, Shanghai, China (2013) 2097–2099.

17. E. Ikarios et al., "The Drive Beam Phase Stability in CTF3 and its Relation to the Bunch Compression Factor", in Proc. of IPAC'13, Shanghai, China (2013) 1655–1657.

18. I. Syratchev et al., "High-Power Testing of X-Band CLIC Power Generating Structures", in Proc. 23rd IEEE Particle Accelerator Conf., 4-8 May 2009, Vancouver, British Columbia, Canada (2009), 1873–1875.

19. E. Adli, " A Study of the Beam Physics in the CLIC Drive Beam Decelerator", (University of Oslo, 2009).

20. I. Syratchev, G. Riddone, S. Tantawi, "CLIC RF High Power Production Testing Program", in Proc. 11th European Particle Accelerator Conf., 23- 27 June 2008, Genoa, Italy (2008), 1909–1911.

21. E. Adli et al., "X-band rf power production and deceleration in the two-beam test stand of the Compact Linear Collider test facility", Phys. Rev. ST Accel. Beams 14, 081001 (2011).

22. I. Syratchev, & A. Cappelletti, "A New High-Power RF Device to Vary the Output Power of CLIC Power Extraction and Transfer Structures (PETS)", in Proc. 1st Int. Particle Accelerator Conf., 23-28 May 2010, Kyoto, Japan (2010), 3407–3409.

23. I. Syratchev et al., "High Power Operation with Beam of a CLIC PETS Equipped with On/Off Mechanism", in Proc. IPAC 2012, New Orleans, Louisiana, USA, 1852–1854.

24. Peauger, F., Bogard, d., Cheymol, G., Contrepois, P. et al. "Status of the CTF3 Probe Beam Linac CALIFES", in Proc. XXIV Linear Accelerator Conf., 29 September - 3 October 2008, Victoria, British Columbia, Canada (2008), 389–391.

25. P.K. Skowronski et al., "The CLIC Feasibility Demonstration in CTF3", in Proc. IPAC 2011, September 2011, San Sebastian (2011), 1042–1044.

26. F. Toral, et al. in Proc. 11th European Particle Accelerator Conf., 23-27 June 2008, Genoa, Italy (2008), 1517–1519.

27. J.J. Garcia Garrigos, "Design and Construction of a Beam Position Monitor Prototype for the Test Beam Line of the CTF3" CLIC-Note-769 (Universitat Politecnica de Valencia, Valencia, Spain, 2008).

28. F. Toral et al. in Proc. 1st Int. Particle Accelerator Conf., 23-28 May 2010, Kyoto, Japan (2010), 3768–3770.

29. M. Olvegaard et al., "Beam Profile Monitoring at the Test Beam Line at CTF3", Phys. Rev. ST Accel. Beams 16, 082802 (2013).

30. R.L. Lillestol, "Experimental Results from the Test Beam Line in the CLIC Test Facility 3", in Proc. of IPAC 2013, Shanghai, China (2013), 1814–1816.
31. A. Palaia et al., "Effects of RF breakdown on the beam in the Compact Linear Collider prototype accelerator structure", Phys. Rev. ST Accel. Beams 16, 081004 (2013).
32. F. Tecker et al., "Experimental Study of the Effect of Beam Loading on RF Breakdown Rate in CLIC High-Gradient Accelerating Structures", in Proc. of IPAC 2013, Shanghai, China (2013), 1691–1693.

2.16 The CTF3 Two-beam Test Stand

Roger Ruber, Andrea Palaia, Volker Ziemann, Uppsala University, Sweden
Wilfrid Farabolini, Roberto Corsini, Igor Syratchev, CERN, Switzerland
Mail to: Roger.Ruber@physics.uu.se

Abstract

The Two-beam Test Stand (TBTS) is the main location to demonstrate the feasibility of the CLIC two-beam acceleration scheme. Drive and main beam, here also called probe beam, are available to test and verify both RF production and high gradient acceleration. Individual components and complete two-beam CLIC modules can be tested. The TBTS is particularly well suited to investigate the effects on the beam of RF breakdown in the high gradient accelerating structures.

2.16.1 Introduction

In the CLIC two-beam acceleration scheme the required radio-frequency (RF) power needed to accelerate the main beam to high energies is generated by decelerating the so-called drive beam, a second, lower energy but higher intensity and higher power density electron beam that runs parallel to the main beam, in the context of CTF3 also called the probe beam. This process is schematically shown in Figure 1. The RF field is produced in so-called power extraction and transfer structures (PETS) which, as the name implies, also transfer it to the accelerating structures of the main beam. These accelerating structures are normal-conducting, designed for 12 GHz (X-band) operation, and are expected to achieve high-accelerating gradients, which is the requirement for keeping the length of the accelerator within reasonable limits.
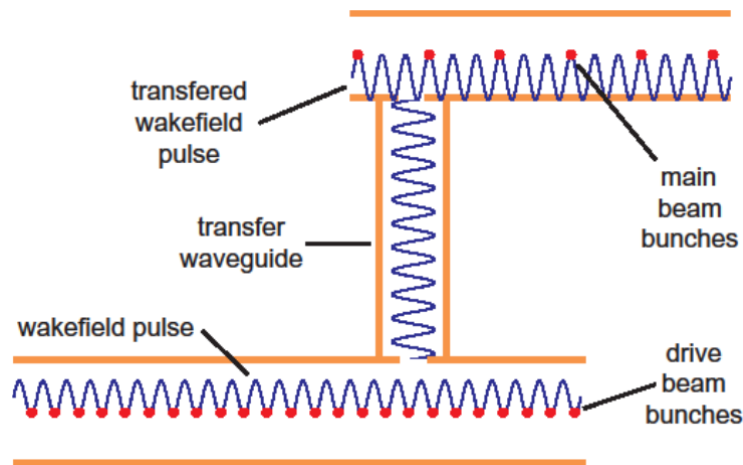
Figure 1: Two-beam acceleration scheme. The RF wakefield created by the drive beam is transferred to the main (probe) beam accelerating structures. Due to differences in the group velocity of the RF wave, the energy density is increased and thereby the electric field magnitude.

One of the central issues for the CTF3 test facility is the verification of the feasibility of the two-beam acceleration scheme including the PETS power extraction structures and the main beam acceleration structures. This verification and the investigation of various limiting aspects of the scheme is the principal task of the TBTS [1]. The previous CTF1 and CTF2 test facilities have provided the proof of principle for the two-beam acceleration scheme, albeit with low intensity and low energy beams [2, 3]. The CTF3 beam intensity is considerable higher than in the previous test facilities, but still lower than in CLIC: The drive beam reaches a final beam intensity of 30 A compared to 100 A in CLIC. The drive and probe beam (main beam in CLIC) energies are in the range of 100 to 200 MeV. The TBTS uses a prototype CLIC accelerating structure and an extra long PETS structure (to compensate for lower beam current) for the two-beam acceleration feasibility study and addresses these issues at the same RF power level and 100 MV/m accelerating gradient as proposed for CLIC. In the TBTS, the RF power is used to accelerate the probe beam which is prepared in the CALIFES linac. The TBTS is the only facility where CLIC type accelerating structures can be tested with beam. It is used in an extensive program to investigate both PETS power generation structures and high gradient accelerating structures.

2.16.2 Goals and Requirements

The TBTS is designed as a versatile facility focused on research and development of the two-beam acceleration concept. The main aim is to demonstrate two-beam acceleration and facilitate research related to the two-beam acceleration concept. The research scope includes prototype CLIC structures for high gradient beam acceleration and power generation in PETS structures as well as the effects on the beam of acceleration, deceleration during power generation and RF breakdown. Furthermore, the two-beam acceleration concept requires an accurate timing between the arrival phase of the two beams.

The experimental program is summarized as:
- Fundamental mode behaviour of the structures; acceleration and deceleration,

beam kicks.

- RF breakdown; especially in the presence of beam and resulting beam kicks.
- Effect of higher order modes; their influence on the beam (wakefields) and their usefulness for beam based alignment.
- Timing of the two beams, to align the RF phase for optimal acceleration.
- Full system behaviour; step from component prototypes to two-beam acceleration unit prototype. Cross talk between drive and probe beam. Intra-unit alignment studies between multiple two-beam acceleration units.

The fundamental mode studies are intended to understand the effects of acceleration and deceleration on the respective beams. These effects can, among others, depend upon the bunch train structure and beam phase variation along the pulse, beam current and RF power. The studies involve measurements of the energy loss and gain of the beams, as well as energy spread and beam emittance.

The RF breakdown and higher order mode studies are intended to understand their effects on the traversing beams. Especially the effect of transverse beam kicks is important as it may have severe influence on both the drive and main beam behaviour.

Such beam kicks can be due to higher order mode fields in the structure, as function of the beam offset, but also due to the breakdown of the RF field in the accelerating structure, the so-called RF breakdown.

For optimal acceleration of the probe beam it is required to achieve accurate timing of the probe beam arrival to the phase of the RF power produced by the drive beam. This makes it necessary to ensure both a coarse timing of drive and probe beam arrival, and then a fine timing adjustment to the phase of the 12 GHz drive beam generated RF pulses, which is on a sub-ps level. If the intensity of the arrival phase of the drive beam fluctuates, the amplitude and phase of the drive beam generated RF will affect the energy gain of the probe beam.

The full system studies are intended to understand the behaviour of a complete two-beam acceleration module, as opposed to the individual component studies. These studies will use prototype CLIC two-beam acceleration modules that contain drive and probe beam components in one mechanical set-up. The studies are used to validate the design and integration of all technical systems as well as intra-module alignment.

The experimental program requires that the beam lines and RF structures are equipped with instrumentation to perform the studies which require different configurations of the TBTS beam lines and RF structures. Therefore studies are performed during different build-up and instrumentation phases:

A. Single component tests Test of basic RF components;
- pure RF power tests without beam.
- investigation of behaviour with beam.

This includes beam kick and wakefield monitoring studies. The RF power tests without beam can be performed at a klystron based test stand.

Phase 0 with beam lines only, before installation of PETS or accelerating structure in the experimental areas.

Phase 1 with one PETS installed in the drive beam line.

Phase 2 with one PETS in the drive beam line and one or two accelerating structure(s) in the probe beam line, enabling study of two-beam acceleration.

B. Complete unit tests Test of complete two-beam acceleration units;
- complete module with multiple PETS and accelerating structures.

Uses the probe beam as a diagnostics tool for the module girder alignment by wakefield monitoring.
Phase 3 with one CLIC prototype two-beam acceleration module installed.

At the present writing of this article (Fall 2013), the TBTS is in phase 2. It is expected to start installation of phase 3 during mid-2014.

2.16.3 **Overall Design**

The TBTS consists of two parallel beam lines fed with the drive and probe beam, respectively, as shown as schematic in Figure 2. The actual installation is shown in Figure 3. The optics of the two beam lines is similar with differences in the drift spaces to adjust for the physical constraints in the CLEX hall so as to have the test areas for drive and probe beam next to each other while allowing sufficient space for beam instrumentation and other diagnostics including spectrometer lines at the end of both beam lines. Quadrupole triplets and steering magnets adjacent to the experiment area are used to adjust the beam size in the experiment area and guide the beam. The transverse positions of the beams are observed using beam position monitors (BPM) and the beam size using screens that can be remotely inserted into the beam path and observed with cameras. At the end of each beam line there is a spectrometer dipole magnet in conjunction with a BPM and a screen, used to analyze the energy lost or gained by the respective beams.
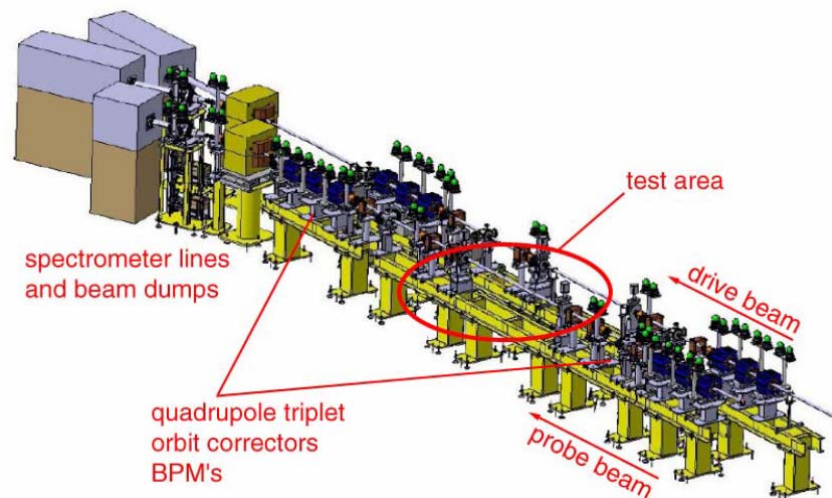
Figure 2: Two-beam Test Stand layout with the drive and probe beam lines.

Figure 3: Photo of the Two-beam Test Stand with the drive beam line (left) and probe beam line (right) [18] before installation of PETS and accelerating structure.
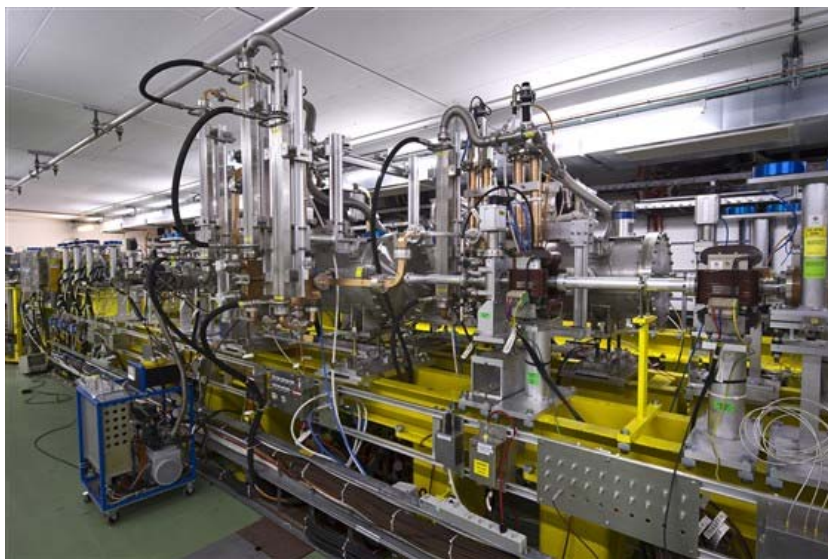
Figure 4: Photo of the TBTS experiment area with vacuum tanks for PETS (to theright) and accelerating structure (at the left) [19].

In the experiment area, see Figure 4, large vacuum tanks installed in the drive and probe beam contain the RF structures for power extraction and beam acceleration respectively.

The PETS power extraction structure installed in the drive beam transfers RF power to the accelerating structure (ACS) in the probe beam through interconnecting waveguides which are equipped with directional couplers to monitor the RF power flow. The experiment areas of 1.8 m length in the drive beam and 2 m in the probe beam are bordered by vacuum sector valves to allow for changing experiment equipment without affecting the accelerator vacuum [4]. The beam line vacuum tubes are made of 40 mm diameter aluminium pipes.

2.16.4 CALIFES Probe Beam Accelerator

The TBTS uses both the drive beam, generated in the main part of the CTF3 facility, and the probe beam, generated in the same hall as the TBTS. The probe beam is generated in the 24 m long CALIFES linac (Concept d'Accelrateur Lineaire pour Faisceau d'Electron Sonde) which is situated in the same experiment hall as the TBTS. It has been developed to deliver single bunches as well as bunch trains at 1.5 GHz bunch repetition rate [5]. Detailed parameters are listed in Table 1. CALIFES is based on three LEP Injector Linac (LIL) 3 GHz accelerating structures of which one can be used as buncher. The beam is generated in a laser triggered photoinjector of which the photocathode can be regenerated in an adjacent cathode preparation chamber [6]. The laser produces infra-red pulses at 1.5 GHz repetition rate, which are converted to green and then to ultra-violet before hitting the photocathode [7]. Excellent beam quality is required for the high gradient acceleration tests in the TBTS. Therefore the end of the linac has been equipped with a diagnostics sections to measure bunch train charge, energy, pulse length and beam emittance [8]. A 3 GHz traveling wave deflecting cavity is used for bunch length measurements by transverse tilting of the electron bunches.

Bunch lengths in the order of 1.4 ps have been measured. In full acceleration mode, in which the buncher cavity is used in acceleration mode, a further acceleration of the probe beam is obtained above its design value from 180 MeV up to 200 MeV, albeit with longer bunch lengths. The energy spread can be tuned to less than 1%RMS. A normalized beam emittance of 10 mm.mrad has been achieved [8].

Table 1: Main parameters of the CALIFES probe beam.

Parameter		Unit
energy	180	MeV
energy spread (RMS)	1	%
pulse length	0.6-150	ns
bunch frequency	1.5	GHz
bunch charge	0.05-0.6	nC
intensity		
- short pulse	1	A
- long pulse	0.13	A
repetition rate	0.8-5	Hz
beam parameters (example)		
- β	1	m
- ε	2.6×10^{-8}	m
- relative momentum spread	0.014	
- beam size (4σ)	0.65	mm

2.16.5 Instrumentation

A central role in the TBTS is played by the instrumentation to diagnose the behaviour of the beam under normal operation as well as, very important, in the presence of RF discharges (also called RF breakdown) in the accelerating structures that will limit the performance of CLIC and therefore need to be understood. Moreover the

diagnostic system is needed to analyze the power transfer from the PETS to the ACS, to investigate the two-beam acceleration and RF breakdown phenomena. An overview of the diagnostic system is shown in Figure 5.
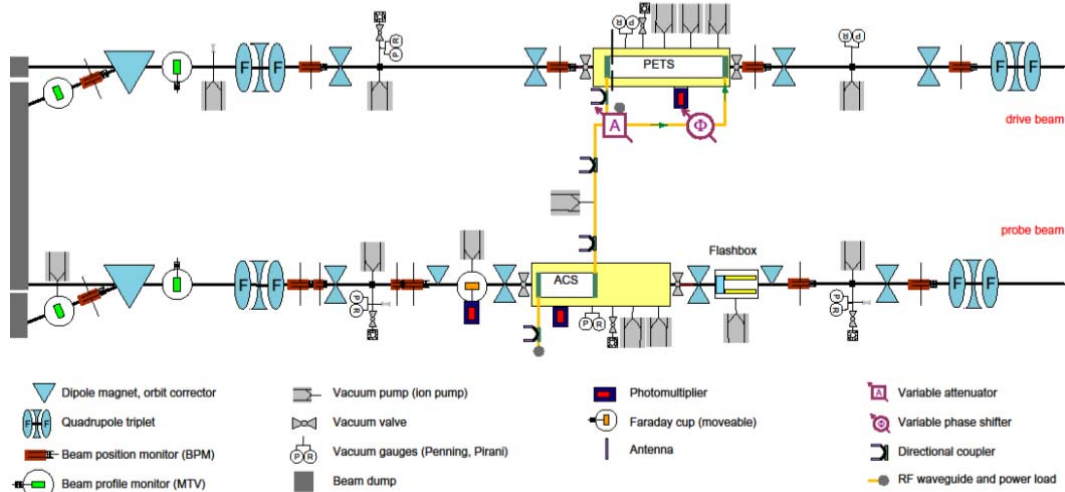
Figure 5: Layout of the two beam lines and installed equipment. The drive beam is theupper line, the probe beam is the bottom line.

CTF3 operates on a pulsed basis and discharges are just occurring occasionally and are therefore rare events, which implies that all diagnostic devices need to be read out synchronized on a per-pulse basis. Moreover, the beam pulses are rather short, on the order of 100 ns, which implies that fast digitizers are employed also for the beam generated signals, such as those from the BPMs and the RF and breakdown diagnostics instrumentation.

Beam energy measurements are done with spectrometer lines equipped with beam position and beam profile monitors. The beam kick studies require the beam lines to be equipped with beam position monitors before and after the structures in the experimental areas. In addition, the study of RF breakdown requires diagnostics to measure breakdown currents emitted from the structures in presence of the beam.

Two quadrupole triplets are used to vary and optimise the beam size in the experiment area and on a beam profile monitor screen positioned downstream of a spectrometer dipole in order to maximise the energy resolution. Small beam sizes below 0.2 mm can be reached in the experiment area, see Table 1. A beam profile monitor for emittance measurements is installed after the second quadrupole triplet. The spectrometer lines include one beam position monitor and one video profile monitor with a nonmoveable screen. The downstream quadrupole triplet is tuned as to make an upright elliptical spot on the beam screen in order to maximize the energy resolution.

Table 2: Parameters of the beam line instrumentation.

Parameter		Unit
Inductive beam position monitor		
amount	10	
beam impedance	10	Ω
length electrodes	90	mm
signal bandwidth (after front electronics)		
- ΔH, ΔV	0.8 – 150000	kHz
- Σ	0.3 – 250000	kHz
achieved resolution		
- drive beam	0.06	mm
- probe beam	0.3	mm
Re-entrance cavity beam position monitor		
amount	2	
resonance frequency	5.997	GHz
signal bandwidth	600	MHz
achieved resolution	0.02	mm
Beam profile monitor		
amount	4	
screen		
- probe beam, straight line	40x40 YAG	mm
- probe beam, spectrometer	150x48 St.Gobain AF995R	mm
- drive beam, straight line	20x20 stainless steel OTR	mm
- drive beam, spectrometer	170x38 parabolic aluminium OTR	mm
camera type	CCD	
achieved resolution	0.1	mm

Five inductive beam position monitors (BPM) are installed for intensity and position measurements [9]. They are used in combination with four steering magnets to control the beam position and the incident angle of the beam in the experiment area. The steering magnets can also adjust the beam trajectory inside the experiment area with a closed bump. The probe beam includes two extra horizontal steering dipoles just before the experiment area. They are used as a small chicane to separate low energy electrons and ions emitted by RF breakdowns in the experiment area from the accelerator beam. This can be used to protect the BPM readout from being overloaded with background. Table 2 lists the basic parameters. Unfortunately the initial resolution of the BPMs in the probe beam line was not satisfactory due to low signal gain and high noise levels. The front end electronics on these BPMs in the probe and drive beam were set-up for the same signal gain, however the drive beam has a much lower current and thus signal level. Therefore the front end electronics on the BPMs in the probe beam were modified to increase the signal gain. Recently (2012) two re-entrant cavity BPMs have been

installed in probe beam line in direct connection with the two inductive BPMs behind the experimental area. In the probe beam, these BPMs achieve a ten times higher resolution than the inductive BPMs. Beam profile monitors are used for emittance measurements, measurements of beam energy spread and to optimize the beam conditions. For the emittance measurements, the monitors are placed at the end of the straight line, after the second quadrupole triplet and before the spectrometer dipole. Table 2 lists the basic parameters. The beam profile monitors in the straight line are equipped with an aluminium deposit optical transition radiation (OTR) screen for the drive beam and a YAG screen for the probe beam [10]. For the spectrometer lines, an OTR screen is used in the drive beam, made of aluminium in a parabolic shape to reduce the vignetting effect in the optical system [11]. The probe beam spectrometer line, with its lower beam intensity, has a high sensitivity fluorescent ceramic screen.

RF breakdown can be detected from the RF amplitude and phase measurements before and after the accelerating structure by analyzing the signals for reflected and transmitted power and missing energy. In addition RF breakdowns can be detected with photomultipliers sensitive to UV and visible light that are installed viewing one of the PETS and ACS.

An insertable Faraday cup is installed on the downstream side of the probe beam experiment area to measure discharges in the ACS in the absence of beam. It can be used to measure both dark and breakdown currents. A so-called Flashbox is installed on the upstream side with which it is possible to detect discharges also if the probe beam is present. It includes sensors for electron and ion detection from possible breakdown currents emitted from the accelerating structure. No measurements had yet been performed with the Flashbox nor Faraday cup when preparing this article.

2.16.6 Power Generation

After the first commissioning of the beam lines and the installation of a PETS structure in the drive beam, an external RF power recirculation system was installed that recirculates the RF power produced by the PETS in order to increase the RF power inside the PETS and to test the PETS structure more thoroughly and under higher RF power levels. Figure 6 shows the conceptual setup of the recirculation loop. Experience gained in running showed that the PETS performed reliably [12, 13]. In order to understand the dynamical behaviour of the RF power build-up due to RF power recirculation in the PETS, an analytical model was devised with which the measured RF pulse can be predicted from beam intensity data as measured by a BPM. Figure 7 shows an example of measured and predicted (reconstructed) RF power level. This analysis model led to a detailed understanding of the energy balance of the entire system with beam and RF power by analyzing the energy lost by the beam and the RF power measured in the RF diagnostics. The lost energy, or deceleration, of the beam can be measured with the drive beam spectrometer or estimated from the RF power production. The results are published in [14].
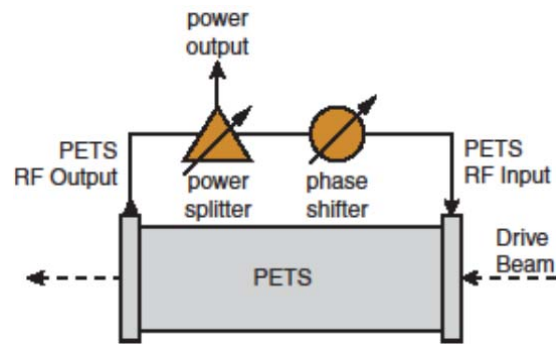
Figure 6: Layout of a PETS with external RF power recirculation option.
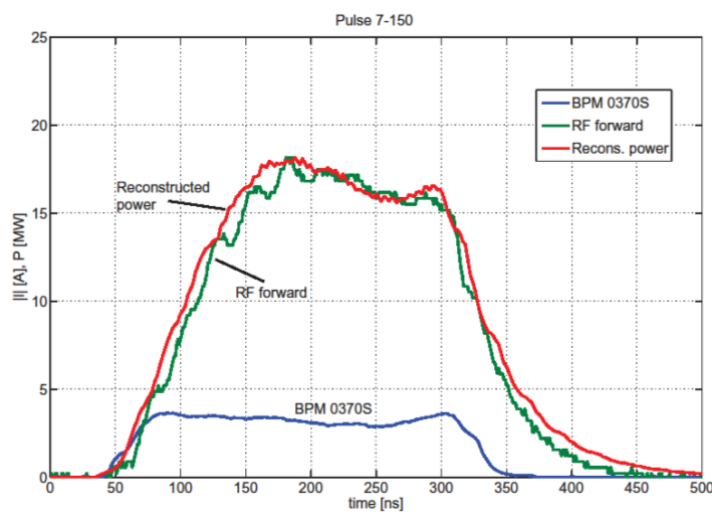
Figure 7: Example of a drive beam pulse with measured (marked RF forward) and reconstructed RF power generation from the PETS. RF recirculation gain $g = 0.75$ and phase shift $\varphi = 18^{\circ}$. Recirculation round-trip time $\tau = 26$ ns. For comparison, the BPM pulse is also shown.

During the 2009 run, the PETS produced over 170 MW peak power in full RF recirculation mode, exceeding the 240 ns nominal pulse length and well above the nominal 135 MW foreseen in CLIC. However, many pulses during that run exhibited sudden drops in RF power, a pulse shortening which was linked to RF breakdown in the RF power recirculation system. The performance was limited by this effect, linked to a high power variable splitter and phase shifter. These parts were repaired and improved for the 2010 run.

2.16.7 Two-beam Acceleration

During the 2010 run the first two-beam acceleration of the probe beam was achieved [15] using a 12 GHz high gradient accelerating structure (see Figure 8 and Table 3). This first required to carefully synchronize the arrival time of the probe beam bunches to the phase of the RF power generated with a precision of a few degrees. This measurement is done by observing the position of the drive beam on a screen in the spectrometer beam line at the end of the TBTS and observing how the position moves

while varying the relative phase or arrival time of the probe beam with respect to that of the drive beam.
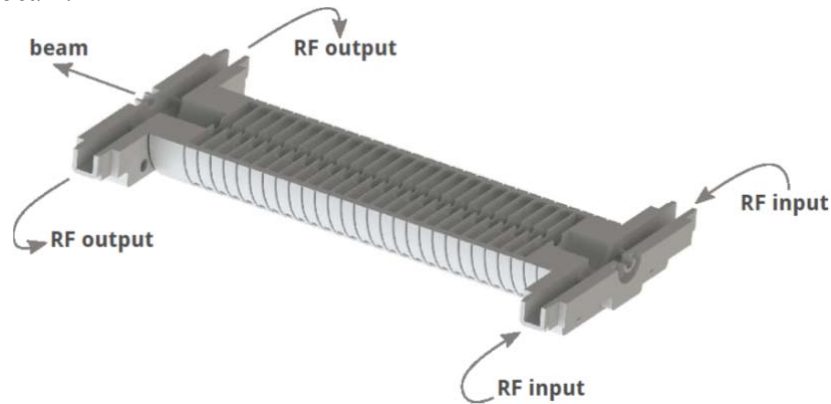
Figure 8: Longitudinal cross section of a type 12WDSDVG1.8 accelerating structure.

Table 3: Parameters of the accelerating structure.

Parameter	
name	12WDSDVG1.8 or TD24_vg1.8_disk
frequency	11.995 GHz
number of cells	24 + input cell + output cell
length	22.77 cm
filling time	64.55 ns
inner radius	3.15 tapered down to 2.35 mm
group velocity	1.617 or 0.811% of c
phase advance per cell	$2\pi/s$
input power	
- loaded	46.55 MW for 100 MV/m
- unloaded	42.20 MW for 100 MV/m

Once the timing is adjusted, the power level in the PETS can be adjusted and it is then possible to actually measure the probe beam acceleration in the ACS. The accelerating gradient and energy gain as function of the RF input power is shown in Figure 9, and compared to the nominal expectation of this accelerating structure (black line). The nominal CLIC accelerating gradient of 100 MV/m correspond to a $\Delta E = 21.4$ MeV in the 22 cm long ACS. The acceleration measurements were done with the beam screen in the spectrometer line while running the probe beam at twice the repetition rate of the drive beam. Thus accelerated and non-accelerated beam energies can be measured alternatively. Figure 10 shows an example 23 MeV probe beam acceleration.
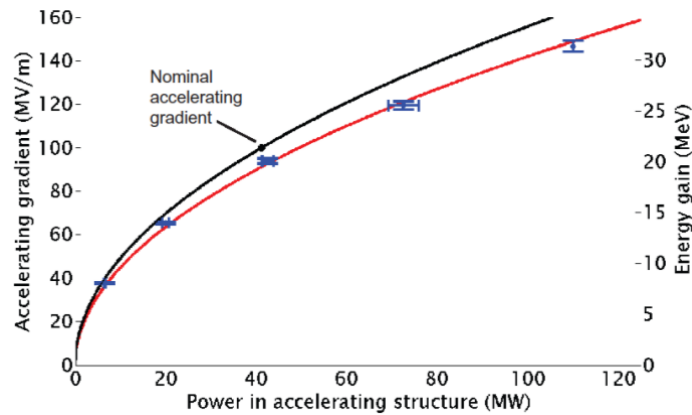
Figure 9: Measured and nominal (upper line) accelerating gradient as function of the RF input power for accelerating structure 12WDSDVG1.8 (2011 run). The corresponding beam energy gain is given on the right hand axis.
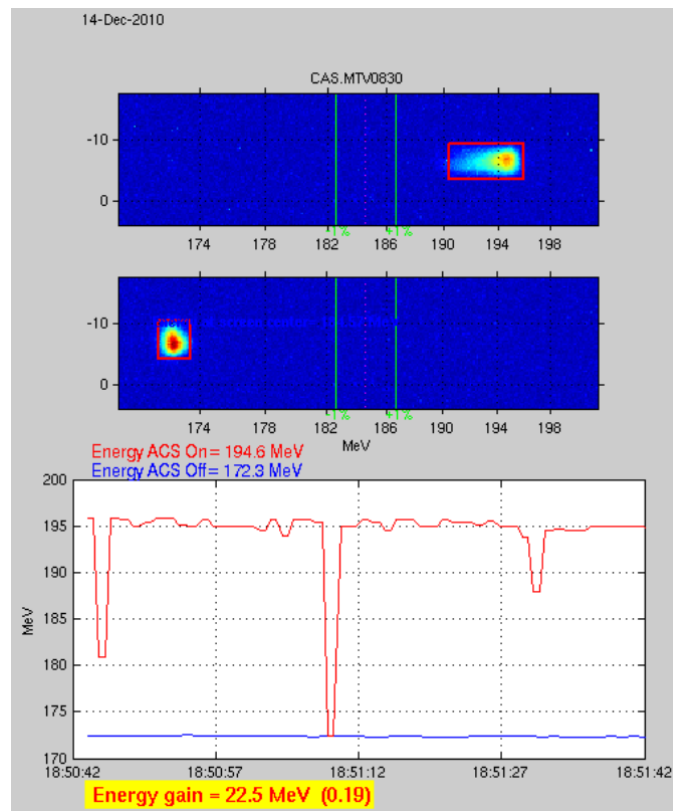
Figure 10: Two-beam acceleration measurement of the probe beam. The probe beam is operated at double repetition frequency compared to the drive beam and RF power pulse. Thus every other pulse is accelerated (top beam profile monitor snap-shot) while the pulse in between is not (bottom beam profile snap-shot). The bottom graph shows the stability of the probe beam energy with (ACS on, upper line) and without acceleration (ACS off, lower line).

In Figure 9 the measured accelerating gradient is consistently below the calculated gradient. We believe that the measured RF power level is overestimated due to the used calibration procedures. Methods are investigated to improve the calibration procedure.

2.16.8 Beam Trajectory Kicks

By RF breakdown we denote an electric discharge in vacuum in the presence of the RF field that provides the accelerating gradient in the accelerating structure. RF breakdown is considered to limit the transmission of the RF wave in the travelling wave accelerating structure and thereby limiting the beam acceleration. RF breakdown seems to occur randomly when the structures are driven by RF power pulses and its rate depends among others on the RF power level, the length of the RF power pulses and the length of the run period.

RF breakdown and beam induced higher order modes in PETS and accelerating structures can affect the beam, modifying its trajectory and energy. For the design

of a stable two-beam accelerator it is important to understand these effects. A beam trajectory kick can be determined using the horizontal and vertical beam position measurements in the BPMs [16]. The layout of the set-up used to measure such beam trajectory kicks comprises five BPMs in the beam line and is shown in Figure 11.
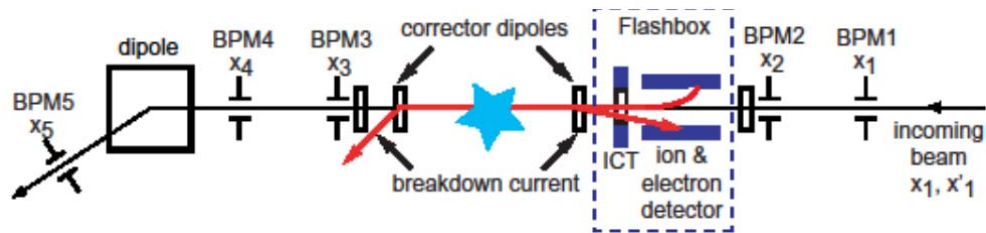
Figure 11: Scheme of the transverse kick and breakdown current measurements.
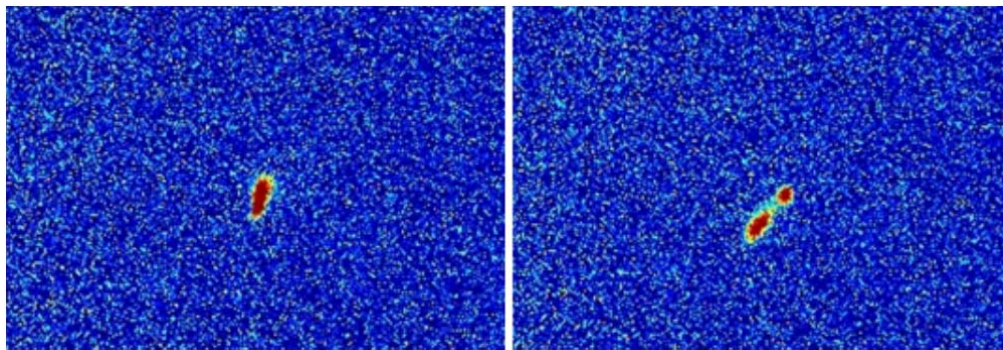
Figure 12: Example of a double beam spot detected on a beam screen in correspondence of a RF breakdown in the accelerating structure (right) and the beam under normal operating conditions (left). The image on the right is interpreted as one part of the beam pulse having received a kick during an RF breakdown event.

The first measurements of the effects on the beam trajectory by RF breakdown in the accelerating structure were performed in 2011. They are based on measurements of the beam spot with a YAG type beam profile monitor situated just in front of the spectrometer line dipole because the achieved position resolution was at that time better than with the BPMs. Double spots, of which one example is shown in Figure 12, were occasionally measured on the same beam pulse. This is interpreted as resulting from a change of the beam trajectory during the pulse. In a preliminary analysis the double spots that appeared on 35 individual breakdown events were considered. They were

recorded during 24 hours within a period of three days during Aug 2011. Plotting the difference of the center of gravity of the two spots leads to the distribution shown in the compass plot in Figure 13. During these measurements the RF power into the accelerating structure was fluctuating between 60 and 85 MW due to drive beam variations. The probe beam energy was 195 MeV with 30 MeV acceleration in the accelerating structure. Beam pulse length was 132–136 ns with bunch spacing of 0.666 ns (determined by the laser structure), bunch charge of 0.07 nC and beam repetition rate of 0.8 Hz. The magnitude of the measured kicks is about 0.13 mrad, which corresponds to a transverse momentum of about 25 keV/c in the accelerating structure. The number of events is unfortunately too small to draw any further conclusions. Detailed studies are continuing and eventually this analysis will give valuable information about the severity of the disturbance to the beam trajectory that is caused by breakdown events and how much operation of CLIC would be disrupted by this phenomenon. The latest results of the measured kick magnitude are shown in Figure 14 and have recently been published in detail [17].
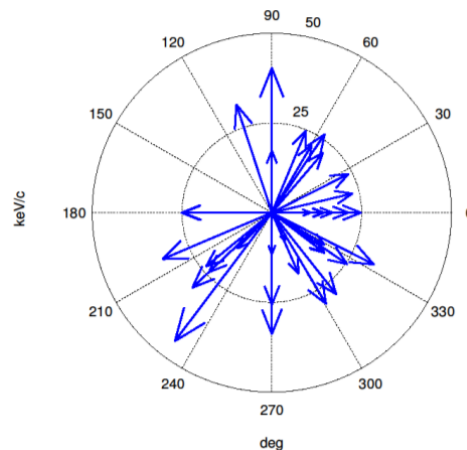
Figure 13: Compass plot showing direction and transverse momentum of beam trajectory kicks in correspondence to a RF breakdown in the accelerator structure. The transverse momentum is calculated considering the beam energy and the distance between the screen used for the measurement and the accelerator structure.
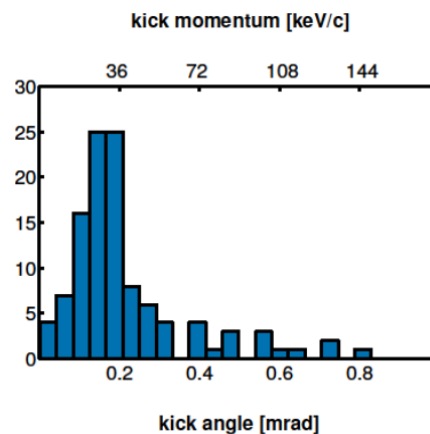
Figure 14: Distribution of the total magnitude of observed RF breakdown kicks to the probe beam.

2.16.9 **Conclusions**

The construction and commissioning of the originally designed TBTS is completed. It is currently used as an active research facility and continues to be upgraded and recommissioned. The facility is a central part of the ongoing effort to demonstrate the feasibility of the two-beam acceleration scheme for CLIC. The achieved 100 MeV/m acceleration gradient is the highlight of TBTS operation so far and represents a decisive milestone for demonstrating the feasibility of two-beam acceleration and the CLIC project. In the continued studies reliability aspects, such as the rate of breakdown events and their effect on the beam, will assume a more central role. Special developed diagnostics such as the Flashbox will be used to investigate the energy and charge profile of the RF breakdown currents.

2.16.10 **Acknowledgements**

2.16.11 **References**

1. Tord Ekelöf et al. The Two-beam Test-stand in CTF3. In Proc. EPAC'06 [20], page 2445. http://www.JACoW.org.
2. Hans Braun et al. Results from the CLIC Test Facility. In Proc. EPAC'96, page 42. EPAC 1996, June 1996, Sitges. http://www.JACoW.org.
3. Hans Braun. Experimental Results and Technical Research and Development
4. at CTFII. In Proc. EPAC'00, page 48. EPAC 2000, June 2000, Vienna. http://www.JACoW.org.
5. R. Ruber et al. The CTF3 Two-beam Test-stand: Installation and Experimental Program. In Proc. EPAC'08 [21], page 2821. http://www.JACoW.org.
6. A. Mosnier et al. The Probe Beam Linac in CTF3. In Proc. EPAC'06 [20], page
7. 679. http://www.JACoW.org.
8. Julien Brossard et al. Construction of the Probe Beam Photo-injector of CTF3. In Proc. EPAC'06 [20], page 828. http://www.JACoW.org.
9. F. Peauger et al. Status of the ctf3 probe beam linac califes. In Proc. LINAC'08, page 389. LINAC 2008, September-October 2008, Victoria, Canada. http://www.JACoW.org.
10. Wilfrid Farabolini et al. CTF3 Probe Beam Linac Commissioning and Operation. In Proc. LINAC'10, page 46. LINAC 2010, September 2010, Tsukuba, Japan. http://www.JACoW.org.
11. Marek Gasior. An inductive pick-up for beam position and current measurements. In Andreas Peters and Volker Schaa, editors, Proc. DIPAC 2003, page 53. DIPAC 2003, May 2003, Mainz. http://www.JACoW.org.
12. Wilfrid Farabolini et al. Video Profile Monitors Development for the CTF3 Probe Beam Linac. In Proc. EPAC'08 [21], page 1101. http://www.JACoW.org.
13. C. Welsch et al. Design Alternatives for Beam Halo Monitors in High Intensity

Accelerators. In Proc. DIPAC'05, page 54. DIPAC 2005, June 2005, Lyon. http://www.JACoW.org.

14. Igor Syratchev et al. High power testing of x-band clic power generating structures. In Proc. PAC'09, page 1873. PAC 2009, May 2009, Vancouver, Canada. http://www.JACoW.org.

15. Igor Syratchev. High Power Operation with Beam of a CLIC PETS Equipped with ON/OFF Mechanism. In Proc. IPAC'12, page 1852. IPAC 2012, May 2012, New Orleans, Louisiana, U.S.A. http://www.JACoW.org.

16. Erik Adli et al. Characterization of RF power production and deceleration in a power extraction structure with field recirculation. Phys. Rev. ST Accel. Beams, 14:081001, 2011.

17. Wilfrid Farabolini et al. Two Beam Test Stand Experiments in the CTF3 Facility. In Proc. IPAC'11, page 29. IPAC 2011, September 2011, San Sebastián, Spain. http://www.JACoW.org.

18. Magnus Johnson. Beam-based Diognostics of RF-breakdown in the Two-beam Test-stand in CTF3. CLIC Note 710, CERN, CH-1211 Geneva 23, Switzerland, 2007.

19. Andrea Palaia et al. Effects of RF breakdown on the beam in a CLIC prototype accelerator structure. Phys. Rev. ST Accel. Beams, 16:081004, 2013.

20. Claudia Marcelloni. The Two-beam Test Stand. CERN Photolab, 2008.

21. Max Brice. The CLIC Test Facility. CERN Photolab, 2010.

22. EPAC 2006. European Particle Accelerator Conference, June 2006, Edinburgh. http://www.JACoW.org

23. EPAC 2008. European Particle Accelerator Conference, June 2008, Genua. http://www.JACoW.org

2.17 Kicker And Monitor for Ctf3 Phase Feed Forward

Fabio Marcellini, INFN-LNF, Frascati, Italy and PSI, Villigen, Switzerland
Mail to: Fabio.Marcellini@psi.ch

2.17.1 Introduction

The two beams acceleration scheme, basic feature of the Compact LInear Collider CLIC, asks for precise synchronization between the Main Beam and the RF power produced by the Drive Beam in order to keep the energy of the Main Beam constant. Drive Beam timing and intensity errors lead to phase and amplitude RF variation in the accelerating structures, with consequent different acceleration gradient. Main Beam energy variations cause collider luminosity reduction.

To keep, as required, the luminosity reduction less than 2%, the RF phase jitter should be less than 0.1° (23fs @ 12GHz) [1].

The synchronization between Main Beam and Drive Beam must be implemented by means of a feed-forward system, where the two beams arrival time are compared and the proper correction is applied to the Drive Beam.

A feed forward system, similar to the CLIC one, will be tested in the CLIC Test Facility CTF3 now in operation at CERN [2]. The phase is measured at the end of the Drive Beam linac and the correction is applied in the chicane after the combination rings through two transverse kickers. A second phase monitor, placed before the RF power production system, measures the changes in longitudinal position due to the feed forward system. The RF power production in the decelerating structures is also monitored.

202

2.17.2 **The Monitor Pick-Up**

The front end of the phase forward system is the monitor that detects the bunch longitudinal position and provide a time resolution of the order of 20 fs [3]. The beam signal from the monitor pickup is mixed with a low phase noise local oscillator with less than 5 fs integrated timing jitter [4]. The pickup is composed by four slots, equally distributed around the vacuum chamber. Attached to the slots are four waveguides with transitions to 50Ω coaxial lines. Commercial vacuum feedtroughs to SMA standard connectors are placed in the coaxial section. Double ridged design of the waveguide has been chosen to optimize the transition frequency response and reduce the cross section.

Two notch filters, realized with bumps in the beam pipe at a distance tuned at the bunch detection frequency, are placed at both the pick up sides, providing a resonant volume for the beam electromagnetic field. The filters provide also the rejection of the RF noise and wake field in the working bandwidth that can induce spurious signals that affect the measurements. The sketch in Fig.1 shows the inner profile of the phase monitor simulated with HFSS electromagnetic code.
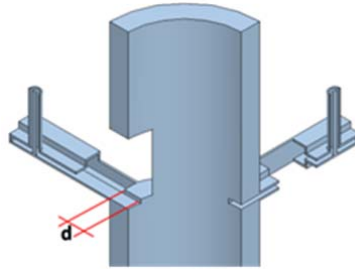
Figure 1: Phase monitor schematic drawing.

The fast response of the monitor is mandatory because after the acquisition of a few bunches of the Drive Beam train the feed forward system must perform the correction of the longitudinal position of the rest of the bunch train. Low values of the pickup quality factor and shunt impedance allow to obtain the monitor fast rise time and to reduce the extraction of power from the beam.

Time domain simulations (see Fig.2) have been performed to characterize the pickup response applying a phase jump in a certain bunch of the train and looking at the signal at the monitor exit. The response time is approximately 50 bunches on 2100 bunches of the train that is a reasonable value for the feedback.
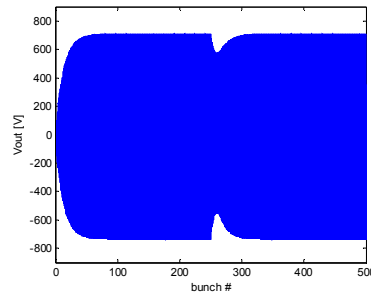
Figure 2: pickup outputs given by a bunch train with a phase jump (beam current 28A): tuned version on the left, detuned on the right.

2.17.3 **The Stripline Kicker**

The phase correction is provided by changing the electron beam trajectory in a dispersive region by transversally kicking the bunch with fast kickers: the path length variation due to the trajectory closed bump provides the longitudinal position correction. A two strip-line kicker structure has been chosen to satisfy the following requirements:
- Fast response to the input pulse signal (few ns):
- High kick efficiency
- 50Ω impedance to match the output impedence of the high voltage (2kV) pulser.
- Low longitudinal coupling impedance to limit the energy spread degradation.

A diameter of 40 mm in the stripline section has been chosen to maintain the same beam stay clear aperture of the rest of the pipe. The kickers are installed in the dog-leg line that connects the Combiner Ring to the CLIC experimental area. The stripline length is about 1m. Stripline ends are tapered both in transverse dimension and distance from the vacuum chamber to match better the transition to the 50Ω coaxial line supporting the feedtrough and to reduce the stripline beam coupling impedance.

With this configuration a voltage of 1.4kV applied to each strip, with opposite polarity, provides the requested 1mrad kick angle at the CTF3 beam energy (150 MeV).

Kickers with similar design have been realized for the DAFNE collider injection [5].
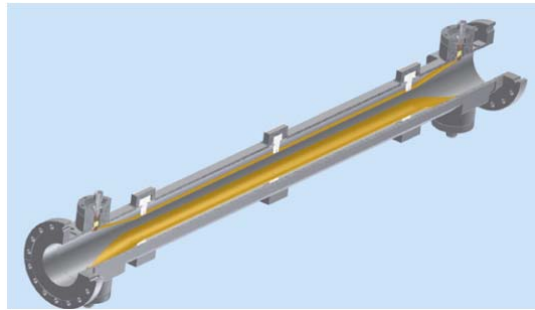
Figure 4: Kicker mechanical design.

2.17.4 **References**

1. D.Schulte et al. "Status of the CLIC phase and amplitude stabilization concept" Proceedings of LINAC 2010, Tsukuba, Japan, September 2010, MOP024, p. 103 (2010); http://www.JACoW.org.
2. R. Ruber et al. "CLIC feasibility demonstration at CTF3" Proceedings of IPAC'10, Kyoto, Japan, May 2010, WEPEB035, p.2764 (2010); http://www.JACoW.org.
3. F. Marcellini et al. "The CLIC drive beam phase monitor" Proceedings of IPAC'10, Kyoto, Japan, May 2010, WEPEB035, p.2764 (2010); http://www.JACoW.org.
4. A. Andersson and J.P.H. Sladen "Precision beam timing measurement system for CLIC synchronization", Proceedings of EPAC'06, Edimburgh, Scotland, June 2006, TUPCH086, p.1211 (2006); http://www.JACoW.org.
5. F. Marcellini et al., "Tests and operational experience with the DAFNE stripline injection kicker", PAC'09, Vancouver BC, Canada, May2009, TU6RFP082, p. 1739 (2009); http://www.JACoW.org

3   Other Activities

3.1   C-Band Accelerating Structures for SPARC Energy Upgrade

David Alesini, INFN-LNF, Via Enrico Fermi 40, 00044 Frascati, Italy
Mail to: David.Alesini@lnf.infn.it

3.1.1   SPARC Energy Upgrade

SPARC is a 150-MeV photoinjector test facility in operation since 2001 in the Laboratories of the National Institute of Nuclear physics in Frascati (LNF-INFN, Italy). The photoinjector has been constructed to produce high-brightness electron beams for several experiments like SASE-FEL in visible light [1], velocity bunching [2] and seeding [3]. The beam is generated in a 1.6-cell standing-wave RF gun of the UCLA/BNL/SLAC type [4] and accelerated with three constant-gradient $2\pi/3$ Traveling Wave (TW) structures. All systems operate in S-Band at 2.856 GHz.

The energy upgrade of the SPARC photo-injector at LNF-INFN from 150 to more than 240 MeV will be done by replacing a low gradient S-Band accelerating structure with two C-band structures [5]. The choice of the C-Band for the energy upgrade was dictated by the opportunity to achieve a higher accelerating gradient, enabled by the higher frequency, and to explore C-Band acceleration combined with a S-Band injector that from beam dynamics simulations looks very promising [6].

The use of C-Band structures for electron acceleration and production of high quality beams has been also proposed and adopted in several FEL projects all over the world [7-12]. The two main projects that adopted C-band structures are the Japanese FEL project in Spring-8 and the SwissFEL project at PSI. In the first project travelling wave (TW) damped structures have been adopted for multi-bunch operation. In the PSI project the structures have been designed as constant gradient and will operate at an average gradient of 26 MV/m.

The C-band structures for SPARC have been developed in the LNF-INFN Laboratories with the support of local firms for their construction. The details of the electromagnetic design are reported in [5]. The main structure parameters are given in Table I. They are TW and Constant Impedance (CI), have symmetric axial input couplers and have been optimized to work with a SLED RF input pulse. The SPARC linac operates in single bunch mode and the choice of a CI structure was made partly to reduce the fabrication costs but mainly to obtain a quasi-uniform accelerating field along the structure when the structure is fed by the SLED RF pulse. The decay of the RF pulse amplitude along a CI structure is, in fact, compensated by the exponential shape of the SLED pulse, resulting in a rather constant profile of the RF field along the accelerating section. The mechanical drawings of the structure and of the prototype are given in Fig. 1 (a).
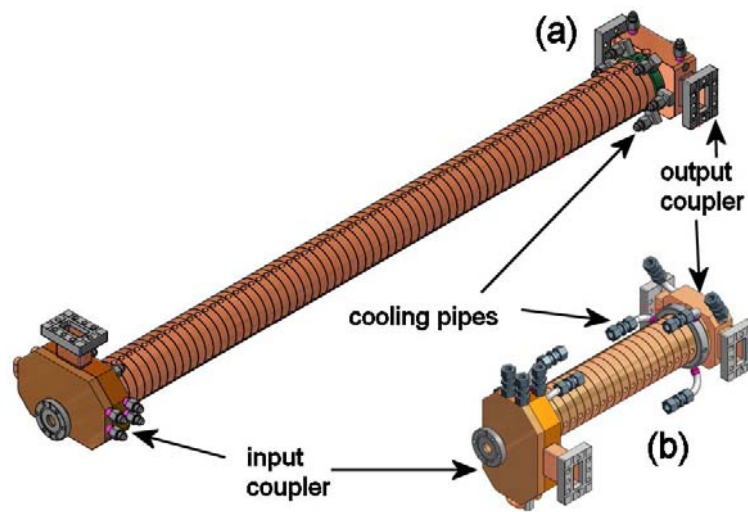
Figure 1: Mechanical drawing of the C-Band Structure (a) and prototype (b). Picture taken from [5].

Previous to the realization of the final devices a prototype with a reduced number of cells has been realized and high power tests have been carried out at KEK by the Frascati INFN group in close collaboration with the Japanese KEK laboratory. The details of the high power test results on the prototype are reported in [5]. The mechanical drawing of the prototype is given in Fig. 1 (b).

Experimental results on this first prototype confirmed the reliability of its operation at 50 MV/m accelerating gradient with about 10^{-6} breakdowns per pulse per meter, as shown in the Fig. 2, where the breakdown rates measured at different field values before and after conditioning are given.
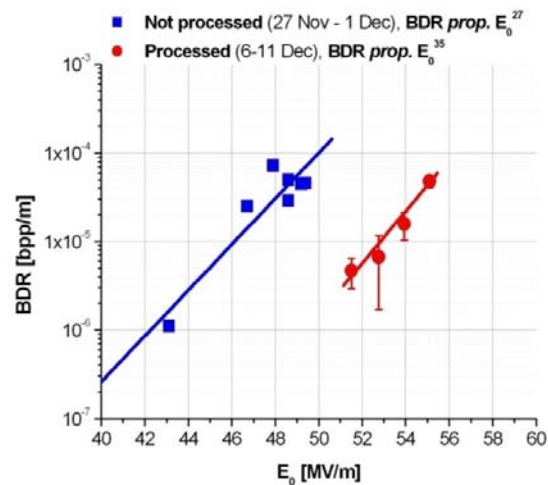
Figure 2: Breakdown rates as measured at different field values before and after conditioning of the SPARC C-Band prototype (plots taken from [5]). After processing, about 50MV/m accelerating field has been reached, with a breakdown rate per meter of the order of 10^{-6}.

The program of building the two final SPARC structures was carried out in the framework of the EU FP7 TIARA project. The new C-band structures will be fed by a Toshiba ET37202 50-MW C-band klystron. The HV pulsed modulator and the 400 W solid state driver for the klystron were manufactured by ScandiNova (Sweden) and Mitec Telecom (Canada), respectively. The new C-band system will also include a SKIP-type pulse compressor [6] that has been manufactured by IHEP (Beijing). The picture of the first structure under high power test in the SPARC experimental hall is given in Fig. 3.

Figure 3: First C-Band structure under high power test in the SPARC experimental hall.

The structure has been tuned after the brazing process adopting the procedure reported in [14]. The measured electric field before and after the tuning and the phase advance per cell are given in Fig. 4.

High power tests started on November 2013. In about 15 full days equivalent conditioning time we finally reached 38 MW input power in the structure (44 MW from the klystron), with nominal 10 Hz rep. rate and nominal 165 ns RF pulse length. The corresponding accelerating field was 36 MV/m peak and 32 MV/m average with BDR $<10^{-5}$.

The test of the second structure will follow and the installation in the SPARC accelerator and commissioning with beam will be scheduled next year.
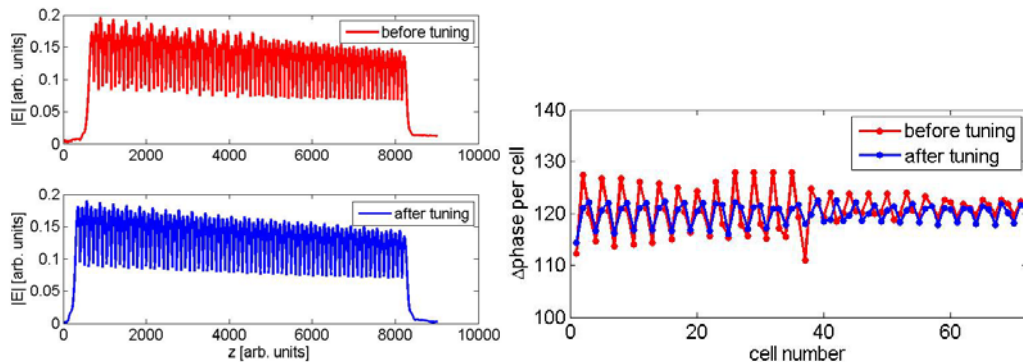
Figure 4: Measured field and phase advance per cell before and after the tuning.

Table I: Main C-Band structure parameters

PARAMETER	Value
Frequency (f_{RF})	5.712 [GHz]
Phase advance per cell	$2\pi/3$
Number of accelerating cells (N)	71
Structure length including couplers (L)	1.4 [m]
Cell length (d)	17.495 [mm]
Iris radius (a)	7 [mm]
Group velocity (v_g/c):	0.0283
Field attenuation (α)	0.206 [1/m]
Shunt impedance (r)	82.8 [MΩ/m]
Filling time (τ_F)	150 [ns]
Accelerating gradient	>35 [MV/m]
Output power	0.60·P_{in}
Average dissipated power @ 10 Hz	59.6 [W]

3.1.2 Acknowledegements

3.1.3 References

1. M. Ferrario et al., Proceedings of PAC09, Vancouver, BC, Canada
2. M. Ferrario et al., Phys. Rev. Lett. 104, 054801 (2010)
3. M. Labat, et al., Phys. Rev. Lett. 107, 224801 (2011)
4. D.Palmer PhD thesis "The next Generation Photoinjector", June 1998
5. D. Alesini, et al, JINST, 8, P05004, 2013.
6. V. Fusco and M. Ferrario, Beam Dynamics study of a C-Band LINAC driven FEL with S-Band photo-injector, Proceedings of PAC09, Vancouver, BC, Canada.
7. SCSS X-FEL R&D Group, SCSS X-FEL Conceptual Design Report, edited by T. Shintake and T. Tanaka (RIKEN Harima Institute/SPring-8, Sayo, Japan, 2004).
8. Tsumoru Shintake, et al., PHYSICAL REVIEW SPECIAL TOPICS - ACCELERATORS AND BEAMS 12, 070701 (2009)
9. T. Shintake, N. Akasaka, K. Bane, H. Hayano, K. Kubo, H. Matsumoto, S. Matsumoto, K. Oide, and K. Yokoya, in Proceedings of the 1995 Particle Accelerator Conference, Dallas, Texas, 1995 (IEEE, Piscataway, NJ, 1996), pp. 1099–1101.
10. T. Shintake, Jpn. J. Appl. Phys. 31, L1567 (1992).
11. R.Ganter et al. SwissFEL CDR, report n.10-04, V19, 3.3.2011, http://www.psi.ch/swissfel/HomeEN/SwissFEL_CD R_web_small.pdf.
12. R. Zennaro, J. Alex, M. Bopp, H. Braun, A. Citterio, H.R. Fitze, M. Pedrozzi and J. -Y. Raguin, "Conceptual Design of the C-band Module for the SwissFEL", Linac2010, Tsukuba, September 2010, TUP001, p. 392.
13. T. Sugimura, SKIP - A pulse Compressor for SuperKEKB, Proceedings of LINAC

2004, Lübeck, Germany, 2004.

14. D. Alesini, et al, JINST 8, P10010, 2013.

3.2 Ultra-Low Vertical Beam Size Instrumentation and Emittance Determination at the Swiss Light Source[1]

Ángela Saá Hernández, Masamitsu Aiba, Michael Böge, Natalia Milas[2],
Martin Rohrer, Volker Schlott, Andreas Streun; Paul Scherrer Institut, Switzerland
Åke Andersson, Jonas Breunlin; MAX IV Laboratory, Sweden
Mail to: angela.saa-hernandez@psi.ch

3.2.1 Introduction

The achievement and control of ultra-low vertical emittances is of large interest for present and future storage ring based light sources in order to use small period/gap undulators allowing for higher photon energies and for the design of damping rings for future linear colliders to obtain their desired high luminosities. In this context, at the Swiss Light Source (SLS), at Paul Scherrer Institut (PSI), a program was launched towards: (a) the minimization of the vertical equilibrium emittance via the suppression of betatron coupling and vertical dispersion by beam-assisted realignment of the storage ring magnet supports and the subsequent application of correction schemes using skew quadrupoles, (b) the measurement of small vertical beam sizes by means of a high resolution beam size monitor.

In the ideal case of a flat storage ring, an extremely low vertical equilibrium emittance can be obtained, which is only limited by the direct recoil of the emitted photons [1]. For SLS this so called quantum limit of the vertical emittance is at 0.2 pm·rad. In reality, however, magnet field errors and misalignments (typically in the order of few tens of μm) as well as beam position measurement errors lead to betatron coupling and vertical dispersion causing a subsequent emittance growth to several pm·rad even for well corrected machines. The emittance minimization procedure at SLS, which accounts for all these imperfections [2], will be briefly reviewed in Sec. 3.2.2.

To enable an emittance measurement at a storage ring an image formation method is typically used for the determination of the beam size. The emittance determination thus relies on a beam size measurement and the knowledge of the storage ring optical function values at the observation point. At SLS the beam size can be determined using three complementary methods: imaging through a pinhole using X-ray synchrotron radiation (SR) [3], a π-polarization imaging method, where images are formed from vertically polarized visible/UV SR [4][5], and an interference method using also vertically polarized light. A similar method, but with double slits and using horizontally polarized light has been previously realized at KEK [6]. While the pinholes at SLS are useful for measurements of the horizontal beam size of about 60 μm, the resolution of the SLS pinhole beam line with a point-spread function (PSF) of ~10 μm [7] is insufficient to determine the very small vertical beam sizes of typically < 12 μm. The π-polarization imaging and interference methods follow an implication of the van Cittert-

Zernike theorem [8]: all electrons in the beam are spatially incoherent SR sources. Nevertheless, because they are observed at sufficiently large distances and wavelengths, the light emitted from the electrons exhibits a non-zero degree of coherence. By measuring the degree of coherence it is possible to reconstruct the source distribution, and thus, to infer the beam size. The resolution of these methods can reach down to an rms vertical beam size of 2 μm at the SLS new beam size monitor. The vertical beam size instrumentation is treated in detail in Sec. 3.2.3.

3.2.2 Vertical Emittance Minimization in a Nutshell

The first step towards emittance minimization was a beam-assisted re-alignment campaign of the SLS storage ring magnet supports, i.e. a remote alignment of the girders with stored beam at full current while running the fast orbit feedback system. This led to a substantial reduction of the rms vertical corrector strength from initially ~130 μrad to ~50 μrad. On the way to a systematic vertical dispersion correction, the beam position monitor (BPM) roll errors were determined in order to eliminate fake vertical dispersion readings caused by the projection of the horizontal dispersion. Then, a model-based correction was applied using 12 dispersive skew quadrupoles to suppress the spurious vertical dispersion, resulting in <1.3 mm rms. A model-based betatron coupling correction was performed using 24 non-dispersive skew quadrupoles, which reduced the coupling part of the coupled dipole corrector/BPM response matrix to values close to its measurement error. These two correction steps were iterated a few times and lead to a vertical beam size of 4.3 ± 0.6 μm. After a final random optimization a vertical beam size of 3.6 ± 0.6 μm corresponding to a vertical emittance of 0.9 ± 0.4 pm·rad was achieved [2].

3.2.3 The Beam Size Monitor Concept

A diagnostic beam line for the π-polarization imaging method was first build in 2007 [4]. Fig. 1 exemplifies the principle: the vertically polarized light in the visible/UV range travels almost non-obstructed along this beam line and it is focused on a CCD camera situated at the image plane. At the camera the two lobes of the π-polarized radiation, which have a phase difference of 180°, are imaged showing the characteristic destructive interference at the mid-plane. For a point-like beam, this interference is complete and the central intensity is zero. For an extended source, however a non-zero intensity between the lobes (valley) is observed. The ratio of the intensities between the valley and the peaks is defined as the valley-to-peak ratio (VPR).
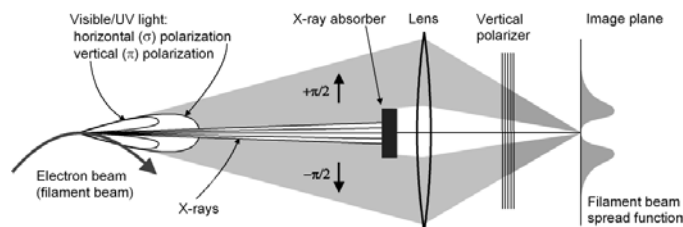
Figure 1: Schematics of the π-polarization imaging beam size monitor.

The VPR depends on the vertical source size and thus the vertical beam size, σ_y, can be deduced from a model-based calibration curve, which relates the VPR to the vertical

beam size (see Sec. 3.2.4). An example of vertical image profiles for beams of different sizes is represented in Fig. 2 to illustrate this measurement method based on the image properties.
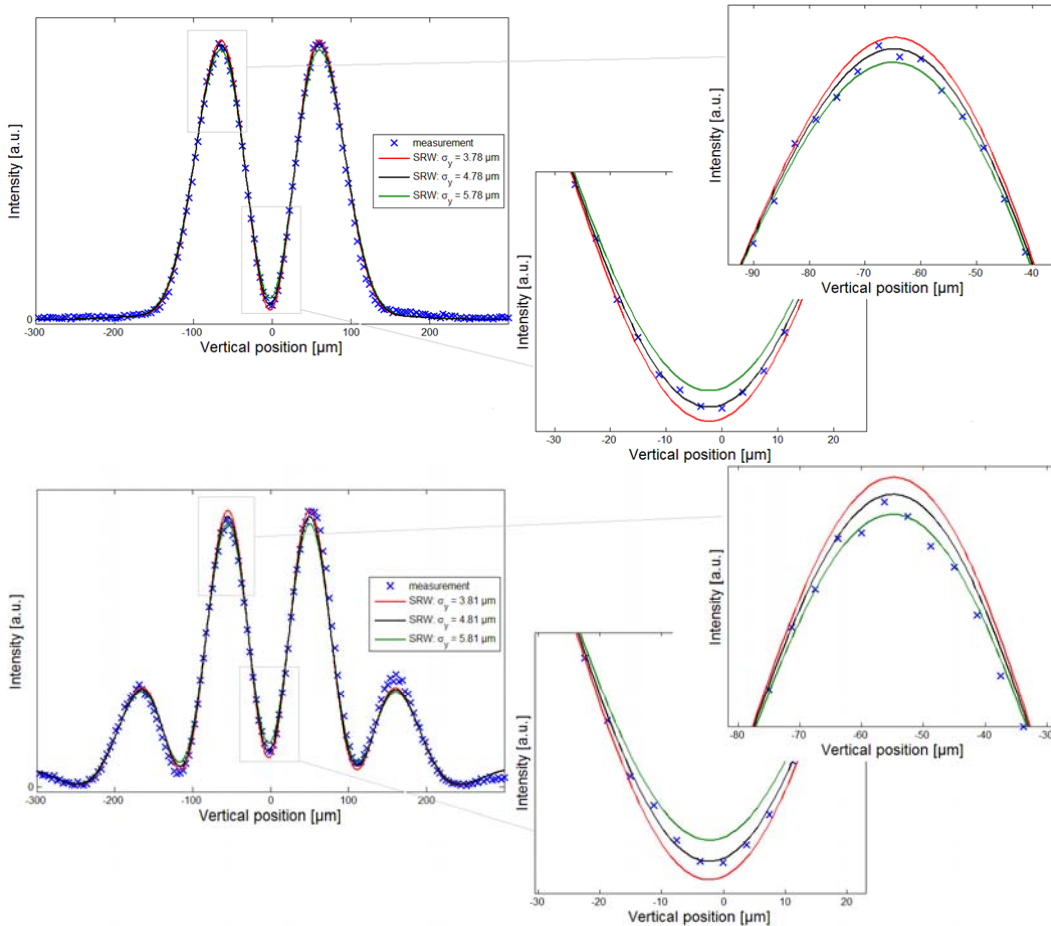
Figure 2: Measured (crosses) and calculated (solid lines) vertical image profiles for different beam sizes, for the new beam size monitor X08DA. The measured valley-to-peak ratio leads to the conclusion that the corresponding vertical beam size is 4.78 μm using the imaging method (top) and 4.81 μm using the interference method (bottom).

A program on vertical emittance minimization and measurement was supported by the TIARA Work Package "SLS Vertical Emittance Tuning" [9]. Funding was provided to build an improved monitor based on the experiences acquired with the first one. The first monitor could resolve a minimum beam size of about 3.5 μm, which was considered insufficient for the ultra-low emittance envisaged, furthermore it soon was integrated into standard user operation of the SLS and thus became less available for experimental use. The second beam size monitor provides two complementary measurement methods using vertically polarized light: the imaging method with improved resolution, and the interference method using horizontal obstacles. The main characteristics and improvements of the new monitor with respect to the first monitor are:

- The beam line extends outside the storage ring tunnel and ends at an optical table which is accessible also during machine operation.

- Larger magnification ratio, M = −1.45, approximately a factor two larger than for the old beam line, which increases the measurement precision.
- Reflective optics using a toroidal mirror in place of the lens for wavelength-independent focusing.
- Use of shorter wavelengths down to 266 nm to obtain a better resolution.
- Two complementary measurement methods: imaging and interference using horizontal obstacles of different sizes, to enable the cross-checking of the results and the extension of the measurement range.
- Calibration and alignment by means of a dedicated laser setup.

3.2.4 Synchrotron Radiation Imaging Model and Simulations

A model for SR emission and propagation through the monitor beam line is needed to find the relation between the VPR and the actual beam size. The model used is based on a near-field calculation, using the retarded potentials of the SR electromagnetic fields at the first optical element. Preserving all phase information, the fields are then propagated through the optical elements and apertures of the beam line within the frame of scalar diffraction theory. Finally the intensity distribution is calculated in the image plane. This distribution, resulting from a single relativistic electron, called "filament-beam-spread-function" (FBSF) is the equivalent to a point-spread-function in the case of a virtual point source. Convoluting the FBSF with a Gaussian distribution (or any assumed electron distribution) gives the resulting image, which is an observable. The program Synchrotron Radiation Workshop (SRW) [10] is based on this model and is used for the calculations. Look-up tables of the VPR as a function of the beam size are then generated based on SRW simulations.
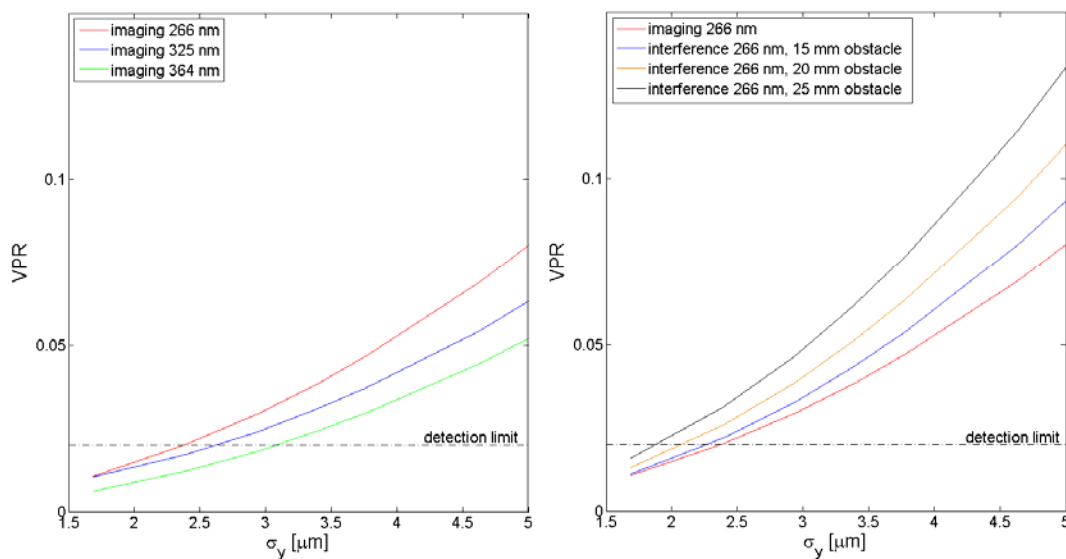
Figure 3: Calculated valley-to-peak ratio (VPR) as a function of the rms vertical beam size for different wavelengths (left) and for different measurement methods (right).

Fig. 3 (left) shows the VPR as a function of the beam size for three different wavelengths. For shorter wavelengths it is easier to resolve the beam size as the slope of the curve is steeper, thus increasing the sensitivity of the valley-to-peak intensity. As

indicated by the dashed lines in Fig. 3, a VPR of about 2% is the estimated lowest detection limit of the monitor considering the rather low and smooth image background, the camera pixel size and the beam line magnification. By detection of light at the lowest possible wavelength (266 nm), a beam size σ_y of about 2.5 µm rms could potentially be measured with the imaging method.

Fig. 3 (right) shows the VPR as a function of the beam size for the complementary methods of the new monitor (X08DA): the imaging method and the interference method with the three available obstacle sizes, all for π-polarized light. Also the corresponding curve for the first monitor (X09DA), using the imaging method at 364 nm, is represented for comparison. Assuming again a 2% lowest limit of VPR detection, a beam size σ_y of around 2 µm rms could potentially be measured by use of the interference method.

3.2.5 The Monitor Beam Line Layout

The layout of the beam size monitor X08DA is presented in Fig. 4, and the center part containing the focusing element is sketched in Fig. 5. The source point of the beam line is the central bending magnet of sector 8 (BX08).
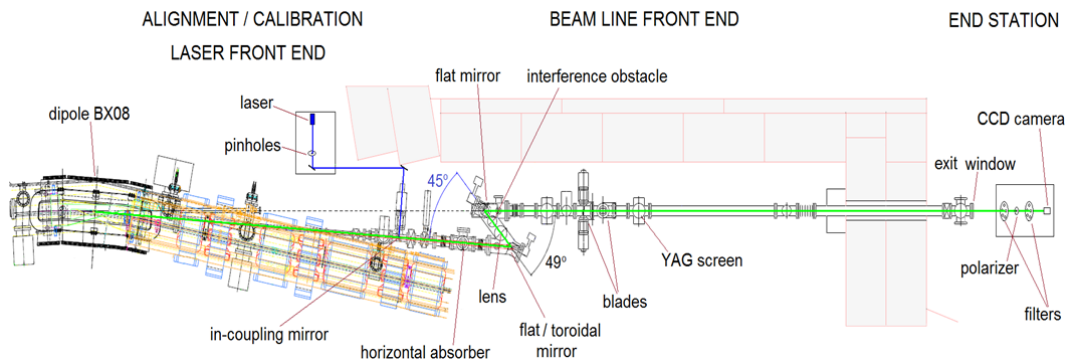
Figure 4: Layout of the X08DA beam line, laser front end and end station are schematic.

The emitted SR in the X-ray range, which has a small vertical opening angle (~$1/\gamma$) and contains most of the energy, is absorbed by a water cooled horizontal finger absorber blocking 0.9 mrad of the central SR distribution to avoid heat-load induced distortion of the first optical element. Vertically polarized light in the range of visible/UV, distributed in two lobes with a phase difference of 180° travels almost non-obstructed along the beam line, whereas the horizontally polarized visible/UV light is partially blocked by the finger absorber too. The beam line has been designed in zigzag to ensure that no bremsstrahlung from beam electron scattering on residual gas atoms and no remanent X-ray SR can reach the optical table in the hutch, outside of the SLS shielding wall.
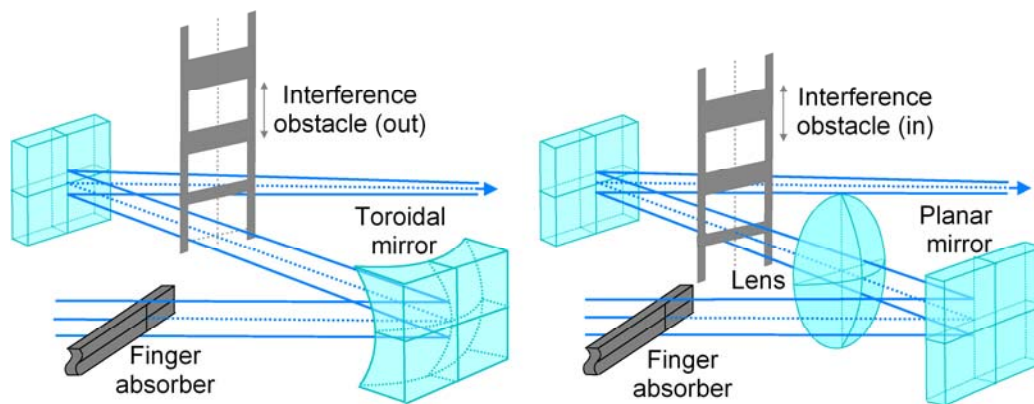
Figure 5: Schematic view of the X08DA beam line central region in final and intermediate configurations, using a toroidal mirror (left) and a lens with planar mirror (right). The measurement method is defined by the position of the interference obstacle; in the imaging method the obstacle is out of the beam path (left), in the interference method the obstacle obstructs the center of the beam (right).

As sketched in Fig. 5, the beam line in its final configuration contains a toroidal mirror for wavelength-independent focusing. An intermediate configuration employs a plano-convex fused silica (FS) lens with a planar mirror. The surface quality of the three central optical elements is necessarily chosen as high as possible: the lens surfaces have an rms deviation of 3 nm and 8 nm for the convex and planar sides, respectively.

The flat mirror in front of the lens is made from silicon carbide (SiC), and thus is able to withstand direct X-ray SR incidence at reduced beam current (few mA), when the finger absorber is retracted. This mirror has a surface rms deviation of 6 nm. After the lens follows a flat UV enhanced Al-coated FS mirror with peak-to-valley errors below 20 nm. The Si toroidal mirror has a peak-to-valley below 8 nm. Apart from these high accuracy optical elements, the beam line is also equipped with horizontal and vertical blades to determine the acceptance angle of the light, and with a diagnostic element consisting of a YAG screen, that can be introduced into the light path to inspect the footprint of the SR several meters before the image plane in order to check for possible obstructions.

The beam line ends with a FS exit window at an optical table located in an experimental hutch, outside of the SLS storage ring tunnel. External to the vacuum a series of optical elements filter the beam before it is measured; neutral density filters can be selected to lower the transmission down to 30%, 10%, 3% or 1%, a Glan-Taylor polarizer can be remotely rotated to eliminate non-vertically polarized light, and a combination of bandpass and laser-line filters can be included to narrow the bandwidth of the selected wavelength down to 2 nm FWHM. The two lobes of vertically polarized light are finally imaged onto a CCD camera located at the image plane of the lens. The CCD cameras are mounted over a remotely controlled linear translator in order to finely adjust its position to that of the image plane.

In the vicinity of the focusing element (lens or toroid), three horizontal obstacles of different heights, 15, 20 and 25 mm, as shown in Fig. 5, may be inserted in the light path, blocking approximately 3, 4 or 5 mrad of the central vertical SR distribution, respectively. This turns the imaging method into an interference method, and the measurement results can be cross-checked with both methods.

A fully remote controlled optical table with three lasers of wavelengths 266 nm, 405 nm and 532 nm is located inside the storage rings tunnel. The lasers are used for alignment of the beam line optics and for calibration of the monitor by means of imaging quality tests. At the same distance as the SR source point from the BX08 bending magnet, a set of pinholes, with diameters between 1 μm and 200 μm, can be inserted in the laser beam path to be imaged with the beam line optics. To this end the laser is coupled through a window into the beam line, where an in-coupling mirror reflects the laser along the same path as the SR until the CCD camera, as shown in Fig. 4.

3.2.6 Analysis and Specification of Toroidal Mirror Quality

Alignment errors and surface imperfections of the optical elements produce aberrations and distortions at the image plane, which affect the measured VPR. The toroidal mirror seems to be especially sensitive to some error sources and for that reason an extensive investigation of the expected performance has been done [11].

The surface imperfections of an optical element prevent the reflected rays to meet at one unique point on the image plane, producing a blurred image. Simulations are necessary during the design process in order to set the specifications and tolerances to the product manufacturers. Afterwards, once the optical elements have been produced and the measured profiles are available, it is desirable to include the imperfections in the simulation for a more realistic description of the beam line.

A realistic surface profile for the toroidal mirror has been generated following the model from Ref. [12], based on the simulation of the surface waviness as a series of sine signals with frequencies which are multiples of the fundamental, and randomly generated amplitudes, initial phases and wave train lengths. The surface roughness, a random irregularity in the range of Ångströms, is randomly generated and superposed to the surface waviness. The surface texture is included in the SRW performance simulations as a plane just behind the mirror that defines its transmission pattern, thus modifying the path length of the light in the same manner as the surface texture would do.

As a result the surface errors of the mirror are found to cause a peak asymmetry in the image observed at the CCD camera. A separated analysis of waviness and roughness shows that the effect of the roughness is negligible up to a roughness of 2 nm rms. The waviness distorts the image if the waves have a peak-to-valley >21 nm and a slope variation (slope error) ≥ 0.25" rms. An additional parameter seems to play an important role in the observed distortions: the orientation of the waves or surface ripples. This orientation depends on the polishing process performed on the mirror. Thus, for a polishing with circular movements the surface presents a radial waviness pattern (this is usually the case for the lenses), while for a polishing with linear movements it presents a horizontal or vertical striped pattern. The peak asymmetry is more pronounced for the horizontally striped pattern than for the radial or the vertically striped pattern. This effect seems to be purely geometrical: in the case of a surface with horizontal waves the two lobes of vertically polarized light hit different crests and valleys of neighboring stripes and the path length of the two light lobes is modified in a different manner. Instead, in the case of a surface with vertical waves the two lobes of vertically polarized light hit the same stripe, thus suffering a much smaller path length variation, generated only by the roughness within a stripe. For a mirror with radial waves the two lobes of

vertically polarized light will hit approximately symmetric areas of the mirror, as long as the mirror is correctly aligned and there is a negligible vertical offset.

In order to define the tolerances on mechanical alignment and beam positioning necessary to resolve small beam sizes, the possible misalignments of the toroidal mirror have been included in the SRW simulations. The results of these simulations are also aimed to guide during the commissioning phase of the toroidal mirror, as some misalignments result in a characteristic image distortion at the CCD camera.

A horizontal or vertical offset of the toroidal mirror results in a scaled offset of the image at the camera. Offsets within ±50 μm do not affect the valley-to-peak ratio and, thus, are harmless for the determination of the beam size. On the contrary, a horizontal or vertical tilt, or a rotation of the mirror around its axis have dramatic effects on the valley-to-peak ratio, as shown in Fig. 6.
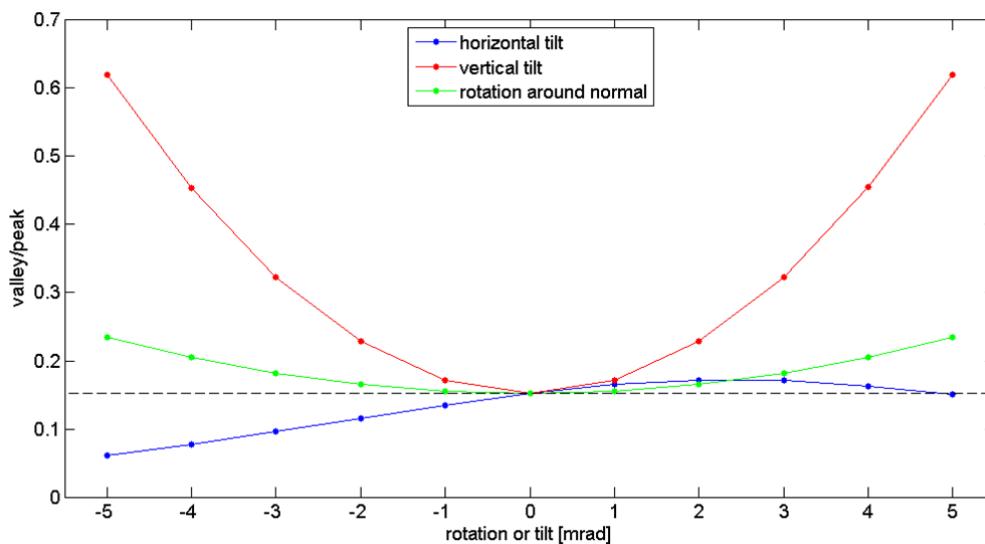
Figure 6: Calculated valley-to-peak ratio (VPR) as a function of the different misalignments.

A vertical tilt or a rotation around the mirror axis changes the effective toroidal horizontal and vertical radii. In this case a peak asymmetry is observed and the valley-to-peak ratio and, correspondingly, the vertical beam size are overestimated. A horizontal tilt, instead, is equivalent to a change of the light incidence angle and causes astigmatism by affecting the horizontal and vertical focusing length in opposite ways. If the image plane is out of focus, the peaks in the vertical profile are washed out and the beam size thus could be underestimated. However, supervising the distance between the peaks allows to detect a horizontal tilt immediately and to correct the astigmatism. The toroidal mirror is mounted over a gimbal mount, a pivoted support with two rotational degrees of freedom, which compensate the vertical and horizontal tilts, but not the mirror rotation around its axis. For this reason the rotation has to be constrained to ≤0.1 mrad, which corresponds to an error on the determination of the beam size of less than 5%.

3.2.7 **Beam Size Measurements**

The new monitor is equipped with filters for measurements of π-polarized SR of 266, 325, 365, 405 and 532 nm. Measurements at the shortest wavelengths, 266 and 325 nm, are preferred due to the higher resolution.

All measurements are performed in a multi-bunch top-up operation mode (400 mA, 390 out of 480 buckets populated) for two different machine settings: (1) the "user operation settings", with ID gaps at varying positions, a golden-orbit containing steerings for the beam lines and a vertical beam size of ~11 μm tuned with skew-quadrupoles for suitable beam lifetime; (2) the "low emittance settings", with open ID gaps, a zero-orbit (i.e. an orbit centered in all BPMs), and a skew quadrupole setting optimized for minimum vertical beam size as described in section 1.1.2.

As previously mentioned, X-ray pinholes are usually employed for measurement of horizontal beam size, but the π-polarized monitor may also be used: the horizontal projection of the image is of almost Gaussian shape. A deconvolution of the sigma derived from the full-width half-maximum (FWHM) and the sigma of the FBSF of the beam line then results in the sigma of the electron distribution. A more general and accurate measurement method, however, would use a SRW-based look-up table, as it is done for the vertical beam size measurement.

For the vertical beam size measurement, first the vertical projection of the image is obtained by summation of pixel intensities within a narrow vertical corridor located at the maximum of the horizontal profile, in order to avoid blurring due to a possible rotation of the two lobe images. Fig. 7 shows the beam size measurement application displaying acquired images of 325 nm SR during the user operation, using the imaging method and the interference method with a horizontal obstacle of 25 mm. The corridors defining the image areas used for compilation of the transverse profiles are indicated by orange line pairs. After identification of minimum and maxima in the vertical profile, local parabolas are fitted near the extrema to improve precision by interpolation and to increase robustness to noise. The resulting VPR is compared to the tabulated results from the SRW simulation as explained in section 3.2.4.
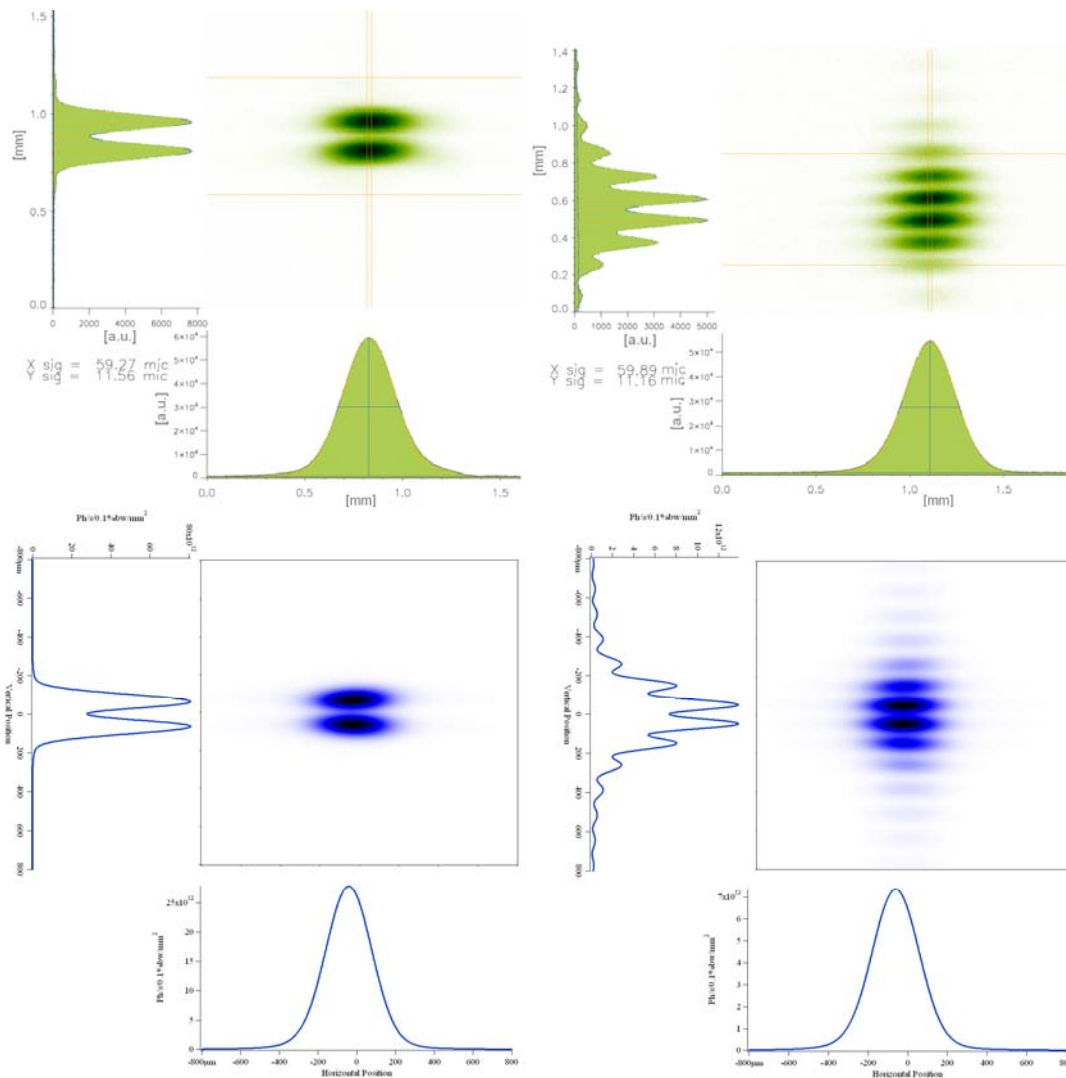
Figure 7: Measured image intensity (upper) and simulated image intensity (lower) during nominal user operation, for 325 nm wavelength using the imaging method (left) and the interference method with a 25 mm horizontal obstacle (right).

A CCD camera with 3.75 μm pixel size takes images in visible and near UV light, between 325 nm and 532 nm. At 266 nm, however, a UV-sensitive CCD camera with a larger pixel size of 8 μm is used. Images are acquired at a rate of 10 Hz.

The linearity of the camera response is checked by measuring the variation of the light intensity at the CCD as a function of the exposure time for different neutral density filters. Both CCD cameras show a linear response with an R-squared value > 0.99 for light intensities ≤ 90 % of the maximum intensity.

The exposure time of the camera is reduced to ≤ 0.4 ms in order to minimize the blur of the image due to vibrations. The integrated vibrational noise with unknown spectrum is on the level of 50−100 μm rms, which appears to be much larger than the possible contribution from the electron beam, since the residual vertical electron beam motion with running fast orbit feedback is <0.5 um rms up to 100 Hz at the two BPMs adjacent to BX08, which translates to <1 μm rms at the camera taking into account the storage

ring and the beam line optics. This corresponds to only a fraction of a pixel and thus would not affect the VPR value. Work is in progress to identify and suppress the sources.

The angular alignment of the camera is optimized for a maximum roll error of 2.4 mrad relative to the bending plane of the dipole, to make sure that observation of significant image rotations can be attributed to a tilt of the electron beam itself. In fact, tilts visible during "standard user settings", originating from betatron-coupling and spurious vertical dispersion, disappear when loading the optimized "low emittance settings".

Consistent vertical beam size measurements are obtained for the different wavelengths and different measurements methods (imaging and interference with the three different obstacles), as shown in Fig. 8 for the user operation settings at about 10 pm·rad vertical emittance, which corresponds to about 11.5 μm rms vertical beam size.
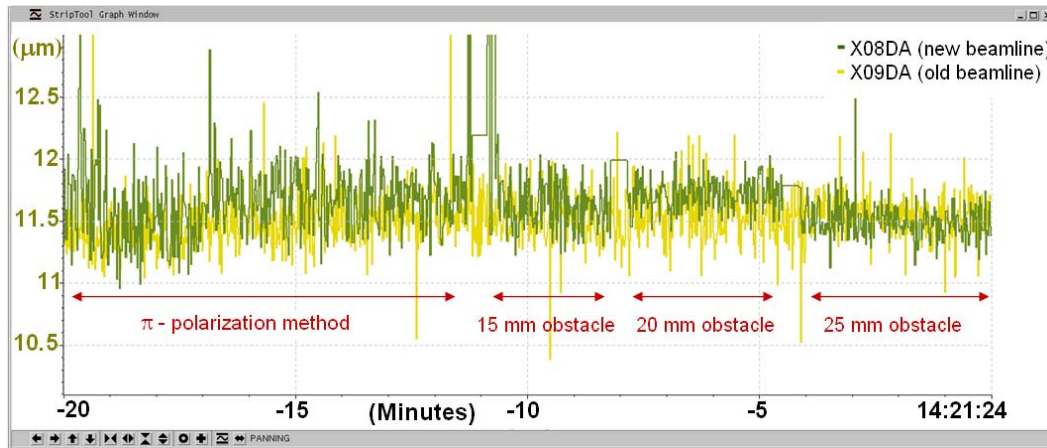
Figure 8: Comparison of the vertical beam sizes measured simultaneously with the old and the new beam size monitor, which are located at ring positions with identical beta functions. The measurements on the new beam size monitor are done with the imaging and the interference measurement methods using different obstacle sizes.

3.2.8 Determination of Beam Emittance

If the betatron coupling is well suppressed (which is the case after minimization of the coupling quadrants of the orbit response matrix) any beam rotation in the x-y-plane is due to vertical and horizontal dispersions only, and fluctuations of the vertical emittance around the storage ring circumference can be neglected.

The cross section area of a Gaussian beam is given by $A = \pi[\langle x^2\rangle\langle y^2\rangle - \langle xy\rangle^2]^{1/2}$, where a particle position y has contributions from the betatron oscillation, y_β, and from dispersion: $y = y_\beta + \eta_y\delta$ (same for x), with δ the relative momentum deviation and η_x, η_y the dispersions. Since x_β, y_β, δ are uncorrelated in absence of betatron coupling, the apparent rms vertical beam size is $\langle y^2\rangle = \sigma_y^2 = \varepsilon_y\beta_y + (\eta_y\sigma_\delta)^2$ (same for x), and the apparent coupling is $\langle xy\rangle = \eta_x\eta_y\sigma_\delta^2$, with β_x, β_y the beta functions and σ_δ the rms momentum spread.

The vertical beam size σ_{yo} as measured by the monitor is deduced from the image profile taken over a narrow vertical corridor (see corresponding lines in Fig. 7, top) to avoid blurring due to a possible rotation of the two lobe images. Simple geometry then

tells, that $A = \pi \sigma_{yo} \sigma_x$. Equating the two definitions of the beam cross section area A gives an applicable formula for the vertical emittance:

$$\varepsilon_y = \frac{1}{\beta_y}\left(\sigma_{yo}^{\;2} - \left(\sigma_\delta \eta_y \right)^2 \left[1 - \left(\frac{\sigma_\delta \eta_x}{\sigma_x} \right)^2 \right] \right)$$

Figuratively, the attenuation of the vertical dispersion terms to be subtracted takes into account a skew of the beam spot due to the correlation of the dispersive contributions to the particle coordinates.

Determination of vertical emittance thus requires knowledge of several beam parameters at the location of the SR source point, i.e. dipole center. The beta functions at the SLS are corrected to ~2% rms level with respect to the design optics [13]. The beta functions at the SR source point can be interpolated from the average beta function at the location of the quadrupoles adjacent to the monitor, which is determined by modulating the corresponding quadrupole strength and observing the resulting tune variation. The dispersion is measured by variation of beam energy, i.e. by detuning the radio-frequency, and by either observing the position of the image at the camera, or recording the off-momentum orbit and interpolation to the monitor location. Horizontal beam size can be measured with the monitor as well. For the rms energy spread, the theoretical equlibrium value for SLS at 2.411 GeV beam energy is used: $\sigma_\delta = 8.6 \cdot 10^{-4}$. Any increase of energy spread would only lead to an overestimation of the vertical emittance.

At the centre of dipole BX-08, which is the SR source point for the new X08DA monitor, following beam parameters were measured in the 2013 campaign (design values in brackets), which may be considered as typical:

$$\eta_x = 27.2 \pm 0.4 \text{ mm (29 mm)}, \; \eta_y = -1.0 \pm 0.2 \text{ mm (0 mm)},$$
$$\beta_y = 13.41 \pm 0.05 \text{ m (13.6 m)}, \; \sigma_x = 54 \pm 2 \text{ μm (56 μm)}.$$

After application of the "low emittance settings", a vertical beam size of $\sigma_y = 4.3 \pm 0.3$ μm was measured with the monitor in its intermediate lens-based configuration and using the π-polarization imaging method. A screen shot is shown in Fig. 9. The resulting vertical emittance is $\varepsilon_y = 1.3 \pm 0.2$ pm·rad. The error margin is dominated by the statistical error of the beam size measurement due to the shot-to-shot fluctuations as visible in Fig. 8. Work is going on to reduce these fluctuations and to eliminate any systematic errors. Nevertheless, the error margin is significantly reduced compared to the first monitor X09DA due to the higher resolution.
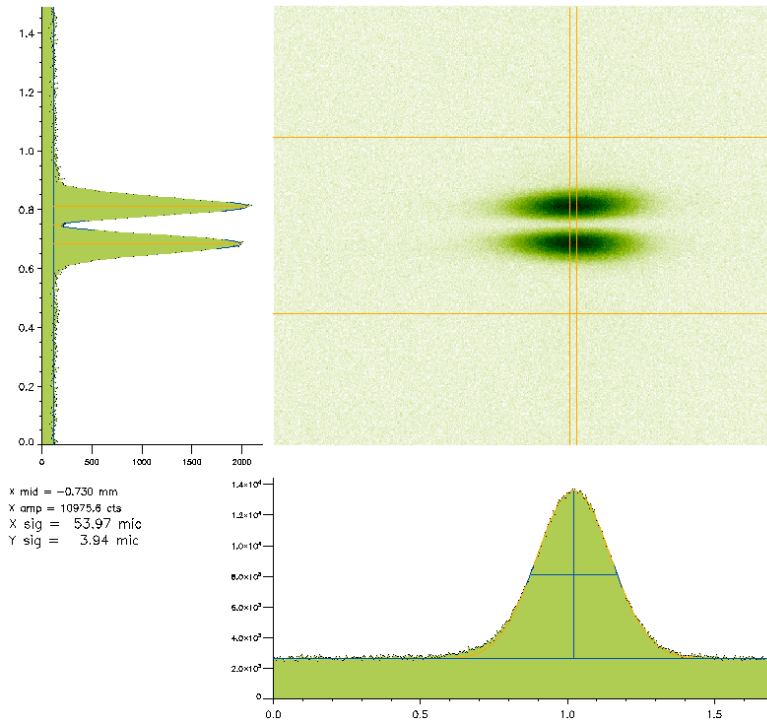
Figure 9: Screen shot of smallest vertical beam size of σ_y ~4 μm measured so far with the SLS X08DA beam size monitor using the π-polarization imaging method.

3.2.9 Conclusion and Outlook

Visible and near UV π-polarized synchrotron radiation can be used to resolve an electron beam size down to a level of a few μm rms. A first monitor of this type was built in 2007 at the SLS and was used to verify an ultra-low vertical emittance of 0.9 ± 0.4 pm·rad, however, reached its limit of resolution.

A new monitor, significantly improved with respect to performance and operation, was established at the SLS: the resolution is increased by larger magnification and using shorter wavelengths; the possible variation of wavelength and switching between imaging and interference methods allows consistency checks of the results; reflective optics instead of refractive optics provides wavelength independent focusing; continuation of the beam line out of the storage ring tunnels facilitates access and measurements.

An intermediate configuration using a lens and a planar mirror instead of the toroidal mirror of the final configuration has been commissioned in 2013 and was used to measure low vertical emittance with reduced error margins: $\varepsilon_y = 1.3 \pm 0.2$ pm·rad.

After installation of the toroidal mirror in 2014 and further work to suppress the image jtter in order to the reduce the statistical error of the beam size measurement, a new emittance minimization campaign, including another realignment of the storage ring girders, will aim for verification of sub-pm·rad vertical emittance at 10% error level.

3.2.10 **References**

1. T. O. Raubenheimer, "Tolerances to Limit the Vertical Emittance in Future Storage Rings", SLAC-PUB-4937 (1991).
2. M. Aiba, M. Böge, N. Milas and A. Streun, "Ultra low vertical emittance at SLS through systematic and random optimization", Nuclear Instruments and Methods A, 694 (2012) 133.
3. Å. Andersson, A. Lüdeke, M. Rohrer, V. Schlott, A. Streun and O. Chubar, "Recent Results from the Electron Beam Profile Monitor at the Swiss Light Source", proc. of the DIPAC2007 Conference, Venice, Italy.
4. Å. Andersson, M. Böge, A. Lüdeke, V. Schlott and A. Streun, "Determination of a small vertical electron beam profile and emittance at the Swiss Light Source", Nuclear Instruments and Methods A, 591 (2008) 437.
5. Å. Andersson, M. Eriksson, O. Chubar, "Beam Profile Measurements with Visible Synchrotron Light on Max-II", proc. of the EPAC 1996 Conference, Sitges, Spain.
6. T. Mitsuhashi, "Measurement of small transverse beam size using interferometry", proc. of the DIPAC 2001 Conference, ESRF, France.
7. N. Milas and A. Saa Hernandez, "Calculation of the point spread function for X09DA Pinholes in SLS", SLS-TME-TA-2013-0321.
8. P. H. van Cittert, "Die wahrscheinliche Schwingungsverteilung in einer von einer Lichtquelle direkt oder mittels einer Linse beleuchteten Ebene", Physica 1 (1934) 201. See also M. Born and E. Wolf, "Principles of Optics", chapter 10, Pergamon press (1980).
9. For more information on the TIARA work package 6 see: http://www.eu-tiara.eu/rtd/index.php?id=42
10. O. Chubar and P. Elleaume, "Accurate and Efficient Computation of Synchrotron Radiation in the Near Field Region", proc. of the EPAC98 Conference (1998).
11. N. Milas et al., "Specifications for the new SLS beam size monitor", TIARA report TIARA-REP-WP6-2012-015, August 2012.
12. M. Sanchez del Rio and A. Marcelli, "Waviness Effects in Ray-Tracing of Real Optical Surfaces", Nuclear Instruments and Methods A, 319 (1992) 170.
13. M. Aiba et al. "Comparison of linear optics measurement and correction methods at the Swiss Light Source", Phys. Rev. Sp. Top. Acc. & Beams, 16, 012802 (2013). DOI: 10.1103/PhysRevSTAB.16.012802

3.3 Emittance Measurements at the Australian Synchrotron Storage Ring

Mark Boland

Australian Synchrotron, 800 Blackburn Rd, Clayton, Victoria 3168, Australia

Mail to: mark.boland@synchrotron.org.au

3.3.1 **Introduction**

The Australian Synchrotron is a 3 GeV electron storage ring light source for user experiments on photon beamlines in the wavelength range from IR to hard x-rays [1]. The design performance of the machine was realised in late 2006 and user beam commenced in 2007. The storage ring is a DBA lattice and the parameters are listed in Table 1.

Table 1: Design parameters for the Australian Synchrotron storage ring.

Parameter	Unit	Design	Measured
Energy	GeV	3	3.013416(9) [2]
Circumference	m	216	215.9924
Current	mA	200	200
Periodicity		14	14
H tune		13.30	13.290
V tune		5.20	5.216
chromaticity (ξ_x,ξ_y) (nominal / user beam)		(+2,+2)	(+3.5,+13.5)
Harmonic number		360	360
Filled RF buckets (user beam)			300
Single bunch current I_b (user beam)	mA		0.667
Charges per bunch (user beam)			8×10^{11}
Horizontal emittance (bare lattice / user)	nm	15	10

Two diagnostic beamlines, one x-ray one optical were designed for daily measurement of the nominal design parameters such as the horizontal and vertical profile and emittance [3] (see Table 2 for source point parameters). The initial performance of the diagnostic beamlines was sufficient to meet the design criteria, however as the facility went through the commissioning phase, on to user beam operations and then into a research and development phase, new diagnostics were required to match the improved performance of the beam. Most notably the research on emittance coupling minimisation for the international damping ring collaboration led to a reduction of the vertical beam profile by a factor of ten, far below the measurement capabilities of the existing diagnostics. Motivated by the achievement of ultralow emittance [4] comparable to the ILC and CLIC damping ring requirements, the measurement capabilities were improved using a number of techniques, including the invention of a new technique of observing the vertical emittance minimisation using a soft x-ray vertical undulator [5]. This article will describe the measurement techniques used at the Australian Synchrotron storage ring to measure the beams that were created for the research into vertical emittance minimisation for damping ring studies, mainly as collaborators and co-authors on the CLIC design reports [6-8]. The techniques for minimising the coupling are not discussed here but the reader is referred to recent descriptions in Ref. [4] and references therein.

Table 2: Source point parameters for the beamlines at the Australian Synchrotron storage ring.

Optics	Parameter	Insertion Device	Dipole 1 Optical source	Dipole 2 X-ray source
0.1 m Dispersion in the Straight Section	β_x [m]	8.993	0.398	0.398
	β_y [m]	2.452	32.752	32.709
	σ_x [μm]	320	87	87
	σ_y [μm] (1% Coupling)	16	58	58
	σ_x' [μrad]	34	178	178
	σ_y' [μrad]	6	6	6

3.3.2 **X-ray Diagnostic Beamline**

3.3.2.1 *Pinhole Principle*

The principle of the x-ray pinhole camera comes from the ancient camera obscura for making images with visible light, the key difference is the penetrating power and the wavelength of x-rays complicate the design and analysis. In order to obscure the unwanted x-rays a high Z material like tungsten with a thickness of a few hundred microns is required. For the x-ray wavelengths the pinhole needs to be a few tens of microns in diameter resulting in an aspect ratio of approximately 10:1 making it more a tube hole rather than a pinhole. Nevertheless, for source sizes of around 100 μm the x-ray pinhole does a good job of imaging the beam and provides an easy online diagnostic in the control room. There are a few limitations that arise when precision measurements are required for research purposes which will be touched on below.

3.3.2.2 *Phase Space*

When measuring the beam profile what needs to be determined from the data is the beam emittance, which is the area of the beam in phase space. Using a single pinhole it is not possible to cover all of phase space, so early on, for example at TRISTAN, it was realised either the beam needed to be bumped across the pinhole to scan phase space or to use a pinhole array to a similar effect [9]. In Figure 1 is shown how a pinhole array in the horizontal plane overlaps with the e-beam phase ellipse to ensure for example the maximum beam width is properly measured.
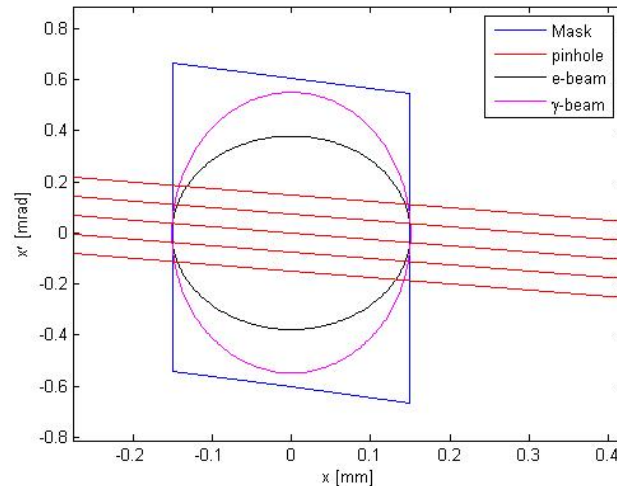
Figure 1: Horizontal phase space diagram of a pinhole array showing the overlap of the pinhole phase space with the x-ray and electron beam phase space.

3.3.2.3 *Pinhole Array*

The pinhole array design at the Australian Synchrotron was based on the work at BESSY [10, 11] and the analysis of the images obtained is similar to that described in Ref [12]. An array of 20 μm pinholes with a spacing of 1.4 mm horizontally and 0.7 mm vertically is placed ~3.3 m from the source point and a YAG screen is located at ~10 m resulting in a magnification of ~2. A typical beam array image can be seen in Figure 2

and the vertical profile showing the opening angle of the radiation is shown in Figure 3, where the opening angle of 0.19 mrad is comparable to the expected $1/\gamma$ value of 0.17 mrad. For daily monitoring the images are sufficient to measure the horizontal and vertical profiles, beam tilt as an indication of the emittance coupling, slow time scale beam drift or centroid motion, beam size blow-up due to instabilities and the beam divergence. As seen in Tables 1 and 2 the nominal electron beam sizes for the storage ring are not challenging to measure. However, once the vertical emittance coupling was reduced from the nominal 1% for longer lifetimes during user beam to less than 0.01% for damping ring studies the vertical beam size at the x-ray pinhole camera source point is only a few microns. At this size the diffraction effects caused by the pinhole are several factors larger than the beam size itself and it is impossible to get an accurate quantitative measure from the vertical profile. Figure 4 shows the effective point spread function of the pinhole calculated using a simple Fresnel model and the 0. 01% emittance ratio gives a beam size of 17 μm, while the LOCO calibrated model deduced the beam size at the source point to be 5 μm.
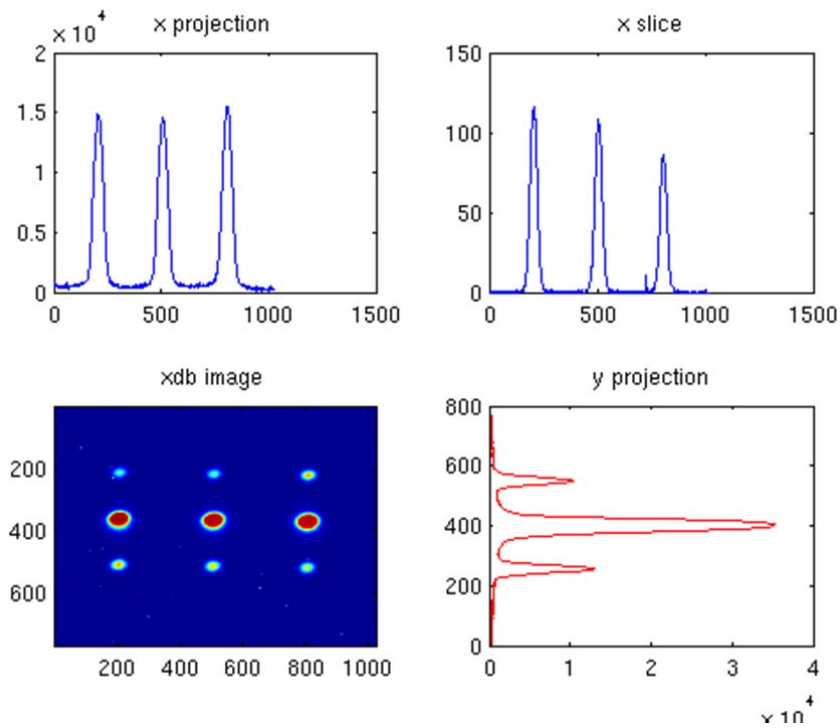
Figure 2: Image created by the x-ray pinhole array.
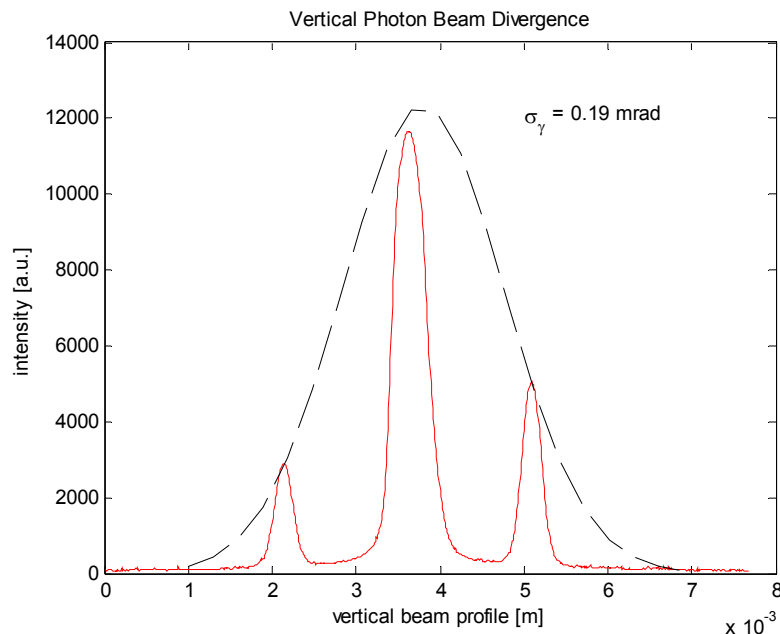
Figure 3: Vertical projection of the x-ray pinhole array image showing the natural opening angle of the dipole radiation.

A more thorough treatment of the pinhole data analysis using an adjustable square aperture has managed to reduce the PSF to 6 μm [13], however this is still too large an uncertainty for the sensitivities required for ultralow vertical emittance optimisation and measurement. In addition, due to the glancing angle scattering of the x-rays from the inside of the pinhole that are effectively tube walls results in a distortion of the profile shape from the expected Gaussian distribution. These effects have not been modeled and further reduce the sensitivity of the x-ray pinhole camera to ultralow vertical emittance.
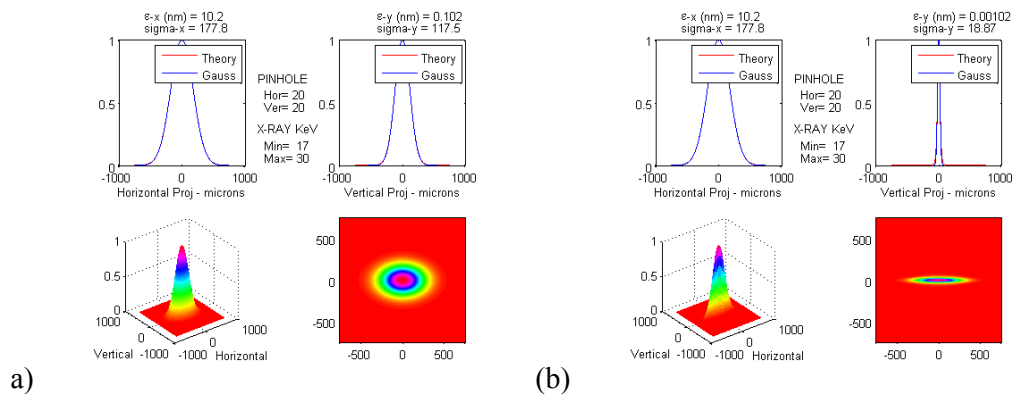
Figure 4: Effective point spread function for pinhole camera and YAG screen system for (a) nominal 1% and (b) minimised 0.01% emittance coupling.

At the Australian Synchrotron x-ray diagnostic beamline, all the components were kept within the storage ring tunnel wall for practical reasons. As a result, the CCD camera used to capture the images is a relatively radiation hardened device and does not have fast gating capabilities. As a consequence the CCD shutter times used to capture

images are relatively slow. The low intensity of the fluorescence from the YAG screen is such that the light needs to be integrated from thousands of turns in the ring to obtain a satisfactory image. This further introduces a broadening of the beam profile due to beam motion on a number of time scales. The storage ring currently does not have a fast orbit feedback system so 50 Hz mains line noise couples into the beam and is observed on the BPMs as periodic motion of the beam centroid, up to several percent of the beam size. The nature of this motion has been confirmed by observation on the optical diagnostic beamline using 2D optical diodes and a fast gated ICCD camera which can measure down to a single bunch at a time [14].

3.3.2.4 *Profile, Divergence, Emittance and Tilt Angle*

Despite the limitations described above the x-ray pinhole has proved useful during operational use of the machine and for getting a first order estimates during machine development time. Plotting the trend of the changed in the beam profile and tilt angle have been used as a cross check for measurement using new instrumentation. For example while testing the vertical undulator measurements shown in the section below. Figure 5 shows an example of the title angle of the beam image from the x-ray pinhole for various settings of the skew quadrupoles. The skew quadrupole values were calculated to produce a range of emittance coupling values using a LOCO model of the storage ring [15]. Once again it can be seen that the errors in the fit are too large at the ultralow emittance values to give an accurate measurement but the trend indicates that the coupling minimisation algorithm is in principle working correctly. Similarly in Figure 6 the vertical beam size cannot be reliably extracted from the x-ray pinhole data but there is a consistent trend from 20% emittance coupling, through the nominal 1% for user beam and down to the ultralow values obtained using the minimisation technique.
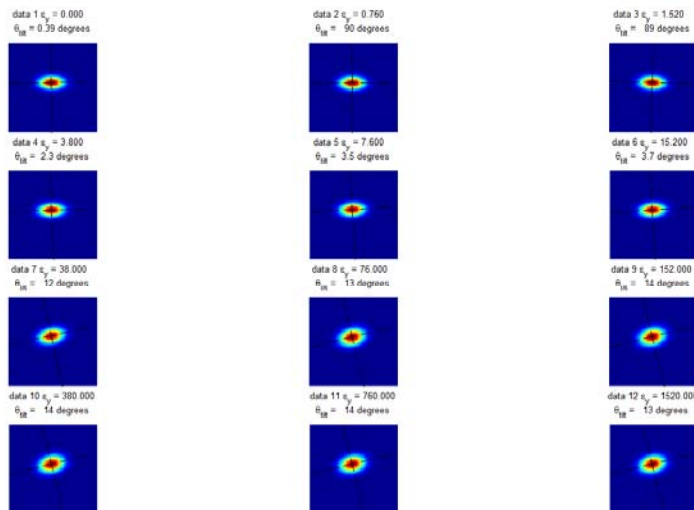
Figure 5: X-ray pinhole beam axis title measurement for a range of emittance coupling settings.
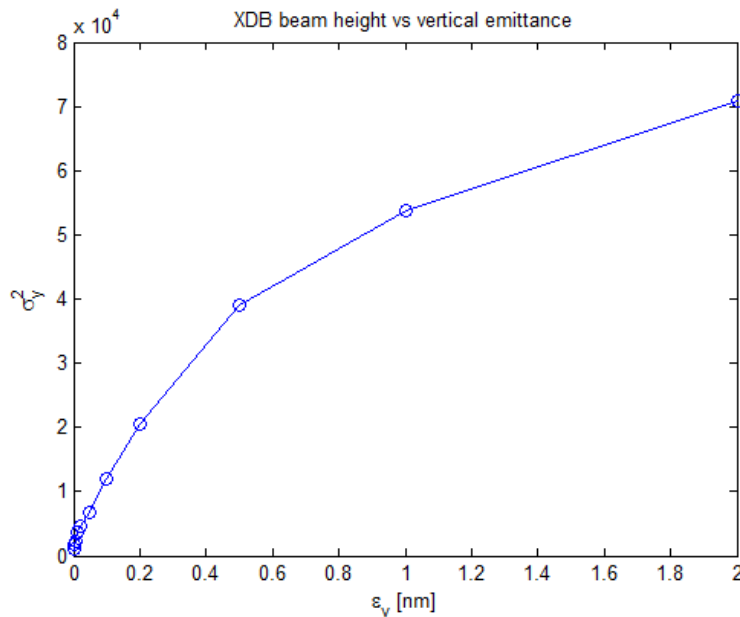
Figure 6: Square of the vertical beam size plotted against a calculated emittance coupling using the calibrated LOCO model using an emittance minimisation process.

3.3.3 Optical Diagnostic Beamline

3.3.3.1 *Designed for Longitudinal Measurements*

The design of the optical diagnostic beamline followed Ref [16] and was initially only planned for longitudinal measurements since the x-ray frontend it was assigned to only had a ~2 mrad vertical opening angle. Since the full vertical opening of the optical radiation fan is ~10 mrad the dipole crotch absorber causes significant diffraction that adds unwanted features to any profile measurement. For simplicity the extraction mirror only intercepts the top half of the radiation fan and the hard x-rays pass below the base of the mirror to avoid unwanted deformation from heating. The visible light is bounced vertically down 0.5 m and then a second mirror sends it back horizontal and parallel to the initial beam. An achromatic lens with $f = 3.5$ m was placed 6.6 m from the source and the focused beam then extracted from the storage ring tunnel into an optical hutch. A 1:1 image was formed over an optical table and distributed to various instruments; fast photo diode fill pattern monitor, streak camera, ICCD, 2D photo diode, APD photon counter for bunch purity monitoring. Figure 7 shows the initial images obtained with a clear diffraction tail from the bottom of the mirror and some smaller diffraction tails from the frontend mask.
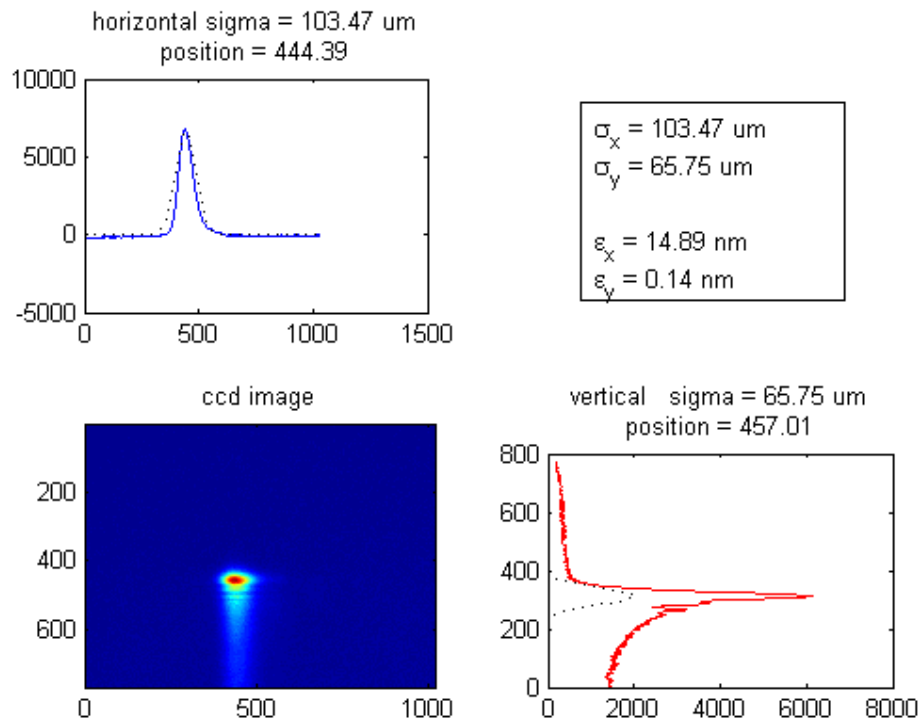
Figure 7: Initial images from the optical diagnostic beamline before correcting diffraction effects from the front end mask and the extraction mirror.

3.3.3.2 *Direct Imaging Limitations*

In part due to the long focal length but also due to the fundamental issues with making high quality lenses, there were other aberrations that limited the quality of the direct imaging techniques that were used to measure the beam profile. Using some apertures along the beam path most of the diffraction could be eliminated to obtain an image that was useful for user beam operations and compared reasonably with the x-ray pinhole image for large beam sizes (see Figure 8). However, like with the x-ray pinhole, once the emittance minimisation research program started and the ultralow vertical emittance was achieved, the direct imaging of the beam with the optical diagnostic beamline was inadequate for accurate measurements and new techniques were required.
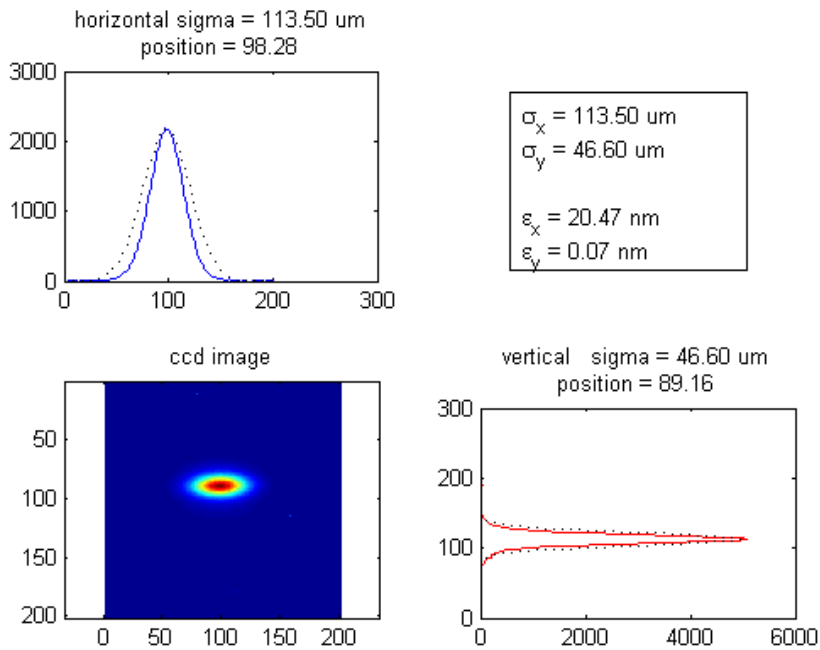
Figure 8: Beam profiles from direct visible light imaging with an f = 3.5 m focal length achromatic focussing lens and an optical aperture that reduces the diffraction from the frontend mask and the mirror edge.

Table 3: Comparison of the beam profile aspect ratios for the x-ray and optical diagnostic beamlines.

	ODB (a.u.)	XDB (a.u.)
X position	494	412
Y position	364	373
σ_x	64	17
σ_y	34	8.5
σ_x / σ_y	**1.9**	**2**

3.3.3.3 *Interferometry*

In an attempt to improve the beam size measurements using the optical diagnostic beamline an interferometer system was introduced [17]. Initially a new type of apparatus was developed using the existing beam optics with the f = 3.5 m achromatic lens in place but the data proved too noisy [18], while later versions followed the simple design from Mitsuhashi (see Ref. [19,20] for details of the apparatus). The interferometer technique works best with only the minimal number of elements between the source point and the double slits, namely an extraction mirror and a vacuum window. Great care should be taken on the quality of the extraction mirror and vacuum window, both should be well-polished so as not to introduce any unwanted scatter. For daily monitoring, distortions in the extraction mirror due to the x-ray heat load can be measured using the Hartmann technique [21,22], however for once off precision measurements a low current beam will yield the best results. An interference pattern

from the Australian Synchrotron optical diagnostic beamline interferometer captured by a high dynamic range camera can be seen in Figure 9 [23].
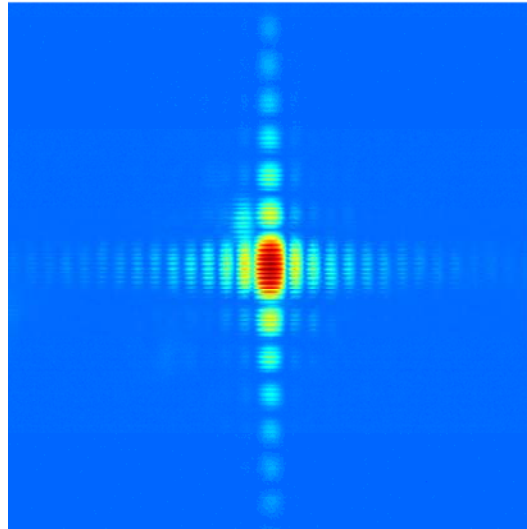
Figure 9: Interference pattern from the Mitsuhashi Interferometer at the Australian Synchrotron storage ring optical diagnostic beamline.

Once again the interferometer proved very useful for the daily operational monitor, where beam sizes were around 60 μm, however for measuring the 5 μm beams generated by the ultralow emittance coupling there were a few limitations. Firstly, the visibility of the interference pattern is very close to 1 for small beam sizes and valleys of the interference pattern can be in the noise of the CCD camera increasing the error of the measurement (see below how this can be overcome). Secondly, the front end mask and the extraction mirror position above the beam axis mean that the full beam opening angle cannot be used for the interferometer measurement at the Australian Synchrotron. This limits the slit separation and as a result the number of spatial frequencies that can be used and as a result the small source point cannot be unambiguously reconstructed. Finally, the quality of the objective lens is critical and any aberrations in this lens directly affect the measurement. High quality refractive lenses can be obtained and alternatively a focusing reflector can be used for the interferometer [24].

3.3.3.4   *Intensity Imbalanced Interferometer*

The problem of having a visibility of close to 1 can be overcome using an intensity imbalanced interferometer [25] in order to change in a controlled way the quantum mechanical probability of interference between the two arms of the interferometer. An optical flat with one half of the front surface covered in a 20% transmission coating was placed after the double slit. As a result the visibility is reduced and lifts the modulation of the sinc function out of the noise floor in the CCD (see Figure 10 [25]).
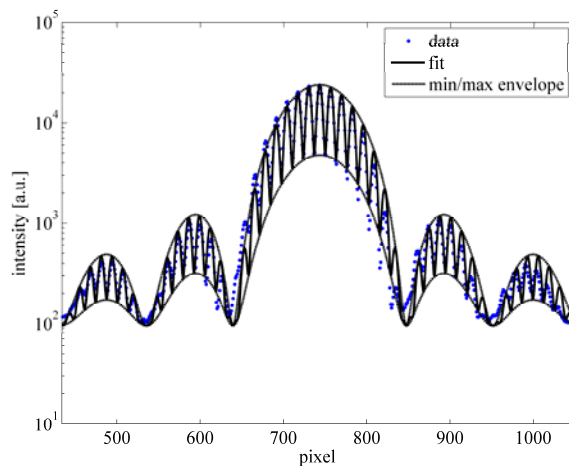
Figure 10: Intensity imbalance interferometer pattern where the visibility has been reduced in a controlled way to reduce the error in the measurement.

The imbalanced method has been demonstrated to be capable of measuring a beam size down to 10 μm at the ATF damping ring [25], however this measurement was only limited by the fact the machine had not been retuned following an earthquake. A beam size of 4.7 ± 0.6 μm was measured at the ATF damping ring with an optimised lattice using a focusing reflector interferometer [24] and could be further improved with the imbalance method if smaller beam sizes needed to be measured.

3.3.4 Indirect Measurements

To demonstrate the record low emittance coupling achieved in the Australian Synchrotron storage ring [4] the above mentioned limitations in the beam size measurement diagnostics meant that a series of indirect measurements were needed to deduce the vertical emittance. The details of indirect measurement of vertical emittance from lifetime and closest tune approach have already been described previously (Ref. [26], section 3.9.6 and references therein) and so will not be repeated here.

In order to minimise the emittance coupling a calibrated lattice model was made by measuring the linear optics and fitting using LOCO. An algorithm for calculating the emittance from the lattice model [27] is built into the AT [28] code that is used by LOCO and the minimisation procedure. After settings for a certain emittance coupling were calculated in the model they were applied to the machine and a series of measurement were made to deduce the vertical emittance and test the algorithm. In addition to the tune approach and lifetime measurement already mentioned, the beam tilt angle on the x-ray pinhole camera and the Touschek parameter with RF voltage were also measured to deduce the vertical emittance [4].

3.3.5 Vertical Undulator Technique

3.3.5.1 *Radiation field from Undulator at Ultra low Emittance*

The idea for using a vertical undulator to observe the emittance minimisation in the Australian Synchrotron came from a discussion with a user on the effect of the

horizontal emittance on an undulator spectrum. It led to measurement of the APPLE II undulator spectrum on the soft x-ray beamline [29] with the four arrays of magnets phased to produce a horizontal magnetic field (see Figure 11). The electron beam then undulated in the vertical plane and the ratio of the odd and even harmonic peaks in the spectrum gives a measure of the vertical emittance (see Ref [5] for details).
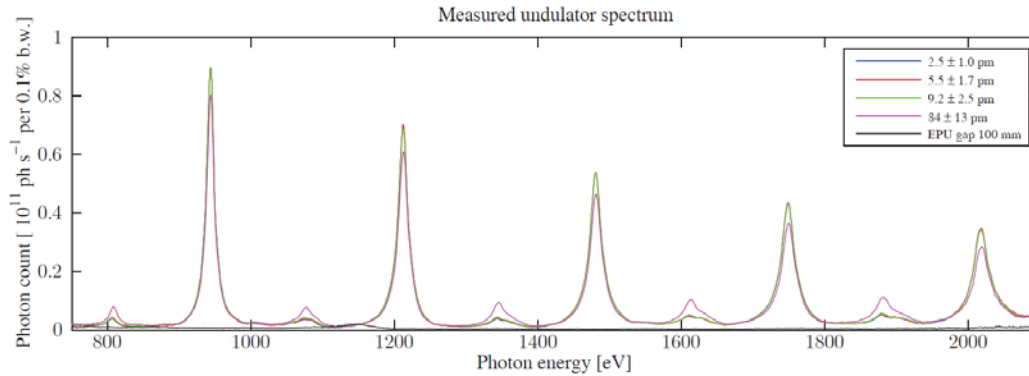
Figure 11: Measured undulator spectrum in vertical polarisation mode on the soft x-ray beamline at the Australian Synchrotron.

The results show the sensitivity of the measurements is approximately 1 pm rad down at an estimated emittance of 3 pm rad. The vertical emittance was set using the skew quadrupole values calculated from the calibrated model. Applying a range of decreasing emittance coupling values to machine produces results which when measured with the vertical undulator show a monotonically decreasing ratio of the even to odd harmonics, consistent with the other diagnostics.

3.3.5.2 *Blade Scan*

This technique was however very sensitive to the pinhole size and position which the beamline was not designed to have precise control over. An attempt to use a blade scan to get improved sensitivity failed to improve the measurement but did lead to an interesting observation of an up/down asymmetry in the even harmonics which was characterised and explained [30]. Figure 12 shows a good agreement for the measurements and the simulations of the x-ray flux through a pinhole where a measured field map of the undulator is used in the code SPECTRA [31]. There is a qualitative indication that the measurement can observe the difference but the errors are too large to put an accurate value on the minimum emittance achieved.
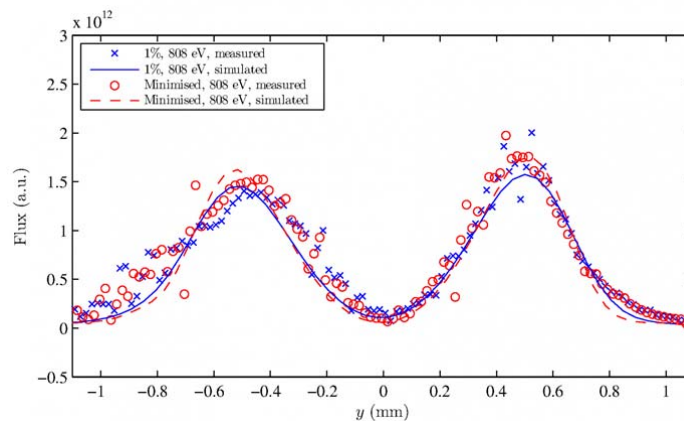
Figure 12: Vertical blade scan across the vertical undulator radiation at an even harmonic for 1% emittance coupling and for minimum emittance coupling (modelled to be 0.5 pm rad).

3.3.5.3 *Improved Measurement with Beam Bumps*

Due to the lack of precision in the control of the pinhole and blade scanning system on the soft x-ray beamline a new method was developed using the electron beam vertical and horizontal steering magnets. The idea is that electron beam orbit bumps using the BPM system and the magnet power supplies are better able to steer the photon beam through a fixed pinhole, rather than move the blades. The angle and position changes of the beam through the undulator are assumed to be smaller perturbation than the emittance changes.
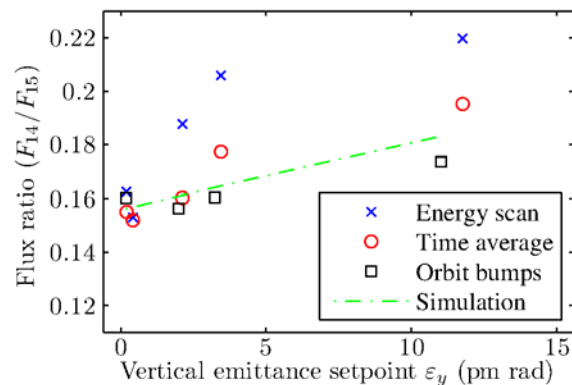
Figure 13: Comparison of the flux ratio measurements for the range of set vertical emittances using various techniques to take the flux data.

3.3.6 **Conclusion**

Emittance measurements at the Australian Synchrotron are adequate to demonstrate the design performance for the daily monitoring of user operations. The ability to achieve ultralow vertical emittance where the dominant contribution comes from the quantum limit has proved too challenging for the original diagnostics. New approaches using an optical interferometer and a vertical soft x-ray undulator have yielded promising results and new hardware is planned to achieve the theoretical optimum performance from these apparatus. Record low emittance coupling has been

demonstrated using indirect measurement techniques in the Australian Synchrotron storage ring, which meet the CLIC and ILC damping ring design goals for vertical emittance of ~1 pm rad. However, the horizontal emittance is much larger and IBS effects remain to be quantified for this configuration. Nevertheless progress has been made and once again the usefulness of light sources has been demonstrated as testing grounds for future high energy machines.

3.3.7 **References**

1. J. W. Boldeman and D. Einfeld, Nuclear Instruments and Methods in Physics Research Section A: Accelerators, Spectrometers, Detectors and Associated Equipment **521** (2-3), 306 - 317 (2004).
2. K. P. Wootton, M. J. Boland, W. J. Corbett, X. Huang, G. S. LeBlanc, M. Lundin, H. P. Panopoulos, J. A. Safranek, Y. R. E. Tan, G. N. Taylor, K. Tian and R. P. Rassool, Physical Review Special Topics-Accelerators and Beams **16** (7), 074001 (2013).
3. M. J. Boland, A. C. Walsh, G. S. LeBlanc, Y.-R. E. Tan, R. Dowd and M. J. Spencer, X-ray and Optical Diagnostic Beamlines at The Australian Synchrotron Storage Ring, in Proceedings of EPAC 2006, Edinburgh, 26-30 June, (2006), p. THPLS002.
4. R. Dowd, M. Boland, G. LeBlanc and Y. R. E. Tan, Physical Review Special Topics-Accelerators and Beams **14** (1), 012804 (2011).
5. K. P. Wootton, M. J. Boland, R. Dowd, Y. R. E. Tan, B. C. C. Cowie, Y. Papaphilippou, G. N. Taylor and R. P. Rassool, Physical Review Letters **109** (19), 194801 (2012).
6. P. Lebrun, L. Linssen, A. Lucaci-Timoce, D. Schulte, F. Simon, S. Stapnes, N. Toge, H. Weerts and J. Wells, *The CLIC Programme: Towards a Staged e+ e-Linear Collider Exploring the Terascale: CLIC Conceptual Design Report*. (CERN, Geneva, 2012).
7. M. Aicheler, P. Burrows, M. Draper, T. Garvey, P. Lebrun, K. Peach, N. Phinney, H. Schmickler, D. Schulte and N. Toge, *A Multi-TeV Linear Collider Based on CLIC Technology: CLIC Conceptual Design Report*. (CERN, Geneva, 2012).
8. L. Linssen, A. Miyamoto, M. Stanitzki and H. Weerts, *Physics and Detectors at CLIC: CLIC Conceptual Design Report*. (CERN, Geneva, 2012).
9. A. Ogata, T. Katsura, T. Kawamoto, T. Mitsuhashi and N. Yamamoto, presented at the Proceedings of the 1989 IEEE Particle Accelerator Conference, Chicago, (1989), p. 1498.
10. W. B. Peatman and K. Holldack, J. Synchrotron Rad. **5**, 639-641 (1998).
11. M. Gerner, K. Holldack, R. Lu¬ttge, M. Schmidt, Microsystem Technologies **4**, 184-186 (1998).
12. P. Elleaume, C. Fortgang, C. Penel, and E. Tarazona, J. Synchrotron Rad.**2**, 209 (1995).
13. C. Thomas, G. Rehm, I. Martin and R. Bartolini, Physical Review Special Topics - Accelerators and Beams **13** (2), 022805 (2010).
14. M. J. Boland, T. M. Mitsuhashi and K. P. Wootton, Turn-by-turn Observation of the Injected Beam Profile at the Australian Synchrotron Storage Ring, *Proceedings of the International Beams Instrumentation Conference 2012*, Tsukuba, Japan, October 2012, MOPB83.
15. M. J. Spencer, ICFA Beam Dynamics Newsletter 44, pp. 81-91 (2007).
16. J. C. Bergstrom and J. M. Vogt, Nuclear Instruments and Methods in Physics Research, Section A: Accelerators, Spectrometers, Detectors and Associated Equipment **562** (1), 495-512 (2006).
17. T. Mitsuhashi, Proceedings of the Joint US-CERN-Japan-Russia School on Particle Accelerator Beam Measurements (World Scientific Publishing, Singapore, 1999), pp. 399–427.
18. K. P. Wootton and M. J. Boland, A Novel Synchrotron Radiation Interferometer for the Australian Synchrotron, in Proceedings of IPAC 2010, Kyoto, Japan, May, 2010,

MOPD079.

19. T. Mitsuhashi, Spatial coherency of the synchrotron radiation at the visible light region and its application for the electron beam profile measurement, in Proceedings of PAC97, p. 766-768, Vancouver, Canada, May, 1997.

20. T. Mitsuhashi and T. Naito, in Proceedings of EPAC98, p. 1565, Stockholm, Sweden, June, 1998.

21. N. Takeuchi, T. Mitsuhashi, M. Itoh, T. Yatagai, Wavefront Distortion Measurement of a SR Extraction Mirror for the Beam Profile Monitor Using Shack-Hartmann Method, in Proceedings of PAC 1997, p. 859, Vancouver, Canada, May, 1997.

22. T. Mitsuhashi and M. Tadano, in Proceedings of APAC 2001, p. 704, Beijing, China, 2001.

23. M. J. Boland, T. Mitsuhashi and K. P. Wootton, Low Noise and High Dynamic Range Optical Interferometer Beam Size Measurements, presented at the International Beam Instrumentation Conference 2013, Oxford, UK, September, 2013, TUPF20.

24. T. Naito and T. Mitsuhashi, Physical Review Special Topics - Accelerators and Beams **9** (12), 122802 (2006).

25. M. J. Boland, T. Mitsuhashi, T. Naito and K. P. Wootton, Intensity Imbalance Optical Interferometer Beam Size Monitor, in Proceedings of International Beam Instrumentation Conference 2012, Tsukuba, Japan, October, 2012, WECC03.

26. A. Franchi and L. Farvacque, ICFA Beam Dynamics Newsletter 57, pp. 105-118 (2007).

27. K. Ohmi, K. Hirata and K. Oide, Phys. Rev. E, **49** (1), 751 (1994).

28. A. Terebilo, Proceedings of PAC01, p. 3203, Chicago, Illinois, USA (2001).

29. B. C. Cowie, A. Tadich, and L. Thomsen, AIP Conf. Proc., **1234**, 307 (2010).

30. K. P. Wootton, R. P. Rassool, M. J. Boland and B. C. C. Cowie, APPLE-II Undulator Magnetic Fields Characterised from Undulator Radiation, in Proceedings of International Beam Instrumentation Conference 2013, Oxford, UK, September, 2013, TUPF19.

31. T. Tanaka and H. Kitamura, J. Synch. Rad. **8**, 1221 (2001).

3.4   Beam Dynamics Activities at PETRA III

Alexander Kling and Rainer Wanzenberg, DESY, Hamburg, Notkestr. 85, Germany

Mail to: rainer.wanzenberg@desy.de

3.4.1   Introduction

PETRA III [1] is a third generation synchrotron radiation facility at DESY. The PETRA ring was originally built as an electron and positron collider in 1976. From 1988 until 2007 PETRA was used as a pre-accelerator for the HERA lepton hadron collider ring. During the conversion to a synchrotron radiation facility from 2007 to 2009 one octant of the PETRA ring has been completely redesigned to provide space for 14 undulators. The commissioning with beam started in April 2009 and user runs have been started in 2010 [2]. Until the end of 2012 PETRA III was running in a top-up operation mode with positrons since PETRA III was sharing the same pre-accelerator chain with the synchrotron light source DORIS, which was running with positrons to avoid problems with ionized dust particles. The main design parameters are listed in Table 1.

Table 1: PETRA III design parameters

Parameter		PETRA III	
Energy	GeV	6	
Circumference	m	2304	
Total current	mA	100	
Number of bunches		960	40
Bunch population	10^{10}	0.5	12
Bunch separation	ns	8	192
Emittance (horz. / vert.)	nm	1 / 0.01	

The design current of 100 mA has been achieved but using different filling schemes than originally foreseen, since a vertical emittance blow-up has been observed for a filling scheme with 960 equidistantly spaced positron bunches. In 2010 studies with different filling schemes indicated already that the vertical emittance blow-up is related to an Electron Cloud (EC) instability [3].

In 2011 three filling schemes, with bunch to bunch spacing of 192 ns (40 bunches), 128 ns (60 bunches) and 32 ns (240 bunches) have been used. For a filling scheme with 40 and 60 bunches no phenomena were observed which could be related to EC effects. However, for the filling scheme with 240 bunches (32 ns spacing) a slight vertical emittance growth was observed (ε_y~0.025 nm), which was still acceptable for user operation. During the start-up phase for the 2012 running period scrubbing runs with 480 equidistant bunches and a total beam current of 100 mA have been done for 4 days. During the scrubbing run, phenomena related to EC effects have been observed: horizontal and vertical emittance growth and extra lines in the vertical tune spectra. After the scrubbing run it was possible to operate PETRA III with 240 bunches with a smaller vertical emittance (ε_y~0.01 nm) than in 2011. It was also possible to run with 320 equidistantly spaced bunches and a small vertical emittance growth. But for filling schemes with 480 bunches and 960 bunches (8 ns bunch spacing, design parameter) a significant emittance growth has been observed, which excludes these filling schemes for user runs. The present understanding of the EC effects at PETRA III is summarized in Refs. [4, 5].

Since January 2013 PETRA III is running with electrons. It is now possible to operate the storage ring with 960 bunches (8 ns bunch spacing) without any vertical emittance growth. But the filling schemes with fewer bunches, which were successfully used during positron operation, suffer from ion effects. Some details are reported in the next section.

Further beam dynamics activities at PETRA III concentrated on the understanding of the beam dynamics of very low emittance beams (160 pm rad) at 3 GeV and the investigation of beam losses during user runs at 6 GeV.

3.4.2 Investigation of Ion Effects

At PETRA III it is now possible to compare the measurement with positron and electron beams for several filling schemes. For some filling schemes a vertical emittance growth was observed in 2013 with an electron beam while this effect was not observed during positron operation. This strongly indicates that the emittance growth is due to ion

effects. Classical ion trapping and the fast ion instability were studied via computer simulations in Ref. [6] for PETRA III. However, the measurements indicate that a different ion effect seems to cause the emittance growth, which was first reported from the TRISTAN accumulator ring [7] using a theory of a two beam instability [8]. The transverse motion of the ions, which are produced and trapped by the stored electron beam, and the betatron motion of the beam are coupled. The transverse oscillation of the ions is ~ exp(i Ω t) while the beam oscillates ~ exp(i (m θ - Ω t)), where m is the transverse mode number and θ is the azimuthal coordinate along the storage ring. The frequency Ω is the solution of the fourth order mode equation [7, 8]:

$$(\Omega^2 - \omega_i^2)\left((\Omega - m\,\omega_0)^2 - \nu_y^2\omega_0^2 - \omega_e^2\right) = \omega_e^2\omega_i^2, \tag{1}$$

where ω_i is the oscillation frequency of the ions in the beam potential and ω_e is the oscillation frequency of the electrons of the beam in the potential of the ions, while ω_0 is revolution frequency and ν_y is the vertical betatron tune.

For the measurement of the vertical emittance an interferometric vertical beam size measurement [9, 10] is used. Synchrotron light from a bending magnet is sent through a double slit and generates an interference pattern. The beam size is calculated from the visibility of the interferogram, which indicates the degree of spatial coherence of the photons. Furthermore, the spectrum of the multibunch oscillations and the tune spectrum of individual bunches are measured using the signals from the feedback system [11].

During studies the filling schemes, which are shown in Fig. 1, were used in 2013. There are 960 nominal positions in PETRA III with spacing of 8 ns, which is presently the smallest possible bunch-to-bunch distance determined by the bandwidth of the multibunch feedback system (the harmonic number is 3840 = 4 x 960). The first four filling schemes (40, 60, 480 and 960 bunches) do not suffer from any vertical emittance growth at a total current of 100 mA and were used for user runs. All the other filling schemes showed a significant vertical emittance growth at a threshold current of about 60 mA. The filling scheme with 240 bunches was used during positron operation without any significant emittance growth in 2012 for user runs.

238
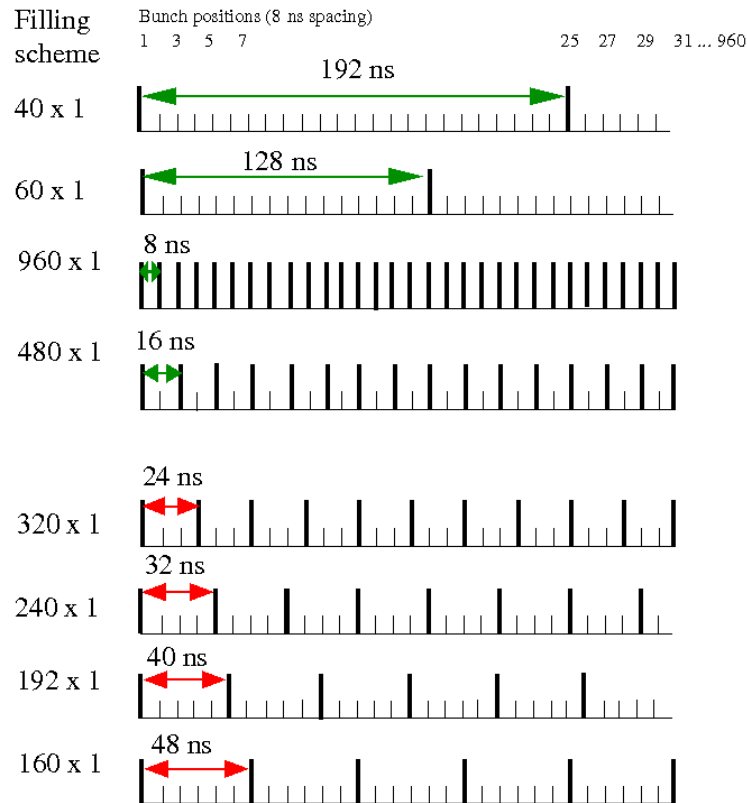
Figure 1: Different bunch filling schemes of PETRA III.

For the filling scheme with 240 bunches a multibunch mode with mode number m=71 corresponding to a frequency of about 9.2 MHz was measured in the multibunch spectrum during studies in March 2013. Eqn. (1) has only a complex solution for mode number m=71 if one assumes an rms beam size of 800 μm (horz.) / 10 μm (vert.) and an ion density of about 20 ions/cm. The solutions of Eqn. (1) for all other mode numbers have four real solutions (no instability). The imaginary part of the complex solution corresponds to the inverse of the growth rate of the two beam instability, which is larger than the damping rate of the multibunch feedback system. These preliminary results indicate that the observations at PETRA III are in agreement with a two beam instability due to ions using the same theory as in Ref. [7, 8].

3.4.3 Very Low Emittance Beams at 3 GeV

The interest in realizing a next generation, storage ring based, diffraction limited light source, a so called "ultimate" storage ring (USR), is growing [12]. The design of these machines, which have electron emittances of < ~100 pm in both transverse planes, requires R&D in various accelerator physics and engineering areas before such machines can actually be implemented. Especially collective effects could limit the achievable emittances in an USR.

To contribute to the R&D for an ultimate storage ring PETRA III was operated at an energy of 3 GeV for the first time during a study period in July 2013. It was possible to achieve a horizontal emittance of 160 pm rad which seems to be a new world record

with respect to smallest achieved beam emittance in storage rings. An interferometric horizontal beam size measurement [9, 10] was used to measure the emittance. The interferogram is shown in Fig. 2 for a total beam current of 5 mA in 480 bunches or a single bunch current of 10.4 µA. The measured value of 160 pm rad is in agreement with predictions. For higher bunch currents a significant emittance blow-up was observed. The measured emittance versus the single bunch current is shown in Fig. 3.
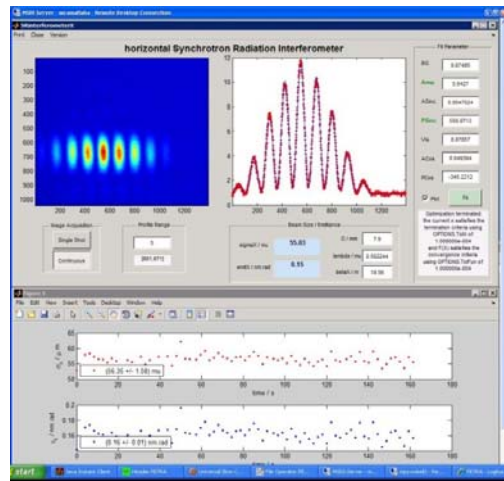
Figure 2: Measured horizontal emittance of 160 pm (calculated from the visibility of the interferogram) for a total beam current of 5 mA in 480 bunches at 3 GeV.
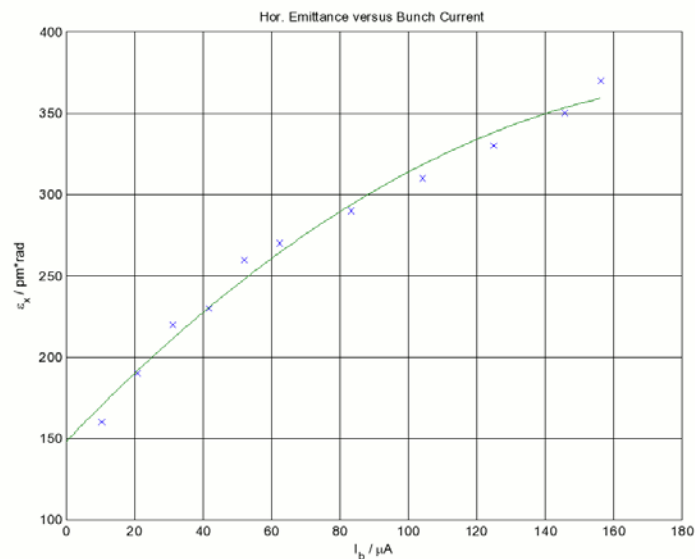
Figure 3: Horizontal emittance versus the single bunch current of PETRA III at 3 GeV.

The emittance increase can be associated with intra-beam scattering (IBS) [13], which leads to an increase of the beam dimensions in all three directions due to multiple Coulomb scattering within the beam. Whether the observed emittance increase is completely in agreement with IBS-theory could not be comprehended from the data taken in July 2013 since only the horizontal beam size was measured. The vertical emittance depends on the degree of coupling compensation and dispersion correction.

Recent measurements in October 2013 indicate that the vertical emittance is for all considered single bunch currents of Fig. 3 smaller than 10 pm rad. Further investigations are necessary to model the measured beam size data in detail.

3.4.4 Beam Losses and Radiation Damage at the Insertion Devices

Radiation damage of machine hardware, electronics and magnet structures has been observed for some time in PETRA III. First signs of radiation damage were observed in the wiggler sections. Performance losses have been observed at several beamlines. The gaps operated at some beamlines have to be decreased or tapers introduced over time and distortions of higher harmonics have been measured. Similar signs of performance loss due to radiation damage have been observed and thoroughly investigated in, e.g., [14, 15].

In situ measurements of the longitudinal peak field profile of all insertion devices (IDs) revealed a partial demagnetization of certain undulators, see Fig. 4.
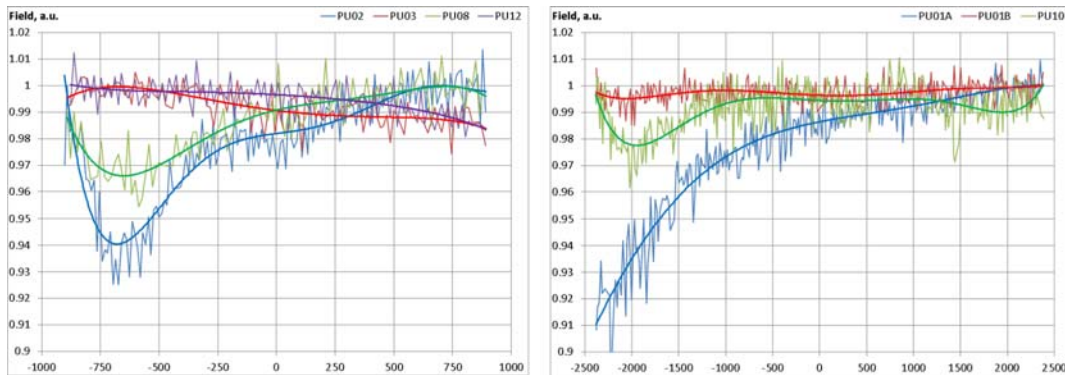
Figure 4: Recent in situ measurements of the longitudinal peak field profile of undulators affected by radiation damage. The lhs shows data for selected 2m IDs. PU02 and PU08 are located upstream in canted straights while PU03 and PU12 are located downstream. On the rhs data for 5m IDs are depicted. All data are normalized to values measured in the laboratory.

In PETRA III 5m long IDs are installed in long straight sections while 2m long undulators are installed in canted straight sections. At the beginning of the experimental hall two 5m IDs, PU01A and PU01B, are installed in the same straight to serve beamline P01. Demagnetization is observed either at the upstream or the downstream end of the IDs but in all cases at positions where the normalized vertical aperture becomes small. The normalized vertical aperture around the ring is shown in Fig. 5.

Together with the fact that at PU01A/B the upstream dipole is located 40m away from the undulator a damage due to synchrotron radiation emitted by dipoles located upstream of the IDs seems to be ruled out. In order to investigate particle losses at the IDs PIN-diode beam loss monitors (BLMs) formerly used in the HERA-e ring [16] have been installed in all straight sections of the new octant. The BLMs are operated in the so called coincidence mode being primarily sensitive to particle losses while suppressing the synchrotron radiation background.
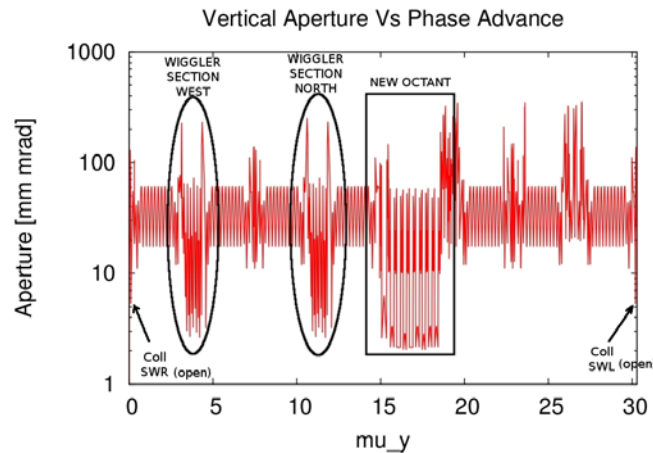
Figure 5: Normalized vertical aperture in PETRA III. Small vertical apertures are set by absorbers in the wiggler sections west and north and by the small gap chambers at the IDs in the new octant. The movable vertical collimators are closed down to ~0.4 mm mrad during user operation.

For global collimation two movable vertical collimators are available in PETRA III. Their main purpose is to intercept injected particles with amplitudes exceeding the available vertical physical aperture. Optimizing the collimator positions reduces the particle losses at injection measured by the PIN beam loss monitors up to a factor of 100, however on the cost of reducing the injection efficiency by ~20%.
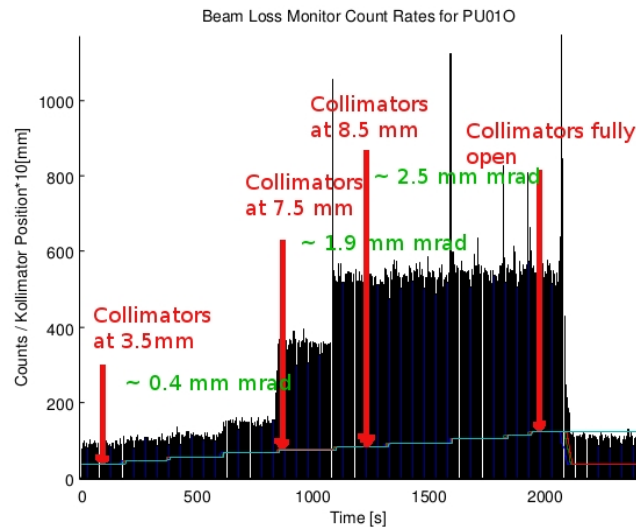
Figure 6: Counts measured at PIN-diode PU01(out) during top up operation with 100mA stored in 960 bunches. The set values of the collimators are varied during the measurement from nominal 3.5 mm (0.4 mm mrad) to fully open corresponding to 12 mm (4.8 mm mrad). The aperture set by the small gap undulator chamber at PU01 corresponds to 2.5 mm mrad.

The collimators are installed in a non dispersive section with large vertical beta-function. The vertical phase advance between them is approximately 75 degree. The efficiency of the collimation system with respect to particle losses occurring from the

stored beam has been the subject of dedicated machine studies. During these studies the set points of the collimators have been varied from 3.5 mm (used during user runs) to fully open (12.5mm). In Fig. 6, the counts detected at the PIN-diodes are plotted over time along with the set values of the collimators. The measurement was done with 100mA stored in 960 bunches using top up operation with a 1% variation of the stored current.

While opening the collimators an increase in BLM counts is observed when the normalized aperture set by the collimators becomes comparable to the size of the vertical aperture given by the small gap undulator chambers. Below and above that value the count rates are essentially not affected by the collimator set values indicating the fact that the IDs lie completely inside/outside of the shadow of the collimators. The result for the same experiment performed with 50mA stored in 40 bunches displayed in Fig. 7 shows some remarkable differences.
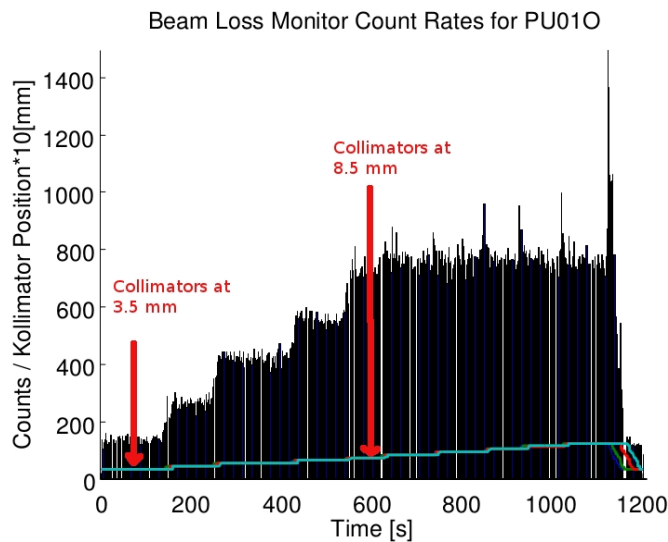
Figure 7: Counts measured at PIN diode PU01(out) during top up operation with 50mA stored in 40 bunches. The set values of the collimators are varied during the measurement from nominal 3.5 mm (0.4 mm mrad) to fully open corresponding to 12 mm (4.8 mm mrad). The aperture set by the small gap undulator chamber at PU01 corresponds to 8.5mm (2.5 mm mrad).

A region of constant count rates at narrow gap values of the collimators is not observed when PETRA III is operated with large single bunch currents. When closing the collimators stepwise the number of counts is gradually reduced without reaching a minimal count rate independent of the aperture limit set by the collimators. The count rate at large single bunch currents is considerably higher reflecting the low beam lifetime dominated by Touschek scattering [17]. Touschek scattered particles are lost due to the large longitudinal momentum deviation resulting from the collision. These scattering events occur all around the ring and scattered particles may be lost within a single turn whereas it can take them several turns to be intercepted by collimators depending on the phase advance and the collimation system. Off momentum beta beating leads to an asymmetry in the aperture limits as seen by particles with large momentum offset. This might provide a route for off momentum particles to escape the collimation system.

More investigations concerning the efficiency of the collimation system are planned in order to improve the understanding and further enhance the protection of the insertion devices. Extensive tracking studies are currently in progress to clarify the observed patterns of particle losses and optimize the placement of additional (local) collimation insertions. An upgrade of the collimation system during the reconstruction phase of the PETRA III extension in 2014 is under consideration.

3.4.5 Acknowledgements

3.4.6 References

1. PETRA III, Technical Design Report, DESY 2004-035, 2004.
2. K. Balewski, "Comissioning of PETRA III", IPAC'10, Kyoto, Japan, 23-28 May 2010
3. R. Wanzenberg, "Emittance Growth and Tune Spectra at PETRA III", DESY Report, DESY 11-140, 2011.
4. R. Wanzenberg, "Observation of Electron Cloud Phenomena at PETRA III", ECLOUD'12, CERN-2013-002, April 2013.
5. D. R. Grosso et al., "Effect of the surface processing on the secondary electron yield of Al alloy samples", Phys. Rev. ST Accel. Beams 16, 051003 (2013).
6. G. Xia et al., "Ion Effect Issues in PETRA III", PAC09, Vancouver, Canada, (2009)
7. S. Matsumoto et al., "Experimental Study of the Ion Trapping Phenomenon in Tristan-AR", PAC97, Vancouver, Canada, 1997
8. D.G. Koshkarev, P.R. Zenkevich, "Resonance of Coupled Transverse Oscillations in Two Circular Beams", Part. Acc., 1972, Vol 3. pp.1-9
9. T. Naito and T. Mitsuhashi, "Very Small Beam-Size Measurement By a Reflective Synchrotron Radiation Interferometer", Phys. Rev. ST Accel. Beams 9 (2006) 122802.
10. G. Kube, et al. , "Overview of the Diagnostics Systems of PETRA III", EPAC'08, 2008. 23-27 Jun 2008, Genoa, Italy, Conf. Proc. C 0806233 (2008) TUPC111.
11. J. Klute, et al. , "The PETRA III Multibunch Feedback System", DIPAC2011, Hamburg, Germany (2011).
12. Yi Jiao, "Workshop on Accelerator R&D for Ultimate Storage Rings", in ICFA Beam Dynamics Newsletter No. 60 (April 2013, edited by G. Neil).
13. A. Piwinski, "Intra-Beam Scattering", Proc. 9th Int. Conf. on High Energy Acc., Stanford (1974) p 405.
14. M. Borland et al., "Touschek Lifetime and Undulator Damage in the Advanced Photon Source", PAC2005, Knoxville, Tennessee, USA, Conf. Proc. C0505161 (2005) 3835
15. S. Sasaki et al., "Radiation Damage to Advanced Photon Source Undulators", PAC2005, Knoxville, Tennessee, USA, Conf. Proc. C0505161 (2205) 4126
16. K. Wittenburg, "The PIN-diode beam loss monitor system at HERA", DESY HERA Report, DESY-HERA-00-03, 2000
17. A. Piwinski, in Handbook of Accelerator Physics and Engineering, A. Chao and M. Tigner, eds, section 2.5.9 (World Scientific: 1998)

3.5 DESY Mourns Gustav-Adolf Voss

Prof. Gustav-Adolf Voss, former director of the accelerator division at Deutsches Elektronen-Synchrotron DESY, passed away on 5 October in Hamburg at the age of 84.

Gustav-Adolf Voss was the director of DESY's accelerator division from 1973 to 1994 and had a major impact on the development of particle accelerators worldwide. He was highly respected throughout the world and was a strong lifelong advocate of international cooperation in the field of science.

After studying physics and subsequently earning a Ph.D. at the Technical University of Berlin, Gustav-Adolf Voss had his first contact with DESY already when the research centre was founded in 1958/59. At that time, Voss was involved in the construction of the linear accelerator Linac I. In 1959 he went to Harvard University in Massachusetts, where he worked together with Kenneth Robinson to convert the Cambridge Electron Accelerator (CEA) into a storage ring, using a bypass. A special magnetic lens arrangement enabled the system to achieve electron-position collisions of several giga-electronvolts for the first time ever. This promising result led to the construction of additional storage rings for high energy physics worldwide, including the DORIS ring at DESY in Hamburg.

Gustav-Adolf Voss, who became an Assistant Director at Harvard in 1964, was appointed to DESY's Board of Directors in 1973. Under his leadership, DORIS was successfully put into operation and expanded. Beginning in 1975, he directed the planning and construction of the electron-positron storage ring PETRA, which achieved previously unprecedented collision energies. Under Voss' skilled leadership, this

accelerator was completed sooner than its American counterpart and constructed at a lower cost than planned. PETRA's design and construction are still considered exemplary for all modern electron storage rings. In 1979 PETRA achieved one of DESY's most notable scientific successes — the discovery of the gluon, the "glue" that holds together the quarks in the building blocks of atomic nuclei. PETRA was rebuilt several times later on and is today the most intense source of X-rays in the world.

Construction of Germany's largest particle accelerator, the electron-proton storage ring HERA, began at DESY in 1984. The facility was successfully put into operation in 1991. Many projects were entrusted to Gustav-Adolf Voss' capable hands, including the construction of the engineering buildings and the electron storage ring and the conversion of PETRA into a pre-accelerator. In addition, he recognized early on the great potential linear accelerators would have for the future of high energy physics. He also promoted promising and innovative accelerator concepts such as wakefield acceleration, as well as the further development of conventional normally conducting accelerators.

After Gustav-Adolf Voss retired in 1995, he remained in close contact with the DESY research centre and was always willing to provide personal assistance and expert advice.

In his later years, he actively promoted the SESAME synchrotron radiation source, which is currently being built in Jordan. The international SESAME research project brings together countries in the Middle East for the advancement of science. The facility also contains components from the former BESSY storage ring in Berlin.

Voss received many honours in recognition of his outstanding achievements in international physics, his important contributions to the development of particle accelerators in Europe and elsewhere, his support of Eastern European researchers after the collapse of the Soviet Union and his strong commitment to the SESAME project. Among other things, Voss was honoured with Germany's Order of Merit, an honorary doctorate from the University of Heidelberg and the renowned Tate Medal of the American Institute of Physics. In 2009 Gustav-Adolf Voss also became the first recipient of DESY's Golden Pin of Honour in recognition of his many achievements and great service to DESY.

With the death of Gustav-Adolf Voss, the DESY research centre has lost one of its most influential figures. His charismatic leadership, expert skills and foresight have greatly contributed to DESY's current standing as an internationally leading accelerator laboratory. We owe him our sincere gratitude and will always hold him in high regard.

3.6 Remembering Gustav-Adolf Voss

Herman Winick, SSRL, SLAC National Accelerator Laboratory, USA
Mail to: Winick@slac.stanford.edu

Gus and I met in 1959, 54 years ago, when we both came to the Cambridge Electron Accelerator (CEA) at Harvard University. We worked closely together there for 14 years. It was a wonderful experience and opportunity for me, and other young physicists, to learn from a master. Gus combined a broad understanding of accelerator theory with an extraordinary and broad comprehensive knowledge of the engineering of all the technical components of accelerators (injectors, radio frequency, magnets, power

supplies, vacuum, etc.). Once the CEA became operational in 1962, the Director of CEA, Professor Stanley Livingston, appointed Gus to be head of operations.

A few years later Gus and Ken Robinson conceived of the idea of transforming CEA from a cyclic synchrotron to an e+/e- colliding beam storage ring. Gus took charge of the implementation of the extremely complex and pioneering project, called the Bypass Project.

To focus his own efforts on this great challenge Gus asked me to take over responsibility for operations. I was honored that he had confidence that I could do this. But I told him that I wanted to be part of the excitement and challenge of the Bypass Project. Gus said "FINE, YOU CAN DO BOTH".

As many of you know, this was his management style. Everyone was welcome to contribute to developing a hot new project, as long as they continued their responsibilities for daily lab operations.

CEA closed in 1973. Gus returned to DESY at the end of 1972 and I went to SLAC at Stanford University. The Director of DESY at the time was the famous physicist Wolfgang Paul, who lured Gus back to DESY by offering him the job of Technical Director of the lab, in charge of all accelerator activities. Gus plunged into this job with his remarkable talent and energy, leading the lab in the reconfiguration of DORIS from a double to a single ring, followed by the PETRA, and HERA colliding beam projects. The success of these projects established DESY as a world-class accelerator lab, and brought recognition to Gus as the pre-eminent accelerator physicist in the entire world. He was courted as an advisor on accelerator projects all over the world.

In 1985 Gus nominated me for the Alexander von Humboldt senior scientist award. My wife and I spent 7 months at DESY in 1986, including touring Germany and all of Europe in a von Humboldt rented BMW. I became friendly with Professor Wolfgang Paul, who was President of the Alexander von Humboldt Stiftung at the time. Over dinner one night with Paul I complimented him on his many scientific accomplishments, which later led to the Nobel Prize in physics. I also said I was impressed that he was also Director of DESY. He told me that he only took the job as Director of DESY to fill a gap for a brief period between the founding director, Willie Jentschke, and his successor, Herwig Schopper. Paul also said that his most important accomplishment while Director of DESY was hiring Gus Voss.

Gus and I maintained contact from time to time from 1973 to the 1990's, when we found ourselves both on the Machine Advisory Committee (MAC) for the BESSY II project in Berlin. It was at a MAC meeting in Berlin in September, 1997 that I asked what would happen to the 0.8 GeV BESSY I machine, one of the most successful light sources in the world, when BESSY II began operation. I was surprised to be told that the BESSY I management planned to have a junk yard dealer cut BESSY I into small pieces and take it away at the lowest cost. I turned to Gus at this meeting and said that it was a shame to destroy such a valuable research tool, and that it should be upgraded and offered as a gift to the Middle East to serve as the centerpiece of a new light source facility there.

In 1997 there were about 50 light sources around the world. However there were none in the Middle East. My suggestion was the origin of what is now called SESAME.

Gus brought my suggestion to the attention of Middle East scientists at a November, 1997 meeting in Torino, Italy. When these scientist showed strong interest in the idea Gus contacted me and Ernst Weihreter at BESSY, and we got to work in developing an

upgrade plan to make BESSY I into a broad spectrum light source, including the x-ray range not covered by the original BESSY I.

I could not have picked a better person with whom to share this idea. Gus provided critical leadership for SESAME for several years, while he still had his health and energy. Before the end of 1997 Gus brought the idea to the attention of the BESSY management, the German Government, UNESCO and many prominent scientists, and Herwig Schopper in early 1998.

Due mainly to the efforts of Gus in the early days of SESAME, the project has developed to the point that 9 countries (Bahrain, Cyprus, Egypt, Israel, Iran, Jordan, Pakistan, Palestinian Authority and Turkey) have formed a Council, similar to the CERN Council, with complete responsibility for the project. SESAME is now on track to start operation at the end of 2015.

To stress his involvement and commitment, in the funeral announcement, in place of flowers and wreaths, the family asked for a donation towards a SESAME fund for the next generation of men and women wishing to enter physics (account details: Ute Binnie, Kto.-Nr. 2886411, BLZ 500 107 00, IBAN: DE3150010700 0002886411 BIC/SWIFT CODE: DEGUDEFF - DEGUSSA BANK, Regards: "Funeral Voss").

Most of you know that Gus Voss was a champion for Human Rights. For example, he brought Soviet dissidents to DESY, and he reached out to an Iranian physicist who was imprisoned for criticizing the Iranian regime.

Gus was a master builder of accelerators, an incomparable project leader, and a strong defender of Human Rights. He held a unique place of honor and respect in the worldwide accelerator community.

He will be remembered as a friend, a valued colleague, and a giant in the accelerator field.

He was truly Lord of the Rings.

4 Workshop and Conference Reports

4.1 FFAG'13 Workshop, TRIUMF, Vancouver, Canada, Sept 21-24, 2013

Shane Koscielniak, TRIUMF.
Mail to shane@triumf.ca

4.1.1 The Workshop

The 2013 International Workshop on Fixed Field Alternating Gradient (FFAG'13) Accelerators was held at the TRIUMF Laboratory, Vancouver, B.C., Canada, 21-24 September 2013. This was the 22nd in the series of workshops inaugurated in 1999, and the second held at TRIUMF. Highlights from the FFAG'13 are reported below. Details of the workshop, including a complete timetable and talks for download are available here: http://ffag13.triumf.ca

The FFAG'13 workshop followed the "20th International Conference on Cyclotrons and their Applications", also hosted by TRIUMF in Vancouver. In view of the similarity of FFAGs and cyclotrons - both in beam dynamics and in technology - this juxtaposition facilitated attendance of both meetings and the exchange of ideas to their mutual benefit. FFAG'13 had 26 delegates: 7 from Asia, 8 from Europe and 11 from North America. The workshop was chaired by Michael Craddock (University of British Columbia & TRIUMF) and a member of the team that built the 500 MeV H$^-$ ion cyclotron.

The workshop was organised in three broad themes: (1) Results from recently commissioned FFAGs; (2) Beam dynamics and computer codes; (3) New concepts and technology; and (4) Applications of FFAGs - in areas such as particle physics, cancer therapy, ADSRs, and medical and industrial irradiation.

In one respect, the wheel had turned full circle. At the previous workshop held in Vancouver, FFAG 2004, the idea of building a demonstration model of a linear-field non-scaling FFAG was first fleshed out. This model was inspired by a vision for muon acceleration and storage/decay rings for muon and neutrino physics. At this 2013 workshop, the Daresbury and Rutherford laboratory teams that built and operated the model, named EMMA, reported conclusive results from its two most important objectives: (i) demonstration of betatron tune resonance crossing, with low beam loss, and serpentine acceleration in a near-isochronous regime with fixed radio-frequency. Moreover, ten years on, the experimental discovery of a large neutrino mixing angle θ_{13} has galvanized the HEP community to pursue muon rings and a neutrino factory with renewed vigour.

4.1.2 Recent Results

The workshop opened with a report from the Kyoto University Research Reactor Institute (KURRI) FFAGs which operate 60% as a user test facility for Accelerator Driven Subcritical Reactor (ADSR) operation and nuclear engineering materials irradiation. The original booster ring injecting H$^+$ into the main ring has now been bypassed by an 11 MeV H$^-$ linac. KURRI is the host of an active collaboration pursuing future space-charge studies at their ring, and an experiment "S-Pod" that emulates tune crossing in a Paul Trap; a collaboration meeting was held during the workshop.

Kyushu University reported early commissioning results from their 150-MeV-capable scaling FFAG and injector cyclotron, including demonstrated acceleration to 80

MeV in July 2013 and the investigation of three possible working points in the tune diagram. Previously it was observed that stray magnetic flux from the ring magnets links the magnetic alloy (MA) cavities degrading their performance and leading to closed orbit distortion; both effects have been addressed by magnetic shielding and correction coils.

After opening talks on scaling FFAGs, the EMMA collaboration presented "lessons learned" from the world's first linear-field non-scaling FFAG: (i) one can construct a "cyclotron" with synchrotron size (i.e. small) magnets; (ii) the physical acceptance is very large; (iii) serpentine acceleration works; (iv) strong dependence of orbital period on betatron amplitude; (v) synchrotron-style closed orbit correction works; (vi) integer tune crossing leads to coherent oscillation, not to emittance growth; (vii) the large natural chromaticity leads to decoherence; (viii) specialist diagnostics are needed to detect orbit and envelope mismatch at injection. The next step is to eliminate as strong source of orbit distortion, believed to be from the injection septum.

4.1.3 New Concepts and Technology

Perhaps the most exotic application of FFAGs proposed at the workshop was their use in the muon-catalyzed transmutation of nuclear wastes – presented by Y.Mori and J.B. Lagrange. The required muon flux is enormous, and this might be obtained in an Emittance Recovery Internal Target (ERIT) ring configuration. There are many issues to be resolved.

P. McIntyre, Texas A&M University, reported the design of an (isochronous) Separated Orbit Cyclotron (SOC) proton driver for ADSR and medical applications. This machine which aims at the high-current frontier has many novel and distinguishing features, such as: multiple stacked beams, shared main magnetic field and yoke, and (of course) totally separated orbits[3] each with individual transport channels having an D,F doublet in each sector. Superconducting technologies have been identified for the main magnet and RF cavities. The many new features of the SOC along with high current operation lead to challenges for computer simulation, and a suite of codes has been integrated into the modeling process. Simulations have confirmed transport of beams up to 10 mA.

The Japan Proton Accelerator Research Complex (J-PARC) is considering gold ion acceleration. The Kyoto University group presented two scenarios for implementation relying on spiral sector FFAGs injecting either into the Rapid Cycling Synchrotron (RCS) at 75 MeV/u or the Main Ring at 117 MeV/u.

C. Johnstone, FNAL, presented a variety of FFAG lattices for medical, security, and energy applications. The power of the FFAG is that magnetic confinement terms (gradient, edge angles) can be varied independently to optimize machine parameters such as footprint, aperture, and tune giving remarkably compact designs with large dynamic aperture and significant ratio of extraction to injection momenta. Studies have progressed beyond optimization of lattices (including race-track type) to engineering investigation of magnets and RF cavities, and requirements for turn separation (i.e. extraction systems).

Brookhaven has an active proposal to collide electrons with heavy ions, the eRHIC. D. Trbojevic (BNL) presented studies for the electron ring. The non-scaling FFAG

---

[3] Machines of this type, dreamed of since the 1960's, are usually referred to as Separated Orbit Cyclotrons (SOC).

optics compacts a very large momentum range into a small physical aperture. This feature is used as the basis of two lattices that accelerate first from 1-1.9 GeV, and the second 2.8-10 GeV by recirculating through a common 0.9GeV linac. The former 2-pass lattice is a racetrack, while the latter 8-pass lattice is a ring around the RHIC tunnel. Chromaticity control is by sextupoles. The by-passes around the detectors at the existing RHIC intersection points are based on the compact medical gantry optics previously devised by Trbojevic. In an accompanying talk dedicated to a carbon ion gantry, Dr. Trbojevic contrasted the massive designs adopted at PSI and HIT (Heidelberg) against the compact low-mass designs resulting from the adoption of FDF linear-field FFAG optics. A two orders-of-magnitude weight reduction is believed possible. Trbojevic presented 3 designs of increasing sophistication that allow momentum scanning with fixed beam position and focusing at the patient, along with possible superconducting combined-function magnet technology for implementation.

M. Craddock gave a clear over-view of the cyclotron and FFAG family and their distinguishing features; and noted that there is a degree of freedom not yet exploited in sector cyclotrons (a.k.a. AVF cyclotrons), namely separate radial field profiles in the hill and valley sectors. With this new freedom, he has achieved tune flattening versus momentum in the vertical plane with only a modest increase in the range of the radial tune. It is the focusing in the vertical plane, which is weak and falling with energy that limits conventional designs.

The final two talks in this session were concerned purely with technology. W. Kleeven, of Ion Beam Applications, gave a very thorough account of the characterization of the magnet circuit of the IBA S2C2 synchro-cyclotron. Its superconducting coil is a signature component of the S2C2, which is anticipated to be a mainstay of their medical products line for years to come. The magnet has an iron core driven well into saturation by the coil, making the system very non-linear; for example the magnetic circuit depends on the level of excitation current. Several difficult calculations have been performed: the dynamical self-inductance, the mechanical stresses, AC losses and propensity to quench; the behaviour of all of these varies during the up- and down-ramps.

In a second talk, in the technology session, Johnstone elaborated space-charge tracking studies (by Suzie Sheehy, ASTeC/STFC) in support of 4-cell and 6-cell 1 GeV proton driver designs for beams up to 10 mA - first reported at FFAG'12 in Osaka Japan. A key ingredient is large voltage per turn, necessitating super-conducting cavities. P. Ostroumov's SRF group at ANL has advanced rectangular and elliptical concepts for a large aperture 200 MHz cavity; the former have better RF parameters but are vulnerable to multi-pactoring.

4.1.4 **Beam Dynamics**

Most of the talks had a good sprinkling of beam dynamics, but three highlights are reported. The first, purely theoretical, was a detailed analysis and optimization of serpentine acceleration in radial-sector scaling FFAGs with fixed RF leading to designs with large momentum range and credibly small energy gain per turn. The remarkable feature of this acceleration regime, first explored by E. Yamakawa (Kyoto University), is that it spans from Newtonian to ultra-relativistic.

The second, largely experimental, was a detailed account of the Slow Integer Tune Crossing in EMMA by J. Garland of the University of Manchester U.K. The linear

dependence between crossing speed and amplitude growth anticipated from the Fresnel integral by Guignard and Baartman is observed approximately, but there are several complicating effects: first that the accelerated orbit is not closed, and second that transverse-amplitude and chromatic dependence of betatron tune leads to strong decoherence.

The third, by T. Planche, is a technique for designing a cyclotron or FFAG starting from a prescription for its closed orbits parametrised as a Fourier series in polar coordinates and proceeding immediately to orbit length and expansion of the magnetic fields out of the mid-plane and finally to betatron tunes. Designs are selected by choosing an objective, such as isochronous or achromatic, followed by numerical optimization of the Fourier coefficients.

The theme of "computer simulation programs" (or codes) was strongly represented. A. Adelmann, Paul Scherrer Institute, gave an in-depth account of the OPAL code and the challenges presented by modelling MW-class accelerators: particle-loss prediction, multi-scale physics, and Coulombic space-charge effects. The OPAL architecture allows it to run computers ranging from laptops to massively-parallel clusters. A recent addition to the OPAL capability is to particle track through non-scaling FFAGs.

C. Johnstone reported three new software tools, developed by the "Particle Accelerator Corporation", to be used with COSY INFINITY. The "FFAG and Cyclotron Tools" (FACT) has 4 components: (i) a magnetic field expansion, including fringing fields, for non-linear elements with arbitrary edge angles; (ii) efficient multi-objective optimizers; (iii) a module that exports the fields in polar coordinates to classic codes such as CYCLOPS or ZGOUBI; and (iv) a batch processing manager. The interface with COSY allows for multi-turn tracking and high-order map generation. The tools are applied, for example, to a GeV-scale ultra-compact non-scaling FFAG proton driver.

Y.N. Rao traced the history of the CYCLOPS code, originated by M. Gordon and T. Welton, from Oak Ridge National Laboratory and then to Michigan State University and thence to TRIUMF where it was further developed by G. MacKenzie and C. Kost. Dr Rao then gave an account of the inner workings of CYCLOPS, and the accuracy that can be achieved – remarkably a few parts per million. Finally, he noted that certain authors have mis-represented the capabilities of CYCLOPS as inferior to their own codes, and gave ample evidence that such statements are incorrect.

F. Méot presented a survey of the physics capabilities of the ZGOUBI tracking code, along with a machine motivated exam0ple of each. A wide variety of magneto- and electro-static optical elements is supported, along with tracking through field maps. Beyond simple, multi-particle trajectory tracking, capabilities range from spin tracking to synchrotron radiation emission to particle losses and in-flight decays. In addition, the code permits fitting with constraints of several linear-optics objectives such as closed orbit, tunes, etc. As an extended example, Méot presented tracking through the Daresbury EMMA ring including the injection and extraction septa time dependence. The work was performed in the support of the analysis of experimental data taken at EMMA.

4.1.5 Future Prospects

The final session of the workshop was reserved for futuristic concepts and proposal. J.B. Lagrange (Kyoto University) led off with v-STORM (neutrinos from stored muons) which calls for achromatic racetrack-type decay rings with 10-20% momentum and

1000π µm transverse acceptances. The designs combine circular- and straight-scaling FFAG optics with intervening matching insertions. Three variants with similar acceptances but differing length of straight sections were compared and ranked by cost.

J. Pasternak (Imperial College London) continued with the muon theme. The unexpectedly large experimentally observed mixing angle θ_{13} has renewed the interest (in Europe, EUROnu, and the U.S. nuSTORM) in muon storage rings as the source of neutrino beams – but at lower energy, 10 rather than 25 GeV. Ring-and-linac, and RLA with NS-FFAG arcs, designs are being competitively pursued; and there is increased motivation for ionization cooling studies. Pasternak continued with an update on the extant muon storage ring, PRISM scaling FFAG at Osaka University. There is a proposal to improve injection and extraction by the insertion of four additional large aperture magnets. Finally, Pasternak presented recent advances in the study of non-linear, non-scaling nearly achromatic FFAGs illustrated first by a 3-8 GeV muon ring and second by a proton therapy gantry.

4.1.6   **Conclusion**

FFAGs have come a long way in the last decade. Two proton scaling FFAGs and one electron non-scaling FFAG are now operating for research purposes. The dream of magnetic lattices which are both nearly isochronous and nearly achromatic over a large momentum range is achieved; and, moreover, there are now successful methods for introducing matched insertions to provide long straight sections. As demonstrated by the examples reported at FFAG'13, FFAGs continue to be a fertile ground for applications in cancer therapy, particle physics and energy science, etc. Ten years on, after FFAG 2004, there is no diminishment of the energy, enthusiasm and creativity of that earlier workshop.

The next FFAG Workshop, FFAG'14, will be held at Brookhaven National Laboratory in Fall 2014, organized by Scott Berg, François Méot and Dejan Trbojevic. For details of FFAG'14 see: http://www.bnl.gov/ffag14/ We wish them every success.

4.2   **Eighth International Accelerator School for Linear Colliders**

Avni Aksoy (IAT/Ankara Univ.) and Weiren Chou (Fermilab)
mail to: avniaksoy@ankara.edu.tr, chou@fnal.gov

The Eighth International Accelerator School for Linear Colliders was held at Rixos Downtown Hotel, Antalya, Turkey from December 4 to December 15 2013 (http://www.linearcollider.org/school/2013/). This school, which is focused on accelerator science related to the next-generation TeV-scale colliders including the International Linear Collider (ILC), the Compact Linear Collider (CLIC) and other advanced accelerators, continued the successful series: 2006 in Japan, 2007 in Italy, 2008 in the U.S., 2009 in China, 2010 in Switzerland, 2011 in the U.S. and 2012 in India. This year's school was organized by the Linear Collider Collaboration (LCC) and the ICFA Beam Dynamics Panel. The Institute of Accelerator Technologies (IAT) of Ankara University hosted the school. The school was focused on training PhD students, postdocs and young researchers, especially young experimentalists.

The interest to the school was very pleasurable. We have selected 54 highly qualified students from an increased pool of 254 applications. We received applicants

from 38 countries, of which 66% were from countries having programmes in high-energy physics. The attendees at the LC school are graduate students, postdoctoral fellows and junior researchers from around the world, including physicists who are considering a career change from experimental physics to accelerator physics. The country distribution of the accepted students includes 15 from Asia and Oceania, 34 from Europe and 5 from North and South America. For personal reasons two admitted students could not attend the school.

The first two and half days were plenary sessions with introductory lectures: introduction, ILC, CLIC, linac basics and beam instrumentation basics. This gave the students a wider vision of the entire field. After the plenary sessions the students were divided into two parallel classes. Class A (28 students) for accelerator physics and Class B (24 students) for accelerator technology. Class A, accelerator physics, included four lectures: e+ and e- sources, linacs, damping rings and ring colliders, and beam delivery systems. Class B, accelerator technology, also included four lectures: room temperature RF, superconducting RF, beam instrumentation and high power and low level RF. Dividing the class, following introductory common lectures into two tracks was introduced in previous schools and enables a more in-depth school and opens the possibility of accepting some returning students. These students successfully met the challenge of an intensive 11-day education program.

All lecturers were carefully chosen and are renowned scientists in their respective fields. They not only gave lectures during the day, but also gave tutorials and helped students with their homework in the evenings. They designed the examination problems and graded them. The final exam on the last day lasted four-and-a-half hours. All 52 students took the final exam. The lecture slides and homework problems can be found on the school web site.

The exam problems were different for Class A and B but were equally challenging. Most students did well. The top 8 students (4 from Class A and 4 from Class B) were honored at the banquet and each was awarded a certificate and a book (*Reviews of Accelerator Science and Technology*, Volume 5, edited by A. Chao and W. Chou, and published by World Scientific in 2012).

In addition to lectures, the students attended two excursions. One was to the old town of Antalya and the second to the Side town and the ancient Aspendos theatre. Making visit to these beautiful and wonderful places of Turkey gave them a much needed break during their busy school work. Since there exists no accelerator facility around Antalya region students could not make any visit to a facility.

Throughout the school period, the students were encouraged to make new friends since this was a once-in-a-lifetime opportunity for many of them to meet with other young talented people from different origins who shared the same interest (accelerators) and career goals (future colliders). Some of the friendships nurtured at the school will last a lifetime.

The Local Committee (LC) was chaired by Prof. Dr. Omer Yavas who is Director of IAT and Turkish Accelerator Center (TAC) Collaborarion. Other members of LC from IAT, Dr. Avni Aksoy, Dr. Ozlem Karsli, Dr. Sinan Kuday and Prof. Dr. Suat Ozkorucuklu from İstanbul University spent much effort for a successful organization. Cynthia Sazama and Suzanne Weber from the Fermilab Conference Office played a big role throughout the school planning and preparation. We are thankful to all of them for their dedication and wonderful work.

The school received generous sponsorship from a number of funding agencies and institutions from all over the world: U.S. National Science Foundation (NSF), Fermilab, SLAC, CERN, DESY, INFN, IN2P3, CEA, KEK, IHEP, RRCAT, POSTECH and TAC Project.

We carried out a student survey on the last day of school. The results will be given to the lecturers and committee members for improvements for future schools.

Based on the interest, demand and success of the first eight schools, it was decided to continue in 2014. The ninth school will take place in Vancouver, Canada. The venue and dates are yet to be chosen.

2013 LC Accelerator School – Applicants Distribution

254 applicants from 38 countries

- 66% from 15 HEP countries
- 23% from 23 other countries
- 11% unknown

Regional Distribution of Applicants

Asia/Oceania	Europe/Africa	America	Unknown
102	98	25	29

Distribution of Applicants in HEP Countries

China	India	Japan	Korea	Finland	France	Germany	Italy	Russia	Serbia	Switzerland	Turkey	U.K.	Mexico	U.S.A.
23	43	5	2	2	3	4	6	4	1	5	45	5	3	16

Distribution of Applicants in Other Countries

Azerbaijan	Bangladesh	Indonesia	Iran	Kenya	Nepal	Pakistan	Srilanka	Vietnam	Algeria	Belarus	Egypt	Greece	Madagascar	Morocco	Poland	Romania	Sudan	Ukraine	Brazil	Colombia	Cuba	Guatemala
2	2	4	11	2	1	4	1	2	2	1	6	1	2	1	3	2	1	4	2	1	2	1

2013 LC Accelerator School – Students Distribution

- 54 students selected from 18 countries
- 94% from 15 HEP countries
- 6% from 3 other countries

Regional Distribution of Students

Asia/Oceania	Europe/Africa	America
15	34	5

Country Distribution of Students

China	India	Iran	Japan	Korea	Belarus	Finland	France	Germany	Italy	Poland	Romania	Russia	Switzerland	Turkey	UK	Mexico	USA
9	2	1	3	2	1	2	1	2	2	1	1	2	4	13	3	1	4
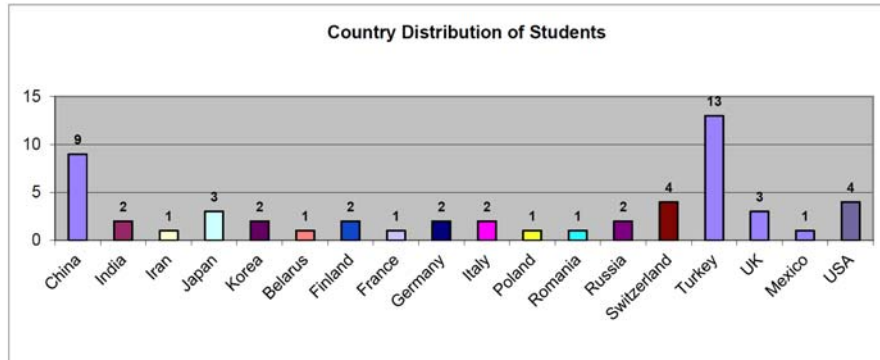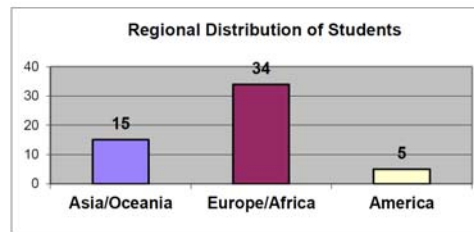
5 Recent Doctorial Theses

5.1 Lattice Design and Beam Dynamics Study of ERL-FEL Test-Facility at IHEP, Beijing

Xiaohao Cui
Mail to: cuixh@ihep.ac.cn

Graduation date: 23 May 2013
Institution: Institute of High Energy Physics, CAS, China
Supervisor: Prof. Jiuqing Wang

Abstract:
ERL and FEL are both considered as candidates of the fourth generation light source, since both of them are based on linac technologies it is possible to combine FEL into an ERL facility, resulting in a compact two-purpose light source. The work of this thesis is on lattice design and Beam dynamics study of the ERL-FEL test-facility at IHEP. Based on a study of previous designs of other facilities, parameters of the test-facility are optimized in order to minimize the effects of space charge effects (SC) and coherent synchrotron radiation (CSR). The ERL bunch length at the radiator and the ERL energy spread before the beam dump are also compressed by a longitudinal phase space manipulation.

Moreover, the multipass beam-break-up effect (BBU) in a ERL-FEL two-purpose machine is studied. We found that two effects emerge as a result of the introduction of FEL beams: a reduction in the threshold current and a central orbit fluctuation for ERL current under threshold. Due to the fact that the repetition rate of FEL bunches is much smaller than that of ERL, the introduction of FEL beam should not have a fatal effect on the threshold current. As for the orbit fluctuation, we gave a simple model and found a resonance relation between the voltage spread and FEL repetition rate. by choosing an appropriate FEL bunch repetition rate, the central orbit fluctuation amplitude can be well controlled.

5.2 Design of the Extraction Arc for the 2nd Beam Line of the Free–Electron Laser FLASH

Matthias Scholz
Mail to: matthias.scholz@desy.de

Graduation date: 27 September 2013
Institution: University of Hamburg
Supervisors: Prof. Dr. J. Rossbach (University Hamburg), Dr. W. Decking (DESY) and Dr. T. Limberg (DESY)

Abstract
In the thesis the design of the extraction arc for the second beam line of the FEL (Free-Electron Laser) user facility FLASH at DESY Hamburg is presented. Both beam lines share the same linear accelerator and the separation section is placed immediately

downstream of the last accelerating module. The constraints for the extraction arc are determined by the beam line layout of the existing machine, by the building environment of the new beam line, and, most essential, by the effect of coherent synchrotron radiation (CSR) on the beam. The impact of CSR is presented and it is show how to mitigate these effects and how that affects the beam line design. The final layout of the extraction arc including the following matching section is presented. This layout fulfills all given constraints and is capable of providing the required electron beam quality for FEL operation. In order to prove this, a start–to–end simulations for different bunch charges and for two different wave lengths is also presented.

5.3 Transverse Phase Space Studies with the New CDS Booster Cavity at PITZ

Grygorii Vashchenko
Mail to: grygorii.vashchenko@desy.de

Graduation date: 30 September 2013
Institution: University of Hamburg
Supervisors: Prof. Dr. J. Rossbach (University Hamburg) and Dr. F. Stephan (DESY)

Abstract

Light is one of the main tools for the investigation of natural phenomena. Light produced with the help of synchrotron machines serves to investigate many phenomena in natural sciences for many years. However the syn- chrotron light has a limited degree of spatial coherence, restriction on the minimum achievable pulse duration at the level of about 30 ps and not suf- ficient brilliance to perform a lot of experiments. With the invention of free electron lasers (FELs) new opportunities are opened as the light produced by the free electron lasers is spatially coherent, the pulse duration of the produced light can be in the order of 10 fs and below and the brilliance is much higher compared to synchrotron light. To produce high quality laser light with a short wavelength free electron lasers like the European XFEL and FLASH require electron beams with a high charge and low transverse emittance. The photo injector test facility at DESY, Zeuthen site, was built with the aim to develop and characterize electron sources for future usage at FLASH and the European XFEL. The emittance of the produced electron beam plays a key role as it influences the final brilliance and the minimum achievable wavelength of the produced laser light. This work is devoted to investigations of the emittance of electron beams with different charges. The emittance of the electron beam depends on many machine parameters such as UV laser pulse shape and its size, solenoid fo- cusing current and accelerating cavities settings. Methodical studies of the emittance dependencies on these parameters were done in simulations using a particle tracking code as well as experimentally.

5.4 Optimization Studies and Measurements for Ultra-low Emittance Lattices

Simone Maria Liuzzo
Mail to: rho.quadro@gmail.com

Abstract:

In recent years the interest in the design of low horizontal emittance ($\varepsilon_X \sim 100$ pmrad) lattices for light sources and colliders has become very strong. Light sources benefit from a higher brilliance and coherence, colliders from higher luminosity. Various lattice designs have been developed, evidencing strong requirements in terms of non-linear optimization to obtain a suitable stable phase space region. The optimization of the parameters of interest iterates between linear lattice properties (horizontal emittance, beta and dispersion functions, phase advances, and the like) and nonlinear quantities (such as tune variation with amplitude, chromaticity and resonant driving terms). The atmatch optimizer developed using Accelerator Toolbox has been used to perform this optimizations and in particular to improve the dipole field distribution (reducing the emittance by 18%) and to minimize the variation of tune with amplitude and momentum.

The optimal solution has to maintain its properties also in presence of lattice errors, that introduce modulation of beta functions, spurious dispersion, and coupling, leading to a deterioration of the emittance and of the stable phase space area compared to the ideal lattice. It is then necessary to study the impact of lattice errors and to define adequate techniques to recover the nominal machine and beam parameters during the commissioning of the accelerator as well as during operation. Experimental results on the Low Emittance Tuning (LET) technique are presented in this thesis, evidencing the possibility to perform corrections of coupling and beta-beating using only orbit steerers in lattices with sextupoles. An analysis of the influence of errors on the stable phase space region and on emittance is also presented.

5.5 Study on the Beam Dynamics of the CLIC Main Linac and the Beam Optics of the ILC/CEPC Final Focus System

Yi Wei Wang
Mail to: wangyw@ihep.ac.cn

Abstract

The international particle physics community has agreed that the results of the Large Hadron Collider (LHC) will need to be complemented by experiments at a lepton

collider in the TeV energy range. This kind of lepton collider will provide more detailed study on the physics such as Higgs boson. The energy range and detailed physics requirements of the lepton collier will be determined by the large integrated luminosity after full energy running (14TeV, by 2015-2016) of LHC for some years. As the only two existing linear e+e- collider projects, the study for the Compact Linear Collider (CLIC) and International Linear collider (ILC) are keeping go ahead: The CLIC working group has published the CLIC Concept Design Report (CDR) in 2012. The ILC working group has published the ILC Reference Desing Report (RDR) and Technical Design report (TDR) respectively in 2007 and 2013. On 4th Jun 2012, the detectors of ATLAS and CMS found the Higgs boson. As the light mass of the Higgs boson (about 126GeV), a circular e+e- collider as a Higgs Factory become closer to reach. The Circular Electron Positron Collider (CEPC) proposed by IHEP is such a circular collider whose center-of-mass energy is 240GeV and circumference is 50km or 70km. The CEPC can be upgraded to be a Super Proton Proton Collider (SPPC) whose center-of-mass energy is 50 to 70TeV and the same circumference as CEPC. This thesis concentrates its subjects on the CLIC main linac beam dynamics and ILC/CEPC Final Focus System beam optics. The substantial works of these researches can be summarized as follows: 1) For the reason of easily to upgrade the machine, we use the Ecm =3TeV CLIC accelerating structure for the lattice design of the Ecm =1TeV CLIC main linac and make optimization based on the beam dynamics study. As we use the same design principles as 3TeV CLIC main linac, this optimization is basically identical to the 3TeV one. This's the first optimization of main linac lattice when the accelerating technology changed from 30GHz to 12GHz. 2) The CLIC main linac accelerating structures will be powered by the Power Extraction and Transfer Structures (PETS) located in the drive beam decelerators. When the drive beam traverses the PETS with an offset, wakefields are induced in the PETS extractor. These wakefields can slip into the coupler of accelerating structures in the main linac and kick the main beam. The impact of such dipolar kicks is studied, and tolerances based on analytical estimations are derived. Numerical simulations obtained using the tracking code PLACET confirms the analytical estimates. 3) The present ILC Final Focus System (FFS) correct the chromaticity for both horizontal and vertical planes. We proposed a new chromaticity correction scheme: Decrease the vertical chromaticity by increasing the horizontal beta function at IP, then use less sextuple to make chromaticity correction mainly on the vertical plane. Compared with the results of present design, we get a smaller vertical beam size and a not so large horizontal beam size as the decreased horizontal chromaticity. This new chromaticity correction scheme will lead to a more compact, easier to tune and less beamstrahlung FFS when roughly keeping the luminosity. Of course, a shorter bunch is necessary for mitigating the hourglass effect. 4) For the low power parameters of CEPC, we present a preliminary study on the CEPC FFS design with the local chromaticity correction scheme. Keywords: CLIC, main linac, ILC, Final Focus System, CEPC

6   Forthcoming Beam Dynamics Events

6.1   1st Topical Low Emittance Ring (LOWεRING) Workshop on Instabilities, Impedance and Collective Effects

Dates: 16 - 17 January 2014
Place: Synchrotron SOLEIL, France
Chairmen: R. Nagaoka (ryutaro.nagaoka@synchrotron-soleil.fr)
                 E. Al-Dmour (eshraq.al-dmour@maxlab.lu.se)
                 F. Antoniou (fanouria.antoniou@cern.ch)
                 T. Demma (demma@lal.in3p3.fr)
                 E. Karantzoulis (karantzoulis@elettra.trieste.it)
                 A.-S. Müller (anke-susanne.mueller@kit.edu)
                 G. Rumolo (giovanni.rumolo@cern.ch)

We are pleased to announce that a Topical Workshop on Instabilities, Impedance and Collective Effects shall be organized by Synchrotron SOLEIL on the 16th and 17th January 2014 as a sub-series of Low Emittance Rings (LOWεRING) Workshops:
                 http://www.synchrotron-soleil.fr/Workshops/2014/TWIICE

The goal of the workshop is to gather experts working on collective beam instabilities and related subjects in low emittance lepton rings. The latter include damping rings, test facilities for linear colliders, B‑factories and electron storage rings. The theme will be generically all potentially important collective effects that may arise and jeopardise the performance of currently running and future low emittance lepton rings. Participants will benefit from the experience of colleagues who have theoretically and experimentally studied the physics behind, and have developed and operated countermeasures.

This shall be the first topical workshop after the three general ones organised in the past since 2010:
        LER2010: http://ler2010.web.cern.ch/
        LER2011: http://lowering2011.web.cern.ch/lowering2011/
        LER2013: http://www.physics.ox.ac.uk/lowemittance13/

The state of the art in the design of accelerator systems in light source storage rings has today many challenges and issues in common with those of linear collider damping rings and future e+/e- circular collider upgrade projects. The series of workshops specifically aims at strengthening the collaborations within the low emittance ring community, including the LOWεRING collaboration network and the DLSR (Diffraction Limited Storage Ring)workshops community. The workshop is supported by the EuCARD2 project.

Workshop sessions will include the following topics:
        - Impedances and Instabilities
        - Two-Stream Instabilities
        - Particles Scattering
        - Coherent Synchrotron Radiation Instabilities
        - Instrumentation and Feedback

6.2 EIC14 Workshop

Dates: 17-21 March 2014
Place: Jefferson Lab (Virginia, USA)
Co-Chairs: Andrew Hutton, Yuhong Zhang

We are happy to announce that EIC14 -- The International Workshop on Accelerator Science and Technology for Electron-Ion Colliders -- will be held from March 17 to 21, 2014 at Thomas Jefferson National Accelerator Facility (Jefferson Lab), Newport News, Virginia, USA.

An electron-ion collider is likely one of the future large accelerator facilities for high energy and nuclear physics. Presently, there are five proposals under active development worldwide. They are LHeC at CERN and ENC at GSI in Europe; eRHIC at Brookhaven National Laboratory and MEIC at Jefferson Lab in the USA; and HIAF at Institute of Modern Physics in China. Each of these proposed facilities covers a distinct energy range and adopts either ring-ring or linac(ERL)-ring collider scenarios. In order to deliver high machine performance to satisfy the science needs, an array of advanced accelerator concepts and technologies has been integrated into each of these accelerator designs. Further, these facility proposals share many common accelerator R&D elements, such as high energy/current multi-pass energy recovery linacs (ERL); cooling of proton and ion beams; highly polarized sources and colliding beams. Collaborations among the researchers working on these facility proposals are emerging and growing. This workshop will provide a forum for exchanging new ideas, concepts, and progress in accelerator technology development for electron-ion colliders. The workshop will be organized by four working groups:

- Beam physics (covering beam dynamics, beam-beam, collective effects, polarization, cooling and beam diagnostics, etc.)
- Interaction Region, detector integration and backgrounds
- Accelerator technology topic 1: SRF and ERL
- Accelerator technology topic 2: electron/positron sources, proton/ion sources, and polarimetry

Additional information about EIC14 workshop could be found in the workshop web site: http://www.jlab.org/conferences/eic2014/index.html

6.3 ICFA Mini-Workshop on "Electromagnetic Wake Fields and Impedances in Particle Accelerators".

Dates: 23-29 April 2014
Place: Erice (Sicily, Italy)
Co-Chairs: Vittorio Vaccaro (vittorio.vaccaro@na.infn.it)
                 Elias Métral (Elias.Metral@cern.ch).

Scientific and commercial applications of particle accelerators require ever higher performance in the sense of large beam current, small momentum spread, high repetition rate, small emittance and other beam characteristics...

The stringent requirements of new and more sophisticated experiments and applications may conflict with beam stability and quality because of the strong electromagnetic interaction of the beam current with the surrounding equipment.

An awareness of the importance of these interactions gradually emerged in the 1960s. In 1966, they were put on a firmer conceptual basis with the introduction of the concept of the impedance of an accelerator.

Nowadays accelerator designers are keenly aware of the need to manage their "impedance budget" in order to avoid instabilities and other undesirable consequences.

Large values of the Accelerator Impedance influence the motion of trailing particles, in the longitudinal and transverse directions, leading to energy loss, beam instabilities, or secondary effects such as excessive heating of sensitive components at or near the chamber wall (the so-called beam-induced RF heating). Beam-induced RF heating has been observed in many places, for instance in several CERN LHC components during the 2011 and 2012 runs when the bunch/beam intensity was increased and/or the bunch length reduced. This caused beam dumps and delays in operation (reducing integrated luminosity) as well as considerable damage to some equipment. These limitations could be more severe in future operation.

Hence, the importance of gathering experts on the electromagnetic interaction between a particle beam and its surrounding environment to review all the recent activities and progress in theory, simulations, bench and beam-based measurements with a view to tackling these challenges.

7 Announcements of the Beam Dynamics Panel

7.1 ICFA Beam Dynamics Newsletter

7.1.1 Aim of the Newsletter

The ICFA Beam Dynamics Newsletter is intended as a channel for describing unsolved problems and highlighting important ongoing works, and not as a substitute for journal articles and conference proceedings that usually describe completed work. It is published by the ICFA Beam Dynamics Panel, one of whose missions is to encourage international collaboration in beam dynamics.

Normally it is published every April, August and December. The deadlines are 15 March, 15 July and 15 November, respectively.

7.1.2 Categories of Articles

The categories of articles in the newsletter are the following:
1. Announcements from the panel.
2. Reports of beam dynamics activity of a group.
3. Reports on workshops, meetings and other events related to beam dynamics.
4. Announcements of future beam dynamics-related international workshops and meetings.
5. Those who want to use newsletter to announce their workshops are welcome to

do so. Articles should typically fit within half a page and include descriptions of the subject, date, place, Web site and other contact information.

6. Review of beam dynamics problems: This is a place to bring attention to unsolved problems and should not be used to report completed work. Clear and short highlights on the problem are encouraged.

7. Letters to the editor: a forum open to everyone. Anybody can express his/her opinion on the beam dynamics and related activities, by sending it to one of the editors. The editors reserve the right to reject contributions they judge to be inappropriate, although they have rarely had cause to do so.

The editors may request an article following a recommendation by panel members. However anyone who wishes to submit an article is strongly encouraged to contact any Beam Dynamics Panel member before starting to write.

7.1.3 How to Prepare a Manuscript

Before starting to write, authors should download the template in Microsoft Word format from the Beam Dynamics Panel web site:

<div align="center">

http://www-bd.fnal.gov/icfabd/news.html

</div>

It will be much easier to guarantee acceptance of the article if the template is used and the instructions included in it are respected. The template and instructions are expected to evolve with time so please make sure always to use the latest versions.

The final Microsoft Word file should be sent to one of the editors, preferably the issue editor, by email.

The editors regret that LaTeX files can no longer be accepted: a majority of contributors now prefer Word and we simply do not have the resources to make the conversions that would be needed. Contributions received in LaTeX will now be returned to the authors for re-formatting.

In cases where an article is composed entirely of straightforward prose (no equations, figures, tables, special symbols, etc.) contributions received in the form of plain text files may be accepted at the discretion of the issue editor.

Each article should include the title, authors' names, affiliations and e-mail addresses.

7.1.4 Distribution

A complete archive of issues of this newsletter from 1995 to the latest issue is available at

<div align="center">

http://icfa-usa.jlab.org/archive/newsletter.shtml.

</div>

This is now intended as the primary method of distribution of the newsletter.

Readers are encouraged to sign-up for electronic mailing list to ensure that they will hear immediately when a new issue is published.

The Panel's Web site provides access to the Newsletters, information about future and past workshops, and other information useful to accelerator physicists. There are links to pages of information of local interest for each of the three ICFA areas.

Printed copies of the ICFA Beam Dynamics Newsletters are also distributed (generally some time after the Web edition appears) through the following distributors:

Weiren Chou	chou@fnal.gov	North and South Americas
Rainer Wanzenberg	rainer.wanzenberg@desy.de	Europe[++] and Africa
Toshiyuki Okugi	toshiyuki.okugi@kek.jp	Asia[**] and Pacific

[++] Including former Soviet Union.

[**] For Mainland China, Jiu-Qing Wang (wangjq@mail.ihep.ac.cn) takes care of the distribution with Ms. Su Ping, Secretariat of PASC, P.O. Box 918, Beijing 100039, China.

To keep costs down (remember that the Panel has no budget of its own) readers are encouraged to use the Web as much as possible. In particular, if you receive a paper copy that you no longer require, please inform the appropriate distributor.

7.1.5 Regular Correspondents

The Beam Dynamics Newsletter particularly encourages contributions from smaller institutions and countries where the accelerator physics community is small. Since it is impossible for the editors and panel members to survey all beam dynamics activity worldwide, we have some Regular Correspondents. They are expected to find interesting activities and appropriate persons to report them and/or report them by themselves. We hope that we will have a "compact and complete" list covering all over the world eventually. The present Regular Correspondents are as follows:

Liu Lin	Liu@ns.lnls.br	LNLS Brazil
Sameen Ahmed Khan	Rohelakan@yahoo.com	SCOT, Oman
Jacob Rodnizki	Jacob.Rodnizki@gmail.com	Soreq NRC, Israel
Rohan Dowd	Rohan.Dowd@synchrotron.org.au	Australian Synchrotron

We are calling for more volunteers as Regular Correspondents.

7.2   ICFA Beam Dynamics Panel Members

Name	eMail	Institution
Rick Baartman	baartman@lin12.triumf.ca	TRIUMF, 4004 Wesbrook Mall, Vancouver, BC, V6T 2A3, Canada
Marica Biagini	marica.biagini@lnf.infn.it	LNF-INFN, Via E. Fermi 40, C.P. 13, Frascati, Italy
John Byrd	jmbyrd@lbl.gov	Center for Beam Physics, LBL, 1 Cyclotron Road, Berkeley, CA 94720-8211, U.S.A.
Yunhai Cai	yunhai@slac.stanford.edu	SLAC, 2575 Sand Hill Road, MS 26 Menlo Park, CA 94025, U.S.A.
Swapan Chattopadhyay	swapan@cockroft.ac.uk	The Cockcroft Institute, Daresbury, Warrington WA4 4AD, U.K.
Weiren Chou (Chair)	chou@fnal.gov	Fermilab, MS 220, P.O. Box 500, Batavia, IL 60510, U.S.A.
Wolfram Fischer	wfischer@bnl.gov	Brookhaven National Laboratory, Bldg. 911B, Upton, NY 11973, U.S.A.
Yoshihiro Funakoshi	yoshihiro.funakoshi@kek.jp	KEK, 1-1 Oho, Tsukuba-shi, Ibaraki-ken, 305-0801, Japan
Jie Gao	gaoj@ihep.ac.cn	Institute for High Energy Physics, P.O. Box 918, Beijing 100039, China
Ajay Ghodke	ghodke@cat.ernet.in	RRCAT, ADL Bldg. Indore, Madhya Pradesh, 452 013, India
Ingo Hofmann	i.hofmann@gsi.de	High Current Beam Physics, GSI Darmstadt, Planckstr. 1, 64291 Darmstadt, Germany
Sergei Ivanov	sergey.ivanov@ihep.ru	Institute for High Energy Physics, Protvino, Moscow Region, 142281 Russia
In Soo Ko	isko@postech.ac.kr	Pohang Accelerator Lab, San 31, Hyoja-Dong, Pohang 790-784, South Korea
Elias Metral	elias.metral@cern.ch	CERN, CH-1211, Geneva 23, Switzerland
Yoshiharu Mori	mori@rri.kyoto-u.ac.jp	Research Reactor Inst., Kyoto Univ. Kumatori, Osaka, 590-0494, Japan
George Neil	neil@jlab.org	TJNAF, 12000 Jefferson Ave., Suite 21, Newport News, VA 23606, U.S.A.
Toshiyuki Okugi	toshiyuki.okugi@kek.jp	KEK, 1-1 Oho, Tsukuba-shi, Ibaraki-ken, 305-0801, Japan
Mark Palmer	mark.palmer@cornell.edu	Wilson Laboratory, Cornell University, Ithaca, NY 14853-8001, USA
Chris Prior	chris.prior@stfc.ac.uk	ASTeC Intense Beams Group, STFC RAL, Chilton, Didcot, Oxon OX11 0QX, U.K.
Yuri Shatunov	Yu.M.Shatunov@inp.nsk.su	Acad. Lavrentiev, Prospect 11, 630090 Novosibirsk, Russia
Jiu-Qing Wang	wangjq@ihep.ac.cn	Institute for High Energy Physics, P.O. Box 918, 9-1, Beijing 100039, China
Rainer Wanzenberg	rainer.wanzenberg@desy.de	DESY, Notkestrasse 85, 22603 Hamburg, Germany

The views expressed in this newsletter do not necessarily coincide with those of the editors. The individual authors are responsible for their text.